Photocatalytic coatings in the built environment

Nuño, Manuel

Award date:
2015

Awarding institution:
University of Bath

Photocatalytic Coatings in the Built Environment

Manuel Nuño

A thesis submitted for the degree of Doctor of Philosophy

University of Bath

Department of Architecture and Civil Engineering

July 2015

PHOTOCATALYTIC COATINGS IN THE BUILT ENVIRONMENT

Manuel Nuño

A dissertation submitted to the University of Bath in accordance with the requirements of the award of the Degree of Doctor of Philosophy in the Department of Architecture and Civil Engineering

Authors' Declaration

I declare that the work in this dissertation was carried out in accordance with the requirements of the University's Regulations and Code of Practice for Research Degree Programmes and that it has not been submitted for any other academic award. Except where indicated by specific reference in the text, the work is the candidate's own work, work done in collaboration with, or with the assistance of, others, is indicated as such. Any views expressed in the dissertation are those for the author.

SIGNED:  DATE: 11/09/2015

Acknowledgements

I would like to thank my supervisors, Dr Richard J. Ball and Prof. Chris R. Bowen for their support during these past years, I learned a lot during our discussions about new ideas; their comments and suggestions have improved every published article and of course, this thesis. I am also deeply indebted to them for the knowledge I acquired during the three (ish) years.

I am also very grateful to them for encouraging me to collaborate with fantastic people from whom I learned and with whom I enjoyed working, Dr Vana Adamaki, (future Dr) Andrea Giampicolo, Prof. Rajnish Kurchania, and of course, my dear boss, Dr^2 Gianluca Pesce. Thank you very much.

This thesis would not have been possible without the help of Dr John Mitchels and Ursula Potter from the MAS suit, where I learned so many things (including electron microscopy!); Prof. Geoffrey Allen and his contagious passion for chemistry, and the amazing staff members of the Department of Architecture and Civil Engineering.

Besides chemistry, I have to thank all the friends I have made during these years, with a special mention to Fionn McGregor, Nick Williams, Alistair Bradley, Dominic Van Der Waals and (obviously) the best housemates/officemates/friends ever, Dragoş Naicu, Daniel Brandon and Lizette Reitsma. You made this experience unforgettable. Thank you very much!

Also, thanks to my office colleagues/friends in 6E 4.15, the best office where we shared meals, celebrations and interesting discussions (that usually finished in Parade). The lack of sunlight was balanced thanks to you.

Thanks to the Bath Saracens R.U.C. for the last four seasons, not only rugby, but our "exquisite social events"; with a special mention to Liam Emmett, Robbie, Mr Biss and Russell, amongst others. We had a great time!

I also have to acknowledge Dr Con Robert McElroy, the best friend (and supervisor) I possibly could have made during my time in York. Thank you for all your help, you know this thesis would not be possible without you.

I want to express my gratitude to my best friends, Alejandro Beltrán, Santiago Silvero and Daniel Nosti for not letting the distance to undermine our friendship and be there for me at any time of the day (or night). One day I will pay it back!

A special mention has to be dedicated to my partner in crime/landlady Diana Alves, thanks to you, we faced the end of the thesis and the uncertainty of future together, making it less horrible (or more enjoyable!); and this is just the beginning.

To conclude, I want to dedicate this thesis to my parents Águeda and Manuel and my amazing sister Ague. If I have been able to finish this thesis, it is entirely thanks to you. I will never be able to express how all the patience, affection and encouragement I received from you helped me throughout my entirely life. I could not ask for more. You suffered the most the "distance" between us during this time, but you have always been there for me. Os quiero mucho.

Abstract

The photocatalytic properties of titanium dioxide have been widely studied over recent decades since the discovery in 1972 of water photolysis by TiO_2 electrodes. There are a number of different TiO_2 polymorphs. Rutile and anatase are the most studied due to their chemo-physical properties. Under ultraviolet light, TiO_2 is able to absorb photons, creating a charge separation on the surface, an electron and a positive "hole". This electron-hole pair then reacts with water and oxygen, generating radicals, very unstable and reactive species which show great potential for neutralisation of pollutants. In the introduction the state of art of photocatalysis; chemo-physical principles, applications and current analysis are described. A number of protocols to test photoactivity are discussed with particular emphasis on the importance of gas phase reactions.

The development of a novel system to study gas phase reactions by mass spectrometry was explored, detailing the conditions and parameters that were optimised. This instrument was used to analyse photocatalytic properties of TiO_2 powders and photocatalytic coatings under different UV light conditions. The results showed how TiO_2 in the form of anatase and rutile removed nitrogen and carbon dioxide under different UV light sources, with anatase being more effective.

A comprehensive study of several commercially available TiO_2 powders and coatings was performed to identify the differences between photocatalytic properties, using electron microscopy, Raman and UV-vis diffusive spectroscopy, X-ray diffraction and X-ray photoelectron spectroscopy. An important question that was answered in this thesis is whether the physical properties of nanoparticles or their electronic properties are critical for their photocatalytic behaviour. Results for anatase powders of different particle size and surface area showed how the positioning of their electronic band gap with the wavelength of the UV light source was fundamental for an effective photocatalyic process.

In order to improve the photocatalytic process, "self-doping" TiO_2 was investigated. Different reduction temperatures were studied to generate the best ratio of Ti^{3+}-Ti^{4+} that stabilised the charge distribution process to maximize the electron-hole pairs generated per photon in the gas phase. From a wide range of reduction temperatures, titanium sub-oxime reduced at 400 ^{o}C showed the best performance in removing carbon dioxide.

In the application of TiO_2 for the built environment, the best commercially available TiO_2 powder, anatase P25 was applied with two different techniques. Electrophoretic deposition has the potential to scale up the process for prefabricated panels in construction. Solvent,

deposition time, voltage and substrate were optimised. The resulting photoactivity of the coatings was evaluated showing a higher efficiency than a compressed pellet of anatase P25.

The final part of the thesis was dedicated to the formulation and application of a photocatalytic enhanced lime based coatings for the built heritage. The use of calcium hydroxide dispersions is widely used in the conservation and restoration community, reinforcing limestone when it carbonates. Anatase P25, was added to improve the performance in polluted atmospheres, acting as a sacrificial barrier. Results showed that by adding anatase to the formulation, calcium hydroxide reacted preferentially with sulphur dioxide over carbon dioxide. The final product in the formulation with anatase was calcium sulphate, whereas the final product for the calcium hydroxide formulation was calcium sulphite.

Finally, a general discussion of the results is presented and the conclusions of this research are drawn. Recommendations for further work are presented in the last chapter.

Dissemination of the research work

Conferences

- M. Nuño, R.J. Ball, C.R. Bowen. Presentation entitled:'Antimicrobial and antipollution properties of photocatalytic coatings', Interactive Systems, Nanosolar Photovoltaics and Coatings for a Sustainable Built Environment. Bhopal (India), 2013.
- M. Nuño, R.J. Ball, C.R. Bowen Presentation entitled:'Study pollution removal of photocatalytic coatings in the built environment ' Interfaces Against Pollution (IAP). Leeuwarden (The Netherlands), 2014
- M. Nuño, R.J. Ball, C.R. Bowen. Poster: 'Use of photocatalyst for pollution remediation'. Urban Environmental Pollution. Toronto (Canada), 2014

Publications in international journals

- M. Nuño, R.J. Ball, C.R. Bowen, 2014. Study of solid/gas phase photocatalytic reactions by electron ionization mass spectrometry. *Journal of Mass Spectrometry*. **49** (8), pp. 716-726
- M. Nuño, R.J. Ball, C.R. Bowen, R. Kurchania, G.D. Sharma, 2015. Photocatalytic activity of electrophoretically deposited (EPD) TiO_2 films. *Journal of Materials Science*. **50** (14), pp. 4822-4835
- M. Nuño, G.L.A. Pesce, P. Xenophontos, R.J. Ball, C.R. Bowen, Environmental performance of nano-structured $Ca(OH)_2/TiO_2$ photocatalytic coating for buildings. *Building and Environment*. **92,** pp. 734-742

Acronyms and abbreviations

Abbreviation	Full name
7000	Anatase Kronos vlp 7000
P25	Anatase Aeroxide P25
PC500	Anatase CristalACTiV™ PC500
BE	Binding energy
Cfu	Colony forming units
E. coli	*Escherichia coli*
EDX	Energy dispersive X-ray
FESEM	Field emission scanning electron microscope
FTO	Fluorine tin oxide
LED	Light emitted diode
PHREEQC	*pH REdox EQuilibrium in C language*
PM	Particulate matter
SEM	Scanning electron microscope
TEM	Transmission electron microscope
UV	Ultra violet
λ	Wavelength
XPS	X-ray photoelectron spectroscopy
XRD	X-ray diffraction

Molecular formula	Full name
CH_3CHO	Acetaldehyde
$Ca(OH)_2$	Calcium hydroxide
$CaCO_3$	Calcium carbonate
$CaCl_2$	Calcium chloride
$CaSO_3$	Calcium sulphite
$CaSO_4$	Calcium sulphate
C	Carbon
CO	Carbon monoxide
CO_2	Carbon dioxide
CFCs	Chlorofluorocarbons
e^-	Electron
CH_3CH_2OH	Ethanol
h^+	Hole
H_2	Hydrogen
$^{\bullet}OH$	Hydroxyl radicals
CH_3OH	Methanol
N	Nitrogen
NO_2	Nitrogen dioxide
NO	Nitrogen monoxides
NO_x	Nitrogen oxide

O_2	Molecular oxygen
$^1O_2$	Singlet state molecular oxygen
H^+	Proton
NaOH	Sodium hydroxide
SO_2	Sulphur dioxide
H_2SO_3	Sulphurous acid
H_2SO_4	Sulphuric acid
$O_2^{\bullet-}$	Superoxide anion
Ti	Titanium
TiO_2	Titanium dioxide
$TiCl_4$	Titanium chloride
VOCs	Volatile organic compounds
H_2O	Water

Abbreviation	Unit
bar	Bar
°C	Celsius degree
cm^3/cc	Cubic centimetre
cm^{-1}	Wavenumber
eV	Electronvolt
h	Hour
l	Litre
ml	Millilitre
µl	Microlitre
m	Metre
mm	Millimetre
µm	Micrometre
nm	Nanometre
min	Minute
Pa	Pascal
s	Second

Table of Contents

Acknowledgements i

Abstract iii

Dissemination of the research work v

Acronyms and abbreviations vii

Table of Contents xi

Table of Figures xviii

Table of Tables xxiii

1 Chapter One – Introduction and review of the literature 1

1.1 General introduction 2

1.2 Review of the literature 5

1.2.1 Air quality 5

1.2.1.1 Associated risk for human health 6

1.2.1.2 Effect of pollutants on buildings 6

1.2.1.2.1 Mathematical modelling of stone degradation 9

1.2.2 Physical properties of semiconductors 9

1.2.2.1 Semiconductor characteristics 12

1.2.3 Titanium dioxide 13

1.2.3.1 Rutile 15

1.2.3.2 Anatase 16

1.2.3.3 Brookite 17

1.2.3.4 High pressure polymorphs 19

1.2.4 Photoinduced processes 19

1.2.4.1 Photocatalytic behaviour of titanium dioxide 21

1.2.4.1.1 Removal of atmospheric pollutants 23

1.2.4.1.2 Microcyde properties of titanium dioxide coatings 25

1.2.4.1.2.1 Photocatalytic neutralisation of pathogens 26

1.2.4.2 Study of photocatalytic reactions 27

1.2.5 Tailoring TiO_2 photocatalytic properties 28
1.2.6 Photocatalytic film preparation 29
1.2.6.1 Electrophoretic deposition of TiO_2 30
1.2.6.2 Dip coating 32
1.2.7 Application of photocatalytic coatings and materials in pre-built environments 32
1.2.8 Concluding remarks 35
1.3 Aims and objectives 36
1.4 Thesis structure 37
1.5 Bibliography 38
2 Chapter Two - Analytical techniques 64
2.1 X-ray Photoelectron Spectroscopy 65
2.1.1 X-ray sources 65
2.1.2 Software and peak fitting 66
2.1.3 XPS apparatus and conditions 67
2.2 X-ray Diffraction 67
2.2.1 Scherrer Equation 68
2.2.2 XRD apparatus and conditions 69
2.3 Electron microscopy 69
2.3.1 Scanning electron microscope 69
2.3.1.1 Energy dispersive X-ray analysis 70
2.3.1.2 Specimen preparation 70
2.3.1.3 SEM apparatus and conditions 70
2.3.2 Field Emission SEM (FESEM) 71
2.3.2.1 Specimen preparation 71
2.3.2.2 FESEM apparatus and conditions 71
2.3.3 Transmission electron microscopy (TEM) 71
2.3.3.1 Specimen preparation 71
2.3.3.2 TEM apparatus and conditions 72

2.4 Raman spectroscopy 72
2.4.1 Apparatus and conditions 73
2.5 UV-Visible diffuse reflectance spectroscopy 73
2.5.1 Apparatus 73
2.6 Dielectric Spectroscopy 74
2.6.1 Apparatus 75
2.7 White light interferometry 75
2.7.1 Apparatus 75
2.8 BET surface area analysis 76
2.8.1 Apparatus 76
2.9 Bibliography 77
3 Chapter Three - Experimental methods 79
3.1 Light source 80
3.1.1 Wavelength spectra 80
3.1.2 UVA probe 80
3.1.3 UV halogen lamp 81
3.1.4 UV LED 81
3.2 Bacteria removal 83
3.2.1 Pour plate technique and colony forming unit 83
3.2.2 Parameter optimization 84
3.2.2.1 Volume of microbial suspension 86
3.2.2.2 Reaction 86
3.2.2.3 UV conditioning 87
3.3 Methylene blue degradation 88
3.4 Glass reactor 88
3.4.1 Design 88
3.5 Summary 90
3.6 Bibliography 91
4 Chapter Four - Analysis of photocatalytic reactions in the gas phase 92

4.1 Theoretical background 93
4.2 Design 94
4.3 Interpretation of the results 100
4.3.1 Mathematical approach 103
4.4 Case of study: reactivity of anatase 109
4.5 Summary 112
4.6 Bibliography 113
5 Chapter Five – Evaluation and characterisation of commercially available materials and coatings 115
5.1 Characterisation of commercially available TiO_2 particles 116
5.1.1 Electron microscopy 116
5.1.1.1 7000 117
5.1.1.2 PC500 118
5.1.1.3 P25 119
5.1.1.4 Rutile 120
5.1.1.5 Brookite 121
5.1.2 Raman spectroscopy 122
5.1.3 X-ray photoelectron spectroscopy 124
5.1.4 X-ray diffraction 127
5.1.5 UV-Vis diffusive spectroscopy 130
5.1.6 Photocatalytic performance 133
5.1.6.1 Photocatalytic degradation of methylene blue 133
5.1.6.2 Photocatalytic degradation of gaseous pollutants 136
5.2 Commercial coatings 142
5.2.1 Electron microscopy 142
5.2.1.1 Bionictile© 142
5.2.1.2 TiO_2 powder coating 144
5.2.1.3 Cement render 146
5.2.1.4 TiO_2 mesh 147

5.2.2 X-ray photoelectron spectroscopy 149
5.2.3 Photocatalytic performance 151
5.2.3.1 Photocatalytic degradation of methylene blue 151
5.2.3.2 Photocatalytic degradation of gaseous pollutants 153
5.2.3.3 Case of study, BionicTile 155
5.3 Summary 156
5.4 Bibliography 157
6 Chapter Six – Titanium sub-oxide species 161
6.1 Preparation of titanium sub-oxides species 162
6.2 Characterisation of titanium sub-oxide species 163
6.2.1 UV-visible diffuse reflectance spectroscopy 164
6.2.2 Electrical characterisation 165
6.2.3 Scanning electron microscopy (SEM) 167
6.2.4 Photo-catalytic performance 168
6.3 Summary 173
6.4 Bibliography 174
7 Chapter Seven – Electrophoretic deposited coatings of anatase TiO_2 176
7.1 Materials and preparation of anatase TiO_2 coatings 177
7.1.1 Titanium dioxide 177
7.1.2 Substrates 177
7.1.3 Medium 177
7.1.4 Reactor, power supply and furnace conditions 178
7.2 Electrophoretic deposition parameters 178
7.2.1 Effect of deposition time 178
7.2.2 Effect of applied voltage 180
7.2.3 Effect of substrate 180
7.2.4 Effect of solvent 181
7.3 Coating characterisation 182
7.3.1 Crystal phase composition 182

7.3.2 Surface morphology 185
7.3.3 Photocatalytic degradation of NO_2 190
7.4 Summary 193
7.5 Bibliography 194
8 Chapter Eight – Nano structured lime/anatase photocatalytic coatings 196
8.1 Material and sample preparation 197
8.1.1 Substrate 197
8.1.2 $Ca(OH)_2$ suspension 197
8.1.3 $Ca(OH)_2$-TiO_2 suspension 197
8.2 Coating preparation 197
8.3 Experimental performance 198
8.4 PHREEQC modelling 199
8.4.1 PHREEQC SIMULATION 200
8.5 Coating characterisation 202
8.5.1 SEM imagining 203
8.5.2 EDX analysis 205
8.5.3 X-ray photoelectron spectroscopy 206
8.6 Photocatalytic degradation of gaseous pollutants 210
8.7 Discussion 212
8.8 Summary 214
8.9 Bibliography 215
9 Chapter Nine – General discussion 217
9.1 Assessment of TiO_2 photocatalysis 218
9.2 Tailing photocatalytic properties 219
9.3 TiO_2 Coatings 219
10 Chapter Ten – Conclusions and further work 221
10.1 Further work 224
11 Publications 226

Table of Figures

Figure 1.1 - Global average greenhouse gas concentrations 5
Figure 1.2 – Global anthropogenic CO_2 emissions 5
Figure 1.3 - Degraded balustrade in North parade, Bath (UK) 7
Figure 1.4 - Bar-chart of room temperature electrical conductivity ranges for metals, ceramics, polymers, and semiconducting materials 10
Figure 1.5 - Distribution of conduction and valence bands in various materials 11
Figure 1.6 - Titanium-Oxygen phase diagram 14
Figure 1.7 - Phase equilibria between anatase, rutile and srilankite 14
Figure 1.8 - UV-visible reflectance spectra of for the phase-pure titania nanomaterials. A=anatase, R=rutile, B=brookite 15
Figure 1.9 - Rutile crystal structure 15
Figure 1.10 - Anatase crystal structure 16
Figure 1.11- Brookite crystal structure 17
Figure 1.12 - Electronic promotion by light 20
Figure 1.13 - Electrochemical cell in which the TiO_2 electrode (numbered 1) is connected through a permeable membrane (numbered 3) to a platinum electrode (numbered 2) with a surface area of approximately 30 cm^2 21
Figure 1.14 - Measured characteristic time for primary processes in TiO_2 photocatalyst 23
Figure 1.15 - Schematic representation of the photocatalytic reduction of CO_2 25
Figure 1.16 - Phospholipid structure, the separation of charges create a polar region and the fatty acids are the non-polar region 25
Figure 1.17 - Model representing the photoreaction chain with the photocatalyst, water and cell 26
Figure 1.18 - Chemical structure of methylene blue oxidised state (left) and reduced state (right) 28
Figure 1.19 - Scheme of an electrophoretic cell, showing the electrodes (black) under magnetic stirring fly (grey) 31
Figure 1.20 - Chiesa di Dio Padre Misericordioso 33
Figure 1.21 - Toyota's Tsutsumi plant (Image property of TOTO ltd.) 34
Figure 1.22 – Chubu International Airport terminal 34
Figure 2.1 - Origin of characteristic X-ray lines, the more intense transitions are in bold 66
Figure 2.2 - Diagram of XRD flatplate mode configuration 69
Figure 2.3 - Different emissions generated by X-ray interaction with the surface 70
Figure 3.1 - Spectrum of UV halogen lamp. Wavelength ranges of 364-383 nm calculated at full width half maximum (FWHM) 81

Figure 3.2 - Spectrum of UV halogen lamp. Wavelength ranges of 364-383 nm calculated at full width half maximum (FWHM) 82
Figure 3.3 - Spectra of LED arrays. Wavelength ranges of 376-387 nm and 381-392 nm calculated at full width half maximum (FWHM) 82
Figure 3.4 - Petri dish (9 cm diameter) with *E. coli* colonies 84
Figure 3.5 - Colony counting process on a 9 cm diameter pretri dish 84
Figure 3.6 - Application of *E. coli* suspension on the surface's sample with a micropippette 86
Figure 3.7 - Effect of UV intensity on *E. coli* over time 87
Figure 3.8 - Image of the glass reactor 89
Figure 4.1 - Quadrupole mass filter 93
Figure 4.2 - Schematic diagram of how a multichannel plate works 94
Figure 4.3 - Diagram of the system. The reaction chamber has four connections, one input valve connected to the gases, one output valve connected to the detector, one purge valve connected to the rotary pump and one exhausting valve 95
Figure 4.4 - Picture of the reaction chamber coupled to EI-mass spectrometer 96
Figure 4.5 - Pictures of the reaction chamber showing all its connections 97
Figure 4.6 - Electronic head Microvision 2 and turbomolecular pump and pressure detector 98
Figure 4.7 - Effect of emission current on the NO_2 signal (46 a.m.u.) at 70 eV electron energy and 5.5 mA ion energy 99
Figure 4.8 - Effect of electron energy on the NO_2 signal (46 a.m.u.) at 1.0 mA emission current and 5.5 mA ion energy 100
Figure 4.9 - Mass spectrum of 190 ppm of NO_2, 6 % of zero air grade balance N_2 101
Figure 4.10 - Partial pressures of H_2O, O_2, Ar, CO_2 and NO_2 between 0 and 150 min with the empty chamber in the dark. Right 'y' axis is fixed for Ar partial pressure whereas left 'y' axis shows the value for the species over 150 min 105
Figure 4.11 - Relative intensity of CO_2 and NO_2 normalised with the partial pressure of Ar over time with the empty chamber in the dark. Left 'y' axis shows the relative intensity for NO_2; right 'y' axis shows the relative intensity for CO_2 106
Figure 4.12 - Relative intensity of CO_2 and NO_2 normalised with total pressure between 0 and 150 min with the empty chamber in the dark. Left 'y' axis shows the relative intensity for NO_2; right 'y' axis shows the relative intensity for CO_2 107
Figure 4.13 - Relative changes for Ar, H_2O, N_2, CO_2, NO_2 and the total pressure between 0 and 150 min 108
Figure 4.14- Fractional change of H_2O between 0 and 150 min for a sample in the dark and irradiated with a UV light of wavelength of 381-392 nm 110

Figure 4.15 - Fractional change of O_2 between 0 and 150 min for a sample in the dark and irradiated with a UV light of wavelength of 381-392 nm 110
Figure 4.16 - Fractional change of CO_2 between 0 and 150 min for a sample in the dark and irradiated with a UV light of wavelength of 381-392 nm 111
Figure 4.17 - Fractional change of NO_2 between 0 and 150 min for a sample in the dark and irradiated with a UV light of wavelength of 381-392 nm 111
Figure 4.18 - Relative position of measured band gap and reported within the UV LED range 112
Figure 5.1 - FESEM image of anatase 7000 117
Figure 5.2 - TEM image of anatase 7000 117
Figure 5.3 - FESEM image of anatase PC500 118
Figure 5.4 - TEM image of anatase PC500 118
Figure 5.5 – FESEM image of anatase P25 119
Figure 5.6 – TEM image of anatase P25 119
Figure 5.7 – FESEM image of rutile 120
Figure 5.8 – TEM image of rutile 120
Figure 5.9 – FESEM image of brookite 121
Figure 5.10 – TEM of brookite 121
Figure 5.11 – Raman spectra from 0 to 1000 cm^{-1} of five different TiO_2 powders 123
Figure 5.12 - XPS spectra of Aeroxide® P25 124
Figure 5.13 – EDX spectrum of brookite 126
Figure 5.14 –X-ray diffractogram of brookite, rutile and anatase powders 128
Figure 5.15 – Graphical representation of reflectance against wavelength for rutile, brookite and anatase powders 131
Figure 5.16 - Photo-reduction of aqueous solution of methylene blue under different UV LED (I=4.7 W/m^2) for TiO_2 powders. 134
Figure 5.17 – Fractional reduction of CO_2 related to Ar over time under different conditions 136
Figure 5.18 – Fractional reduction of NO_2 related to Ar over time under different conditions 137
Figure 5.19 – Fractional reduction of H_2O related to Ar over time under different conditions 139
Figure 5.20 – Fractional reduction of O_2 related to Ar over time under different conditions 140
Figure 5.21 – Proposed mechanism of photo-oxidation of CO_2 141
Figure 5.22 – Photography of Bionictile 143
Figure 5.23 – SEM image of Bionictile at x100 magnification 143

Figure 5.24 – SEM image of Bionictile at x1800 magnification 144
Figure 5.25 – Photography of an aluminium plate with TiO_2 powder coating 144
Figure 5.26 – SEM image of TiO_2 powder coating at x500 magnification..... 145
Figure 5.27 – SEM image of TiO_2 powder coating at x3700 magnification..... 145
Figure 5.28 – Photography of cement render..... 146
Figure 5.29 – SEM image of cement render at x500 magnification 146
Figure 5.30 – SEM image of cement render at x1500 magnification 147
Figure 5.31 – Photography of TiO_2 mesh 147
Figure 5.32 – SEM image of TiO_2 mesh at x500 magnification..... 148
Figure 5.33 – SEM image of TiO_2 mesh at x1200 magnification..... 148
Figure 5.34 - Photo-reduction of aqueous solution of methylene blue under different UV LED (I=4.7 W/m^2) for commercial TiO_2 coatings. 152
Figure 5.35 - Fractional reduction of CO_2 related to Ar over time under different conditions 153
Figure 5.36 - Fractional reduction of NO_2 related to Ar over time under different conditions 154
Figure 5.37 – Photography of glass tiles and Bionictiles during UV exposure with a solution of *E. coli* on their surfaces 155
Figure 5.38 – *E. coli* deactivation under UV halogen lamp with a wavelength range of 364-383 nm with an intensity of 0.322 W/m^2 156
Figure 6.1 - Initial TiO_2 (left) and carbo-thermally reduced TiO_n samples. Temperatures indicate the reduction condition. 162
Figure 6.2 - XRD diffraction patterns of non-reduced rutile and TiO_n carbo-thermally reduced from 350 ºC to 1300 ºC 163
Figure 6.3 - Graphical representation of reflectance against wavelength for TiO_2 and TiO_n specimens..... 164
Figure 6.4 - AC conductivity of TiO_2 specimens over the frequency range 1 Hz and 0.1 MHz 166
Figure 6.5 - Complex plane plot of real impedance (Z') vs imaginary impedance (Z'') for TiO_n specimens 166
Figure 6.6 - SEM images of (a) non-reduced TiO_2, (b) TiO_2 carbo-thermally reduced at 1300 ºC..... 167
Figure 6.7 – Photo-reduction of methylene blue in aqueous solution..... 169
Figure 6.8 – Fractional reduction of CO_2 over 150 minutes under UV of wavelengths (a) 376-387 nm and (b) 381-392 nm 171
Figure 6.9 - Fractional reduction of NO_2 over 150 minutes under UV wavelengths of (a) 376-387 nm and (b) 381-392 nm 172

Figure 7.1 - a) Images of TiO_2 films that were electrophoretically prepared in acetylacetone based solution at 80 V after calcination; b) Images of TiO_2 coated FTO coated glass electrophoretically prepared in acetylacetone based solution at 20 V, 40 V and 80 V.....179
Figure 7.2 - a) Images of TiO_2 films coated at 20 V, 40 V, 60 V and 80 V under isopropyl based solution in three different substrates; b) Images of TiO_2 films coated at 80V under isopropyl based solution 180
Figure 7.3 - Images of TiO_2 films coated stainless steel at 80 V under isopropyl based solution and acetylacetone based solution 181
Figure 7.4 - Images of TiO_2 films coated FTO coated glass at 20, 40 and 80 V under isopropyl based solution and acetylacetone based solution 181
Figure 7.5 - XRD Spectra of TiO_2 anatase P25 and a typical XRD spectrum of the films (in this case, FTO-coated glass coated at 20 V for 50 s in isopropanol based solution). R=Rutile, A=Anatase 183
Figure 7.6 - Raman spectra of anatase P25 (top) and the characteristic Raman spectra TiO_2 coatings produced by electrophoretic deposition for all the films 184
Figure 7.7 – Images of the TiO_2 coatings described in table 7.2 186
Figure 7.8 - Surface mapping of titanium plate coated with TiO_2 at 20 V suspended in isopropanol based solution during 15 min obtained from non-contact optical profilometry 187
Figure 7.9 – Typical SEM images of TiO_2 electrophoretically deposited coatings on stainless steel at 20 V for 30 s in isopropyl based solution.....189
Figure 7.10 – NO_2 breakdown under 376-387 nm carried by FTO coated glass coated at 20 V during 30 s in acetylacetone based solution.....190
Figure 7.11 – Bar chart of NO_2 decomposition of 5 samples under 376-387 nm for 100 min 191
Figure 7.12 – Schematic explanation of how microfractures increases the surface area....192
Figure 8.1 - SEM images of: a) uncoated Bath stone after SO_2 exposure; b) nanolime coated Bath stone specimen after SO_2 exposure; c) Bath stone treated with the photocatalytic nanolime coating after SO_2 exposure.....204
Figure 8.2 – XPS spectra of photocatalytic nanolime coated Bath stone after five days of 7 ppm SO_2 exposure under UV irradiation 208
Figure 8.3 –XPS spectra of sulphur $2p_{3/2}$ region for nanolime and photocatalytic nanolime coated Bath stone after five days exposure to 7 ppm SO_2 under UV irradiation.....210
Figure 8.4 - Fractional reduction of CO_2 related to Ar over time under different conditions 211
Figure 8.5 - Fractional reduction of NO_2 related to Ar over time under different conditions 211

Table of Tables

Table 1-1 - Physical parameters of TiO_2 polymorphs 18
Table 3-1 - Results from calibration trend 85
Table 4.1 - Gas composition of Zero air grade (balanced N_2) 95
Table 4.2 - Major ions in the 70 eV EI-mass spectra and the expected species of a gas mixture containing 190 ppm of NO_2, 6 % of air balance N_2 spectrum and their correlations with singular mass spectra of its components. Numbers in parenthesis show the relative intensity for the pure mass spectrum of a molecule 102
Table 4.3 - Average and standard deviation values for NO_2, O_2, H_2O and CO_2 over 150 minutes of reading values of a gas mixture containing 190 ppm of NO_2, 6 % of air balance N_2 with the empty chamber in the dark 109
Table 5.1- Element ratios and chemical state derived from XPS analysis 125
Table 5.2 – d spacing extracted from the X-ray diffractogram of brookite, rutile and anatase powders 129
Table 5.3 – Particle size, BET and optical band gap for TiO_2 powders 132
Table 5.4 – Percentage of absorbed and degraded dye after 60 min under two different UV LED and in the dark. 135
Table 5.5 - Element ratios and chemical state derived from XPS analysis 150
Table 6.1- Optical band gap of TiO_n specimes 165
Table 7.1 – Physical properties of different solvents 178
Table 7.2 – Profile roughness parameters and thickness for the studied coatings 188
Table 8.1 – Experimental conditions showing the gas flow and the RH of each experiment. Pollutant concentrations (in ppm) are calculated considering the initial concentration and the mixed volumes of gas. All the experiments were carried for five days 198
Table 8.2 - Activity of CO_3^{2-}, SO_4^{2-} and NO_2^- ions in pure water as calculated by the PHREEQC 200
Table 8.3 - Activity of CO_3^{2-}, SO_4^{2-} and NO_2^- ions in pure water in equilibrium with calcite and solid phases formed at the end of the simulation 201
Table 8.4 - Activity of CO_3^{2-}, SO_4^{2-} and NO_2^- ions in pure water in equilibrium with Calcite and Portlandite, and solid phases that could be produced at the end of the tests 202
Table 8.5 – Specimen composition determined by EDX spectroscopy on specimens following experimental conditioning exposure 205
Table 8.6 – Element ratios and chemical state derived from XPS analysis 209

Chapter One – Introduction and review of the literature

This chapter presents an overview of historical trends of pollutants and the most relevant environmental mitigation strategies. This will be followed by a review of the literature which is of relevance to the current work. A general review of titanium dioxide's properties which are required to understand how photocatalytic processes can occur and how they can be maximised are included. Following from this, there is an extensive explanation of photocatalysis. Finally the most relevant coating techniques for building environments are described step by step in terms of their effects on performances and applications.

1.1 General introduction

Since the industrial revolution, the increase of factories and their energetic usage of fossil fuels such coal, oil and gas, have led to increase pollution levels. Alongside this technological revolution, the increase of the worldwide population and the associated lifestyle of these industrialised societies have being changed towards to a consumer society. This has led to an increase of greenhouse gases with a straightforward effect on the ecosystems: temperature has raised, alongside with the sea level an acidification of the oceans due to the increment of carbon dioxide by 100 ppm [1].

The situation is clear; the research behind the study shows a deadline and the goals that have to be accomplished by then. To stop before an irreparable damage is done, fossil fuel usage must be reduced, more efficient systems have to be applied and overall the consumer society, as it is known nowadays, has to reinvent itself in order to become more sustainable. This is the main challenge that mankind is facing this century; science and technology have some answers, but education of society is an important tool in this process.

In addition to a worldwide change in perception of global warming (7 billion people and growing), scientists have been pushing the barriers of knowledge in sustainable areas such as energy harvesting, new and more efficient sources of energy (wind, nuclear, solar amongst others) to reduce dependence on fossil fuels. Besides this practical approach, new materials have been developed and other already known materials are being studied more into detail. This is the case of titanium dioxide, a widely used white pigment with fascinating properties and promising potential.

If titanium dioxide is irradiated with an ultraviolet light source, due its physical properties it is able to start a cascade of reactions that, are known to be able to reduce the concentration of pollutants.

The aim of this PhD is to explore new pathways to reduce pollution, beyond political legislation or local actions; photocatalysis can be applied in real life to enforce the needed change. A city, or industrial site are usually considered centres of pollution, but they can also be considered as potential reactors. The “surface area” in a city is not just the extension of the plot where it was built. Buildings have exposed faces, facades and roofs which are in contact with air and under the sunlight, which provides ultraviolet light. Herein is described a chemical reaction, consisted of reactants (air), energy (light) and the supported catalyst (buildings with a photocatalytic surface) which is needed to start the reaction (photodegradation of pollutants).

The beginning of this research was to establish a protocol to analyse the photocatalytic properties of titanium dioxide in the gas phase. Although the existing methods (i.e. decolouration of an aqueous solution) are cheap and accessible to everyone, these methods cannot be extrapolated with regards to pollution removal. A more sophisticated system was developed to study how photocatalysts behave in the gas phase, where moisture is the source of water. For this purpose, Chapter Four describes the analytical use of a mass spectrometer; providing a wide range of molecules to study without making modifications to the system itself. In addition to the technical issues of setting up a new instrument, the complex data and its analysis required the development of new mathematical methods to extract useful information and discard interferences.

Photocatalytic activity of commercial anatase and rutile (polymorphs of titanium dioxide) were studied in the aqueous and in the gas phase in Chapter Five. The role of the crystal structure on the photocatalytic properties is fundamental, showing a higher activity for the anatase polymorph. Following on from this conclusion, the reaction of nitrogen dioxide with water in the presence of titanium dioxide was investigated, with a new result being found. When carbon dioxide is reacted in presence of titanium dioxide, it does not react with water, but with oxygen.

In order to tune physical properties of titanium dioxide and tailor them to new requirements, in Chapter Six the study of the effect of titanium sub-oxide species is discussed; showing that a defective crystal is able to transfer the created charge in the beginning of the photocatalytic process faster to the surface, thereby stabilizing it.

When the properties at the nanoscale were assessed, the next stage was the production of coatings suitable in the built environment. For this, two techniques were considered; electrophoretic deposition (for the potential application of titanium dioxide in prefabricated panels) and dip coating (mimicking how it would be applied in existing buildings).

Chapter Seven focuses in the versatility of electrophoretic deposition as coating technique, which needs an electrolyte with the titanium dioxide dispersed in it. Despite the use of organic solvents, the strong point of this technique is the reusability of the medium, making the solvent waste close to zero. From the architectonic point of view, this technique allows the application of uniform coatings in complex shapes, often needed in building facades.

Dip coating, as its name indicates, consists of submerging the substrate that needs coating in a solution. To preserve titanium dioxide on the surface, a binder is required to ensure its stability with time. For this purpose, a nano suspension of calcium hydroxide in ethanol was chosen due its compatibility with historic buildings, as it is described in Chapter Eight. In the presence of carbon dioxide and water, calcium hydroxide will react and form calcium

carbonate. Based on this reaction, calcium hydroxide will remove carbon dioxide in urban centres, enhancing the adhesion of titanium dioxide, and allowing titanium dioxide to promote photoreactions without covering it and therefore, limiting its reactivity.

At the end of the results section, a general discussion chapter will connect and discuss the aspects of this PhD thesis. Following from this, the last chapter will address all the contributions to knowledge gained during this project, followed from suggestions for further work.

1.2 Review of the literature

1.2.1 Air quality

An *air pollutant* is described as any substance (organic or inorganic) harmful to living organisms, ecosystems and the built environment, from an anthropogenic or natural source (Epa.gov. 2006-06-28). From this definition, microbial contaminants, volatile organic compounds (VOCs), heavy metals, nitrogen oxides (NO_x), sulphur dioxide (SO_2), carbon monoxide (CO) and carbon dioxide (CO_2), chlorofluorocarbons (CFCs) and particulate matter (PM) are listed.

Figure 1.1 shows how nitrous oxides, carbon dioxide and methane concentrations have dramatically increased over the past sixty years, Figure 1.2 shows the amount of CO_2 released to the atmosphere and their sources.

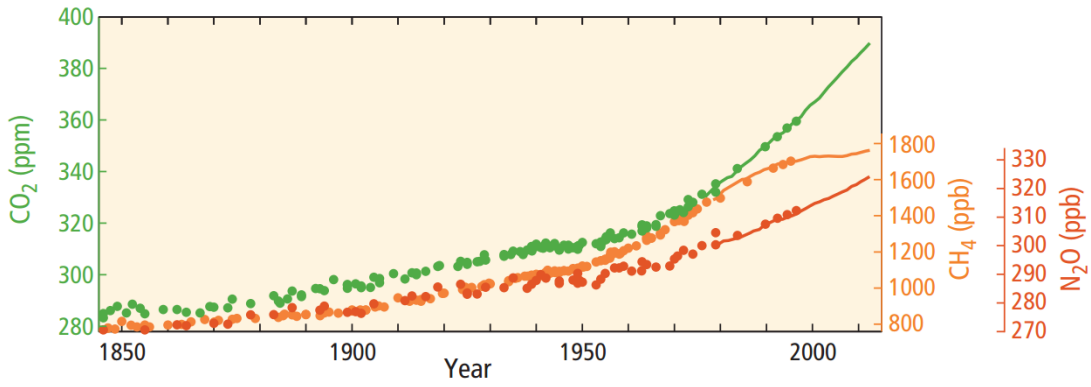

Figure 1.1 - Global average greenhouse gas concentrations [1]

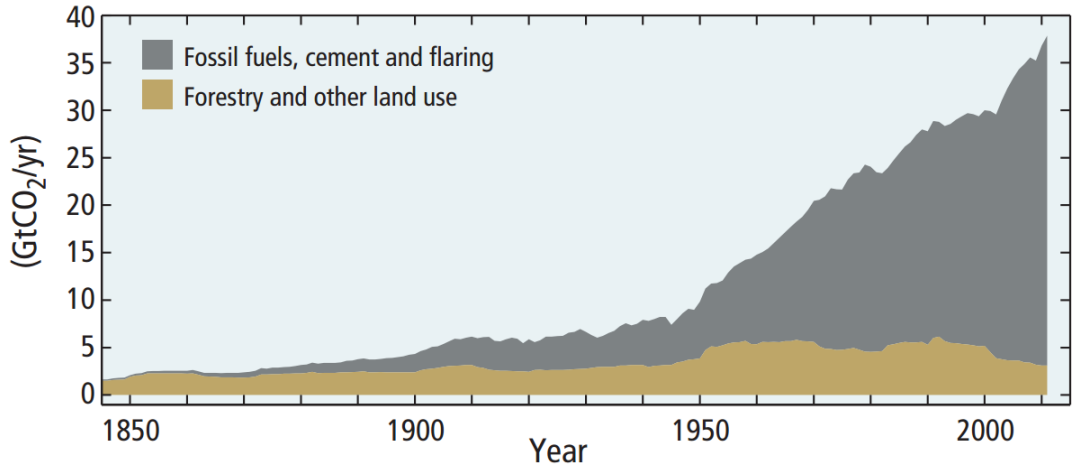

Figure 1.2 – Global anthropogenic CO_2 emissions [1]

1.2.1.1 Associated risk for human health

The release of greenhouse gases such as carbon dioxide, methane, sulphur dioxide and nitrous oxide from industrial and domestic sources pose a significant contribution to global warming. Moreover, those gases present health hazards for the population (associated with respiratory diseases) [2]–[6]. The European Union and United States of America have set maximum levels for emissions of certain pollutants through their environmental standards; the levels for SO_2 were set in 2005 and NO_2 in 2010 [7].

The changes in atmospheric conditions, derived from the release of greenhouse gases, such as average warming [8], more thunderstorms and floods or CO_2-induced stimulation of plant growth [9] have modified the flowering seasons, thereby changing the aeroallergens patterns such as pollen dispersion [10]–[12].

1.2.1.2 Effect of pollutants on buildings

Since the increase of pollutants starting from the 19^{th} century in city centres and industrialised areas; the increase in the concentration of acid forming environmental pollutants including SO_2 and NO_x in the atmosphere have resulted in an increase in the degradation of the materials used in buildings. The city of Bath (world heritage site since 1987) is famous for its Georgian and neoclassical buildings based on Bath Stone. Bath stone is an oolitic limestone with a distinctive honey appearance that has been used as a porous building limestone for centuries in the South West of the United Kingdom as a structural material as well as for panelling (aesthetic purposes). Whereas the foundations of buildings are not in contact with pollutants (and therefore, safe from degradation), structural areas exposed to atmospheric pollutants can be degraded. Figure 1.3 shows how the balustrade built with Bath stone can be degraded by absorbing and reacting with pollutants.

Figure 1.3 - Degraded balustrade in North parade, Bath (UK)

The process of chemical decay of calcium carbonate ($CaCO_3$), which is the main constituents of limestone, has been the focus of a number of studies. The most aggressive chemical attack is mainly attributed to the oxides of sulphur and nitrogen. When SO_2 dissolves in water sulphurous acid (H_2SO_3) is formed and the subsequent dissolution of SO_3 in water generates sulphuric acid (H_2SO_4). Both acids are strong enough to decompose $CaCO_3$ contained in the stones used as outer skins of constructions, releasing carbonic acid (H_2CO_3) which will decompose in H_2O and CO_2. Equations 1.1-1.7 show the proposed mechanism for sulfonation and the role of NO_2 in the oxidation of SO_2 [13], [14]:

$$SO_2 + H_2O \rightarrow H_2SO_3 \quad (1.1)$$

$$H_2SO_3 + CaCO_3 \rightarrow CaSO_3 + H_2CO_3 \quad (1.2)$$

$$SO_2 + NO_2 \rightarrow SO_3 + NO \quad (1.3)$$

$$SO_3 + H_2O \rightarrow H_2SO_4 \quad (1.4)$$

$$H_2SO_4 + CaCO_3 \rightarrow CaSO_4 + H_2CO_3 \quad (1.5)$$

$$NO + NO_2 + 2H_2SO_4 \rightarrow 2NOHSO_4 + H_2O \quad (1.6)$$

$$2NOHSO_4 + SO_2 + 2H_2O \rightarrow 3H_2SO_4 + 2NO \quad (1.7)$$

Sulfonation, however, is not the only process that can lead to chemical degradation of $CaCO_3$. This, in fact, can also be degraded by the products formed by the dissolution of NO_2 in water, as shown in Equations 1.8-1.9 [15], [16]:

$$2NO_2 + H_2O \rightarrow HNO_3 + HNO_2 \quad (1.8)$$

$$2HNO_3 + CaCO_3 \rightarrow Ca^{2+} + 2NO_3^- + CO_2 + H_2O \quad (1.9)$$

To enhance the mechanical properties of limestone at the same time as it is protected, nanolime has been examined as it generates calcium carbonate. Nanolime is as a colloidal suspension of nano-sized particles of calcium hydroxide ($Ca(OH)_2$) in alcohol, such as ethanol or isopropanol. It is commonly used as a consolidant in the field of cultural heritage [17]. The material acts as a binding agent of degraded surfaces because after application the $Ca(OH)_2$ reacts with the atmospheric CO_2 and water to produce $CaCO_3$ in a similar manner to the traditional lime based material, which is totally compatible with the stone itself. In contrast to the more traditional lime, nanolime preparation involves crystal precipitation by mixing supersaturated aqueous solutions of calcium chloride ($CaCl_2$) and sodium hydroxide (NaOH) under carefully controlled conditions. Following precipitation, water is substituted with alcohol to extend the long term stability of the nano sized $Ca(OH)_2$ crystals [18]. Precipitated crystals are plate-like with hexagonal shape and an aspect ratio of approximately 10:1. The average particle size is 150 nm (IBZ-Freiberg n.d.), although crystals can range from some tens to several hundred of nanometres [19].

The product was developed at the beginning of the new millennium as a consolidant for frescos [20], [21] and as de-acidification treatment for paper and canvas [22]. Later, however, its use extended to stone consolidation [18], [23] and as a nano-coating.

1.2.1.2.1 Mathematical modelling of stone degradation

The degradation of Bath stone in the presence of pollutants can be evaluated and modelled by a thermodynamic study of the chemical processes. Although there is a limited study based on the thermodynamics of those processes and the application of a model, the rates of aqueous dissolution for SO_2, NO_2 and CO_2 are known, as well as their chemical equilibrium constants in presence of $CaCO_3$. Those rates can be applied to estimate the effect of such pollutants on bulk materials with time. *PHREEQC* is a C and C++ based computer program that was designed to carry out aqueous geochemical calculations (PHREEQC stands for pH REdox EQuilibrium in C language).

The program is based on equilibrium chemistry of aqueous solutions interacting with several phases, including gases. This software is routinely used in disciplines such as geochemistry, hydrology, environmental pollution, water treatment and the construction industry. PHREEQC is able to calculate saturation levels of solutions, unidimensional transport calculations, also with reversible reactions (such as surface-complexation, and ion-exchange equilibria); by implementing aqueous models using the thermodynamic rates in different databases (Lawrence Livermore National Laboratory model, WATEQ4F, Pitzer specific-ion-interaction aqueous model, and the Specific ion Interaction Theory).

Although the use PHREEQC is not extended yet to study the evolution of building in polluted atmospheres., it has been used to predict the result of chemical processes such as the ion–ion and the ion–solid interactions in the multi-ionic transport in concrete [24], [25], chemical degradation of concrete [26]–[28], dissolution processes of calcium-silicate-hydrate [29], [30] or phase and morphology evolution of $CaCO_3$ precipitated by carbonation of hydrated lime [31].

1.2.2 Physical properties of semiconductors

One of the most important electrical characteristics of a material is its electrical *conductivity*; that is the capability for conducting atomic and subatomic particles with electric charge, such as electrons or ions. These charged chemical systems are responsible for the transmittance of electrical current [32], [33].

Depending on how the substance conducts these charged sub-particles, a semiconductor is a type of material (crystalline or amorphous solids and liquids) that has conductivity between that of a conductor (metals and metal alloys) and an insulator (ceramics and polymers). Figure 1.4 shows the distribution of electrical conductivity as a function of the type of material.

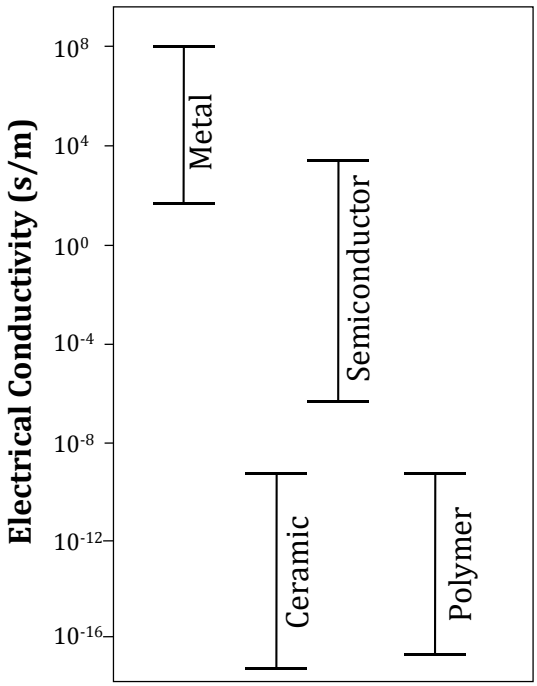

Figure 1.4- Bar-chart of room temperature electrical conductivity ranges for metals, ceramics, polymers, and semiconducting materials [33]

If the molecular orbital theory is applied for TiO_2, its molecular orbital (MO) will be a linear combination of titanium and oxygen atomic orbitals. Due to the geometry implications of different orbitals' shape (s, p and d), the structure of the lattice is important. For the case of rutile with an octahedral structure (also applicable for anatase); the titanium 3d, 4s and 4p orbitals will combine with the oxygen 2s and 2p. In 1972, Fischer [34] deduced the MO diagram of bonding orbitals for rutile from its X-ray band spectra.

The free electron model is an appropriate model which explains the behaviour and properties of metals; but it fails when it is applied to semiconductors or insulators. In solid state physics, *band theory* describes the electronic structure of a material such as band structure energy. In all materials (conductors, semiconductor or insulators) there is electronic conduction, however the conductivity (acceleration of electrons by an electric field) depends on how the electrons act when an electrical field is applied.

A solid consists of a large number of atoms bonded together and in a crystalline material the atoms are arranged in a periodic structure in space.

In crystals, the bond length is sufficient for the electric field generated by an atom to perturb the atomic orbitals of bordering atoms and vice versa. In this situation, electrons are acted upon by the nuclei and electrons of adjacent atoms. This influence transforms discrete sets of

energy levels into electronic bands (atomic orbitals overlap each other due to the small energetic difference) [32]. In this situation, the solid is an electronic system itself and it obeys the Pauli Exclusion Principle in that no two electrons could have the same quantum numbers in an electronic system.

There are energy intervals that are not occupied by electronic bands (or atomic orbitals in an isolated atom) which creates an energetic gap between these bands. This interval, known as *band gap* is a range of energy values in which an electron cannot exist. The band gap is determined by the physical properties of the material, such as bond length and number of free electrons.

The *valence band* is occupied by the valence electrons. These electrons are responsible for chemical bonds, but these electrons are fixed, therefore not free to move and do not participate in the electrical conductivity.

The *conduction band* is an aggregate of perturbed atomic orbitals in which the nuclei's attraction force upon the electrons is weak. This level corresponds to the outer orbits of the atoms. The electrons at this level are able to be shared with the rest of the atoms in the solid.

Three different types of band structure exist at 0 K:

i. Partially filled band, in which the highest occupied energetic state at this temperature is referred to as the *Fermi level* [33] .
ii. Overlapped bands, between and empty and a filled band.
iii. Two energetic bands are separated by a band gap.

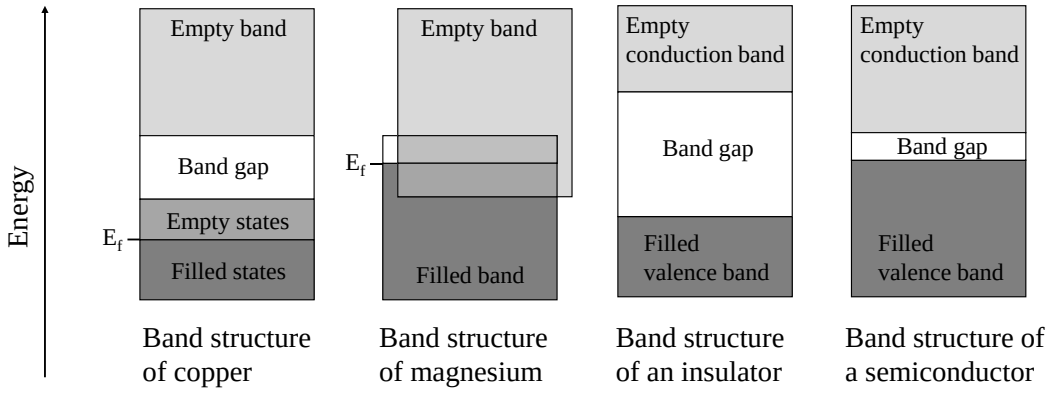

Figure 1.5 - Distribution of conduction and valence bands in various materials [33]

When an atom is excited by additional energy (absorption of a photon, heat, electricity) some of its electrons may absorb enough energy to promote them from the valence band to the conduction band, thus move from one atom to another inside the solid.

The band gap is the key to understanding the differences between insulators, semiconductors and conducting materials. Usually the band gap in an insulator is over 2 eV [33], large enough to prevent promotion between the valence band and the conduction band.

In a semiconductor, the band gap is usually under 2 eV. Depending upon the source of excitation, the promotion of one electron to the conduction band is possible. This will occur only if the energy of excitation is higher than that of the band gap. In conductors such as magnesium, there is an overlap, thus the band gap does not exist. Electrons can therefore move with freedom throughout the entire solid. Other metals such as copper have a partially filled band, therefore in a solid; this band is able to accommodate other electrons.

1.2.2.1 Semiconductor characteristics

The physical properties of a semiconductor provide a wide range of applications in technology. Some semiconductors change their physical properties, such as conductivity in presence of light, heat, force, etc. Semiconductors are essential to the modern world; without them, the technology we rely upon and take for granted simply could not exist. Transistors, circuits, solar cells, light-emitting diode (LED), etc. are all created using semiconductors. Commonly semiconductors are pure crystals, but amorphous solid and liquid semiconductors exist as well.

There are two different types of semiconductors:

i. *Intrinsic semiconductors* which are pure semiconductors.
ii. *Extrinsic semiconductors* which are pure semiconductors with impurities added.

The conductivity can be altered through the addition of different compounds. When an element is added, we refer to the semiconductor as “doped”. The amount of impurities required to modify conductivity is small, between 10^{-6} and 10^{-2} percent (atomic ratio). There are two different types of extrinsic semiconductors, depending on whether the dopant adds electrons to the semiconductor or adds holes.

i. An *n-type* semiconductor is a material which has impurities that add additional electrons, without an associated hole in the solid. For example, if phosphorous (A pentavalent element) is added as a dopant into silicon (tetravalent element); there will be an extra electron for each phosphorous atom. Additionally, the size difference between elements creates distortions of the crystalline structure.
ii. A *p-type* semiconductor is a doped semiconductor in which the dopant adds extra holes. For example, adding boron (trivalent element) into silicon creates a hole. One of the silicon bonding orbitals is able to accept an electron from the boron, creating an "electron hole" [32], [33].

Certain semiconductors, under certain light wavelengths, can excite electrons out of their energy level, creating a charge separation. This unique physical property is the starting point for photocatalysis.

1.2.3 Titanium dioxide

Titanium dioxide is the natural oxide of Ti^{IV} (TiO_2). It occurs in nature in three different crystallographic structures: *rutile, anatase* and *brookite*; although more polymorphs have also been reported. At high pressure there are at least six different crystallographic structures: TiO_2 (II) with the alpha-PbO_2 structure, TiO_2 (B), TiO_2 (H), baddeleyite phase, fluorite phase and pyrite phase. The most common titanium minerals are *rutile* (TiO_2), *ilmenite* ($FeTiO_3$) and *titanite* ($CaTiSiO_5$) [35]–[37]. Due to their different crystal structures, titanium dioxide polymorphs show different physical and chemical properties.

Figure 1.6 shows the Ti-O phase diagram at different temperatures whereas Figure 1.7 shows the TiO_2 phase equilibria. Figure 1.8 shows the UV-visible reflectance spectra for the three main polymorphs, rutile, anatase and brookite.

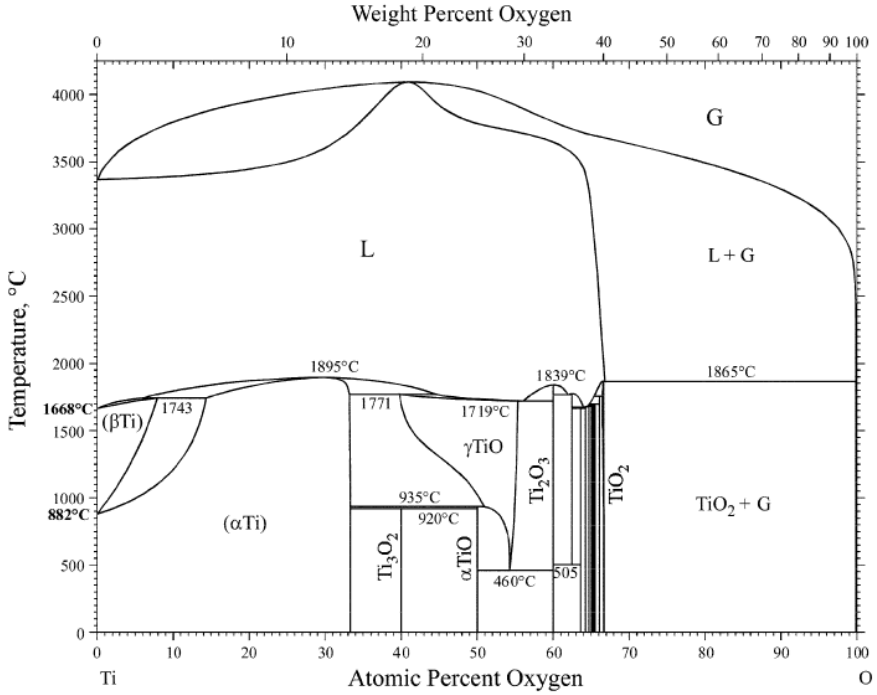

Figure 1.6 - Titanium-Oxygen phase diagram [38]–[40]

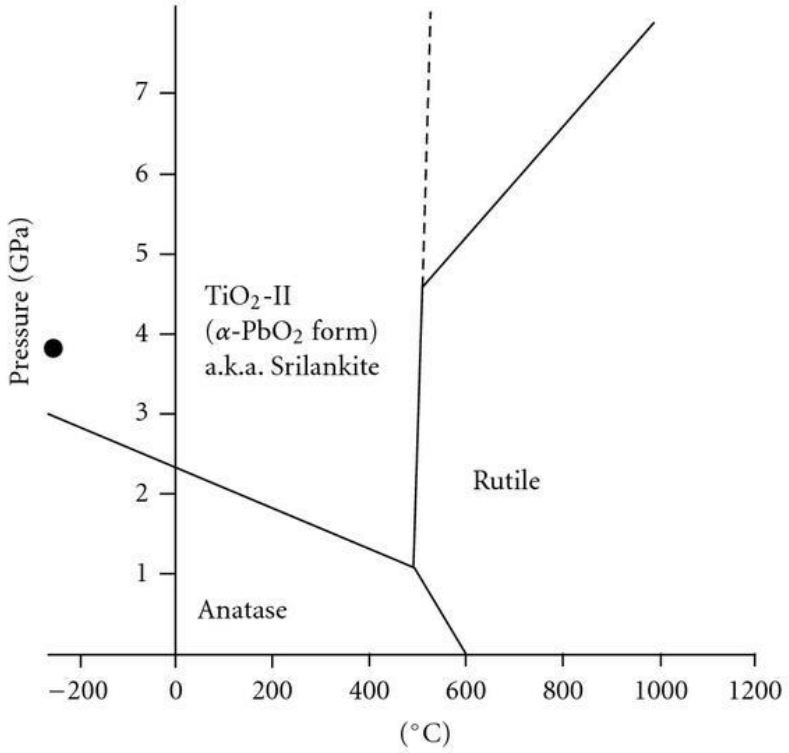

Figure 1.7 - Phase equilibria between anatase, rutile and srilankite [39]

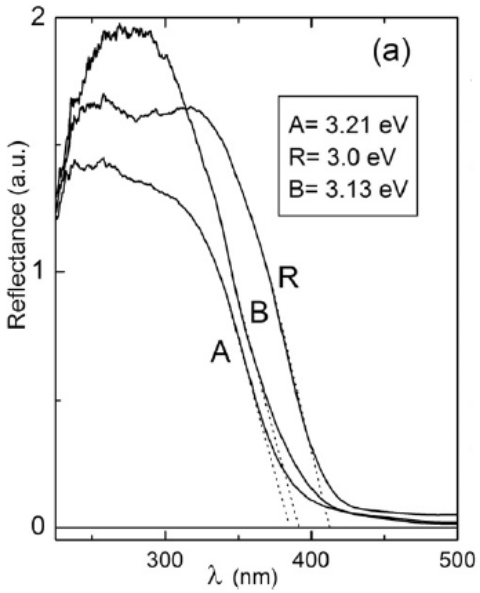

Figure 1.8 - UV-visible reflectance spectra of for the phase-pure titania nanomaterials. A = anatase, R = rutile, B = brookite [41]

1.2.3.1 Rutile

Rutile is the most common crystalline structure of titania on Earth. In 1800, Abraham Gottlob Werner named it from the Latin *rutilus* which means reddish, due to the colour of the mineral. This is a result of it being the most thermodynamically stable polymorph [35]. Rutile has the lowest molecular volume and for this reason, in metamorphic and igneous rocks, most titanium dioxide has rutile's crystal structure. Rutile has been used as a white pigment for polymers, paints and paper, and it is the most common use of titanium dioxide around the world [38]. The unit cell of rutile is a tetragonal cell and the space group is $P4_2/mnm$, as shown in Figure 1.9 and Table 1.1. The optical band gap is ~3.0 eV [41]–[44] as shown in Figure 1.8.

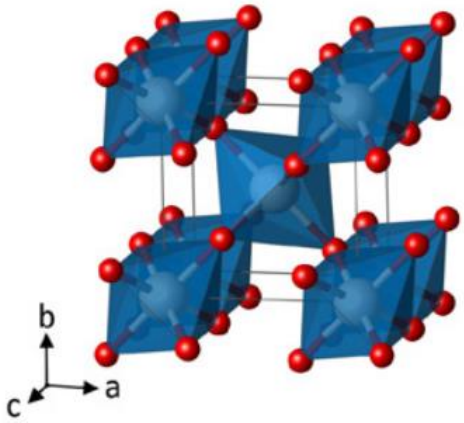

Figure 1.9 - Rutile crystal structure [43]

1.2.3.2 Anatase

Anatase is one of the three natural forms of titanium dioxide. From the Greek *anatasis* which means elongation, it was named in allusion to the high ratio of the length of its pyramidal face by comparison from its base. Anatase is metastable at atmospheric pressure and at room temperature. At elevated temperatures, anatase transforms irreversibility to rutile (stable polymorph) [45], [46]. Anatase's density is the lowest of the natural polymorphs of titanium dioxide (3.82-3.97 g/cm^3) [35]. Figure 1.8 and Table 1.2 show anatase crystal structure and its physical parameters.

Anatase can be formed in a laboratory, by chemical routes, such as the sol-gel method [47]–[55] or novel methods using supercritical carbon dioxide [56]–[58]. Its band gap is ~3.2 eV [41], [59]–[61] although other values have been reported (3.4 eV [62][43], 3.1 eV [63][64]). This difference is attributed to a change in the density of semiconductor carriers [59] and particle size [65]. The position of its band gap (related to the Standard hydrogen electrode) that provides this crystal the photocatalytic properties required to remove pollutants [66].

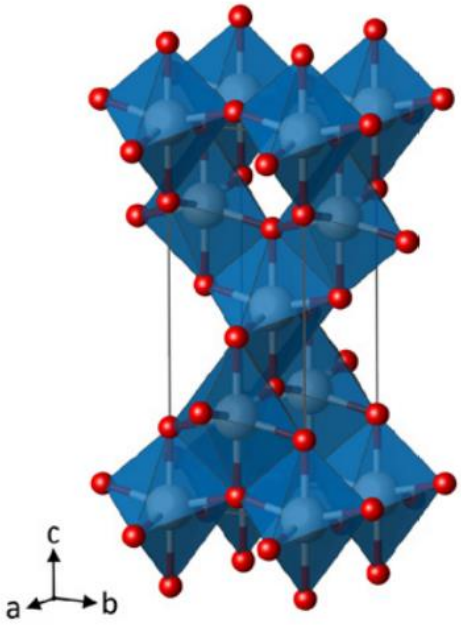

Figure 1.10 - Anatase crystal structure [43]

1.2.3.3 Brookite

Brookite is the third natural polymorph of titanium dioxide (rutile, anatase and brookite can be found on the earth). Brookite's name honoured amateur English crystallographer and mineralogist Henry James Brooke. In comparison with rutile and anatase, its crystal system is orthorhombic (instead of tetragonal) and the space group is Pbca [67], [68]. Its band gap is estimated to be ~3.3 eV [43], [69], [70] Brookite has the same crystalline structure as vanadium dioxide VO_2 [B] as Figure 1.11 shows. Brookite, as well as anatase, has photocatalytic properties [70].

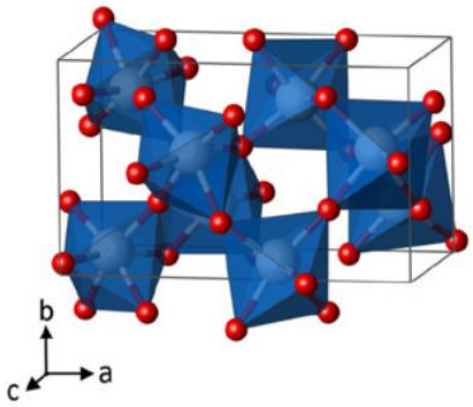

Figure 1.11- Brookite crystal structure [43]

Table 1-1 - Physical parameters of TiO_2 polymorphs [35], [71]

	Rutile	**Anatase**	**Brookite**	**TiO_2(II)**	**TiO_2B**	**Baddeleyite**	**Hollandite**
Crystal system	Tetragonal	Tetragonal	Orthorhombic	Orthorhombic	Monoclinic	Monoclinic	Tetragonal
Space group	P42/mnm	I41/amd	Pcba	Pbcn	C2/m	$P2_1/c$	I4/m
Unit cell parameters (Å)	a=4.594 c=2.959	a=3.785 c=9.514	a=9.184 b=5.447 c=5.145	a=4.59 b=5.44 c=4.94	a=12.16 b=3.74 c=6.51 β=107.29°	a=4.662 b=4.969 c=4.911 β=99.4°	a=10.18 c=2.97

1.2.3.4 High pressure polymorphs

There are more titanium dioxide polymorphs found at high pressures or through artificial creation.

TiO_2(II), also known as *srilankite* is a high pressure polymorph of titanium dioxide, with an orthorhombic unit cell and the *Pbcn* space group. In srilankite, as in rutile and anatase, each titanium atom is coordinated to six oxygen atoms, with Ti-O bond distances similar to those of rutile.

TiO_2 (B) is an artificial metastable polymorph of titanium dioxide and was first reported in 1980 by Marchand [72]. It has the same structure as VO_2(B) and its properties make it ideal for the development of mesoporous materials [72], [73].

The *Baddeleyite* structure of TiO_2 is formed at high pressure and temperatures (about 20 GPa and 1316 °C). The coordination number increases from six to seven across the transition [71], [74]. By increasing the pressure to around 60 GPa, titanium dioxide transforms into a *fluorite* (CaF_2) structure [71].

Hollandite oxide is an artificial structure of titanium dioxide. Its structure consists of tunnels as zeolites containing cations of alkaline elements. It is created from an oxidation of K_xTiO_2 ($0.13<x<0.25$) in an acidic solution of hydrogen peroxide at 80 °C over 48 h. After oxidisation in the acid bath the product is heated to 300 °C in order to dehydrate the oxide, producing an anhydrous yellow solid [75], [76].

These structures are interesting for new lithium batteries. Its large size tunnels would be a pathway for lithium ions diffusion in battery systems.

1.2.4 Photoinduced processes

Light is an electromagnetic wave with only a small range visible to the human eye. The full spectrum includes short wavelength gamma radiation (less than the diameter of an atom) to long wavelength radio waves (km). But only some certain wavelength ranges are able to excite some semiconductors, thus changing their conductivity. *Photocatalysis* is the process by which a reaction is promoted by absorption of light by the catalyst or the reactants.

As a result of a semiconductor's optical band gap, some photons are able to photoexcite semiconductors, but only if the photons are more energetic than the band gap. Chemical processes involve reactants, catalysts and light to carry out reactions. Photochemical processes involve the promotion of an electron, as Figure 1.12 shows. Acceptors are suitable

to accept an electron (reduction), whereas donors can provide one of their electrons (oxidation).

This promotion creates a separation between charges, one negative charge where the electron has been moved, and a positive charge in the valence band. Therefore these materials are suitable to promote redox reactions in function of the position of their band positions.

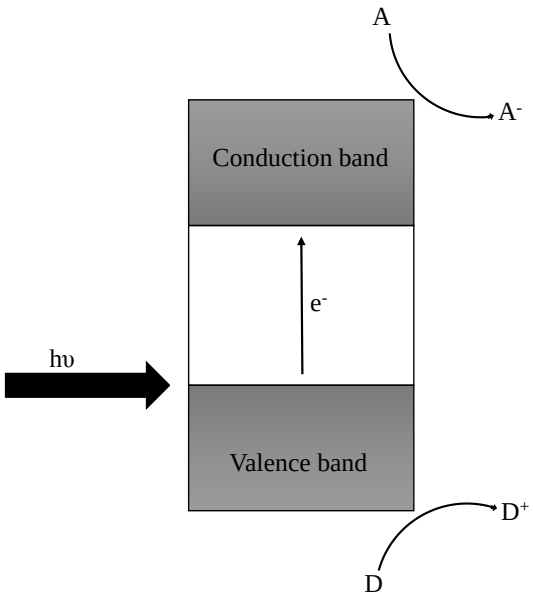

Figure 1.12 - Electronic promotion by light

A general example of a photocatalytic reaction is described below. When a molecule or atom is adsorbed on the surface of a photocatalyst, can be reduced or oxidised as Equation 1.1 shows.

$$(Ox_1)_{ads} + (Red_2)_{ads} \xrightarrow{hv > Eg} (Red_1)_{ads} + (Ox_2)_{ads} \qquad (1.1)$$

The first report concerning photocatalysis, in which metallic silver was obtained from a silver salt on zinc oxide, was published in 1924 [77]. One of the most important articles on the subject of photoelectrochemistry is by Akira Fujishima and Kenichi Honda in 1972. In this article they studied the photoelectrochemistry of the rutile form of titanium dioxide [78], [79] in an electrochemical cell, as shown in Figure 1.13.

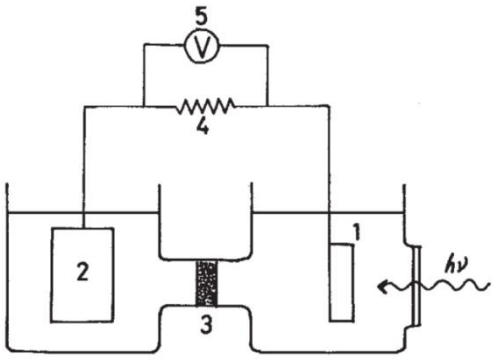

Figure 1.13 - Electrochemical cell in which the TiO_2 electrode (numbered 1) is connected through a permeable membrane (numbered 3) to a platinum electrode (numbered 2) with a surface area of approximately 30 cm^2 [79]

This was the first photoelectrochemical cell to create H_2 and O_2 from water [79], the general process is shown in Equation 1.2:

$$H_2O + 2h\nu \xrightarrow{\Delta G°=475\ kJ/mol} H_2 + {}^1/_2\,O_2 \qquad (1.2)$$

$$TiO_2 \xrightarrow{h\nu} 2e^- + 2h^+ \text{ (Excitation of } TiO_2 \text{ by light)} \qquad (1.3)$$

$$H_2O + 2h^+ \rightarrow 2H^+ + {}^1/_2\,O_2 \text{ (At the } TiO_2 \text{ electrode)} \qquad (1.4)$$

$$2H^+ + 2e^- \rightarrow H_2 \text{ (At the platinum electrode)} \qquad (1.5)$$

1.2.4.1 Photocatalytic behaviour of titanium dioxide

Since the first published research on the photocatalytic properties of TiO_2 [79], greater awareness of the potential ways to exploit this semiconductor's property has led to a significant increase in the quantity of research investigations carried out. This has been largely driven by their promise of becoming a useful method for; pollution remediation [80], water treatment [66], [81], [82], air purification [83]–[86] self-cleaning surfaces [87]–[92] or for the development of new super hydrophilic materials [88].

To apply titania as a photocatalyst it is first necessary to understand how titanium dioxide generates its surface oxidizing species. This has been reported by Akira Fujishima [66], [93], Kenichi Honda [79] and Koichi Iwata [94]. Photocatalysis by TiO_2 is an observed chemical phenomenon that starts with the absorption of UV photons, promoting the migration of electrons from the conduction band to the valence band, creating a charge separation [78],

[79], [93], [95]. This separation produces a reactive hole (h_{vb}^{+}) and the associated electron (e_{cb}^{-}) that migrates to the surface of the material. At the surface the holes and electrons are able to participate in a photocatalytic process by reacting with molecules such as H_2O and O_2. This leads to the formation of free radicals which are described by Equations 1.6-1.12 [78], [79], [93], [95]–[99] and their characteristic timeframe [66], [94], [100]–[107]. *Radicals* are chemical elements or molecules with, at least one, unpaired electron. These species generally have a short half-life due to high reactivity, and are able to react with a wide range of compounds. These processes are very fast with the separation charges occurring in the order of femtoseconds due to the high reactivity. The oxidizing species are commonly h^{+}, hydroxyl radicals, superoxide ($O_2^{\bullet-}$) and singlet state molecular oxygen [66], [97], [108], [109]. Other oxidizing species are hydrogen peroxide and triplet state molecular oxygen [93], [98].

$$TiO_2 \xrightarrow{h\nu} e^- + h^+ \quad (1.6)$$

$$h^+ + H_2O \rightarrow {}^{\bullet}OH + H^+ \quad (1.7)$$

$$e^- + H^+ \rightarrow {}^{\bullet}H \quad (1.8)$$

$$H^+ + O_2^{\bullet-} \rightarrow HO_2^{\bullet} \quad (1.9)$$

$$e^- + h^+ \rightarrow \text{heat or } h\upsilon \quad (1.10)$$

$$e^- + O_2 \rightarrow O_2^{\bullet-} \quad (1.11)$$

$$h^+ + O_2^{\bullet-} \rightarrow {}^1O_2 \quad (1.12)$$

Free radicals are responsible for the reduction-oxidation (redox) processes associated with the neutralisation and subsequent removal of hazardous molecules. Although titanium dioxide has three different metastable polymorphs, anatase with a band gap of 3.2 eV [60], [61] is widely accepted as being the most efficient structure for separating charges on its surface under UV irradiation [110]. It is therefore considered more reactive against pollutants compared to the other polymorphs of TiO_2 such as rutile and brookite.

Water is required to create hydroxyl radicals, but these oxidizing species are not responsible for the primary oxidation for some substances such as organic molecules (benzene, alcohols, etc.). These processes require initiation by holes [66], [97]. Fujishima, Hoffmann, Heller and Serratos [93], [97]–[99] concluded that molecular oxygen traps the generated electrons

(reaction 1.11), displacing the equilibrium; charge-generation/charge-recombination to the separation of charges (holes and electrons) [111]. Figure 1.14 shows the typical timeline of a photocatalytic reaction.

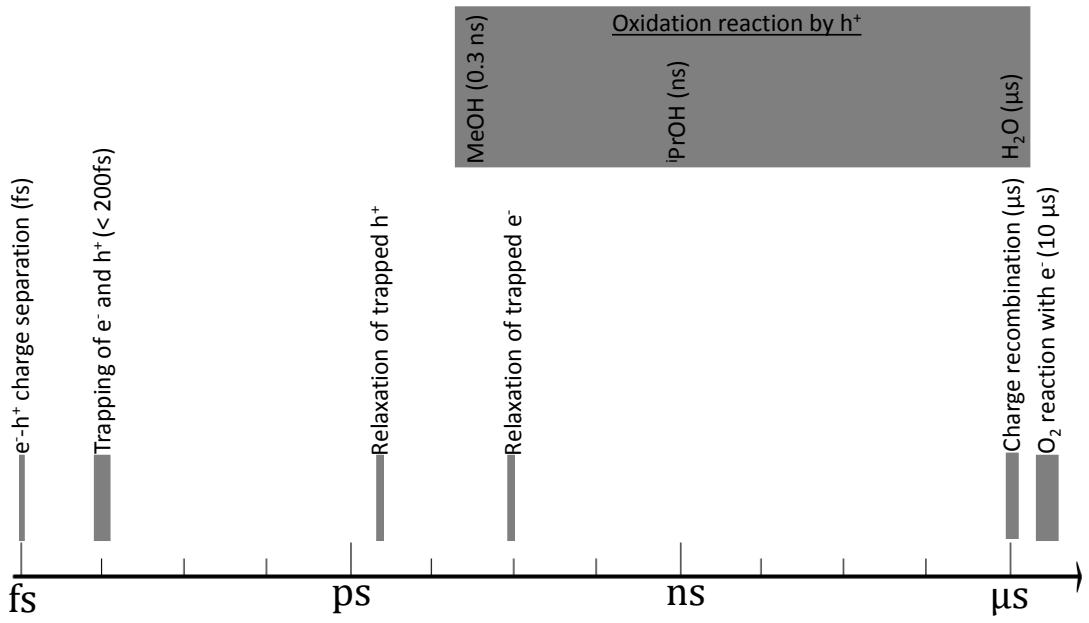

Figure 1.14 - Measured characteristic time for primary processes in TiO_2 photocatalyst [66], [94], [100]–[106]

TiO_2 hydrophilic properties are a result of the photocatalytic process on the material's surface. This process generates a photoexcited hole and electron. Then titanium dioxide reacts with oxygen and produces reduced titanium and an oxygen vacancy [112], [113].

This section has described the photocatalytic properties of titania; the following section examines the application of this photoactivity for the removal of pathogens. As an introduction a review of different pathogens is presented to understand how photocatalytic reactions can be used to kill microorganisms.

1.2.4.1.1 Removal of atmospheric pollutants

The ability to generate free radicals (reactions 1.6-1.12) makes photocatalysts a powerful tool for the removal of air pollutants. The reactive species can reduce or oxidise pollutants forming harmless chemical species.

Nitrogen oxides (NO_x) are a group of two different oxides of nitrogen; nitrogen monoxide (NO) and nitrogen dioxide (NO_2). Both of these oxides are considered air pollutants. They can be produced naturally during electric storms and human activity creates them during

combustion. Photocatalytic processes are able to oxidise these compounds to nitric acid which is held on the photocatalyst's surface [114]

$$NO + {}^{\bullet}OH \rightarrow HNO_2 \quad (1.13)$$

$$HNO_2 + {}^{\bullet}OH \rightarrow NO_2 + H_2O \quad (1.14)$$

$$NO_2 + {}^{\bullet}OH \rightarrow HNO_3 \quad (1.15)$$

Experiments have been performed by Mori, Tseng and Yu with successful results. Nitrogen oxides were oxidised to nitric acid as the proposed mechanism predicted [53], [115], [116]. Sulphur dioxide as well as nitrogen dioxide could be reduced in the presence of carbon monoxide [117], [118] as the following reactions show:

$$SO_2 + 2CO \rightarrow S + 2CO_2 \quad (1.16)$$

$$2NO + 2CO \rightarrow N_2 + 2CO_2 \quad (1.17)$$

In this case, sulphur would be deposited on the photocatalytic surface.

For CO_2, photoreduction in the presence of TiO_2 by H_2O has been previously reported in the gas-solid phase as well as the liquid-solid phase [119]–[127] with CH_4 and CH_3OH as the main products.

After TiO_2's UV charge separation promotion, electrons and hydrogen radicals (from H_2O) are available to react. CO_2 photoreduction has been proposed to consume electrons and hydrogen radicals as shown in Equations 1.18-1.23 [119], [120], [128], [129].

$$CO_2 + e^- \rightarrow {}^{\bullet}CO_2^- \quad (1.18)$$

$${}^{\bullet}CO_2^- + 8{}^{\bullet}H + h^+ \rightarrow CH_4 + 2H_2O \quad (1.19)$$

$${}^{\bullet}CO_2^- + 6{}^{\bullet}H + h^+ \rightarrow CH_3OH + 2H_2O \quad (1.20)$$

$${}^{\bullet}CO_2^- + 2{}^{\bullet}H + h^+ \rightarrow HCOOH \quad (1.21)$$

$${}^{\bullet}CO_2^- + 4{}^{\bullet}H + h^+ \rightarrow HCHO + H_2O \quad (1.22)$$

$$^{\bullet}CO_2^- + 12^{\bullet}H + 2h^+ \rightarrow C_2H_5OH + 3H_2O \qquad (1.23)$$

Halmann [130] reported one of the potential reasons why CO_2 reduction may occur in a less extensive percentage is the reoxidation of CO_2^- by hydroxyl radical [122], [131].

Other studies suggested the mechanism involved the anchoring of CO_2 on the TiO_2 surface as shown in the schematic Figure 1.15 [132], [133].

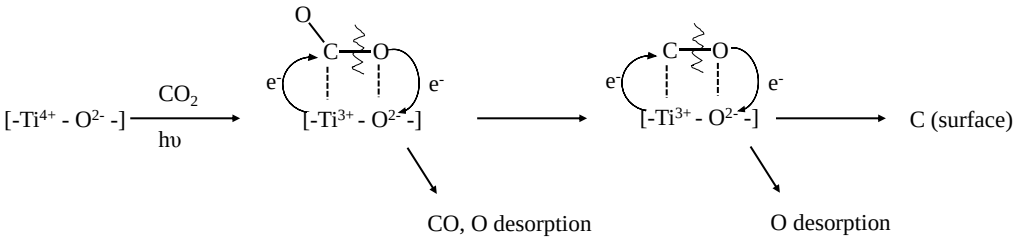

Figure 1.15 - Schematic representation of the photocatalytic reduction of CO_2 [132], [133]

1.2.4.1.2 Microcyde properties of titanium dioxide coatings

Two types of microorganism exist namely [134], Prokaryotes and Eukaryotes. While Prokaryotes are simple organisms without a cell nucleus [135], Eukaryotes are microorganism with a cell nucleus. *Bacteria* belong to one of the Prokaryote domains; with a structure containing a *plasma membrane* (lipid bilayer, formed mainly by phospholipids, see Figure 1.16) and a *cell wall* (formed by peptidoglycan).

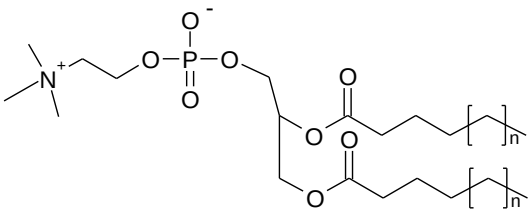

Figure 1.16 - Phospholipid structure, the separation of charges create a polar region and the fatty acids are the non-polar region

Some bacteria have an external membrane (lipid bilayer) which provides extra protection. There are two types of cell wall in bacteria known as Gram-positive or Gram-negative. *Gram staining* is a methodology developed by Hans Christian Gram to distinguish microorganisms based on their cell wall makeup. *Gram-positive* bacteria have a thick cell wall, due to many layers of peptidoglycan and teichoic acid (polysaccharide) between layers. *Gram-negative* bacteria have a thin cell wall, formed only from few peptidoglycan layers and a second lipid membrane.

Fungal cells have a lipid membrane and a cell wall made by chitin (polymer of N-acetylglucosamine). *Candida albicans* is a fungal agent that creates infections in humans, and is a potential target to remove in hospitals.

1.2.4.1.2.1 Photocatalytic neutralisation of pathogens

Photocatalysis generates oxidizing species. These reactive species can react with both organic and inorganic molecules. Macromolecules such as lipids or proteins are structural components of live cells. Thus, photocatalytic processes have biocidal activity. As Figure 1.17 shows Reactive species such as peroxides or hydroxyl radicals attack lipid bilayer membrane proteins, creating holes in the cell wall. By disrupting the membrane these holes are responsible for the death of the cell. Alternatively, if radicals enter into the cell, they can oxidise Fe^{2+} to Fe^{3+} and $^{\bullet}OH$. The $^{\bullet}OH$ radical has the ability to oxidise DNA and proteins, destroying the cell [136]

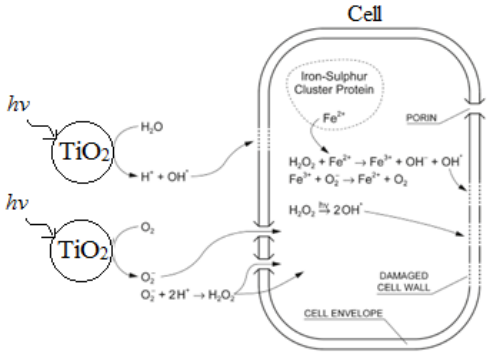

Figure 1.17 - Model representing the photoreaction chain with the photocatalyst, water and cell

Experiments with suspensions of *Staphylococcus aureus* (Gram-positive) [137], *Escherichia coli* (Gram-negative) [138], [139] and some cyanobacteria [140] have been performed with success, showing how the concentration of those microorganisms was dropped from 60 to 80 % within an hour of UV exposure due to photocatalytic reactions carried by TiO_2.

1.2.4.2 Study of photocatalytic reactions

The photocatalytic activity of various materials is routinely studied for powders or nanoparticles whilst in the form of an aqueous suspension. Under these conditions the decomposition rate of a suitable organic dye, such as methylene blue, is used as a measure of activity.

The development of a methodology working with microorganisms is a difficult and tedious task. This is one of the reasons why researchers replaced microorganisms to work with dyes; they have examined methylene blue [48], [57], [115], [141]–[146], 1,3,5,7-tetramethylcyclotetrasiloxane [147], methyl orange [148]–[150], rhodamine B (dye) [141], [151], [152], O,S-dimethyl phosphoramidothioate [153], 1-naphthol-5-sulfonic acid [52]. Other studies have been used stearic acid [154], polymers [155] or DMSO [156].

Methylene blue is an organic poly-heterocycle with a maximum peak at 670 nm (molar extinction coefficient in water, ε= 71089 $l \times mol^{-1} \times cm^{-1}$), which turns colourless in aqueous solution when it reduces (see Figure 1.18). The problem of using methylene blue is related to its structure, which is not equal to a protein or amino acid (monomer of protein), nor a pollutant. This is the reason why it may difficult to correlate the obtained results from methylene blue and an air pollutant or microorganism. This simple method was subsequently standardized in ISO (International Organization for Standardization) 10678.

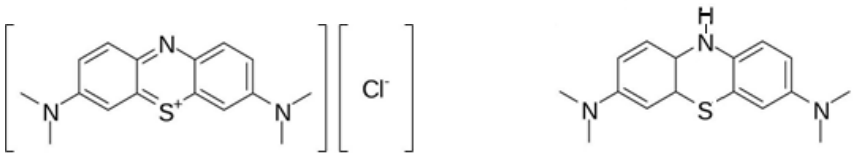

Figure 1.18 - Chemical structure of methylene blue in the oxidised state (left) and the reduced state (right)

However the physical mechanisms involved in such aqueous based methods can be significantly different compared to that of gas-phase reactions making the translation of relative performance problematic. There are currently another three published ISO methods related to air purification, each one being specific to one pollutant:

i. Nitric oxide (NO) ISO 22197-1
ii. Acetaldehyde (CH_3CHO) ISO 222197-2
iii. Toluene ($CH_3C_6H_5$) ISO 22197-3

These three methods use the same system which consists on a UVA light source which irradiates the inside of the reactor through a quartz glass. The gas mixture which contains the pollutant of interest at RH 50 % and room temperature. The end of the reactor is connected to an analyser. For NO, a detection system based on a chemiluminiscent reaction with luminol [157]–[159] is used, whereas for CH_3CHO and $CH_3C_6H_5$ the detector is a gas chromatographer coupled to a flame ionization detector [160].

The main disadvantage is the fact that each test requires a different and expensive detector, so that it is not possible to analyse them with a singular system.

1.2.5 Tailoring TiO_2 photocatalytic properties

If photocatalysts were the ‘first generation’, pure semiconductors such as TiO_2, proved to be very effective against pollutants. To activate them, UV photons are required, which are only less than 5 % from the total solar spectrum. While the visible range is the most abundant with 45 % of the total spectrum [161], visible photons do not have sufficient energy to stimulate the charge separation on TiO_2.

This is the main reason why researchers are investigating the second generation of photocatalysts. A shift of the TiO_2 absorption band towards the visible region would increase the amount of effective photons that can promote the charge separation process. This is a successful strategy confirmed by an extensive investigation to modify TiO_2 physical properties. From an implementation of metallic ions [48], [138], [151], [162] or noble metals [54], [146], [163]–[165] in the lattice to use non-metallic elements, such as nitrogen [138], [151], [166]–[171], sulphur [52], [172]–[175] or carbon [176]–[180] replacing oxygen in the TiO_2 structure.

An alternative strategy to modifying the electronic transfer properties of the structure involves improving the diffusion of charge to the surface of the material by increasing the bulk electrical conductivity. Adding red-ox species, such as alcohols or ions (e.g. Ag^+), slows down the recombination of electrons and holes thereby reducing the carrier losses. This interesting approach can be assessed by "self-doping" TiO_2. Partially reduced TiO_2 contains pairs Ti^{IV}-Ti^{III} [123], [181]–[185], which increases TiO_2 electrical conductivity [181], [186]. A variety of methods can be used to prepare titanium sub-oxides including hydrogenation [182], [187], thermal treatment under an inert atmosphere [188], or by solvo-thermal methods employing $TiCl_4$ and TiF_4 [184].

1.2.6 Photocatalytic film preparation

The development of photocatalytic paints and coatings for environmental remediation applications in both indoor and outdoor urban areas has been identified as a promising field of research [83], [189]–[193]. These coatings are used in different applications; from solar cells, photocatalysts or pigments to screening agents against UV light [194]. There are not only two methods to develop coatings as this literature review showed. Sol-gel [51], [195]–[200], magnetron sputtering [201], [202], chemical vapour deposition [169], [203]–[205], spray-pyrolysis [87], [174], [206]–[209] or anodic oxidation [210]–[212] have been deeply studied and are suitable to develop TiO_2 coatings.

The aim of this research is to use existing film preparation techniques to apply TiO_2 coatings in buildings. For this purpose, two strategies were decided:

i. Application in situ; in the case of existing buildings.
ii. Final coating of prefabricated panels before leaving the factory.

The limitations of an application in situ are determined by the time it requires to apply the coating, the drying time and the toxicity of solvents. The need of an inorganic binder is important, in order to avoid degradation of organic binders [213], [214].

For the application of panel in factories, the important factor is the versatility, cost-effective ratio and ease of the technique. The architecture of buildings usually requires complex surfaces, where a uniform coating is required for high quality finishing.

1.2.6.1 Electrophoretic deposition of TiO_2

Electrophoretic deposition is a versatile technique which has seen widespread use over the last 50 years. It is suitable for coating a wide range of materials including carbides [215], ceramic oxides [216], [217], metals [218] and polymers [219] onto an electrically conducting surface. Electrophoretic deposition has also been employed by industry as a material processing technique for coating automobile frames, heavy equipment and metal parts [220], [221].

Electrophoretic deposition of anatase TiO_2 was studied under different substrates (stainless steel, titanium and fluorine-doped tin oxide coated soda glass). Those substrates were chosen due to their wide use in the construction industry for structural and aesthetical applications in buildings. Many of the associated components are pre-fabricated and are therefore potential candidates for coating using electrophoretic deposition.

It is particularly appropriate for components with complex geometries where other methods may produce unacceptable variations in coating thickness [222]. An additional advantage of this technique includes a relatively rapid processing speed and lower costs when compared to alternative methods such as sol-gel processing. Electrophoretic deposition has been shown to produce coatings of sufficient quality for use in the production of dye-sensitised solar cells. It is well suited for the production of the high purity coatings required for such applications [139], [222]–[224].

Electrophoretic deposition is a processing technique that develops homogenous micro structured or nanostructured deposits (layered materials, thin films, etc.). It consists of a cell that contains two electrodes immersed in an electrolytic solution where the material to coat is dispersed. When an electric field is applied to the solution, the electrical gradient forces to the charged suspended particles to move to the electrode with an opposite charge (electrophoresis), as Figure 1.19 shows. Particles then accumulate on the electrode surface, creating a compact film. To increase the density of this film, heat treatment is required [225]. Electrophoretic deposition can be carried with a stable suspension of any fine powder's solid or colloidal suspension such as metals and polymers [226].

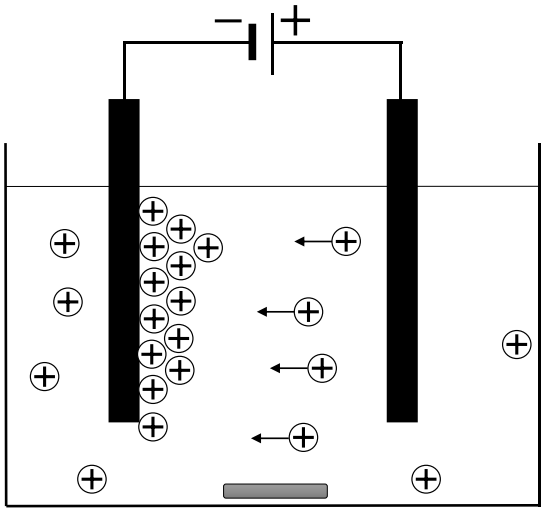

Figure 1.19 - Scheme of an electrophoretic cell, showing the electrodes (black) under magnetic stirring fly (grey)

Studies by Boccaccini, Farnoush, Mohanty, Caya and Fateminia have investigated a number of different solvents suitable for electrophoretic deposition of metal oxides [227]–[231]. Those based on isopropanol and acetylacetone were identified as producing coatings with high durability and uniformly deposited oxide nanoparticles. This is attributed to physical properties including the dielectric constant, 18.6 and 23.1 at 20 °C, viscosity index, 2.4 mPa × s and 0.821 mPa × s at 20 °C for isopropanol and acetylacetone respectively.

Additives can be added to the solvent mixture to modify the electrical conductivity of the media and provide charge stabilisation of the suspended particles [217], [220].

The *deposition voltage* and the *substrate* influence the electric field in the solution, affecting the particle charge and thus the stability of the suspension [222], [226], [232]–[234]. The nature of the *solvent* affects the efficient dispersion of nanoparticles and the deposition of those particles on the substrate [226], [232], [235]. Carrying out the deposition process for longer *durations* leads to a greater thickness of the coating [232], [234], [236], [237]. These four parameters were analysed to optimise the coating application on widely used building materials; steel, titanium and glass (coated to make it electrical conductive with a fluorine doped tin oxide conductive layer).

1.2.6.2 Dip coating

Dip-coating, also known as sol-gel dip-coating is a popular technique to develop thin films on different surfaces. The advantage of this process is the variety of shapes in which the film can be deposited [238], [239] besides the simplicity of the process. This technique was used to reproduce how a TiO_2 coating would be applied to a façade of buildings or structures in cities. The advantage of such a technique for this purpose is the reproducibility in terms of coating quality. Solvents such as alcohols are not considered VOCs, but their exposure to the environment is harmful. Petrol and some of its derivates are considered harmful to the environment also. Therefore, the decision to work with alcohol based solvents was chosen to satisfy environmental standards.

The object to be coated (cylinder, sphere, plate, etc.) is immersed in a solution bath until the substrate is wetted. Once the substrate is saturated with the solution, the evaporation of solvent creates the film. After which a drying process is required [240], [241]. Important factors to consider are the solution's parameters; concentration, viscosity, boiling point of solvent, also immersion time and drying techniques [240].

TiO_2 coatings have been prepared with this technique. Compact nano-TiO_2 coatings were prepared on aluminium using dip-coating method and evaporation [242].

1.2.7 Application of photocatalytic coatings and materials in pre-built environments

Despite the promising applications of TiO_2 coatings, photocatalytic coatings have not been applied widely as a novel coating for buildings beyond laboratory scale. Available products based on this technology are commercialised as ceramic tiles with a photocatalytic coating (BIONICTILE© by Ceracasa or Hydrotect® by TOTO ltd.), photocatalytic paints (KNOxOUT© by Boysen, ECO-EX© by TOTO ltd., Ecogreen plus or Soldalit-ME© by KEIM Mineral Paints Ltd.) or pigments for paints (KRONOCLEAN series). The lack of availability of those products and/or the direct applications in real life show there was not an effective knowledge transfer. The application of TiO_2 usually relies on its hydrophilic properties, an excellent advantage for self-cleaning and antifogging mirrors and windows. Hydrophilic properties originate from the decomposition (photocatalytic oxidation) and adsorption on the surface of the photocatalyst under UV conditions [112], [113].

In big cities with tall buildings, the concentration of pollutants is higher at street level [194]. Research involving coating cementitious material with TiO_2 has been undertaken with encouraging results [50], [84], [243]. The addition of glass as an aggregate combined with long curing times has increased photoactivity [194]. One of the problems for this coating is

the poisoning of the active sites; Ameen and Raupp found that only 100 min of exposure was enough to decrease the photoactivity due to deactivation [244]. Reactants poison the photocatalyst. If NO_2 is the reactant, nitric acid (HNO_3) is accumulated on the coating surfaces inhibiting the reaction with more NO_x. Water can easily remove HNO_3 [194].

Examples of buildings currently using this technology are all over the world. The most representatives for their impact and iconic style are:

i. "Chiesa di Dio Padre Misericordioso" in Rome; where the architect, Richard Meier used white cement based on TiO_2 (developed for Italcementi S.p.A.) to maintain its white colour despite the pollution caused by traffic.

Figure 1.20 - Chiesa di Dio Padre Misericordioso

ii. Toyota's Tsutsumi plant in Aichi (Figure 1.20), where they manufacture hybrid cars, was painted with Hydrotect color coat ECO-EX. This green initiative was part of a green project which involved the installation of photovboltaic solar panels, reduce the amount of generated waste (reduced by 82 %).

Figure 1.21 - Toyota's Tsutsumi plant (Image property of TOTO ltd.)

iii. Chubu International Airport terminal in Japan, opened in 2005, was built with anti-fogging glass to increase visibility on rainy days.

Figure 1.22 – Chubu International Airport terminal

Other “less iconic” buildings are using this technology. In China a residential building was covered with Hydrotect® tile.

Here, in the United Kingdom, KEIM Mineral Paints has provided photocatalytic paints which were used in The City of Edinburgh Council, the Swedish Ambassador’s Residence in London or in the New Co-operative Group Headquarters.

1.2.8 Concluding remarks

Since 1972, the knowledge of photocatalytic processes has led to a better understanding of the physicochemical properties of semiconductors. Among TiO_2 crystal polymorphs, anatase has exhibited higher photocatalytic properties.

Beyond pure crystals, a new approach focused the interest of researchers, named to shift the photocatalyst towards the visible spectrum. To do this, the physical properties of TiO_2 have to change in order to reduce the energetic requirement of incident photons. Doping TiO_2 has been studied with success, demonstrating the use of nitrogen is the most effective dopant to shift the band gap.

Another approach to increase the efficiency of photocatalysts is to maximise the charge separation process. By reducing recombination of electrons with holes, the formation of radicals would increase and therefore, the efficiency relative to absorbed UV, increases.

The study of photocatalytic reactions has been determined for the simplicity of techniques. Whereas gas chromatographers or mass spectrometers require an initial investment and maintenance; the use of organic dyes increased for its simplicity and cost. The problem of this extended use lies on the measure of photoactivity itself. The breakdown of an organic double bond affects the chromophore (conjugated double bonds) which absorbs in the visible region. In addition to this simple effect, the aqueous media effects on the light absorption and diffusion are critical to determine whether or not the tested photocatalyst will be effective in the gas phase.

The application of TiO_2 has been studied using a wide range of techniques suitable to prepare coatings for; solar cells, water splitting or photocatalytic reactions. However the knowledge transfer to real applications is yet to come. The effectiveness of photocatalytic coatings will determine the efficiency of those in the build environment.

1.3 Aims and objectives

The overall aim of this thesis was to investigate the decomposition of pollutants such as carbon and nitrogen dioxide in the gas phase using the photocatalytic properties of TiO_2 to develop novel coatings for the built environment in urban areas.

Therefore, the particular objectives of this research were:

- To design and develop a reaction chamber coupled to an EI-mass spectrometer able to study photocatalytic reactions in the gas phase

- To compare existing analytical methods to study photocatalytic reactions, such as dye degradation in aqueous phase or antibacterial properties with the activity of photocatalysts in the gas phase

- To characterise and evaluate the photocatalytic performance of commercially available TiO_2 powders and photocatalytic coatings to understand the limitations of the current technology

- To develop novel photocatalysts based on titanium sub-oxide species to improve their electronic properties by improving their electric conductivity

- The use of electrophoretic deposition technique to develop anatase based photocatalytic coatings and the optimisation of the process

- To develop a novel photocatalytic formulation based on a suspension of calcium hydroxide and anatase for its use in heritage buildings

1.4 Thesis structure

Chapter One has presented the current state of art in photocatalysis. In addition to this, a relevant review of the literature for this research has been given. The aims and objectives of this research also has been stated in this chapter.

All the analytical techniques used during this research are described in **Chapter Two**, explaining the physical theory behind the studied phenomena.

In **Chapter Three**, the experimental methodology that was used in the course of the research project is described with sufficient detail to be easily reproduced.

The design of a mass spectrometer and optimisation of its parameters are presented in **Chapter Four**. It also describes the mathematical approach that was developed to remove signal deviation from the mass spectrometer´s data.

The characterisation and evaluation of commercially available TiO_2 powders and photocatalytic coatings are shown in **Chapter Five**. The preliminary work done with commercially available photocatalytic coatings is presented and discussed. Different crystal polymorphs of TiO_2 were studied and the results were discussed.

Chapter Six describes how TiO2 photocatalytic properties were tailored by defects on TiO_2 lattice and therefore modifying its electrical properties. TiO_2 was reduced under an inert atmosphere at different temperatures, creating different ratios of titanium sub-oxides. Their photocatalytic properties were studied and the results discussed.

Chapter Seven presents the undertaken work in anatase coatings prepared electrophoretic deposition. Different parameters, such as substrate, solvent, deposition time and voltage affect the finishing quality of the coating. Results in the photocatalytic activity of the coatings from varying the deposition parameters are shown and discuss.

Chapter Eight presents the work in where the effect of adding anatase on nanolime was studied under different polluted gas compositions. Student Panayiotis Xenophontos did the SEM and EDX analysis as final year dissertations´ project. Dr Gianluca Pesce helped to work with the software PHREEQC and understand the calculated coefficients.

In **Chapter Nine** the results from Chapters Five, Six, Seven and Eight are discussed and linked, leading to **Chapter Ten** where the conclusions from the thesis are drawn. At the end of this chapter, recommendations for future work are presented.

1.5 Bibliography

[1] S. Solomon D. Qin, M. Manning, Z. Chen, M. Marquis, K.B. Averyt, M. Tignor, H.L. Miller, "Contribution of Working Group I to the Fourth Assessment Report of the Intergovernmental Panel on Climate Change," 2007.

[2] S. Lin, R. Jones, C. Pantea, H. Ozkaynak, S. T. Rao, S.-A. Hwang, and V. C. Garcia, "Impact of NO_x emissions reduction policy on hospitalizations for respiratory disease in New York State," *J Expo. Sci Env. Epidemiol*, vol. 23, no. 1, pp. 73–80, 2013.

[3] J. Schwartz, "Short term fluctuations in air pollution and hospital admissions of the elderly for respiratory disease.," *Thorax* , vol. 50 , no. 5 , pp. 531–538, 1995.

[4] R. Detels, D. P. Tashkin, J. W. Sayre, S. N. Rokaw, F. J. Massey, A. H. Coulson, and D. H. Wegman, "The UCLA population studies of CORD: X. A cohort study of changes in respiratory function associated with chronic exposure to SO_x, NO_x, and hydrocarbons.," *Am. J. Public Health*, vol. 81, no. 3, pp. 350–359, 1991.

[5] B. Gaston, J. M. Drazen, J. Loscalzo, and J. S. Stamler, "The biology of nitrogen oxides in the airways.," *Am. J. Respir. Crit. Care Med.*, vol. 149, no. 2, pp. 538–551, 1994.

[6] Y. Tao, S. Mi, S. Zhou, S. Wang, and X. Xie, "Air pollution and hospital admissions for respiratory diseases in Lanzhou, China.," *Environ. Pollut.*, vol. 185, pp. 196–201, 2014.

[7] "Directive 2008/50/EC of the European Parliament and of the Council of 21 May 2008 on ambient air quality and cleaner air for Europe." .

[8] K. M. Shea, R. T. Truckner, R. W. Weber, and D. B. Peden, "Climate change and allergic disease.," *J. Allergy Clin. Immunol.*, vol. 122, no. 3, pp. 443–53; quiz 454–5, 2008.

[9] L. H. Ziska and P. J. Beggs, "Anthropogenic climate change and allergen exposure: The role of plant biology.," *J. Allergy Clin. Immunol.*, vol. 129, no. 1, pp. 27–32, 2012.

[10] C. Barne, N. E. Alexis, J. A. Bernstein, J. R. Cohn, J. G. Demain, E. Horner, E. Levetin, A. Nei, and W. Phipatanakul, "Climate change and our environment: the

effect on respiratory and allergic disease.," *J. allergy Clin. Immunol. Pract.*, vol. 1, no. 2, pp. 137–41, 2013.

[11] G. D'Amato, L. Cecchi, M. D'Amato, and G. Liccardi, "Urban air pollution and climate change as environmental risk factors of respiratory allergy: An update," *J Investig Allergol Clin Inmunol*, vol. 20, no. 2, pp. 95–102, 2010.

[12] Y. Chen, E. Forsyth, K. Pan, H. Chen, A. Szema, K. Szema, and P. Chenrachasit, "Atmospheric temperature & pollen counts impact New York city asthma ER Visits," *J. Allergy Clin. Immunol.*, vol. 125, no. 2, p. 208, 2010.

[13] A. Lancia, D. Musmarra, and F. Pepe, "Modeling of SO_2 Absorption into Limestone Suspensions," *Ind. Eng. Chem. Res.*, vol. 36, no. 1, pp. 197–203, 1997.

[14] G. C. Allen, A. El-Turki, K. R. Hallam, D. McLaughlin, and M. Stacey, "Role of NO_2 and SO_2 in degradation of limestone," *Br. Corros. J.*, vol. 35, no. 1, pp. 35–38, 2000.

[15] Y.-N. Lee and S. E. Schwartz, "Evaluation of the rate of uptake of nitrogen dioxide by atmospheric and surface liquid water," *J. Geophys. Res. Ocean.*, vol. 86, no. C12, pp. 11971–11983, 1981.

[16] P. Kirkitsos and D. Sikiotis, "Deterioration of Pentelic marble, Portland limestone and Baumberger sandstone in laboratory exposures to NO_2: A comparison with exposures to gaseous HNO_3," *Atmos. Environ.*, vol. 30, no. 6, pp. 941–950, 1996.

[17] L. Dei and B. Salvadori, "Nanotechnology in cultural heritage conservation: nanometric slaked lime saves architectonic and artistic surfaces from decay," *J. Cult. Herit.*, vol. 7, no. 2, pp. 110–115, 2006.

[18] V. Daniele and G. Taglieri, "Nanolime suspensions applied on natural lithotypes: The influence of concentration and residual water content on carbonatation process and on treatment effectiveness," *J. Cult. Herit.*, vol. 11, no. 1, pp. 102–106, 2010.

[19] V. Daniele, G. Taglieri, and R. Quaresima, "The nanolimes in Cultural Heritage conservation: Characterisation and analysis of the carbonatation process," *J. Cult. Herit.*, vol. 9, no. 3, pp. 294–301, 2008.

[20] R. Giorgi, L. Dei, and P. Baglioni, "A New Method for Consolidating Wall Paintings Based on Dispersions of Lime in Alcohol," *Stud. Conserv.*, vol. 45, no. 3, pp. 154–161, 2000.

[21] P. Baglioni and R. Giorgi, "Soft and hard nanomaterials for restoration and conservation of cultural heritage," *Soft Matter*, vol. 2, no. 4, pp. 293–303, 2006.

[22] R. Giorgi, L. Dei, M. Ceccato, C. Schettino, and P. Baglioni, "Nanotechnologies for conservation of cultural heritage: Paper and canvas deacidification," *Langmuir*, vol. 18, no. 21, pp. 8198–8203, 2002.

[23] P. López-Arce, L. S. Gomez-Villalba, L. Pinho, M. E. Fernández-Valle, M. Á. de Buergo, and R. Fort, "Influence of porosity and relative humidity on consolidation of dolostone with calcium hydroxide nanoparticles: Effectiveness assessment with non-destructive techniques," *Mater. Charact.*, vol. 61, no. 2, pp. 168–184, 2010.

[24] Y. Elakneswaran, A. Iwasa, T. Nawa, T. Sato, and K. Kurumisawa, "Ion-cement hydrate interactions govern multi-ionic transport model for cementitious materials," *Cem. Concr. Res.*, vol. 40, no. 12, pp. 1756–1765, 2010.

[25] P. Brown and A. Doerr, "Chemical changes in concrete due to the ingress of aggressive species," *Cem. Concr. Res.*, vol. 30, no. 3, pp. 411–418, 2000.

[26] D. Jacques, L. Wang, E. Martens, and D. Mallants, "Modelling chemical degradation of concrete during leaching with rain and soil water types," *Cem. Concr. Res.*, vol. 40, no. 8, pp. 1306–1313, 2010.

[27] D. Sugiyama, "Chemical alteration of calcium silicate hydrate (C–S–H) in sodium chloride solution," *Cem. Concr. Res.*, vol. 38, no. 11, pp. 1270–1275, 2008.

[28] M. Moranville, S. Kamali, and E. Guillon, "Physicochemical equilibria of cement-based materials in aggressive environments-experiment and modeling," *Cem. Concr. Res.*, vol. 34, no. 9, pp. 1569–1578, 2004.

[29] C. S. Walker, D. Savage, M. Tyrer, and K. V. Ragnarsdottir, "Non-ideal solid solution aqueous solution modeling of synthetic calcium silicate hydrate," *Cem. Concr. Res.*, vol. 37, no. 4, pp. 502–511, 2007.

[30] F. X. Yao, M. C. Arbestain, S. Virgel, F. Blanco, J. Arostegui, J. A. Maciá-Agulló, and F. Macías, "Simulated geochemical weathering of a mineral ash-rich biochar in a modified Soxhlet reactor.," *Chemosphere*, vol. 80, no. 7, pp. 724–32, 2010.

[31] Ö. Cizer, C. Rodriguez-Navarro, E. Ruiz-Agudo, J. Elsen, D. Van Gemert, and K. Van Balen, "Phase and morphology evolution of calcium carbonate precipitated by carbonation of hydrated lime," *J. Mater. Sci.*, vol. 47, no. 16, pp. 6151–6165, 2012.

[32] C. Kittel, *Introduction to Solid State Physics 8th edition*. Wiley, 2005.

[33] J. William D. Callister, *Materials Science and Engineering - An Introduction 7th edition*. Wiley, 2007.

[34] D. W. Fischer, "X-ray band spectra and molecular-orbital structure of rutile TiO_2," *Phys. Rev. B*, vol. 5, no. 11, pp. 4219–4226, 1972.

[35] G. Meinhold, "Rutile and its applications in earth sciences," *Earth-Science Rev.*, vol. 102, no. 1–2, pp. 1–28, 2010.

[36] H. Zhang and J. F. Banfield, "Thermodynamic analysis of phase stability of nanocrystalline titania," *J. Mater. Chem.*, vol. 8, no. 9, pp. 2073–2076, 1998.

[37] H. Zhang and J. F. Banfield, "Understanding Polymorphic Phase Transformation Behavior during Growth of Nanocrystalline Aggregates: Insights from TiO_2," *J. Phys. Chem. B*, vol. 104, no. 15, pp. 3481–3487, 2000.

[38] U. Diebold, "The surface science of titanium dioxide," *Surf. Sci. Rep.*, vol. 48, no. 5–8, pp. 53–229, 2003.

[39] J. Murray and H. Wriedt, "The O−Ti (Oxygen-Titanium) system," *J. Phase Equilibria*, vol. 8, no. 2, pp. 148–165, 1987.

[40] W.-E. Wang and Y. S. Kim, "A thermodynamic evaluation of the titanium–oxygen system from O/Ti=0 to 3/2," *J. Nucl. Mater.*, vol. 270, no. 1–2, pp. 242–247, 1999.

[41] D. Reyes-Coronado, G. Rodríguez-Gattorno, M. E. Espinosa-Pesqueira, C. Cab, R. de Coss, and G. Oskam, "Phase-pure TiO_2 nanoparticles: anatase, brookite and rutile," *Nanotechnology*, vol. 19, no. 14, p. 145605, 2008.

[42] A. Amtout, R. Amtout, and Leonelli, "Optical properties of rutile near its fundamental band gap," *Phys. Rev. B. Condens. Matter*, vol. 51, no. 11, pp. 6842–6851, 1995.

[43] M. L. and E. R. and W. G. Schmidt, "The electronic structure and optical response of rutile, anatase and brookite TiO_2," *J. Phys. Condens. Matter*, vol. 24, no. 19, p. 195503, 2012.

[44] J. Pascual, J. Camassel, and H. Mathieu, "Fine structure in the intrinsic absorption edge of TiO_2" *Phys. Rev. B*, vol. 18, no. 10, pp. 5606–5614, 1978.

[45] D. A. H. Hanaor, "Review of the anatase to rutile phase transformation," *J. Mater. Sci.*, vol. 46, no. 4, p. 855, 2011.

[46] K. Okada, N. Yamamoto, Y. Kameshima, A. Yasumori, and K. J. D. MacKenzie, "Effect of Silica Additive on the Anatase-to-Rutile Phase Transition," *J. Am. Ceram. Soc.*, vol. 84, no. 7, pp. 1591–1596, 2001.

[47] H. Yamashita, Y. Nishida, S. Yuan, K. Mori, M. Narisawa, Y. Matsumura, T. Ohmichi, and I. Katayama, "Design of TiO_2-SiC photocatalyst using TiC-SiC nano-particles for degradation of 2-propanol diluted in water," *Catal. Today*, vol. 120, no. 2, pp. 163–167, 2007.

[48] J. Zhu, J. Ren, Y. N. Huo, Z. F. Bian, and H. X. Li, "Nanocrystalline Fe/TiO_2 visible photocatalyst with a mesoporous structure prepared via a nonhydrolytic sol-gel route," *J. Phys. Chem. C*, vol. 111, no. 51, pp. 18965–18969, 2007.

[49] H. Nishikiori, Y. Fukasawa, Y. Yokosuka, and T. Fujii, "Nitrogen doping into titanium dioxide by the sol-gel method using nitric acid," *Res. Chem. Intermed.*, vol. 37, no. 8, pp. 869–881, 2011.

[50] C. Shifu, Z. Sujuan, L. Wei, and Z. Wei, "Preparation and activity evaluation of p–n junction photocatalyst NiO/TiO_2," *J. Hazard. Mater.*, vol. 155, no. 1–2, pp. 320–326, 2008.

[51] L. Zhang, Y. Zhu, Y. He, W. Li, and H. Sun, "Preparation and performances of mesoporous TiO_2 film photocatalyst supported on stainless steel," *Appl. Catal. B Environ.*, vol. 40, no. 4, pp. 287–292, 2003.

[52] Y. Wang, J. Li, P. Peng, T. Lu, and L. Wang, "Preparation of S-TiO_2 photocatalyst and photodegradation of L-acid under visible light," *Appl. Surf. Sci.*, vol. 254, no. 16, pp. 5276–5280, 2008.

[53] T. Mori, J. Suzuki, K. Fujimoto, M. Watanabe, and Y. Hasegawa, "Reductive decomposition of nitrate ion to nitrogen in water on a unique hollandite photocatalyst," *Appl. Catal. B Environ.*, vol. 23, no. 4, pp. 283–289, 1999.

[54] S. F. Chin, S. C. Pang, and F. E. I. Dom, "Sol-gel synthesis of silver/titanium dioxide (Ag/TiO_2) core-shell nanowires for photocatalytic applications," *Mater. Lett.*, vol. 65, no. 17–18, pp. 2673–2675, 2011.

[55] C. K. Chung, S. L. Lin, S. Y. Cheng, K. P. Chuang, and H. Y. Wang, "Effect of sol–gel composition ratio and laser power on phase transformation of crystalline titanium dioxide under CO_2 laser annealing," *Micro Nano Lett.*, vol. 6, no. 7, p. 4, 2011.

[56] C. A. García-González, J. M. Andanson, S. G. Kazarian, C. Domingo, and J. Saurina, "Application of principal component analysis to the thermal characterisation of silanized nanoparticles obtained at supercritical carbon dioxide conditions," *Anal. Chim. Acta*, vol. 635, no. 2, pp. 227–234, 2009.

[57] E. Alonso, I. Montequi, and M. J. Cocero, "Effect of synthesis conditions on photocatalytic activity of TiO_2 powders synthesized in supercritical CO_2," *J. Supercrit. Fluids*, vol. 49, no. 2, pp. 233–238, 2009.

[58] C.-I. Wu, J.-W. Huang, Y.-L. Wen, S.-B. Wen, Y.-H. Shen, and M.-Y. Yeh, "Preparation of TiO_2 nanoparticles by supercritical carbon dioxide," *Mater. Lett.*, vol. 62, no. 12–13, pp. 1923–1926, 2008.

[59] S. Tanemura, L. Miao, P. Jin, K. Kaneko, A. Terai, and N. Nabatova-Gabain, "Optical properties of polycrystalline and epitaxial anatase and rutile TiO_2 thin films by rf magnetron sputtering," *Appl. Surf. Sci.*, vol. 212–213, pp. 654–660, 2003.

[60] G. M. Kavan L. Gilbert S. E., Klemenz C., Scheel H. J., "Electrochemical and Photoelectrochemical Investigation of Single-Crystal Anatase," *J. Am. Chem. Soc.*, vol. 118, no. 28, pp. 6716–6723, 1996.

[61] R. Asahi, Y. Taga, W. Mannstadt, and A. J. Freeman, "Electronic and optical properties of anatase TiO_2," *Phys. Rev. B*, vol. 61, no. 11, pp. 7459–7465, 2000.

[62] H. Tang, F. Lévy, H. Berger, and P. E. Schmid, "Urbach tail of anatase TiO_2" *Phys. Rev. B*, vol. 52, no. 11, pp. 7771–7774, 1995.

[63] S. Yin, Q. Zhang, F. Saito, and T. Sato, "Preparation of Visible Light-Activated Titania Photocatalyst by Mechanochemical Method," *Chem. Lett.*, vol. 32, no. 4, pp. 358–359, 2003.

[64] K. Nagaveni, M. S. Hegde, N. Ravishankar, G. N. Subbanna, and G. Madras, "Synthesis and Structure of Nanocrystalline TiO_2 with Lower Band Gap Showing High Photocatalytic Activity," *Langmuir*, vol. 20, no. 7, pp. 2900–2907, 2004.

[65] H. Lin, C. Huang, W. Li, C. Ni, S. Shah, and Y. Tseng, "Size dependency of nanocrystalline TiO_2 on its optical property and photocatalytic reactivity exemplified by 2-chlorophenol," *Appl. Catal. B Environ.*, vol. 68, no. 1–2, pp. 1–11, 2006.

[66] A. Fujishima, X. Zhang, and D. A. Tryk, "TiO_2 photocatalysis and related surface phenomena," *Surf. Sci. Rep.*, vol. 63, no. 12, pp. 515–582, 2008.

[67] Q. M. Pham, D. H. Pham, J.-S. Kim, E. J. Kim, and S. Kim, "Preparation of polyaniline–titanium dioxide hybrid materials in supercritical CO_2," *Synth. Met.*, vol. 159, no. 19–20, pp. 2141–2146, 2009.

[68] E. Baudrin, G. Sudant, D. Larcher, B. Dunn, and J.-M. Tarascon, "Preparation of Nanotextured VO_2 [B] from Vanadium Oxide Aerogels," *Chem. Mater.*, vol. 18, no. 18, pp. 4369–4374, 2006.

[69] A. Mattsson and L. Österlund, "Adsorption and Photoinduced Decomposition of Acetone and Acetic Acid on Anatase, Brookite, and Rutile TiO_2 Nanoparticles," *J. Phys. Chem. C*, vol. 114, no. 33, pp. 14121–14132, Aug. 2010.

[70] A. Di Paola, G. Cufalo, M. Addamo, M. Bellardita, R. Campostrini, M. Ischia, R. Ceccato, and L. Palmisano, "Photocatalytic activity of nanocrystalline TiO_2 (brookite, rutile and brookite-based) powders prepared by thermohydrolysis of $TiCl_4$ in aqueous chloride solutions," *Colloids Surfaces A Physicochem. Eng. Asp.*, vol. 317, no. 1–3, pp. 366–376, 2008.

[71] J. Muscat, V. Swamy, and N. M. Harrison, "First-principles calculations of the phase stability of TiO_2," *Phys. Rev. B*, vol. 65, no. 22, p. 224112, 2002.

[72] R. Marchand, L. Brohan, and M. Tournoux, "TiO_2 (B) a new form of titanium dioxide and the potassium octatitanate $K_2Ti_8O_{17}$," *Mater. Res. Bull.*, vol. 15, no. 8, pp. 1129–1133, 1980.

[73] T. P. Feist and P. K. Davies, "The soft chemical synthesis of TiO_2 (B) from layered titanates," *J. Solid State Chem.*, vol. 101, no. 2, pp. 275–295, 1992.

[74] Y. Hu, H. L. Tsai, and C. L. Huang, "Effect of brookite phase on the anatase–rutile transition in titania nanoparticles," *J. Eur. Ceram. Soc.*, vol. 23, no. 5, pp. 691–696, 2003.

[75] M. Latroche, L. Brohan, R. Marchand, and M. Tournoux, "New hollandite oxides: TiO_2 (H) and $K_{0.06}TiO_2$," *J. Solid State Chem.*, vol. 81, no. 1, pp. 78–82, 1989.

[76] M. Sakao, N. Kijima, J. Akimoto, and T. Okutani, "Synthesis, crystal structure, and electrochemical properties of hollandite-type $K_{0.008}TiO_2$," *Solid State Ionics*, vol 225, pp. 502-505, 2012

[77] P. A. Baur E, "Über die Einwirkung von Licht auf gelöste Silbersalze in Gegenwart von Zinkoxyd," *Helv. Chim. Acta*, vol. 7, pp. 910–915, 1924.

[78] O. Carp, C. L. Huisman, and A. Reller, "Photoinduced reactivity of titanium dioxide," *Prog. Solid State Chem.*, vol. 32, no. 1–2, pp. 33–177, 2004.

[79] A. Fujishima and K. Honda, "Electrochemical photolysis of water at a semiconductor electrode," *Nature*, vol. 238, no. 5358, pp. 37–38, 1972.

[80] A. P. H. García and S. L. Suib, *Solar Photocatalysis for Environment Remediation, In New and Future Developments in Catalysis*, Elsevier. 2013.

[81] S.-A. Lee, K.-H. Choo, C.-H. Lee, H.-I. Lee, T. Hyeon, W. Choi, and H.-H. Kwon, "Use of Ultrafiltration Membranes for the Separation of TiO_2 Photocatalysts in Drinking Water Treatment," *Ind. Eng. Chem. Res.*, vol. 40, no. 7, pp. 1712–1719, 2001.

[82] J. Ryu and W. Choi, "Substrate-Specific Photocatalytic Activities of TiO_2 and Multiactivity Test for Water Treatment Application," *Environ. Sci. Technol.*, vol. 42, no. 1, pp. 294–300, 2007.

[83] J. Kolarik and J. Toftum, "The impact of a photocatalytic paint on indoor air pollutants: Sensory assessments," *Build. Environ.*, vol. 57, no. 0, pp. 396–402, 2012.

[84] G. Hüsken, M. Hunger, and H. J. H. Brouwers, "Experimental study of photocatalytic concrete products for air purification," *Build. Environ.*, vol. 44, no. 12, pp. 2463–2474, 2009.

[85] G. Ramakrishnan and A. Orlov, "Development of novel inexpensive adsorbents from waste concrete to mitigate NO_x emissions," *Build. Environ.*, vol. 72, pp. 28–33, 2014.

[86] A. M. Ramirez, K. Demeestere, N. De Belie, T. Mäntylä, and E. Levänen, "Titanium dioxide coated cementitious materials for air purifying purposes: Preparation, characterisation and toluene removal potential," *Build. Environ.*, vol. 45, no. 4, pp. 832–838, 2010.

[87] Y. Ohko, S. Saitoh, T. Tatsuma, and A. Fujishima, "Photoelectrochemical Anticorrosion and Self-Cleaning Effects of a TiO_2 Coating for Type 304 Stainless Steel ," *J. Electrochem. Soc.* , vol. 148 , no. 1 , pp. B24–B28, 2001.

[88] Z. Wu, D. Lee, M. F. Rubner, and R. E. Cohen, "Structural Color in Porous, Superhydrophilic, and Self-Cleaning SiO_2/TiO_2 Bragg Stacks," *Small*, vol. 3, no. 8, pp. 1445–1451, 2007.

[89] Y. Paz, Z. Luo, L. Rabenberg, and A. Heller, "Photooxidative self-cleaning transparent titanium dioxide films on glass," *J. Mater. Res.*, vol. 10, no. 11, pp. 2842–2848, 1995.

[90] E. I. Cedillo-González, R. Riccò, M. Montorsi, M. Montorsi, P. Falcaro, and C. Siligardi, "Self-cleaning glass prepared from a commercial TiO_2 nano-dispersion and its photocatalytic performance under common anthropogenic and atmospheric factors," *Build. Environ.*, vol. 71, pp. 7–14, 2014.

[91] A. Chabas, S. Alfaro, T. Lombardo, A. Verney-Carron, E. Da Silva, S. Triquet, H. Cachier, and E. Leroy, "Long term exposure of self-cleaning and reference glass in an urban environment: A comparative assessment," *Build. Environ.*, vol. 79, pp. 57–65, 2014.

[92] A. Chabas, T. Lombardo, H. Cachier, M. H. Pertuisot, K. Oikonomou, R. Falcone, M. Verità, and F. Geotti-Bianchini, "Behaviour of self-cleaning glass in urban atmosphere," *Build. Environ.*, vol. 43, no. 12, pp. 2124–2131, 2008.

[93] A. Fujishima, T. N. Rao, and D. A. Tryk, "Titanium dioxide photocatalysis," *J. Photochem. Photobiol. C Photochem. Rev.*, vol. 1, no. 1, pp. 1–21, 2000.

[94] K. Iwata, "Carrier Dynamics in TiO_2 and Pt/TiO_2 Powders Observed by Femtosecond Time-Resolved Near-Infrared Spectroscopy at a Spectral Region of 0.9-1.5 μm with the Direct Absorption Method," *J. Phys. Chem. B*, vol. 108, no. 52, p. 7, 2004.

[95] A. Z. Fujishima, "Titanium dioxide photocatalysis: present situation and future approaches," *Comptes Rendus Chim.*, vol. 9, no. 5–6, pp. 750–760, 2006.

[96] D. A. Tryk, A. Fujishima, and K. Honda, "Recent topics in photoelectrochemistry: achievements and future prospects," *Electrochim. Acta*, vol. 45, no. 15–16, pp. 2363–2376, 2000.

[97] M. R. Hoffmann, S. T. Martin, W. Choi, and D. W. Bahnemann, "Environmental applications of semiconductor photocatalysis," *Chem. Rev.*, vol. 95, no. 1, pp. 69–96, 1995.

[98] A. Heller, "Chemistry and Applications of Photocatalytic Oxidation of Thin Organic Films," *Acc. Chem. Res.*, vol. 28, no. 12, pp. 503–508, 1995.

[99] M. Serratos and A. Bronson, "The effect of oxygen partial pressure on the stability of Magneli phases in high temperature corrosive wear," *Wear*, vol. 198, no. 1–2, pp. 267–270, 1996.

[100] A. M. Peiró, C. Colombo, G. Doyle, J. Nelson, A. Mills, and J. R. Durrant, "Photochemical Reduction of Oxygen Adsorbed to Nanocrystalline TiO_2 Films: A Transient Absorption and Oxygen Scavenging Study of Different TiO_2 Preparations," *J. Phys. Chem. B*, vol. 110, no. 46, pp. 23255–23263, 2006.

[101] Y. Tamaki, K. Hara, R. Katoh, M. Tachiya, and A. Furube, "Femtosecond Visible-to-IR Spectroscopy of TiO_2 Nanocrystalline Films: Elucidation of the Electron Mobility before Deep Trapping," *J. Phys. Chem. C*, vol. 113, no. 27, pp. 11741–11746, 2009.

[102] T. Yoshihara, R. Katoh, A. Furube, Y. Tamaki, M. Murai, K. Hara, S. Murata, H. Arakawa, and M. Tachiya, "Identification of Reactive Species in Photoexcited Nanocrystalline TiO_2 Films by Wide-Wavelength-Range (400−2500 nm) Transient Absorption Spectroscopy," *J. Phys. Chem. B*, vol. 108, no. 12, pp. 3817–3823, 2004.

[103] A. Yamakata, T. Ishibashi, and H. Onishi, "Water- and Oxygen-Induced Decay Kinetics of Photogenerated Electrons in TiO_2 and Pt/TiO_2: A Time-Resolved Infrared Absorption Study," *J. Phys. Chem. B*, vol. 105, no. 30, pp. 7258–7262, 2001.

[104] J. Tang, J. R. Durrant, and D. R. Klug, "Mechanism of Photocatalytic Water Splitting in TiO_2. Reaction of Water with Photoholes, Importance of Charge Carrier Dynamics, and Evidence for Four-Hole Chemistry," *J. Am. Chem. Soc.*, vol. 130, no. 42, pp. 13885–13891, 2008.

[105] C. McCullagh, N. Skillen, M. Adams, and P. K. J. Robertson, "Photocatalytic reactors for environmental remediation: a review," *J. Chem. Technol. Biotechnol.*, vol. 86, no. 8, pp. 1002–1017, 2011.

[106] K. Sayama, R. Abe, H. Arakawa, and H. Sugihara, "Decomposition of water into H_2 and O_2 by a two-step photoexcitation reaction over a $Pt–TiO_2$ photocatalyst in $NaNO_2$ and Na_2CO_3 aqueous solution," *Catal. Commun.*, vol. 7, no. 2, pp. 96–99, 2006.

[107] Y. Tamaki, A. Furube, M. Murai, K. Hara, R. Katoh, and M. Tachiya, "Dynamics of efficient electron-hole separation in TiO_2 nanoparticles revealed by femtosecond transient absorption spectroscopy under the weak-excitation condition," *Phys. Chem. Chem. Phys.*, vol. 9, no. 12, pp. 1453–1460, 2007.

[108] T. Daimon, T. Hirakawa, M. Kitazawa, J. Suetake, and Y. Nosaka, "Formation of singlet molecular oxygen associated with the formation of superoxide radicals in aqueous suspensions of TiO_2 photocatalysts," *Appl. Catal. A Gen.*, vol. 340, no. 2, pp. 169–175, 2008.

[109] S. C. Jensen, J. Haubrich, A. Shank, and C. M. Friend, "Carbonyl Coupling: Defects and O_2 Make or Break the Essential Reaction Intermediate on Titanium Dioxide," *Chem. – A Eur. J.*, vol. 17, no. 30, pp. 8309–8312, 2011.

[110] T. A. Egerton and J. A. Mattinson, "The influence of platinum on UV and 'visible' photocatalysis by rutile and Degussa P25," *J. Photochem. Photobiol. A Chem.*, vol. 194, no. 2–3, pp. 283–289, 2008.

[111] T. Berger, M. Sterrer, O. Diwald, and E. Knözinger, "Charge trapping and photoadsorption of O_2 on dehydroxylated TiO_2 nanocrystals - An electron paramagnetic resonance study," *ChemPhysChem*, vol. 6, no. 10, pp. 2104–2112, 2005.

[112] T. Watanabe, A. Nakajima, R. Wang, M. Minabe, S. Koizumi, A. Fujishima, and K. Hashimoto, "Photocatalytic activity and photoinduced hydrophilicity of titanium dioxide coated glass," *Thin Solid Films*, vol. 351, no. 1–2, pp. 260–263, 1999.

[113] K. Hashimoto, H. Irie, and A. Fujishima, "TiO_2 photocatalysis: A historical overview and future prospects," *Japanese J. Appl. Phys. Part 1-Regular Pap. Br. Commun. Rev. Pap.*, vol. 44, no. 12, pp. 8269–8285, 2005.

[114] S. Devahasdin, C. Fan, K. Li, and D. H. Chen, "TiO_2 photocatalytic oxidation of nitric oxide: transient behavior and reaction kinetics," *J. Photochem. Photobiol. A Chem.*, vol. 156, no. 1–3, pp. 161–170, 2003.

[115] Y. H. Tseng and C. H. Kuo, "Photocatalytic degradation of dye and NO_x using visible-light-responsive carbon-containing TiO_2," *Catal. Today*, vol. 174, no. 1, pp. 114–120, 2011.

[116] Y. H. Yu, Y. T. Pan, Y. T. Wu, J. Lasek, and J. C. S. Wu, "Photocatalytic NO reduction with C_3H_8 using a monolith photoreactor," *Catal. Today*, vol. 174, no. 1, pp. 141–147, 2011.

[117] Z. Zhaoliang, M. Jun, and Y. Xiyao, "Separate/simultaneous catalytic reduction of sulfur dioxide and/or nitric oxide by carbon monoxide over TiO_2-promoted cobalt sulfides," *J. Mol. Catal. A Chem.*, vol. 195, no. 1–2, pp. 189–200, 2003.

[118] Z. Zhaoliang, M. Jun, and Y. Xiyao, "Separate/simultaneous catalytic reduction of sulfur dioxide and/or nitric oxide by carbon monoxide over titanium–tin solid solution catalysts," *Chem. Eng. J.*, vol. 95, no. 1–3, pp. 15–24, 2003.

[119] H. Inoue, T. Matsuyama, B.-J. Liu, T. Sakata, H. Mori, and H. Yoneyama, "Photocatalytic Activities for Carbon Dioxide Reduction of TiO_2 Microcrystals

Prepared in SiO_2 Matrices Using a Sol–Gel Method," *Chem. Lett.*, vol. 23, no. 3, pp. 653–656, 1994.

[120] T. Inoue, A. Fujishima, S. Konishi, and K. Honda, "Photoelectrocatalytic reduction of carbon dioxide in aqueous suspensions of semiconductor powders," *Nature*, vol. 277, no. 5698, pp. 637–638, 1979.

[121] H. Yamashita, H. Nishiguchi, N. Kamada, M. Anpo, Y. Teraoka, H. Hatano, S. Ehara, K. Kikui, L. Palmisano, A. Sclafani, M. Schiavello, and M. A. Fox, "Photocatalytic reduction of CO_2 with H_2O on TiO_2 and Cu/TiO_2 catalysts," *Res. Chem. Intermed.*, vol. 20, no. 8, pp. 815–823, 1994.

[122] B. Aurian-Blajeni, M. Halmann, and J. Manassen, "Photoreduction of carbon dioxide and water into formaldehyde and methanol on semiconductor materials," *Sol. Energy*, vol. 25, no. 2, pp. 165–170, 1980.

[123] H. Yamashita, A. Shiga, S. Kawasaki, Y. Ichihashi, S. Ehara, and M. Anpo, "Photocatalytic synthesis of CH_4 and CH_3OH from CO_2 and H_2O on highly dispersed active titanium oxide catalysts," *Energy Convers. Manag.*, vol. 36, no. 6–9, pp. 617–620, 1995.

[124] K. Ikeue, H. Yamashita, M. Anpo, and T. Takewaki, "Photocatalytic reduction of CO_2 with H_2O on Ti−β zeolite photocatalysts: Effect of the hydrophobic and hydrophilic properties," *J. Phys. Chem. B*, vol. 105, no. 35, pp. 8350–8355, 2001.

[125] B. Srinivas, B. Shubhamangala, K. Lalitha, P. Anil Kumar Reddy, V. Durga Kumari, M. Subrahmanyam, and B. R. De, "Photocatalytic reduction of CO_2 over Cu-TiO_2/molecular sieve 5A composite," *Photochem. Photobiol.*, vol. 87, no. 5, pp. 995–1001, 2011.

[126] C.-C. Lo, C.-H. Hung, C.-S. Yuan, and J.-F. Wu, "Photoreduction of carbon dioxide with H_2 and H_2O over TiO_2 and ZrO_2 in a circulated photocatalytic reactor," *Sol. Energy Mater. Sol. Cells*, vol. 91, no. 19, pp. 1765–1774, 2007.

[127] P. Usubharatana, D. McMartin, A. Veawab, and P. Tontiwachwuthikul, "Photocatalytic process for CO_2 emission reduction from industrial flue gas streams," *Ind. Eng. Chem. Res.*, vol. 45, no. 8, pp. 2558–2568, 2006.

[128] S. Kaneco, Y. Shimizu, K. Ohta, and T. Mizuno, "Photocatalytic reduction of high pressure carbon dioxide using TiO_2 powders with a positive hole scavenger," *J. Photochem. Photobiol. A Chem.*, vol. 115, no. 3, pp. 223–226, 1998.

[129] Y. Taniguchi, H. Yoneyama, and H. Tamura, "Photoelectrochemical reduction of carbon dioxide at p-type gallium phosphide electrodes in the presence of crown ether," *Bull. Chem. Soc. Jpn.*, vol. 55, no. 7, pp. 2034–2039, 1982.

[130] M. Halmann, V. Katzir, E. Borgarello, and J. Kiwi, "Photoassisted carbon dioxide reduction on aqueous suspensions of titanium dioxide," *Sol. Energy Mater.*, vol. 10, no. 1, pp. 85–91, 1984.

[131] C. D. Jaeger and A. J. Bard, "Spin trapping and electron spin resonance detection of radical intermediates in the photodecomposition of water at titanium dioxide particulate systems," *J. Phys. Chem.*, vol. 83, no. 24, pp. 3146–3152, 1979.

[132] M. Anpo, H. Yamashita, Y. Ichihashi, and S. Ehara, "Photocatalytic reduction of CO_2 with H_2O on various titanium oxide catalysts," *J. Electroanal. Chem.*, vol. 396, no. 1–2, pp. 21–26, 1995.

[133] M. Anpo, H. Yamashita, K. Ikeue, Y. Fujii, S. G. Zhang, Y. Ichihashi, D. R. Park, Y. Suzuki, K. Koyano, and T. Tatsumi, "Photocatalytic reduction of CO_2 with H_2O on Ti-MCM-41 and Ti-MCM-48 mesoporous zeolite catalysts," *Catal. Today*, vol. 44, no. 1–4, pp. 327–332, 1998.

[134] N. D. Lehninger A. Cox M., *Lehninger Principles of Biochemistry*, 5th ed. W. H. Freeman, 2008.

[135] W. B. Whitman, D. C. Coleman, and W. J. Wiebe, "Prokaryotes: The unseen majority," *Proc Natl Acad Sci*, vol. 95, no. 12, p. 6, 1998.

[136] T. Bak, J. Nowotny, N. J. Sucher, and E. Wachsman, "Effect of crystal imperfections on reactivity and photoreactivity of TiO_2 (rutile) with oxygen, water, and bacteria," *J. Phys. Chem. C*, vol. 115, no. 32, pp. 15711–15738, 2011.

[137] Y. Oka, W.-C. Kim, T. Yoshida, T. Hirashima, H. Mouri, H. Urade, Y. Itoh, and T. Kubo, "Efficacy of titanium dioxide photocatalyst for inhibition of bacterial colonization on percutaneous implants," *J. Biomed. Mater. Res. Part B Appl. Biomater.*, vol. 86B, no. 2, pp. 530–540, 2008.

[138] C. W. H. Dunnill, Z. A. Aiken, J. Pratten, M. Wilson, D. J. Morgan, and I. P. Parkin, "Enhanced photocatalytic activity under visible light in N-doped TiO_2 thin films produced by APCVD preparations using t-butylamine as a nitrogen source and their potential for antibacterial films," *J. Photochem. Photobiol. A Chem.*, vol. 207, no. 2–3, pp. 244–253, 2009.

[139] F.-J. Zhang, M.-L. Chen, and W.-C. Oh, "Photoelectrocatalytic properties and bactericidal activities of silver-treated carbon nanotube/titania composites," *Compos. Sci. Technol.*, vol. 71, no. 5, pp. 658–665, 2011.

[140] P. J. Senogles, J. A. Scott, G. Shaw, and H. Stratton, "Photocatalytic Degradation of the Cyanotoxin Cylindrospermopsin, using Titanium Dioxide and UV Irradiation," *Water Res.*, vol. 35, no. 5, pp. 1245–1255, 2001.

[141] W.-C. Oh, F.-J. Zhang, and M.-L. Chen, "Characterisation and photodegradation characteristics of organic dye for Pt–titania combined multi-walled carbon nanotube composite catalysts," *J. Ind. Eng. Chem.*, vol. 16, no. 2, pp. 321–326, 2010.

[142] G. K. Mor, O. K. Varghese, M. Paulose, K. Shankar, and C. A. Grimes, "A review on highly ordered, vertically oriented TiO_2 nanotube arrays: Fabrication, material properties, and solar energy applications," *Sol. Energy Mater. Sol. Cells*, vol. 90, no. 14, pp. 2011–2075, 2006.

[143] M. J. Sampaio, C. G. Silva, R. R. N. Marques, A. M. T. Silva, and J. L. Faria, "Carbon nanotube–TiO_2 thin films for photocatalytic applications," *Catal. Today*, vol. 161, no. 1, pp. 91–96, 2011.

[144] T. Ohno, T. Tsubota, K. Nishijima, and Z. Miyamoto, "Degradation of methylene blue on carbonate species-doped TiO_2 photocatalysts under visible light," *Chem. Lett.*, vol. 33, no. 6, pp. 750–751, 2004.

[145] C. Y. Lin, Y. K. Fang, C. H. Kuo, S. F. Chen, C.-S. Lin, T. H. Chou, Y.-H. Lee, J.-C. Lin, and S.-B. Hwang, "Design and fabrication of a TiO_2/nano-silicon composite visible light photocatalyst," *Appl. Surf. Sci.*, vol. 253, no. 2, pp. 898–903, 2006.

[146] F. Zhang, M. Chen, and W. Oh, "Photoelectrocatalytic properties of Ag-CNT/TiO_2 composite electrodes for methylene blue degradation," *New Carbon Mater.*, vol. 25, no. 5, pp. 348–356, 2010.

[147] H. Tada and M. Tanaka, "Dependence of TiO_2 Photocatalytic Activity upon Its Film Thickness," *Langmuir*, vol. 13, no. 2, pp. 360–364, 1997.

[148] Y. Li, J. Wang, H. Yao, L. Dang, and Z. Li, "Efficient decomposition of organic compounds and reaction mechanism with BiOI photocatalyst under visible light irradiation," *J. Mol. Catal. A Chem.*, vol. 334, no. 1–2, pp. 116–122, 2011.

[149] C. Wang, H. S. Shi, P. Zhang, and Y. Li, "Synthesis and characterisation of kaolinite/TiO_2 nano-photocatalysts," *Appl. Clay Sci.*, vol. 53, no. 4, pp. 646–649, 2011.

[150] S. Chen, W. Zhao, W. Liu, and S. Zhang, "Preparation, characterisation and activity evaluation of p–n junction photocatalyst p-ZnO/n-TiO_2," *Appl. Surf. Sci.*, vol. 255, no. 5, Part 1, pp. 2478–2484, 2008.

[151] L. Zhang, X. Li, Z. Chang, and D. Li, "Preparation, characterisation and photoactivity of hollow N, Co co-doped TiO_2/SiO_2 microspheres," *Mater. Sci. Semicond. Process.*, vol. 14, no. 1, pp. 52–57, 2011.

[152] H. Wang, T. Wang, and P. E. I. Xu, "Effects of substrate temperature on the microstructure and photocatalytic reactivity of TiO_2 films," *J. Mater. Sci. Mater. Electron.*, vol. 9, no. 5, pp. 327–330, 1998.

[153] K. Dai, T. Peng, H. Chen, R. Zhang, and Y. Zhang, "Photocatalytic Degradation and Mineralization of Commercial Methamidophos in Aqueous Titania Suspension," *Environ. Sci. Technol.*, vol. 42, no. 5, pp. 1505–1510, 2008.

[154] Y. Paz and A. Heller, "Photo-oxidatively self-cleaning transparent titanium dioxide films on soda lime glass: The deleterious effect of sodium contamination and its prevention," *J. Mater. Res.*, vol. 12, no. 10, pp. 2759–2766, 1997.

[155] A. P. Kumar, D. Depan, N. Singh Tomer, and R. P. Singh, "Nanoscale particles for polymer degradation and stabilization—Trends and future perspectives," *Prog. Polym. Sci.*, vol. 34, no. 6, pp. 479–515, 2009.

[156] M. Mori, K. Tanaka, H. Taoda, M. Ikedo, and H. Itabashi, "Ion-exclusion/adsorption chromatography of dimethylsulfoxide and its derivatives for the evaluation to quality-test of TiO_2-photocatalyst in water," *Talanta*, vol. 70, no. 1, pp. 169–173, 2006.

[157] J. Harper and M. J. Sailor, "Detection of nitric oxide and nitrogen dioxide with photoluminescent porous silicon," *Anal. Chem.*, vol. 68, no. 21, pp. 3713–3717, 1996.

[158] T. J. Kelly, C. W. Spicer, and G. F. Ward, "An assessment of the luminol chemiluminescence technique for measurement of NO_2 in ambient air," *Atmos. Environ. Part A. Gen. Top.*, vol. 24, no. 9, pp. 2397–2403, 1990.

[159] E. J. Dunlea, S. C. Herndon, D. D. Nelson, R. M. Volkamer, F. San Martini, P. M. Sheehy, M. S. Zahniser, J. H. Shorter, J. C. Wormhoudt, B. K. Lamb, E. J. Allwine, J. S. Gaffney, N. A. Marley, M. Grutter, C. Marquez, S. Blanco, B. Cardenas, A. Retama, C. R. Ramos Villegas, C. E. Kolb, L. T. Molina, and M. J. Molina, "Evaluation of nitrogen dioxide chemiluminescence monitors in a polluted urban environment," *Atmos. Chem. Phys.*, vol. 7, no. 10, pp. 2691–2704, 007.

[160] A. Mills, C. Hill, and P. K. J. Robertson, "Overview of the current ISO tests for photocatalytic materials," *J. Photochem. Photobiol. A Chem.*, vol. 237, pp. 7–23, 2012.

[161] J. L. Gole, J. D. Stout, C. Burda, Y. Lou, and X. Chen, "Highly Efficient Formation of Visible Light Tunable $TiO_{2-x}N_x$ Photocatalysts and Their Transformation at the Nanoscale," *J. Phys. Chem. B*, vol. 108, no. 4, pp. 1230–1240, 2004.

[162] W. Choi, A. Termin, and M. R. Hoffmann, "The role of metal ion dopants in quantum-sized TiO_2: Correlation between photoreactivity and charge carrier recombination dynamics," *J. Phys. Chem.*, vol. 98, no. 51, pp. 13669–13679, 1994.

[163] M. J. Santillán, N. E. Quaranta, and A. R. Boccaccini, "Titania and titania–silver nanocomposite coatings grown by electrophoretic deposition from aqueous suspensions," *Surf. Coatings Technol.*, vol. 205, no. 7, pp. 2562–2571, 2010.

[164] V. Diesen, C. W. Dunnill, E. Osterberg, I. P. Parkin, and M. Jonsson, "Silver enhanced TiO_2 thin films: photocatalytic characterisation using aqueous solutions of tris(hydroxymethyl)aminomethane," *Dalt. Trans.*, vol. 43, no. 1, pp. 344–351, 2014.

[165] G. Veréb, L. Manczinger, G. Bozsó, A. Sienkiewicz, L. Forró, K. Mogyorósi, K. Hernádi, and A. Dombi, "Comparison of the photocatalytic efficiencies of bare and doped rutile and anatase TiO_2 photocatalysts under visible light for phenol

degradation and E. coli inactivation," *Appl. Catal. B Environ.*, vol. 129, pp. 566–574, 2013.

[166] S. Sakthivel, M. Janczarek, and H. Kisch, "Visible light activity and photoelectrochemical properties of nitrogen-doped TiO_2," *J. Phys. Chem. B*, vol. 108, no. 50, pp. 19384–19387, 2004.

[167] C. W. Dunnill, Z. Ansari, A. Kafizas, S. Perni, D. J. Morgan, M. Wilson, and I. P. Parkin, "Visible light photocatalysts-N-doped TiO_2 by sol-gel, enhanced with surface bound silver nanoparticle islands," *J. Mater. Chem.*, vol. 21, no. 32, pp. 11854–11861, 2011.

[168] K. Yang, Y. Dai, and B. Huang, "Study of the nitrogen concentration influence on N-doped TiO_2 anatase from first-principles calculations," *J. Phys. Chem. C*, vol. 111, no. 32, pp. 12086–12090, 2007.

[169] H. M. Yates, M. G. Nolan, D. W. Sheel, and M. E. Pemble, "The role of nitrogen doping on the development of visible light-induced photocatalytic activity in thin TiO_2 films grown on glass by chemical vapour deposition," *J. Photochem. Photobiol. A Chem.*, vol. 179, no. 1–2, pp. 213–223, 2006.

[170] G. Liu, Y. Zhao, C. Sun, F. Li, G. Q. Lu, and H.-M. Cheng, "Synergistic Effects of B/N Doping on the Visible-Light Photocatalytic Activity of Mesoporous TiO_2," *Angew. Chemie Int. Ed.*, vol. 47, no. 24, pp. 4516–4520, 2008.

[171] Y. N. and M. M. and J. N. and A. Y. Nosaka, "Nitrogen-doped titanium dioxide photocatalysts for visible response prepared by using organic compounds," *Sci. Technol. Adv. Mater.*, vol. 6, no. 2, p. 143, 2005.

[172] T. Umebayashi, T. Yamaki, H. Itoh, and K. Asai, "Band gap narrowing of titanium dioxide by sulfur doping," *Appl. Phys. Lett.*, vol. 81, no. 3, p. 454, 2002.

[173] T. Ohno, T. Mitsui, and M. Matsumura, "Photocatalytic Activity of S-doped TiO_2 Photocatalyst under Visible Light," *Chem. Lett.*, vol. 32, no. 4, pp. 364–365, 2003.

[174] C. O. Ayieko, R. J. Musembi, S. M. Waita, B. O. Aduda, and P. K. Jain, "Structural and Optical Characterisation of Nitrogen-doped TiO_2 Thin Films Deposited by Spray Pyrolysis on Fluorine Doped Tin Oxide (FTO) Coated Glass Slides," *Int. J. Energy Eng.*, vol. 2, no. 3, pp. 67–72, 2012.

[175] T. Ohno, M. Akiyoshi, T. Umebayashi, K. Asai, T. Mitsui, and M. Matsumura, "Preparation of S-doped TiO_2 photocatalysts and their photocatalytic activities under visible light," *Appl. Catal. A Gen.*, vol. 265, no. 1, pp. 115–121, 2004.

[176] I.-C. Kang, Q. Zhang, S. Yin, T. Sato, and F. Saito, "Preparation of a visible sensitive carbon doped TiO_2 photo-catalyst by grinding TiO_2 with ethanol and heating treatment," *Appl. Catal. B Environ.*, vol. 80, no. 1–2, pp. 81–87, 2008.

[177] H. Irie, Y. Watanabe, and K. Hashimoto, "Carbon-doped Anatase TiO_2 Powders as a Visible-light Sensitive Photocatalyst," *Chem. Lett.*, vol. 32, no. 8, pp. 772–773, 2003.

[178] A. Murphy, "Band-gap determination from diffuse reflectance measurements of semiconductor films, and application to photoelectrochemical water-splitting," *Sol. Energy Mater. Sol. Cells*, vol. 91, no. 14, pp. 1326–1337, 2007.

[179] H. W. and J. P. Lewis, "Effects of dopant states on photoactivity in carbon-doped TiO_2," *J. Phys. Condens. Matter*, vol. 17, no. 21, p. L209, 2005.

[180] S. Sakthivel and H. Kisch, "Daylight Photocatalysis by Carbon-Modified Titanium Dioxide," *Angew. Chemie Int. Ed.*, vol. 42, no. 40, pp. 4908–4911, 2003.

[181] W. H. Saputera, G. Mul, and M. S. Hamdy, "Ti^{3+}-containing titania: Synthesis tactics and photocatalytic performance," *Catal. Today*, 2014.

[182] S. Riyapan, Y. Boonyongmaneerat, O. Mekasuwandumrong, P. Praserthdam, and J. Panpranot, "Effect of surface Ti^{3+} on the sol–gel derived TiO_2 in the selective acetylene hydrogenation on Pd/TiO_2 catalysts," *Catal. Today*, 2014.

[183] X. Zhang, H. Tian, X. Wang, G. Xue, Z. Tian, J. Zhang, S. Yuan, T. Yu, and Z. Zou, "The role of oxygen vacancy-Ti^{3+} states on TiO_2 nanotubes' surface in dye-sensitised solar cells," *Mater. Lett.*, vol. 100, pp. 51–53, 2013.

[184] Q. Zhu, Y. Peng, L. Lin, C.-M. Fan, G.-Q. Gao, R.-X. Wang, and A.-W. Xu, "Stable blue TiO_{2-x} nanoparticles for efficient visible light photocatalysts," *J. Mater. Chem. A*, vol. 2, no. 12, p. 4429, 2014.

[185] G. Lu, A. Linsebigler, and J. T. Yates, "Ti^{3+} Defect sites on TiO_2 (110): Production and chemical detection of active sites," *J. Phys. Chem.*, vol. 98, no. 45, pp. 11733–11738, 1994.

[186] Y. Ren, J. Li, and J. Yu, "Enhanced electrochemical performance of TiO_2 by Ti^{3+} doping using a facile solvothermal method as anode materials for lithium-ion batteries," *Electrochim. Acta*, vol. 138, pp. 41–47, 2014.

[187] M. Xing, W. Fang, M. Nasir, Y. Ma, J. Zhang, and M. Anpo, "Self-doped Ti^{3+}-enhanced TiO_2 nanoparticles with a high-performance photocatalysis," *J. Catal.*, vol. 297, pp. 236–243, 2013.

[188] V. Adamaki, F. Clemens, P. Ragulis, S. R. Pennock, J. Taylor, and C. R. Bowen, "Manufacturing and characterisation of Magnéli phase conductive fibres," *J. Mater. Chem. A*, vol. 2, no. 22, pp. 8328–8333, 2014.

[189] B. Tryba, P. Homa, R. J. Wróbel, and A. W. Morawski, "Photocatalytic decomposition of benzo-[a]-pyrene on the surface of acrylic, latex and mineral paints. Influence of paint composition," *J. Photochem. Photobiol. A Chem.*, vol. 286, pp. 10–15, 2014.

[190] T. Maggos, J. G. Bartzis, M. Liakou, and C. Gobin, "Photocatalytic degradation of NO_x gases using TiO_2-containing paint: A real scale study," *J. Hazard. Mater.*, vol. 146, no. 3, pp. 668–673, 2007.

[191] Q.-J. Geng, X.-K. Wang, and S.-F. Tang, "Heterogeneous Photocatalytic Degradation Kinetic of Gaseous Ammonia Over Nano-TiO_2 Supported on Latex Paint Film," *Biomed. Environ. Sci.*, vol. 21, no. 2, pp. 118–123, 2008.

[192] L. Hochmannova and J. Vytrasova, "Photocatalytic and antimicrobial effects of interior paints," *Prog. Org. Coatings*, vol. 67, no. 1, pp. 1–5, 2010.

[193] M. Baudys, J. Krýsa, M. Zlámal, and A. Mills, "Weathering tests of photocatalytic facade paints containing ZnO and TiO_2," *Chem. Eng. J.*, vol. 261, pp. 83–87, Feb. 2015.

[194] J. Chen and C. Poon, "Photocatalytic construction and building materials: From fundamentals to applications," *Build. Environ.*, vol. 44, no. 9, pp. 1899–1906, 2009.

[195] A. Cannavale, F. Fiorito, M. Manca, G. Tortorici, R. Cingolani, and G. Gigli, "Multifunctional bioinspired sol-gel coatings for architectural glasses," *Build. Environ.*, vol. 45, no. 5, pp. 1233–1243, 2010.

[196] J. Yu, X. Zhao, J. Du, and W. Chen, "Preparation, Microstructure and Photocatalytic Activity of the Porous TiO_2 Anatase Coating by Sol-Gel Processing," *J. Sol-Gel Sci. Technol.*, vol. 17, no. 2, pp. 163–171, 2000.

[197] L. L. Hench and J. K. West, "The sol-gel process," *Chem. Rev.*, vol. 90, no. 1, pp. 33–72, 1990.

[198] Y. Li, M. Ma, S. Sun, W. Yan, and Y. Ouyang, "Preparation of TiO_2–carbon surface composites with high photoactivity by supercritical pretreatment and sol–gel processing," *Appl. Surf. Sci.*, vol. 254, no. 13, pp. 4154–4158, 2008.

[199] D. Macwan, P. Dave, and S. Chaturvedi, "A review on nano-TiO_2; sol–gel type syntheses and its applications," *J. Mater. Sci.*, vol. 46, no. 11, pp. 3669–3686, 2011.

[200] J. Yu, X. Zhao, and Q. Zhao, "Effect of surface structure on photocatalytic activity of TiO_2 thin films prepared by sol-gel method," *Thin Solid Films*, vol. 379, no. 1–2, pp. 7–14, 2000.

[201] A. M. Ali, E. A. C. Emanuelsson, and D. A. Patterson, "Photocatalysis with nanostructured zinc oxide thin films: The relationship between morphology and photocatalytic activity under oxygen limited and oxygen rich conditions and evidence for a Mars Van Krevelen mechanism," *Appl. Catal. B-Environmental*, vol. 97, no. 1–2, pp. 168–181, 2010.

[202] W. Lin, L. Kao, W. Li, C. Hsu, and K. Hou, "Fabricating TiO_2; Photocatalysts by rf Reactive Magnetron Sputtering at Varied Oxygen Partial Pressures," *J. Mater. Eng. Perform.*, vol. 20, no. 6, pp. 1063–1067, 2011.

[203] N. Rausch and E. P. Burte, "Thin TiO_2 Films Prepared by Low Pressure Chemical Vapor Deposition," *J. Electrochem. Soc.* , vol. 140 , no. 1 , pp. 145–149, 1993.

[204] H. Lee, M. Y. Song, J. Jurng, and Y.-K. Park, "The synthesis and coating process of TiO_2 nanoparticles using CVD process," *Powder Technol.*, vol. 214, no. 1, pp. 64–68, 2011.

[205] P. Piszczek, Ż. Muchewicz, A. Radtke, M. Gryglas, H. Dahm, and H. Różycki, "CVD of TiO_2 and TiO_2/Ag antimicrobial layers: Deposition from the hexanuclear μ-oxo Ti(IV) complex as a precursor, and the characterisation," *Surf. Coatings Technol.*, vol. 222, pp. 38–43, 2013.

[206] P. S. Patil, "Versatility of chemical spray pyrolysis technique," *Mater. Chem. Phys.*, vol. 59, no. 3, pp. 185–198, 1999.

[207] A. Conde-Gallardo, M. Guerrero, N. Castillo, A. B. Soto, R. Fragoso, and J. G. Cabañas-Moreno, "TiO_2 anatase thin films deposited by spray pyrolysis of an aerosol of titanium diisopropoxide," *Thin Solid Films*, vol. 473, no. 1, pp. 68–73, 2005.

[208] M. Miki-Yoshida, V. Collins-Martínez, P. Amézaga-Madrid, and A. Aguilar-Elguézabal, "Thin films of photocatalytic TiO_2 and ZnO deposited inside a tubing by spray pyrolysis," *Thin Solid Films*, vol. 419, no. 1–2, pp. 60–64, 2002.

[209] D. Perednis and L. J. Gauckler, "Thin Film Deposition Using Spray Pyrolysis," *J. Electroceramics*, vol. 14, no. 2, pp. 103–111, 2005.

[210] X. Cui, H. M. Kim, M. Kawashita, L. Wang, T. Xiong, T. Kokubo, and T. Nakamura, "Preparation of bioactive titania films on titanium metal via anodic oxidation," *Dent. Mater.*, vol. 25, no. 1, pp. 80–86, 2009.

[211] N. K. Kuromoto, R. A. Simão, and G. A. Soares, "Titanium oxide films produced on commercially pure titanium by anodic oxidation with different voltages," *Mater. Charact.*, vol. 58, no. 2, pp. 114–121, 2007.

[212] Y. Mizukoshi, N. Ohtsu, S. Semboshi, and N. Masahashi, "Visible light responses of sulfur-doped rutile titanium dioxide photocatalysts fabricated by anodic oxidation," *Appl. Catal. B Environ.*, vol. 91, no. 1–2, pp. 152–156, 2009.

[213] P. A. Christensen, A. Dilks, T. A. Egerton, and J. Temperley, "Infrared spectroscopic evaluation of the photodegradation of paint Part II: The effect of UV intensity & wavelength on the degradation of acrylic films pigmented with titanium dioxide," *J. Mater. Sci.*, vol. 35, no. 21, pp. 5353–5358, 2000.

[214] E. Ceresa, L. Burlamacchi, and M. Visca, "An ESR study on the photoreactivity of TiO2 pigments," *J. Mater. Sci.*, vol. 18, no. 1, pp. 289–294, 1983.

[215] K. Yoshida, K. Matsukawa, and T. Yano, "Microstructure and mechanical properties of silicon carbide fiber-reinforced silicon carbide composite fabricated by electrophoretic deposition and hot-pressing," *J. Nucl. Mater.*, vol. 386–388, pp. 643–646, 2009.

[216] I. Corni, M. P. Ryan, and A. R. Boccaccini, "Electrophoretic deposition: From traditional ceramics to nanotechnology," *J. Eur. Ceram. Soc.*, vol. 28, no. 7, pp. 1353–1367, 2008.

[217] A. R. Boccaccini and I. Zhitomirsky, "Application of electrophoretic and electrolytic deposition techniques in ceramics processing," *Curr. Opin. Solid State Mater. Sci.*, vol. 6, no. 3, pp. 251–260, 2002.

[218] M.-S. Wu, D.-S. Chan, K.-H. Lin, and J.-J. Jow, "A simple route to electrophoretic deposition of transition metal-coated nickel oxide films for electrochemical capacitors," *Mater. Chem. Phys.*, vol. 130, no. 3, pp. 1239–1245, 2011.

[219] K. Tada and M. Onoda, "Electrophoretic deposition of conjugated polymer: Deposition from dilute solution and PEDOT coating effect," *Synth. Met.*, vol. 159, no. 9–10, pp. 851–853, 2009.

[220] O. O. Van der Biest and L. J. Vandeperre, "Electrophoretic deposition of materials," *Annu. Rev. Mater. Sci.*, vol. 29, no. 1, pp. 327–352, 1999.

[221] J. Tabellion and R. Clasen, "Electrophoretic deposition from aqueous suspensions for near-shape manufacturing of advanced ceramics and glasses—applications," *J. Mater. Sci.*, vol. 39, no. 3, pp. 803–811, 2004.

[222] I. G. and L. Binder, "Electrodeposition of nanostructured coatings and their characterisation—a review," *Sci. Technol. Adv. Mater.*, vol. 9, no. 4, p. 43001, 2008.

[223] L. Grinis, S. Dor, A. Ofir, and A. Zaban, "Electrophoretic deposition and compression of titania nanoparticle films for dye-sensitised solar cells," *J. Photochem. Photobiol. A Chem.*, vol. 198, no. 1, pp. 52–59, 2008.

[224] G.-S. Kim, H.-K. Seo, V. P. Godble, Y.-S. Kim, O.-B. Yang, and H.-S. Shin, "Electrophoretic deposition of titanate nanotubes from commercial titania nanoparticles: Application to dye-sensitised solar cells," *Electrochem. commun.*, vol. 8, no. 6, pp. 961–966, 2006.

[225] P. Sarkar and P. S. Nicholson, "Electrophoretic Deposition (EPD): Mechanisms, Kinetics, and Application to Ceramics," *J. Am. Ceram. Soc.*, vol. 79, no. 8, pp. 1987–2002, 1996.

[226] A. R. Boccaccini, S. Keim, R. Ma, Y. Li, and I. Zhitomirsky, "Electrophoretic deposition of biomaterials," *J. R. Soc. Interface*, vol. 7, no. Suppl 5, pp. S581–S613, 2010.

[227] C. Kaya, F. Kaya, B. Su, B. Thomas, and A. R. Boccaccini, "Structural and functional thick ceramic coatings by electrophoretic deposition," *Surf. Coatings Technol.*, vol. 191, no. 2–3, pp. 303–310, 2005.

[228] V. Firouzdor, J. Brechtl, B. Hauch, K. Sridharan, and T. R. Allen, "Electrophoretic deposition of diffusion barrier titanium oxide coatings for nuclear reactor cladding applications," *Appl. Surf. Sci.*, vol. 282, pp. 798–808, 2013.

[229] M. Farrokhi-Rad and M. Ghorbani, "Electrophoretic deposition of titania nanoparticles in different alcohols: Kinetics of deposition," *J. Am. Ceram. Soc.*, vol. 94, no. 8, pp. 2354–2361, 2011.

[230] W. Shan, "Electrophoretic deposition of nanosized zeolites in non-aqueous medium and its application in fabricating thin zeolite membranes," *Microporous Mesoporous Mater.*, vol. 69, no. 1–2, pp. 35–42, 2004.

[231] S. M. A. Fateminia, R. Yazdani-Rad, T. Ebadzadeh, and S. Ghashghai, "Effect of dispersing media on microstructure of electrophoretically deposited TiO_2 nanoparticles in dye-sensitised solar cells," *Appl. Surf. Sci.*, vol. 257, no. 20, pp. 8500–8505, 2011.

[232] H. Farnoush, J. A. Mohandesi, and D. H. Fatmehsari, "Effect of particle size on the electrophoretic deposition of hydroxyapatite coatings: A Kinetic study based on a statistical analysis," *Int. J. Appl. Ceram. Technol.*, vol. 10, no. 1, pp. 87–96, 2013.

[233] G. Mohanty, L. Besra, S. Bhattacharjee, and B. P. Singh, "Optimization of electrophoretic deposition of alumina onto steel substrates from its suspension in iso-propanol using statistical design of experiments," *Mater. Res. Bull.*, vol. 43, no. 7, pp. 1814–1828, 2008.

[234] E. M. Wong and P. C. Searson, "ZnO quantum particle thin films fabricated by electrophoretic deposition," *Appl. Phys. Lett.*, vol. 74, no. 20, 1999.

[235] A. R. Boccaccini, J. Cho, T. Subhani, C. Kaya, and F. Kaya, "Electrophoretic deposition of carbon nanotube–ceramic nanocomposites," *J. Eur. Ceram. Soc.*, vol. 30, no. 5, pp. 1115–1129, 2010.

[236] Y. Hara, J. R. S. Brownson, and M. A. Anderson, "Fabrication of thin-films composed of ZnO nanorods using electrophoretic deposition," *Int. J. Appl. Ceram. Technol.*, vol. 9, no. 1, pp. 115–123, 2012.

[237] X. Nie, A. Leyland, and A. Matthews, "Deposition of layered bioceramic hydroxyapatite/TiO_2 coatings on titanium alloys using a hybrid technique of micro-arc oxidation and electrophoresis," *Surf. Coatings Technol.*, vol. 125, no. 1–3, pp. 407–414, 2000.

[238] E. Haimi, H. Lipsonen, J. Larismaa, M. Kapulainen, J. Krzak-Ros, and S. P. Hannula, "Optical and structural properties of nanocrystalline anatase (TiO_2) thin films prepared by non-aqueous sol-gel dip-coating," *Thin Solid Films*, vol. 519, no. 18, pp. 5882–5886, 2011.

[239] H. T. Nguyen, L. Miao, S. Tanemura, M. Tanemura, S. Toh, K. Kaneko, and M. Kawasaki, "Structural and morphological characterisation of anatase TiO_2 coating on χ-Alumina scale fiber fabricated by sol–gel dip-coating method," *J. Cryst. Growth*, vol. 271, no. 1–2, pp. 245–251, 2004.

[240] P. Yimsiri and M. R. Mackley, "Spin and dip coating of light-emitting polymer solutions: Matching experiment with modelling," *Chem. Eng. Sci.*, vol. 61, no. 11, pp. 3496–3505, 2006.

[241] G. Jiang, Z. Lin, L. Zhu, Y. Ding, and H. Tang, "Preparation and photoelectrocatalytic properties of titania/carbon nanotube composite films," *Carbon N. Y.*, vol. 48, no. 12, pp. 3369–3375, 2010.

[242] T. Liu, F. Zhang, C. Xue, L. Li, and Y. Yin, "Structure stability and corrosion resistance of nano-TiO_2 coatings on aluminum in seawater by a vacuum dip-coating method," *Surf. Coatings Technol.*, vol. 205, no. 7, pp. 2335–2339, 2010.

[243] M. M. Ballari, M. Hunger, G. Hüsken, and H. J. H. Brouwers, "NO_x photocatalytic degradation employing concrete pavement containing titanium dioxide," *Appl. Catal. B Environ.*, vol. 95, no. 3–4, pp. 245–254, Apr. 2010.

[244] M. M. Ameen and G. B. Raupp, “Reversible catalyst deactivation in the photocatalytic oxidation of dilute o-xylene in air,” *J. Catal.*, vol. 184, no. 1, pp. 112–122, 1999.

Chapter Two - Analytical techniques

The following subsections of this chapter describe the analytical techniques used and theoretical approaches during this research project.

2.1 X-ray Photoelectron Spectroscopy

X-ray Photoelectron Spectroscopy (XPS) or Electron Spectroscopy for Chemical Analysis (ESCA) is a semi-quantitative technique introduced by Kai Manne Börje Siegbahn (Nobel Prize in 1981). XPS provides information about atomic percentage, the structure and the oxidation state of the atoms of the very outermost layer of a sample.

An X-ray is an electromagnetic wave produced by the deceleration of high energy electrons or electronic transitions in core orbitals. Wavelength ranges from 10 nm to 0.01nm [1]. The XPS technique limits the X-ray wavelength from 0.01nm to 2.5nm.

X-ray Photoelectron Spectroscopy provides quantitative results of elements as a function of their chemical makeup. Each chemical state of an element has specific peaks. If that peak is integrated and the obtained area is normalised with the total area, the result is the atomic percentage.

2.1.1 X-ray sources

For analytical purposes, X-Rays can be produced in different ways, such as bombarding a metal target with high kinetic energy electrons; exposing a substance to a primary X-ray and thereafter generates a secondary ray of X-ray fluorescence; using a radioactive substance or a synchrotron source. Typical X-ray sources have magnesium or aluminium targets. These materials have the thinnest K_α lines (from 0.8 to 0.9 eV) and thin lines provide greater spectral resolution. In order to reduce the noise of the instrument, an optical monochromator is required [2], [3].

The X-ray spectra have two series of lines. The group of shortest wavelength is called K and the other group is called L. For higher elements there are more groups of lines (M, N etc.). K and L are from the German words Kurtz (short) and Lang (long).

X-ray line spectra are the result of electronic transitions between inner orbitals. As shown in Figure 2.1, K series are produced when high energy electrons collide and eject electrons from the closest orbitals to the nuclei. L series X-rays are produced when the ejected electron is from the second principal quantum level.

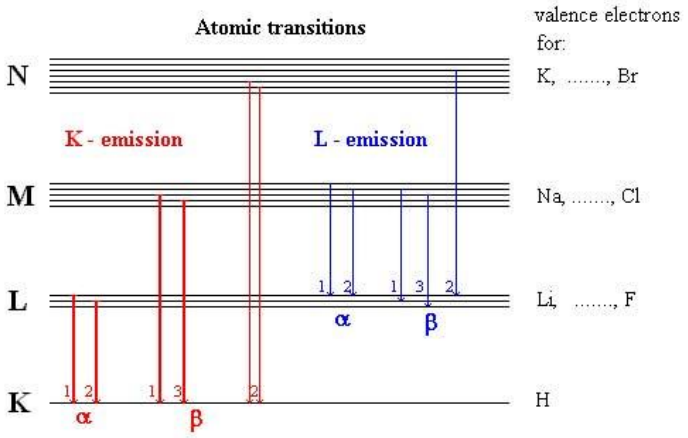

Figure 2.1 - Origin of characteristic X-ray lines, the more intense transitions are in bold

The energetic difference between α_1 and α_2, as well as β_1 and β_2 transitions is so small that it usually appears as one signal. The characteristics wavelengths for elements (excluding lighter elements) are independent of the physical or chemical state. The electrons that provide these transitions are not involved in chemical bonds.

2.1.2 Software and peak fitting

The software CASAXPS 2.3.16 RP 1.6 (Casa Software Ltd., Teingmouth, Devon, UK) was used for data analysis and the peak fitting. The adventitious hydrocarbon C 1s peak at 284.8 eV was used to correct the shifting due to charging effects on the spectra. The atomic percentage of each element detected was calculated from the peak areas, assuming a Shirley background and fitting them by using a Gaussian/Lorentzian ratio and asymmetry factors to give the best fit to the peaks. After deconvoluting the peaks, atomic sensitivity factors were applied to the peak areas to convert the signal into atomic ratios [4]. All the fitted peaks were normalised excluding the area of the adventitious carbon peak.

Full scan spectra were obtained between 0 and 1400 eV binding energy (BE) with a pass energy of 200 eV and a dwell time of 50 ms. In addition, scans with higher resolutions were taken at different BE ranges with pass energy of 40 eV and dwell time of 100 ms for N 1s, O 1s, S 2p, Ca 2p and Ti 2p regions.

2.1.3 XPS apparatus and conditions

The surface layers (within 1-10 nm) were characterised using Thermo Scientific Theta Probe with a micro-focussed monochromatic Al Ka (1486.6 eV) X-ray source (Thermo Fisher Scientific Inc., Waltham, MA.), with an operating voltage of 12 kV and 3 mA of current. The default spot size was 400 × 800 μm using a flood gun, with a 180° double focusing hemispherical analyser with two-dimensional PARXPS detector in an operating vacuum of 10^{-8} mbar.

2.2 X-ray Diffraction

X-ray diffraction (XRD) is a powerful technique commonly used for lattice characterisation of crystallographic structures which does not require vacuum conditions nor sample preparation; making it suitable for the study of raw materials or coatings.

When a monochromatic X-ray beam reaches the surface of the sample, the interaction with the electrons of the three dimensional crystal structure will diffract a reflected beam composed of different constructive interferences in certain directions. Considering the intensity of the incident X-ray beam and the angle that is intersects with the atomic plane, information about the present crystal phase can be extracted [5], [6].

A constructive interference is when the phase difference of the different reflected beams is proportional to 2π, as expressed in Bragg's law (Equation 2.1):

$$n\lambda = 2d\sin\theta \qquad (2.1)$$

Where:

n= integer

λ= X-ray wavelength

d= interplanar spacing in the atomic lattice

θ= angle formed by the scattering plane and the incided X-ray beam

From the diffractogram that XRD provides, it is able to estimate the particle size of the material. Different approaches has been studied; from the width of the line at half the maximum intensity [7], [8], the integral breath [7], [9] of the peak or the analysis of the line broadening by the use of the Voigt function [10]. Due to its rapidity and considering some loss of accuracy, the use of the Scherrer [7], [11] Equation was used in this thesis to estimate the particle size when direct measurements were not possible.

2.2.1 Scherrer Equation

In 1918, Paul Scherrer developed the Equation named after him [11] to determine the size of the ordered crystalline domain, relating it to the peak broadening in a diffraction pattern as Equations 2.2 and 2.3 shows:

$$\varepsilon = \frac{\lambda}{\beta \cos\theta} \quad (2.2)$$

$$\tau = K\varepsilon \quad (2.3)$$

Where

ε= apparent crystallite size

τ=mean size of the ordered domain (nm)

λ= X-ray wavelength (nm)

β= is the broadening at half the maximum intensity (radian)

θ=Bragg angle

K=Scherrer constant (dimensionless)

The peak profiles shown in a X-ray diffractogram are a convolution of discrete contributions, such as instrumental broadening (i.e. wavelength width of K_α, penetration into the sample), crystal size, microstrains, dislocations or temperature factors among others [7], [12]. To correct the broadening caused by the instrumentation, a quasi-perfect sample is usually analysed, considering its broadening contribution negligible, the instrumental broadening can be calculated from a Gaussian shape using Equation 2.4.

$$B_{sample}^2 = B_{total}^2 - B_{intrument}^2 \quad (2.4)$$

The Scherrer constant is a shape factor that is applied to correct the apparent size of the crystallite, the given result is the cube root of the crystallite volume. Assuming the average crystal shape is regular, the value of the Scherrer constant can be calculated depnding of the crystallite shape, k and its size distribution [7]. To calculate the Scherrer constant, the crystallite shape must be known and the Miller index of the lattice plane's peak on the diffractogram. For anatase, rutile and brookite the crystallite shape is an octahedron, Langford and Wilson listed different Scherrer's constants for different crystallite shapes [7].

2.2.2 XRD apparatus and conditions

The equipment used was a Bruker D8 ADVANCE X-ray diffractometer with CuKα radiation (at 40 kV and 40 mA emission current) equipped with a graphite monochromator and a NaI scintillation detector. 2θ scans were recorded within the range of 20° to 60° with a step of 0.016° and a step time of 269 s. The XRD was equipped with a flat plate sample holder configuration as Figure 2.2 shows, where a smooth surface is mandatory for a good spectra acquisition.

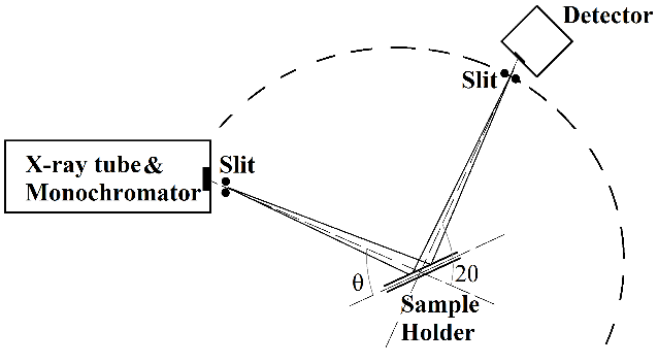

Figure 2.2 - Diagram of XRD flatplate mode configuration

2.3 Electron microscopy

2.3.1 Scanning electron microscope

The Scanning electron microscope (SEM) is an electron beam instrument that scans the surface of a sample. Although it is based on the same principle as optical microscopy, the wavelength of the light limits its resolution, whereas the use of an electron beam leads to a magnification on the image up to x300000 (theoretically) with a spatial resolution of 50 to 100 nm [13]. Also it has greater depth of field and can reveal the morphology of surfaces. By using an X-ray analyser (Energy-Dispersive X-Ray Spectroscopy), the study of the superficial chemical composition is allowed.

The electron source is typically a thermionic emitter which emits electrons by heat induction under vacuum. When the electron beam interacts with the sample, electrons from the beam may rebound after the interaction with the atom (back scattered electrons). The kinetic energy that is dissipated in these collisions is able to excite and eject electrons from the sample, creating another electron beam (secondary), Auger electrons and photons (from the fluorescence or X-ray).

SEM is based on the signal that secondary electrons and back scattered electrons create.

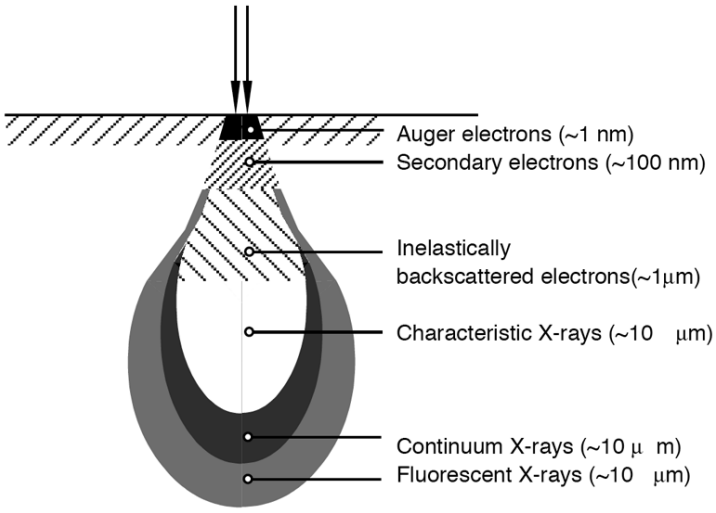

Figure 2.3 - Different emissions generated by x-ray interaction with the surface

2.3.1.1 Energy dispersive X-ray analysis

As Figure 2.3 shows, once the sample is irradiated, different radiation emissions can be analysed. X-ray radiation is unique for each element. If X-ray energy is measured, identification and quantification of elements (EDX) can be performed at low vacuum and with an uncoated sample. The accuracy is limited due to the specifications of the instrument.

2.3.1.2 Specimen preparation

Conductive materials do not require any special preparation. If the material is an insulator, or a semiconductor as is the case of TiO_2, a conductive coating must be deposited over the surface to prevent charging. A film of 10 nm of chromium was deposited using a Q150T S Turbo-Pumped sputter Coater with a thickness control feature.

2.3.1.3 SEM apparatus and conditions

A JEOL SEM6480LV equipped with a motorised stage was used alongside a coupled Oxford INCA X-ray analyser. The electron gun produces a beam of electron which are accelerated with a typical working voltage between 5 kV to 15 kV. The incident electron beam should have a diameter of from 10 nm to 50 nm which is controlled via a magnetic lens.

2.3.2 Field Emission SEM (FESEM)

A field emission scanning electron microscope is based on the same principles as SEM with the difference of the electron source, higher vacuum conditions, more complex lens system and working at lower voltage. Whereas SEM is equipped with a "hot filament", field emission guns consist of a sharp metal (with a high melting point) section of a section of the order of 100 nm which is held in a high electrical potential gradient, required for field emission of electrons. Due to its properties, magnification of an ideal sample can reach x500000.

2.3.2.1 Specimen preparation

Conductive materials do not require any special preparation. If the material is an insulator, or a semiconductor as is the case of TiO_2, a conductive coating can be deposited over the surface to prevent charging and allow a better image to be obtained. 10 nm of chromium was deposited using a Q150T Turbo-Pumped Sputter Coater with a film thickness monitor feature.

2.3.2.2 FESEM apparatus and conditions

The equipment used was a JEOL FESEM6301F equipped with a motorised stage, allowing low accelerating voltages (from 1 to 10kV).

2.3.3 Transmission electron microscopy (TEM)

Transmission electron microscopy was used to characterise raw materials, due to the high resolution of the instrument, allowing magnifications of x500000 at high operating voltages. SEM and FESEM work with scattered electrons, but TEM forms a visual image by the signal of the electrons that pass through an ultrathin sample. This technique allows study of the crystal grains of the materials, being able to determine the particle size.

2.3.3.1 Specimen preparation

Powdered samples were ground and dispersed in ethanol; the supernatant was taken and diluted with ethanol until the colloidal suspension was quasi-transparent. A drop of this dispersion was place on the carbon holders and dried overnight under vacuum.

2.3.3.2 TEM apparatus and conditions

The equipment used was a JEOL JEM 1200 EXII with a tungsten filament and a Thermo Scientific Ultra Dry with Noran 7 EDX, equipped with a motorised stage, and a Gatan Dual View camera. The working accelerating voltages was 120 kV.

2.4 Raman spectroscopy

Raman spectroscopy is a non-destructive technique which observes frequency modes in an excited system. This technique was named after Sir C. V. Raman, who observed in 1928 the inelastic scattering of photons. Since the use of LASER light sources, Raman spectroscopy has been widely used in chemistry, especially in the aqueous phase, as infrared spectroscopy cannot be performed in that medium (water interferes with the spectra). Raman spectorsocpy allows analysis of the chemical composition as well as the molecular structure due to the energetic difference of the vibrational modes, oscillating the dipole moment [14]. These oscillations provoked by the light absorption are subjected to relaxation processes by emission of light:

i. **Elastic Rayleigh scattering** occurs when a molecule is excited to a virtual energy state by absorbing a photon with a frequency υ_0; which will emit a photon with the same frequency (υ_0) in the relaxation process.

ii. **Stokes Raman scattering** is the process in which a molecule excites from the basic vibrational energy state to a virtual state by absorbing a photon with a frequency υ_0. Then the molecule will emit a photon with a lower energy when it relaxes to an excited vibrational state.

iii. **Anit-Stokes Raman scattering** is the light scattered process when an atom or molecule is excited from an excited energy level to a virtual state by absorbing a photon with a frequency υ_0. The molecules which emit a photon with a higher energy then relax to the ground energy state.

The Raman signal depends on the energy gap between the Raman active molecule's modes; the condition to be active in Raman is the change of polarizability between the excited vibro-rotational modes and the normal equilibrium position. This can be predicted from group theory.

2.4.1 Apparatus and conditions

The evaluation of the crystalline phases of the samples were analysed using a Renishaw inVia2012 Raman microscope equipped with an excitation sources of 532 nm and 785 nm Diode Renishaw. The analyses were performed by focusing the laser with objective magnification 50 x and 20 x. Laser power was reduced from 5 to 10 %, the acquisition time was set at 3s with a total of 7 accumulations. Prior to the analysis, a monocrystalline silicon standard was used as reference for the calibration. Renishaw WiRe 4.0 was the software used to work with the raw data.

2.5 UV-Visible diffuse reflectance spectroscopy

The band gap energy of semiconductors can be determined using UV-Vis diffuse reflectance spectroscopy, along with the Kubelka-Munk function [12] (Equation 2.5) converting the reflectance into the absorption coefficient 'F(R)'.

$$F(R) = \frac{(1-R)^2}{2R} \qquad (2.5)$$

Combining the Kubelka-Munk function with the Tauc's plot (Equation 2.6), provides the absorption energy which corresponds to the band gap:

$$(h\upsilon F(R))^2 = A(h\upsilon - E_g) \qquad (2.6)$$

Where R is the reflectance, '*h*' is Planck's constant, 'υ' is frequency of vibration, 'E_g' the band gap energy and 'A' is a proportionally constant.

2.5.1 Apparatus

A PerkinElmer 750 S UV/Vis Spectrometer with a 60 mm Integrating Sphere in a wavelength range between 240 nm and 800 nm was used to characterise the band gap of the photocatalysts studied.

2.6 Dielectric Spectroscopy

Dielectric spectroscopy, also called Impedance spectroscopy (IS) is a technique commonly used for the measurement of electrical properties of a materials over a frequency range. This is based on the interaction between an applied alternating-current (AC) with the dipolar moment of a sample, also referred as permittivity in the frequency domain, Temperature is a parameter that can be kept constant or varied during the experimental measurement.

The current work measurements were taken between 1-10^5 Hz by applying a small voltage perturbation (0.1 Vrms).

Impedance Z (ohms) is a complex variable:

$$Z = Z' + iZ'' \tag{2.7}$$

Where:

Z' = the real component of the impedance (purely resistive)

Z'' = the imaginary part (reactance).

It is then possible to define the admittance '*Y*', which is the reciprocal of impedance:

$$Y = \frac{1}{Z'+iZ''} \tag{2.8}$$

Admittance Y is also a complex variable composed of a real part, the conductance (*G)*, and an imaginary part, the susceptance '*B*':

$$Y = \frac{1}{Z'+iZ''} \times \frac{Z'+iZ''}{Z'+iZ''} = \left(\frac{Z'}{Z'^2+Z''^2}\right) + i\left(\frac{-Z''}{Z'^2+Z''^2}\right) = G + iB \tag{2.9}$$

Therefore the real conductance '*G'*, is given by:

$$G = \frac{Z'}{Z'^2+Z''^2} \tag{2.10}$$

And from the conductance, it is possible to calculate the ac conductivity, 'σ^*' (S/m):

$$\sigma^* = G\frac{t}{A} \quad (2.11)$$

Where 't' is material thickness/length in m and 'A' is the area of material in m^2. As discussed above, at a lower frequency (and providing polarisation effects are not present), the ac conductivity provides a good approximation of the dc conductivity 'σ'.

Materials that contain conductive and insulating phases follow the 'universal dielectric response' having frequency-dependent conductivity. At low frequency the bulk ac conductivity is frequency independent, 'σ_{dc}', while at higher frequencies the ac conductivity increases following a power law behaviour.

$$\sigma(\omega) = \sigma_{dc} + A\omega^n \quad (2.12)$$

2.6.1 Apparatus

The electrical properties of titanium dioxide and sub-oxide species were characterised using a Solartron 1260 Impedance Analyser with a Solatron 1296 Dielectric Interface, applying a small voltage perturbation of 0.1 V_{rms} over a range of frequencies between 1-10^5 Hz

2.7 White light interferometry

A white light interferometer (or three dimensional surface profilometer) is a non-contact technique that allows studying the topography of a surface by applying the wave superposition principle. A light beam from the white light source will be reflected form the surface of the sample and it will combine with a reference light beam with the same frequency. Depending on the phase difference, a constructive or destructive interference can be created. The information from the wave sources can be extracted.

2.7.1 Apparatus

Dimensional surface measurements by non-contact optical profilometry were performed using a Proscan 2000 with a chromatic sensor (resolution 0.01 μm) located in the Mechanical Engineering department at Univeristy of Bath.

2.8 BET surface area analysis

This method was named after Stephen Brunauer, Paul H. Emmet and Edward Teller published their research in 1938 [16]. It is based on the adsorption of a non-corrosive gas (such as N_2, Ar, CO_2 or He) on a solid surface. BET theory extended the Langmuir monolayer molecular adsorption theory to a multilayer adsorption. Two hypotheses based BET model on the extension of Langmuir's theory:

i. Gas molecules physically adsorb on a solid in layers infinitely
ii. None of the adsorbed layers interact with each other

Therefore, Langmuir theory can be applied to each layer. The amount of gas adsorbed at a given pressure allows determining the surface area. The BET Equation correlates the adsorbed gas quantity 'υ', equilibrium and saturation pressure of adsorbates 'p' and p_0' respectively, the monolayer adsorbed gas quantity 'υ_m'. 'c' is the BET constant which depens on the difference between the heat of adsorption for the first layer and the heat of liquefaction.

$$\frac{1}{\upsilon(\frac{p_0}{p}-1)} = \frac{c-1}{\upsilon_m c}\left(\frac{p}{p_0}\right) + \frac{1}{\upsilon_m c} \qquad (2.13)$$

The graphical plot of Equation 2.13 when it is an adsorption isotherm is a straight line. The value of the slope and the interception on the y axis can be used to calculate υ_m and c. The value of the specific surface area is given by:

$$S_{BET} = \frac{\upsilon_m N s}{V a} \qquad (2.14)$$

Where 'N' is Avogadro's number, 's' is the adsorption cross section of the adsorbing species, 'V' the molar volume of adsorbed gas and 'a' the mass of sample.

2.8.1 Apparatus

A Micromeritics Gemini 2380 Surface Area Analyser was used to measure the specific surface area of powders using N_2 as adsorbant.

2.9 Bibliography

[1] K. Siegbahn, "Electron Spectroscopy for Chemical Analysis (E.S.C.A.)," *Philos. Trans. R. Soc. London. Ser. A, Math. Phys. Sci.*, vol. 268, no. 1184, pp. 33–57, 1970.

[2] J. Goldstein, D. E. Newbury, D. C. Joy, C. E. Lyman, P. Echlin, E. Lifshin, L. C. Sawyer, and J. R. Michael, *Scanning Electron Microscopy and X-ray Microanalysis*. Springer, 2007.

[3] A. R. Clarke and C. N. Eberhardt, *Microscopy Techniques for Materials Science* . 2002.

[4] C. D. Wagner, L. E. Davis, M. V Zeller, J. A. Taylor, R. H. Raymond, and L. H. Gale, "Empirical atomic sensitivity factors for quantitative analysis by electron spectroscopy for chemical analysis," *Surf. Interface Anal.*, vol. 3, no. 5, pp. 211–225, 1981.

[5] C. Suryanarayana and M. G. Norton, *X-ray Diffraction: A practical approach*. New York: Plenum Publishing Corporation, 1998.

[6] N. Kasai and M. Kakudo, *X-ray Diffraction by Macromolecules*, vol. 80. Berlin/Heidelberg: Springer-Verlag, 2005.

[7] J. I. Langford and A. J. C. Wilson, "Scherrer after sixty years: A survey and some new results in the determination of crystallite size," *J. Appl. Crystallogr.*, vol. 11, pp. 102–113, 1978.

[8] A. W. Burton, K. Ong, T. Rea, and I. Y. Chan, "On the estimation of average crystallite size of zeolites from the Scherrer Equation: A critical evaluation of its application to zeolites with one-dimensional pore systems," *Microporous Mesoporous Mater.*, vol. 117, no. 1–2, pp. 75–90, 2009.

[9] A. R. Stokes and A. J. C. Wilson, "A method of calculating the integral breadths of Debye-Scherrer lines," *Math. Proc. Cambridge Philos. Soc.*, vol. 38, no. 03, pp. 313–322, 1942.

[10] T. H. de Keijser, J. I. Langford, E. J. Mittemeijer, A. B. P. Vogels, T. H. de Keijser, J. I. Langford, E. J. Mittemeijer, and A. B. P. Vogels, "Use of the Voigt function in a single-line method for the analysis of X-ray diffraction line broadening," *J. Appl. Crystallogr.*, vol. 15, no. 3, pp. 308–314, 1982.

[11] P. Scherrer, "Bestimmung der Größe und der inneren Struktur von Kolloidteilchen mittels Röntgenstrahlen," *Nachrichten von der Gesellschaft der Wissenschaften zu Göttingen, Math. Klasse*, vol. 1918, pp. 98–100., 1918

[12] H. P. Klug and L. E. Alexander, *X-ray diffraction procedures for Polycrystalline and Amorphous Materials*. London, 1974.

[13] R. F. Egerton, *Physical Principles of Electron Microscopy: An Introduction to TEM, SEM, and AEM*. Springer, 2005.

[14] R. L. McCreery, *Raman Spectroscopy for Chemical Analysis*. New York: John Wiley&Sons, 2000.

[15] R. López and R. Gómez, "Band-gap energy estimation from diffuse reflectance measurements on sol–gel and commercial TiO_2: A comparative study," *J. Sol-Gel Sci. Technol.*, vol. 61, no. 1, pp. 1–7, 2012.

[16] S. Brunauer, P. H. Emmett, and E. Teller, "Adsorption of gases in multimolecular layers," *J. Am. Chem. Soc.*, vol. 60, no. 2, pp. 309–319, Feb. 1938.

Chapter Three - Experimental methods

This chapter describes the experiments in which the photoactivity of materials was characterised. There are different stablished methods that test photocatalyst performance of materials; e.g. using dye degradation in the aqueous phase, the direct study of antimicrobial properties or the decomposition of pollutants. This chapter is focused on experiments carried out in the aqueous phase and their experimental conditions, with an emphasis on the light sources used.

3.1 Light source

During this research program, one of the aims was to determine accurately the properties of the light sources, in order to have reproducible conditions. This was one of the issues found in literature about photocatalysis, the lack of descriptive methods regarding on the light source. While intensity is important to determine how many electrons are impacting on the surface of the material, the energy of those is also fundamental. This energy can be extracted from the wavelength of the light beam.

Three different light sources were used, depending the requirements of the experiments a light bulb or LED light source was selected. The following subsections describe how they were characterised.

3.1.1 Wavelength spectra

To record the wavelength spectra of the light sources, the silicon charge-coupled device (CCD) array detector from the Raman spectrometer recorded the light spectrum. With a spectral range from 244 nm to 830 nm the Raman detector covers the ultraviolet A and B and visible range.

3.1.2 UVA probe

To determine the intensity of the light source, a portable photodetector was used. A photodetector is a PIN diode able to convert light into an electrical pulse. The photodiode is made by an intrinsic semiconductor between a p-type semiconductor and an n-type semiconductor. Photons are able to create free electrons and holes after the collision with the photodiode, creating a photocurrent. A LP 471 UVA was provided by Delta Ohm. This photodetector is able to measure light from 315 to 400 nm and intensity from 0.001 to 2000 W/m^2.

3.1.3 UV halogen lamp

For experiments with microorganisms, a 36 W light bulb of wavelength 364-383 nm provided a maximum range was used, due to its low intensity. Figure 3.1 shows the spectral output; its maximum intensity was 25.50 W/m^2.

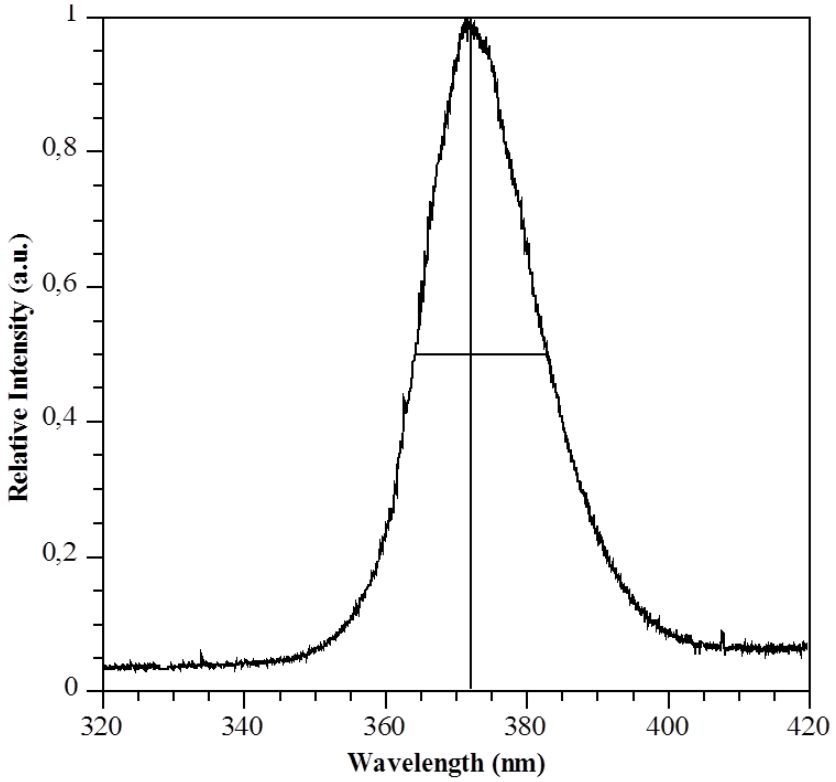

Figure 3.1 - Spectrum of UV halogen lamp. Wavelength ranges of 364-383 nm calculated at full width half maximum (FWHM)

3.1.4 UV LED

Two different UV LED arrays were fabricated specifically for these experiments. The LEDs were chosen as the UV halogen lamp´s emission in the UV range is very broad (~35 nm) and not intense. Each UV source comprised of a 4×4 array of 16 individual GaN UV-LED's. Operation was carried out at a voltage from 15.4 to 15.8 V, a current of 1400 mA at 40 °C. LED's 3.5 mm in diameter were mounted at a spacing of 1.5 mm. The LED of wavelength 376-387 nm provided a maximum intensity at 380 nm with a total intensity of 30.4 W/m^2; whereas the LEDs of wavelength 381-392 nm emitted the maximum intensity at 386 nm with a total intensity of 40.8 W/m^2. Figure 3.2 shows a diagram of the LED arrays and corresponding spectra are shown in Figure 3.3.

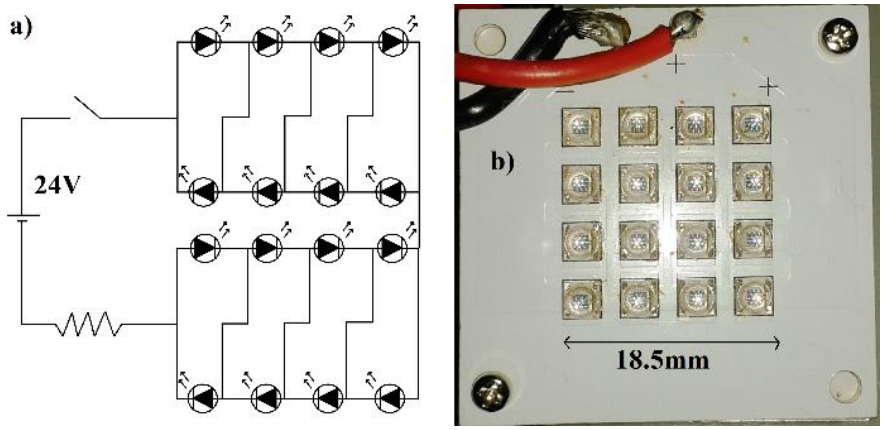

Figure 3.2 - Spectrum of UV halogen lamp. Wavelength ranges of 364-383 nm calculated at full width half maximum (FWHM) [1]

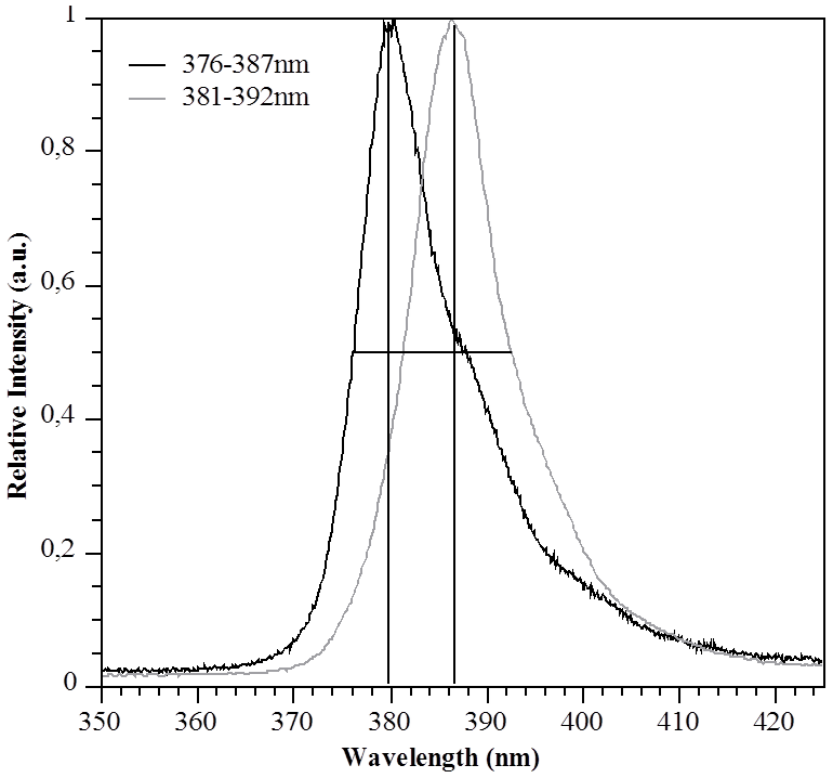

Figure 3.3 - Spectra of LED arrays. Wavelength ranges of 376-387 nm and 381-392 nm calculated at full width half maximum (FWHM) [1]

3.2 Bacteria removal

In order to study the biocide properties of photocatalytic surfaces, *Escherichia coli* (*E. coli*) was chosen as the standard microorganism as it is a well-known bacteria routinely used in research studies.

When working in a microbiology laboratory experiments must be performed under aseptical conditions, that includes sterilisation of all materials by autoclaving at 121 ºC for 15 min. Manipulation of bacteria is performed in a sterile flow hood equipped with a HEPA filter. Studies involving bacterial cultures have as final step for the estimation of the numbers of viable bacterial cells present after the experiment. Estimation of bacterial numbers can be achieved by performing serial dilutions prior to plating out onto a nutrient lawn in a Petri dish.

Performing bacterial serial dilutions can be a time consuming method, for that reason an optimisation of the initial inoculum used in each experiment was performed to minimise the time spent in dilutions and estimation of viable counts of bacteria. An initial study was performed in order to relate the growth of an *E. coli* culture and its absorbance.

E. coli K-12 single colonies from a nutrient agar plate were picked and grown overnight in 10 ml of the rich medium Luria Bethani (LB) broth, at 37 ºC and constant shaking (200 rpm). On the following day the growth of the bacterial cells could be observed by the turbidity of the culture.

3.2.1 Pour plate technique and colony forming unit

The most common method to measure the viability of bacterial cell is the colony forming units (CFU), where serial dilutions of a bacterial suspension are plated out and spread onto a nutrient lawn and incubated overnight at optimum temperature. The basis of such an assay is that each single cell deposited on the nutrient lawn will grow and form a colony. Colonies can be observed on the surface of the petri dish and recorded. The following Equation is applied to estimate the original concentration:

$$\text{Colony forming units/ml(cfuml)} = \frac{\text{Number of colonies}}{\text{d}\times\text{V}} \qquad (4.1)$$

Where *d* is the dilution plated and *V* is the volume of dilutions plated.

Figure 3.4 shows a poured petri dish with a LB agar and several “dots”; which are marking single colonies. Figure 3.5 shows the steps to count colonies.

The count of colonies per plate to be accurate should be in the range of 30 and 400 colonies [2]. Plates with less than 30 or more than 300 growth colonies will increase the percentage of discrepancies from different plates.

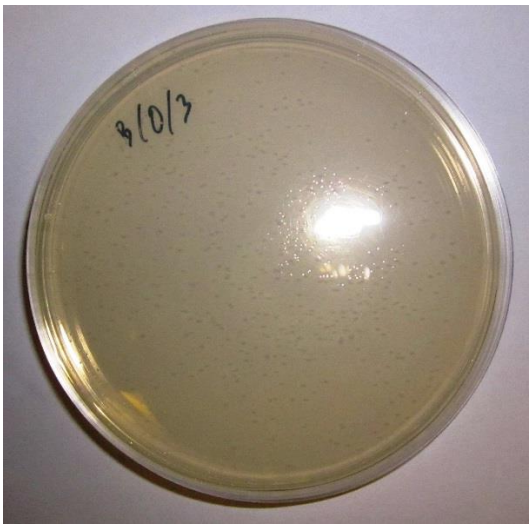

Figure 3.4 - Petri dish (9 cm diameter) with *E. coli* colonies

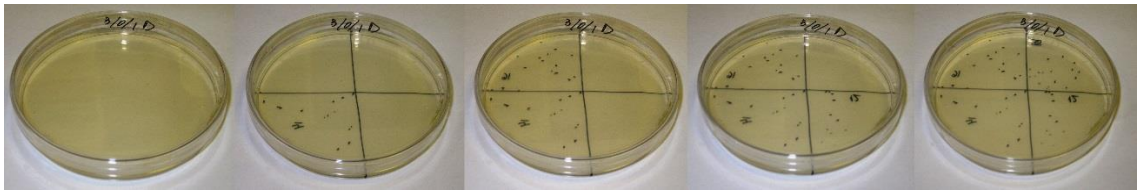

Figure 3.5 - Colony counting process on a 9 mm diameter petri dish

3.2.2 Parameter optimization

E. coli was used as a bacterial strain, being inoculated into a stationary growth nutrient broth (No. 2, provided by Merck, KgaA, Darmstadt, Germany). From this broth, the colonies were suspended in a phosphate buffered saline (PBS) solution (Merck, KgaA, Darmstadt, Germany) by vortexing. A study of optimum initial concentration of *E. coli* was required.

UV-Visible spectroscopy is able to measure the optical density of cells by following the absorbance at 600 nm. This method does not discriminate between live or dead cells as it is used to measure the amount of light which is scattered by suspended bacteria. In order to determine the best concentration of *E. coli* for the experiments, growths were studied at different dilutions. UV-Visible experiments and growths in Luria agar were undertaken simultaneously to observe the relation between CFU/ml and optical density.

Seven dilutions were performed on an *E. coli* suspension on a PBS solution. Each dilution was repeated three times and 250 µl was sprayed in Luria agar to estimate the number of colonies present. Growing conditions were set at 25 ºC for 12 h. Results are shown in table 3.1 which shows the relation between absorption and the counted colonies per place for each dilution.

Table 3-1 - Results from calibration trend

Dilution	**10^{-1}**	**10^{-2}**	**10^{-3}**	**10^{-4}**	**10^{-5}**	**10^{-6}**	**10^{-7}**
Absorption	0.161	0.013	-	-	-	-	-
CFU per plate	Confluent	Confluent	Confluent	Confluent	I=993 II=1236 III=687	I=259 II=273 III=260	I=22 II=38 III=49
CFU per ml	1.1×10^{11}	1.1×10^{10}	1.1×10^{9}	1.1×10^{8}	1.1×10^{7}	1.1×10^{6}	1.1×10^{5}

The first four dilutions were too concentrated to count colonies, whereas the last three dilutions, provided readable results. As the dilutions were accurate, CFU results for 10^{-1} and 10^{-2} dilutions were estimated using results from 10^{-6} dilution. With those estimations a calibration trend was obtained. Equation 4.2 was used to measure in the UV-Visible spectrophotometer the initial *E. coli* concentration.

$$\text{Abs} = 1.7 \times 10^{10} \frac{\text{CFU}}{\text{ml}} \qquad (4.2)$$

3.2.2.1 Volume of microbial suspension

The reactions were carried on the surface of the samples of 100 mm^2. First, the volume of suspension to test was determined by dropping it uniformly with a micropipette as Figure 3.6 shows.

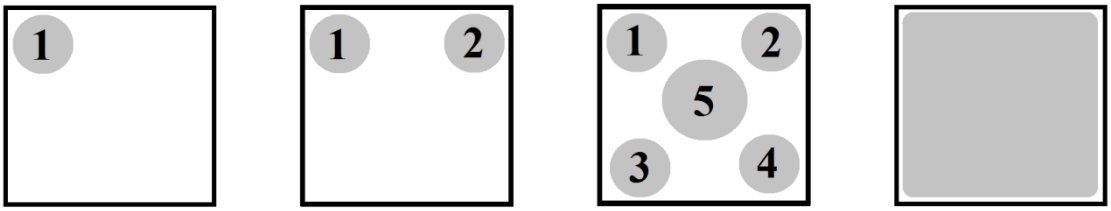

Figure 3.6 – Application of *E. coli* suspension on the surface's sample with a micropipette

Seven different volumes were studied, 400 µl, 300 µl, 200 µl, 150 µl, 100µl, 75 µl and 50 µl. Volumes greater than 300 µl spilled out of the sample, whereas 50 µl were not enough to cover the sample with an aqueous thin film. The optimum volume was set to 75 µl.

3.2.2.2 Reaction

Samples were sterilised in the autoclave the day before, to ensure there were no microorganisms other than *E. coli*. Under no UV light irradiation, 75 µl was applied to the sample's surface. After exposure, the samples were submerged into a tube containing 10 ml of PBS solution in the dark. From this solution, 250 µl were taken and plated on a petri dish and this was repeated as well for a 1/10 dilution. Note that all the plate growths were replicated three times with three different samples.

Assuming there is a total exchange from the surface of the sample to the solution and considering the ideal amount of colonies to count on a petri dish varies between 30-300 CFU per plate, an initial concentration of 2×10^5 CFU/ml was set as optimum to be sprayed on the surface of the samples.

3.2.2.3 UV conditioning

To determine the maximum intensity that *E. coli* can be exposed without being degraded, the UV halogen lamp previously described (Section 1.3) was used at four different intensities, 3.270 W/m^2, 1.627 W/m^2, 0.313 W/m^2 and 0.032 W/m^2. The exposure time was set to five minutes. Results are shown in Figure 3.7. When the UV intensity is higher than 1.6 W/m^2, *E. coli* does not survive under these conditions, whereas they will under UV irradiation less intense than 0.322 W/m^2, UV light has no effect on *E. coli* colonies. Therefore, this intensity was used for further experiments.

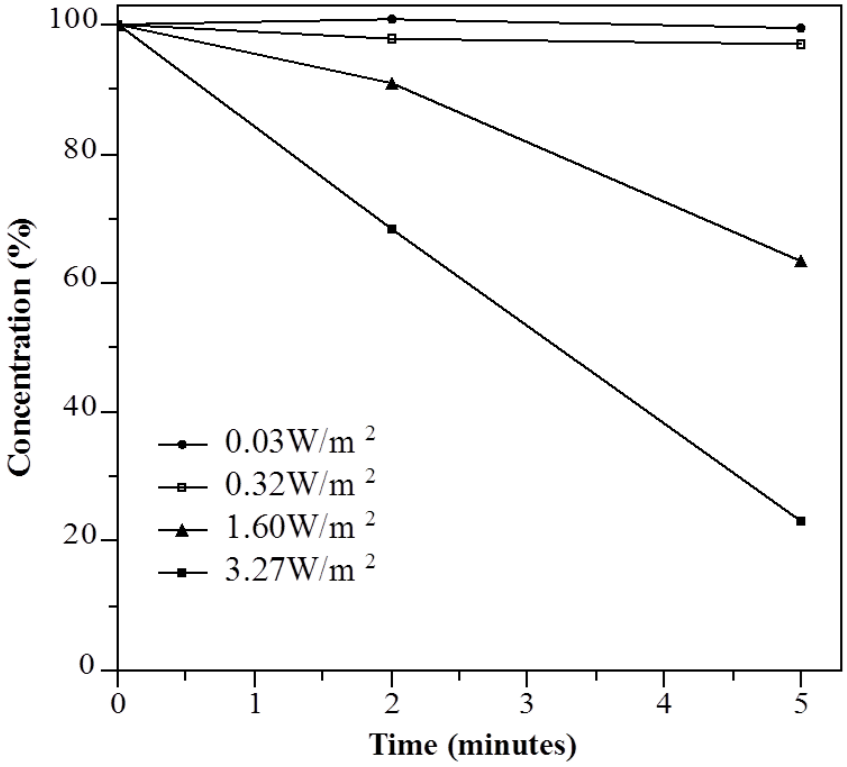

Figure 3.7 - Effect of UV intensity on *E. coli* along time

3.3 Methylene blue degradation

Photocatalytic activity of TiO_2 in solution was studied by following the decay of solution´s absorption by UV-Visible spectrophotometry. Methylene blue was chosen as an organic dye indicator, and the working intensity for both LEDs was 4.7 W/m^2.

An initial solution 2.5×10^{-5} M of methylene blue (methylene blue hydrate, CAS: 122965-43-9 Sigma-Aldrich Chemie GbbH, Riedstr, Germany) in deionised water was prepared. It was found that concentrations higher than 10^{-3} M did not allow TiO_2 to react under UV. Due to methylene blue does not absorb in the range of the UV LED, the logical explanation is the blocking of the TiO_2 surface by methylene blue's absorption.

The degradation of the dye was followed by the decay on the absorption at its maximum peak (670 nm), with a tabulated molar extinction coefficient in water of 71089 $M^{-1} \times cm^{-1}$ using a Jenway 6300 UV-Visible spectrophotometer. 50 ml of methylene blue solution and 2mg/ml of catalyst were placed on the glass reactor of 100 ml capacity under magnetic stirring, and an aliquot of the solution was taken every five minutes and filtered with a PTFE membrane microfilter with a pore size of 200 nm before measuring its absorbance inside a plastic cuvette with a path length of 1 cm. To correct the baseline, deionised water was used. When the sample was a coating, it was held in the middle of the reactor inside the solution.

3.4 Glass reactor

To study the effect of contamination on building materials, a glass reactor was designed in order to allow the exposure of pollutants under a controlled atmosphere. Parameters such as relative humidity and concentration of oxides of sulphur and nitrogen were controlled during the experiments.

3.4.1 Design

The cylindrical 3 mm thick soda glass cell used as a reactor in the tests is shown in Figure 3.8. The cell contained two gas inlets, a gas outlet and a glass lid to facilitate introduction and removal of the specimens. The gas system that allowed production of specific atmospheres was designed in order to be able to introduce all the three gases at the same time. The desired gas compositions for the experiments were produced by combining three gas cylinders:

i. Zero air grade, with a composition of: 0.5 ppm H_2, 2 ppm He, 1 ppm CH_4, <5 ppm H_2O, 5 ppm Ne, ~20.95 % O_2, 9300 ppm Ar, 385 ppm CO_2, 0.8 ppm N_2O, N_2 balance.
ii. Zero air grade containing 10.7 ppm of NO_2 balance with Zero air grade
iii. Zero air grade containing 10.4 ppm of SO_2 balance with Zero air grade

All gases were supplied by BOC Gases Ltd. Each gas cylinder was connected to a gas flow meter capable of measuring gas flows from 5 cm^3/min to 100 cm^3/min with an accuracy of ±0.5 ml/min (Platon Gap meter Type NGX supplied by Roxspur Measurement & Control Ltd).

The gas from the zero air grade cylinders was humidified by passing it through a glass bubbler containing deaerated water before being introduced inside the reactor. The other gas inlet of the cell was used to introduce the dry gas coming from the other two cylinders that beforehand were mixed using a three-way valve.

Figure 3.8 - Image of the glass reactor

Photo-catalytic activity was evaluated for the specimens exposed to different gas mixtures for a period of 120 h under both UV and daylight radiation. As UV source, the UV-LEDs

with a wavelength range of 376–387 nm previously described was used with a total intensity of 8 W/m^2. All other specimens were only exposed to daylight to simulate external environmental conditions. The power of the light in the UVA range was 3 mW/m^2. Three gas compositions were evaluated:

i. Artificial air containing 7 ppm SO_2 and constant 30 % RH
ii. Artificial air containing 7 ppm NO_2 and constant 30 % RH
iii. Artificial air containing 3.5 ppm SO_2 and 3.5 ppm NO_2 and constant 30 % RH

The concentration of pollutants was set to 7 ppm in all the experiments as previous research showed optimum results after exposure to 5-10 ppm of pollutants [3], [4]. RH remained constant at 30 % due to the technical limitation of working with three cylinders; the maximum achievable RH would be 33%.

3.5 Summary

This chapter describes how the different UV light sources used in this research were characterised, attending to their spectral wavelength and intensity.

The methodology used to work with *E. coli* is given in Section 3.2, explaining the steps that are required when microorganisms are involved. This methodology was used to analyse the microbial properties of a commercial TiO_2 coating, showing the results in Chapter Five as well as the degradation of methylene blue in aqueous phase.

A glass reactor was built to study the effect of different pollutants on building materials. Results from the use of this reactor are shown in Chapter Eight.

The following chapter describes in more detail the use of a mass spectrometer as part of a bespoke instrument, designed to follow gas phase reactions.

3.6 Bibliography

[1] M. Nuño, R. J. Ball, and C. R. Bowen, "Study of solid/gas phase photocatalytic reactions by electron ionization mass spectrometry," J. Mass Spectrom., vol. 49, no. 8, pp. 716–726, 2014.

[2] R. S. Breed and W. D. Dotterrer, "The Number of Colonies Allowable on Satisfactory Agar Plates," J. Bacteriol., vol. 1, no. 3, pp. 321–331, May 1916.

[3] G. C. Allen, A. El-Turki, K. R. Hallam, D. McLaughlin, and M. Stacey, "Role of NO_2 and SO_2 in degradation of limestone," *Br. Corros. J.*, vol. 35, no. 1, pp. 35–38, 2000.

[4] G. C. Allen, A. El-Turki, K. R. Hallam, D. McLaughlin, and M. Stacey, "Role of NO_2 and SO_2 on the degradation of limestone," in *Stone deterioration in polluted urban environments*, vol. 3, D. J. Mitchell and D. E. Searle, Eds. CRC publisher, 2004, pp. 119–130.

Chapter Four - Analysis of photocatalytic reactions in the gas phase

This chapter describes a novel methodology for the real time study of solid-gas phase photocatalytic reactions in-situ. A rig incorporating a reaction chamber and analyser was designed, built and commissioned to facilitate the investigation of photoactive materials under different gas compositions. UV irradiation in the wavelength of ranges 376-387 and 381-392 nm was provided using specifically designed high efficiency light emitting diode (LED) arrays. An ultra-high vacuum right angled bleed valve allowed a controlled flow of gas from the main reaction chamber held at atmospheric pressure, to a mass spectrometer operating at a vacuum of 10^{-5} mbar.

4.1 Theoretical background

Mass spectrometry is a powerful technique that extracts analytical information by measuring the concentration of the gaseous ions' mass-to-charge ratio. It is the convention to present data in the form of a plot of ion signal against a mass-to-charge range; allowing the chemical structure can be elucidated by this mass spectrum. Different chemical compounds generated predictable charged fragments, which can be used to identify the gaseous compound.

In a typical electron impact-mass spectrometer, an ion source is responsible for the analyte's ionization; by bombarding the molecules with electrons, creating cations generally in an excited state as Equation 4.1 shows. The relaxation process usually breaks the molecules into smaller charged fragments (Equation 4.2).

$$MNO + e^- \rightarrow MNO^{*+} + 2e^- \quad (4.1)$$

$$MNO^{*+} \rightarrow MN^+ + O^+ \quad (4.2)$$

In order to create sufficient cationic ions, it is necessary that the electrons hit the analyte with a potential higher than 50 eV. After the ion source, ions are focused through electrostatic lenses onto the quadrupole mass filter shown in Figure 4.1. The mass filter consists of four parallel stainless steel cylinders. Opposite rods are connected together and an alternating voltage applied. This current is applied with a radiofrequency gap of 180 degrees allowing the oscillating electrical field to stabilise or destabilise ions. Only ions in a specific mass/charge range pass it. The quadrupole mass filter used in this research project works with ions from 1 to 100 atomic mass unit (a.m.u.). All the other ions are deflected.

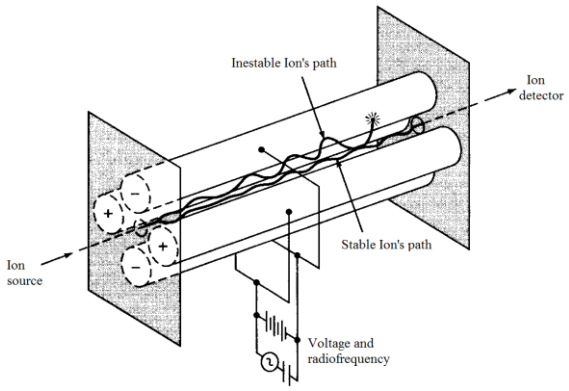

Figure 4.1 - Quadrupole mass filter [1]

Ions are detected by a Faraday cup (a metal conductive cup able to trap ions in vacuum) or a microchannel plate detector. When an ion collides with the metal, a net charge is created. The microchannel plate detector consists in microcontinouos-dynode electro multiplier, made by extruded lead-silicate glass of approximately 10 µm. It generates and amplifies the electric signal after an ion collides by liberating electrons as Figure 4.2 shows. The maximum theoretical gain is 3000 electrons per collided ion. The incoming ion that will be a positive ion (not an electron), with an amount of energy that depends from its mass; therefore the amount of secondary electrons emitted from the plate surface will depend of the ionic mass.

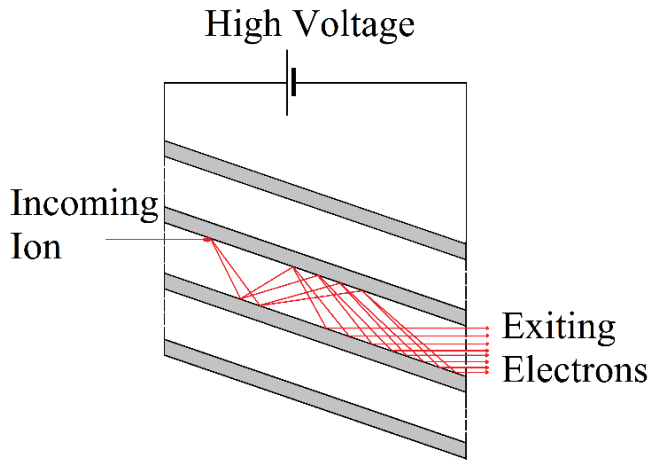

Figure 4.2 - Schematic diagram of how a multichannel plate works

4.2 Design

A schematic diagram of the apparatus is shown in Figure 4.3. The system comprises of several elements including a 203 ppm of NO_2 diluted in N_2 gas cylinder, zero air grade gas cylinder, flowmeters, 100 %RH air channel, reaction chamber, UV source, rotary pump, UHV right angled valve, turbomolecular pump, low pressure RGA system, data logging and data analysis.

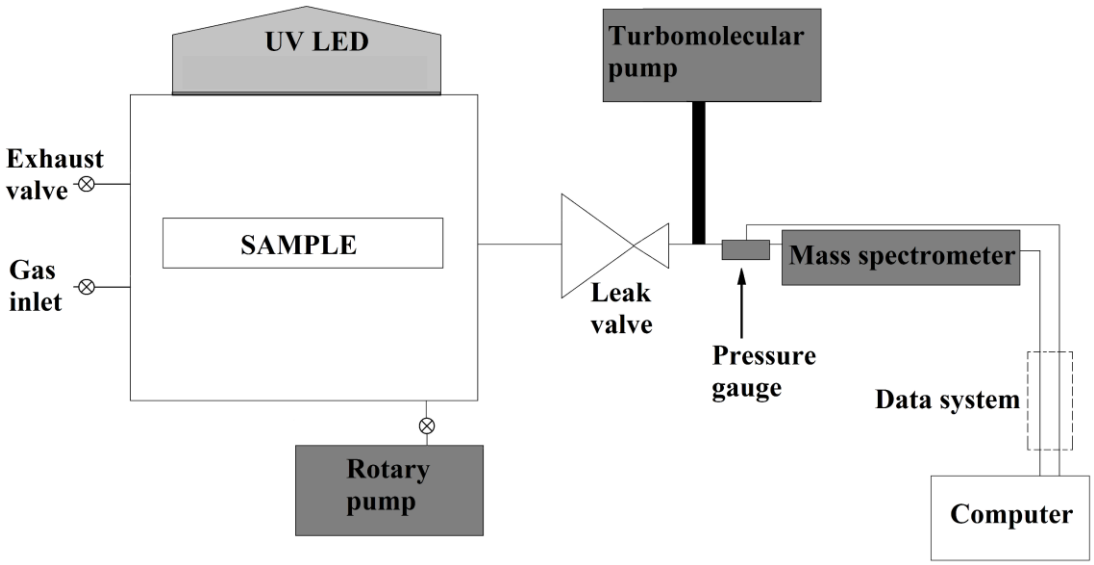

Figure 4.3 - Diagram of the system. The reaction chamber has four connections, one input valve connected to the gases, one output valve connected to the detector, one purge valve connected to the rotary pump and one exhausting valve [2]

Gas flows were regulated using flow meters capable of measuring gas flows from 5 cm^3/min to 100 cm^3/min (Platon Gap meter Type NGX supplied by Roxspur Measurement & Control Ltd) as Figure 4.4 shows. Two different gas cylinders were supplied by BOC Gases Ltd, a zero air (Table 4.1), and 203 ppm of NO_2 diluted in N_2.

Table 4.1 - Gas composition of Zero air grade (balance N_2)

Gas	Concentration
H_2	0.5 ppm
He	2 ppm
CH_4	1 ppm
H_2O	<5 ppm
Ne	5 ppm
O_2	~20.95%
Ar	9300 ppm
CO_2	385 ppm
N_2O	0.8 ppm

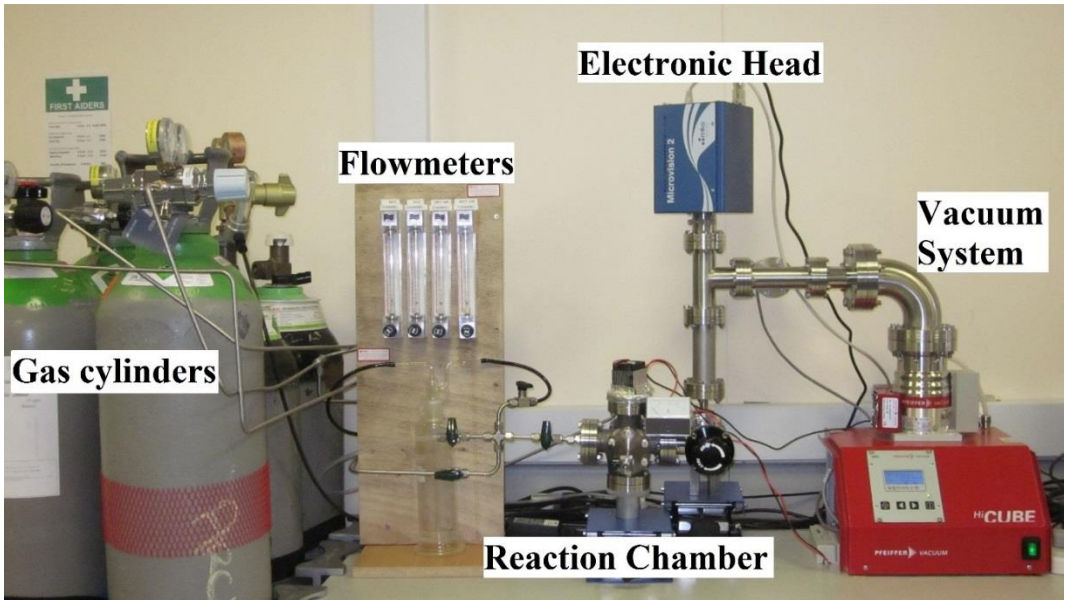

Figure 4.4 - Picture of the reaction chamber coupled to EI-mass spectrometer

Prior to carrying out experimental work all internal surfaces of the reaction chamber were passivated by exposure to 200 ppm of NO_2 diluted in N_2 for 72 h. The reaction chamber gas composition was controlled by adjusting the input flow via flow meters and mixing them with compressed air. A pyrex glass bubbler filled with distilled water connected to the compressed air was used to humidify the gas inside the chamber. Stainless steel pipes provided good corrosion resistance from the NO_2 and were connected using ¼ inch Swagelok® connections.

The reaction chamber was designed to operate at different pressures (from 1 bar to 10^{-6} bar if required); temperatures (0-40 °C) and gas compositions (0-203 ppm of NO_2 and different relative humidity). The chamber consists of a stainless steel (grade 304) chamber (6-way cross) with a volume of 290 cm^3. As Figure 4.5 shows, an input pipe delivered the desired gas composition and an output pipe connected to the residual gas analyser through a right angled valve and an UHV right angled bleed valve to reduce the pressure to 10^{-8} bar. An additional output valve connects the chamber to a secondary rotary pump (Adixen 2010SD) to achieve low vacuum conditions (10^{-6} bar). This was required before each experiment to mitigate incomplete replacement of gas in the chamber caused by 'dead zones'. The right angled valve isolated the entry of gas to the detector through the UHV angled valve when the secondary pump was in operation, and was in the fully opened position when the reaction occurs. All the joints were sealed using vacuum ConFlat flanges with silver coated copper gaskets. A metering valve was installed to provide an emergency exhaust from the chamber.

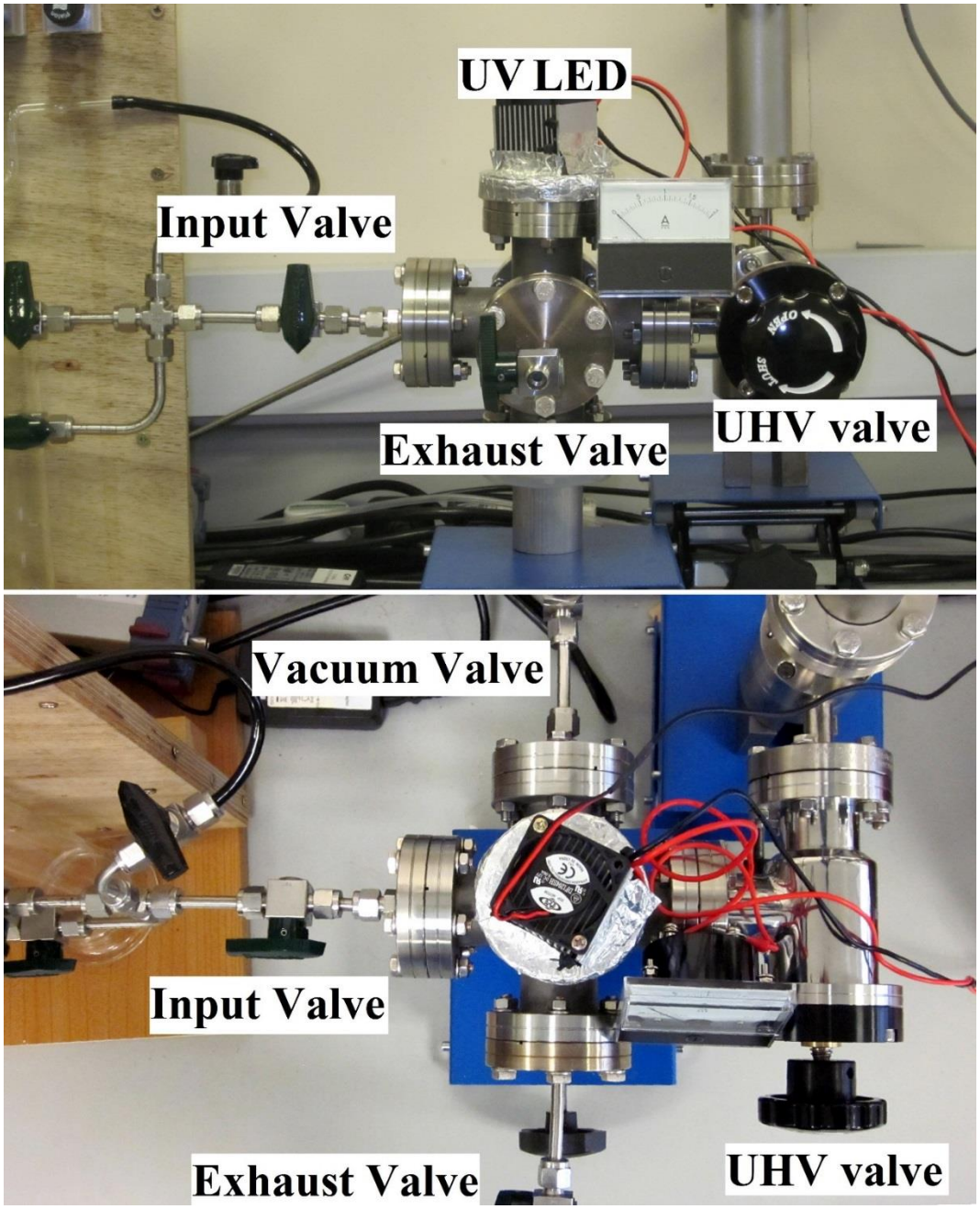

Figure 4.5 - Pictures of the reaction chamber showing all its connections

A Microvision 2 residual gas analyser (RGA) was supplied by MKS Instruments Inc. The ion source consisted of a thoriated tungsten filament that ionised the sample by electron impact followed by a quadrupole to separate the ions. A standard dual detection was provided through a Faraday cup detector for minimum partial pressure detection of 10^{-14} bar and a microchannel plate electron multiplier that amplified the signals up to 10^{-17} bar partial pressures. From a possible scanning range between 1 and 100 mass to charge ratio (m/z) these experiments employed a range from 14 m/z to 70 m/z with a step size of 0.12 m/z scanning 8 points per a.m.u., which takes less than 3×10^{-3} s per point), thereby increasing

the frequency of data collected. Figure 4.6 shows how the turbomolecular pump is connected to the Microvision 2, the electronic head (blue box) is responsible from transferring data gathered from the microchannel plate to the computer through a Category 5 cable, widely used for Ethernet connections.

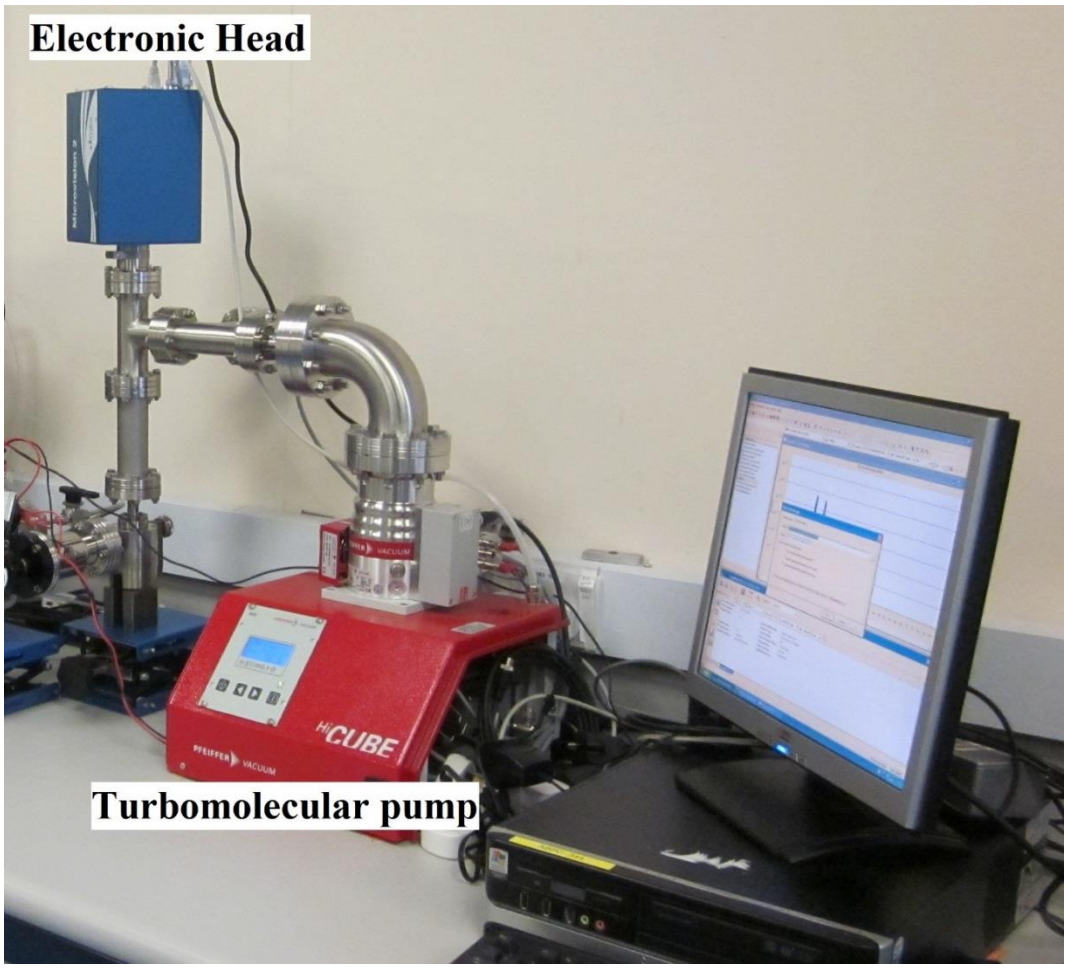

Figure 4.6 - Electronic head Microvision 2 and turbomolecular pump and pressure detector

The sensitivity of 0.45 A/mbar was achieved through operation of the ion source with an emission current of 1.2 mA, electron energy 70 eV and ion energy of 5.5 mA. Electron energy, emission current and ion energy are parameters that were adjusted to optimise the ion source for NO_2 exposure. Figure 4.7 shows the effect of emission current on NO_2 peak (46 a.m.u.) at 70 eV after being normalised by the total pressure. Emission currents higher than 1.2 mA provided a stable peak whereas 1.0 mA decays. 1.2 mA was chosen in order to maximize the ion source's life.

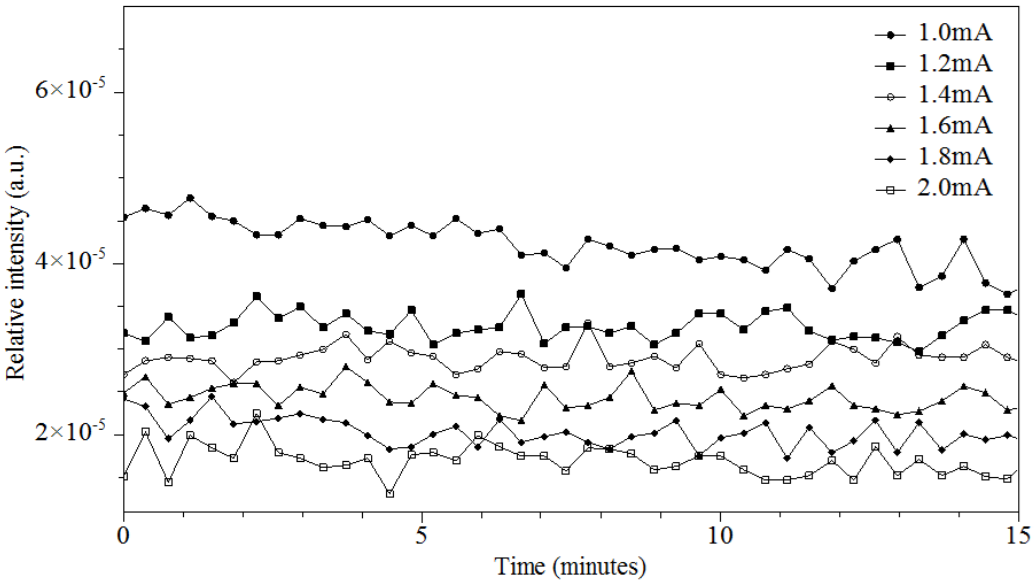

Figure 4.7 - Effect of emission current on the NO_2 signal (46 a.m.u.) at 70 eV electron energy and 5.5 mA ion energy

Electron energy has an influence on how the emitted electrons interact with the molecules, if the energy is insufficient, they will not transfer the required energy to ionise molecules. Whereas at high electron energies, the wavelength of the electrons will be smaller than the intermolecular bond length, passing through the molecules without interacting with them. The electron energy of the incident electrons that matches with the typical molecular bond of the gaseous particles maximises the energy transfer. Figure 4.8 shows how the NO_2 intensity changes at different electron energies (at 1.2 mA emission energy). Electron energies lower that 60 eV were not powerful enough to create a spectrum.

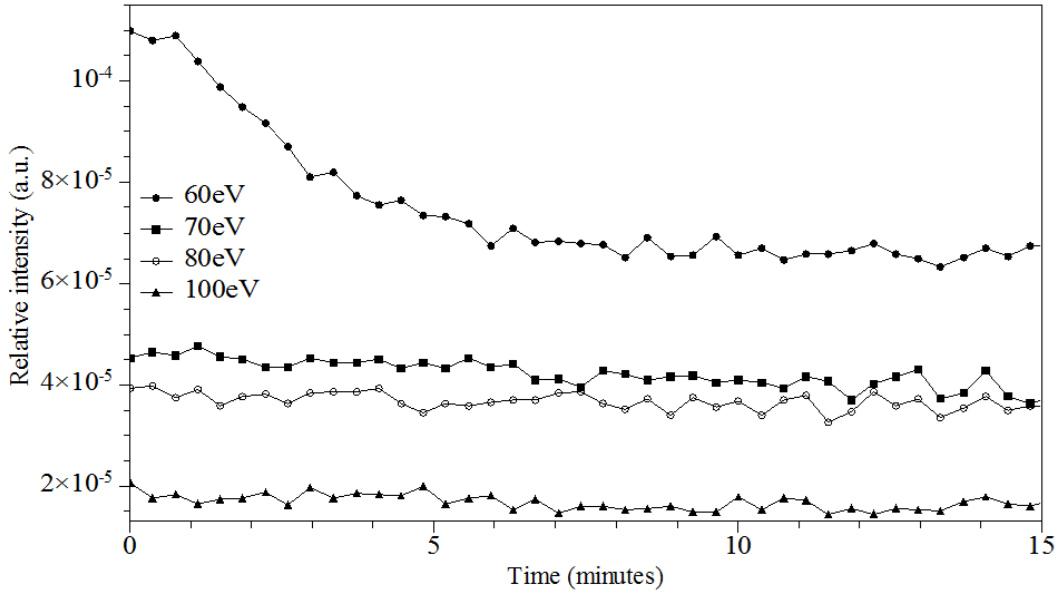

Figure 4.8 - Effect of electron energy on the NO_2 signal (46 a.m.u.) at 1.0 mA emission current and 5.5 mA ion energy

The experiments were carried out at 25 °C and atmospheric pressure for 150 min inside the chamber, whereas the mass spectrometer operated at a pressure of 5.4×10^{-8} bar in the low pressure side of the apparatus. Both LED's operated with an intensity of 30 W/m^2. Air was mixed with 203 ppm of NO_2 diluted in N_2 in order to provide enough O_2 and H_2O for TiO_2 to initiate photocatalytic reactions, leading an initial concentration of 190 ppm of NO_2 and sufficient O_2 and H_2O to promote generation of free radicals. After sealing the sample in the reaction chamber three cycles of vacuum (reaching 6.3×10^{-3} bar) followed by gas filling were undertaken in order to ensure total replacement of the previous gas composition.

4.3 Interpretation of the results

The mass spectrum of a complex gas mixture can be approximated as the sum of the mass spectra of its individual components. The intensity of a given peak in the mass spectrum will be defined by the sum of all contributions in that mass-to-charge range.

Figure 4.9 shows an untreated spectrum obtained from a gas mixture comprising 190 ppm of NO_2, 6 % of air balance N_2, the peak areas are related to the concentration for each molecule present in the gas mixture. The majority of the pressure within the system is due to N_2, at approximately 10^{-10} bar. A peak at any given m/z value can comprise of one or more species,

dependent on the gas composition and Table 4.1 contains details of the species which may contribute to the peaks identified.

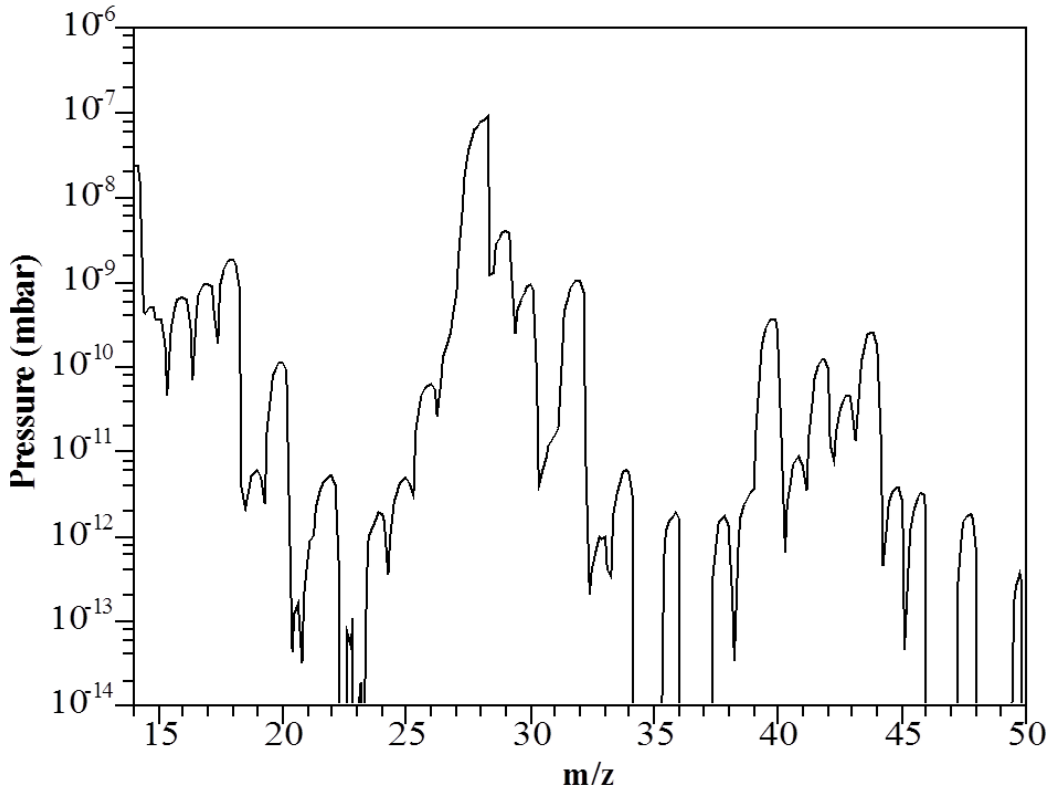

Figure 4.9 - Mass spectrum of 190 ppm of NO_2, 6 % of zero air grade balance N_2

For the case of pure NO_2, its mass spectrum consists in four peaks with two minor peaks from atomic nitrogen and atomic oxygen (14 m/z and 16 m/z respectively); one peak for NO_2^+ at 46 m/z and the most intense peak at 30 m/z from NO^+, which is the most stable specie under electron ionization conditions. When the analysis gas contains molecular oxygen and molecular N_2, NO is formed due to the dissociative ionization of N_2 and O_2 by electron collision and subsequent recombination in the ioniser. Therefore a mass of 46 m/z was followed during the reaction and assumed to reflect the proportion of NO_2. It should be noted that in doing this it is assumed that the contribution from other species with the same mass-to-charge ratio can be ignored. In the case of CO_2, the main peak is at 44 m/z with additional peaks at 12m/z for C^+, 16 m/z for O^+, 22 m/z for CO_2^{2+}, 28 m/z for CO^+, 29 m/z for isotopic $^{13}CO^+$ and 45 m/z for isotopic $^{13}CO_2^+$. The peak at 44 m/z will be referred to as the CO_2 peak and the same definition has been applied for peaks of 18 m/z (H_2O), peak 28 m/z (N_2), peak 32 m/z (O_2) and peak 40 m/z (Ar).

Table 4.2 - Major ions in the 70 eV EI mass spectra and the expected species of a gas mixture containing 190 ppm of NO_2, 6 % of air balance N_2 spectrum and their correlations with singular mass spectra of its components. Numbers in parenthesis show the relative intensity for the pure mass spectrum of a molecule

m/z	H_2O	CH_4	N_2	O_2	Ar	CO_2	NO_2
14		CH_2^+ (20.4%)	N^+ (13.8%)				N^+ (9.6%)
15		CH_3^+ (88.8%)					
16	O^+ (0.9%)	CH_4^+ (100 %)		O^+ (21.8%)		O^+ (9.6%)	O^+ (22.3 %)
17	OH^+ (21.2%)	CH_5^+ (1.6%)					
18	H_2O^+ (100 %)						
19	H_3O^+ (0.5%)						
20	H_2O^+ (0.3 %)				Ar^{++}(14.6 %)		
22						CO_2^{++} (1.9%)	
28			N_2^+ (100 %)			CO^+ (9.8%)	
29			$^{14}N^{15}N^+$ (0.8%)			$^{13}CO^+$ (0.1%)	
30			$^{15}N_2^+$				NO^+ (100 %)
32				O_2^+ (100 %)			
33				$^{16}O^{17}O^+$			
34				$^{16}O^{18}O^+$			
36				$^{18}O_2^+$	$^{36}Ar^+$ (0.3 %)		
38					$^{38}Ar^+$ (0.05%)		
40					Ar^+ (100 %)		
42							
44						CO_2^+ (100 %)	
45						CO_2^+ (1.2%)	
46						CO_2^+ (0.4%)	NO_2^+ (37%)
47							NO_2^+ (0.1%)

To calculate partial pressures of analytes, in addition to the total pressure and relative concentration, the ionization cross-section has to be included, as Equation 4.7 shows:

$$P_i = I \times \frac{A_{CS}}{2.508 Å^2} \times P \times \frac{ppm}{10^6} \quad (4.7)$$

Where `I´ represents the relative intensity of the peak for the pure analyte spectrum; `A_{CS}´ is the ionization cross-section of the analyte (in $Å^2$); `P´ represents the total pressure of the system. 2.508 $Å^2$ is the ionization cross-section for N_2 at 70 eV [3].

Microvision 2 reports that the ion current is converted to pressure using a single calibration point, and that there are no gas specific factors applied; therefore NO_2 can be calculated following the Equation 4.7. At 70 eV the ionization cross-section for NO_2 is 3.532 $Å^2$, thus, the relative ionization sensitivity from NO_2 is 1.41. The total pressure inside the detector is 5.4×10^{-8} bar, and the relative intensity of NO_2 for the 46 m/z peak is 37 % of the partial pressure:

$$P_{NO_2} = 0.37 \times 1.41 \times 5.4 \times 10^{-5} \times 2.0^{-4} = 5.6 \times 10^{-9} \text{mbar} \quad (4.8)$$

Figure 4.9 shows the mass spectra for the gas mixture under study, where the peak 46m/z has an intensity of 1.6×10^{-14} bar. This is two orders of magnitude smaller than that predicted from Equation 4.8. Additionally the peaks for H_2O and CO_2 are not related to their theoretical value if Equation 4.7 is applied which suggests concentrations of 0.23 and 2.85 ppm for H_2O and CO_2 respectively. This observation is attributed to cross-sensitivity effects [4], [5], that can modify the sensitivity of the detector and for CO_2 the signal is greater, and lower in the case of NO_2.

4.3.1 Mathematical approach

Previous researchers employing residual gas analysis to study gas mixtures attempted to correct the data using mathematical methods such as function-based least mean square regression [6], [7], parallel factor analysis [7] or the use of an internal standard [8]. However this approach can be problematic as Turner and colleagues have reported changes in the

response of the detector with time due to the cross-sensitivity effects that species generated when in the same gas mixture [5].

As a visual comparison, Figure 4.10 shows the partial pressure (raw data) of four molecules of interest (H_2O, O_2, CO_2 and NO_2) compared to Ar (which is plotted using a secondary y-axis). It can be observed a similar curvature over the respective pressure ranges.

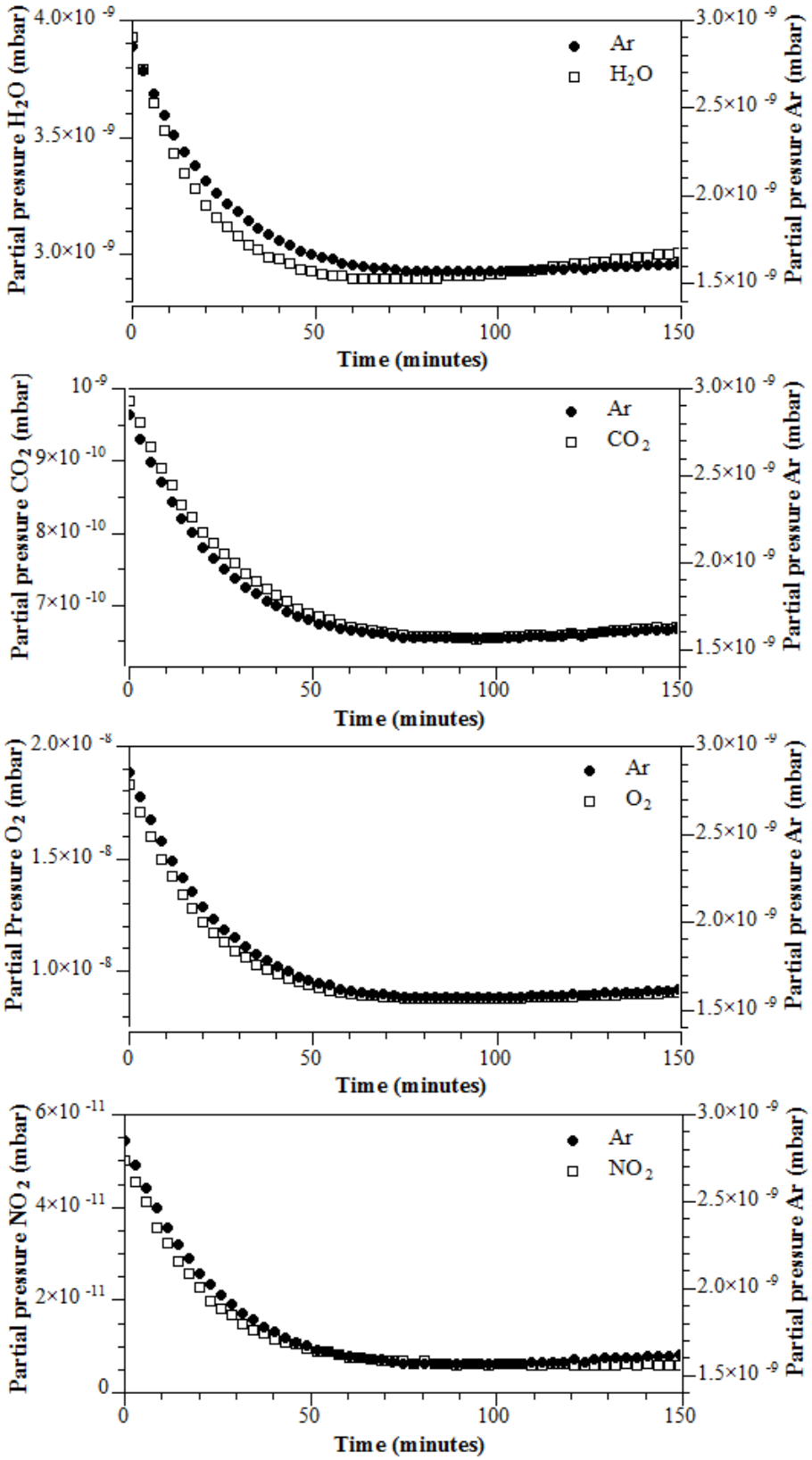

Figure 4.10 - Partial pressures of H_2O, O_2, Ar, CO_2 and NO_2 between 0 and 150 min with the empty chamber in the dark. Right 'y' axis is fixed for Ar partial pressure whereas left 'y' axis shows the value for the species over 150 min

When a sample was held inside the system and a photocatalytic reaction occurred on its surface, the species did not follow the same trend; Figure 4.10 shows the differences observed over 150 min when rutile is not irradiated and the reaction when rutile is irradiated with a UV source.

Figures 4.11 and 4.12 show the measurement for NO_2 and CO_2 processed through different data treatments; which the primary y axis corresponds to the pressure of NO_2 and the secondary for and CO_2. In order to avoid derived errors from pressure fluctuations the measured data can be normalised relative to Ar, also at absolute pressure. Figures 4.11 and 4.12 show the result of these treatments for CO_2 and NO_2; Figure 4.11 shows values for CO_2 and NO_2 after being divided by the Ar partial pressure, whereas Figure 12 shows the result of dividing by the total pressure. The results are identical, but instead of showing a stable signal, NO_2 decreases and CO_2 increases in intensity. Normalizing the data by the partial pressure of Ar or the absolute pressure distorts the real trend of NO_2.

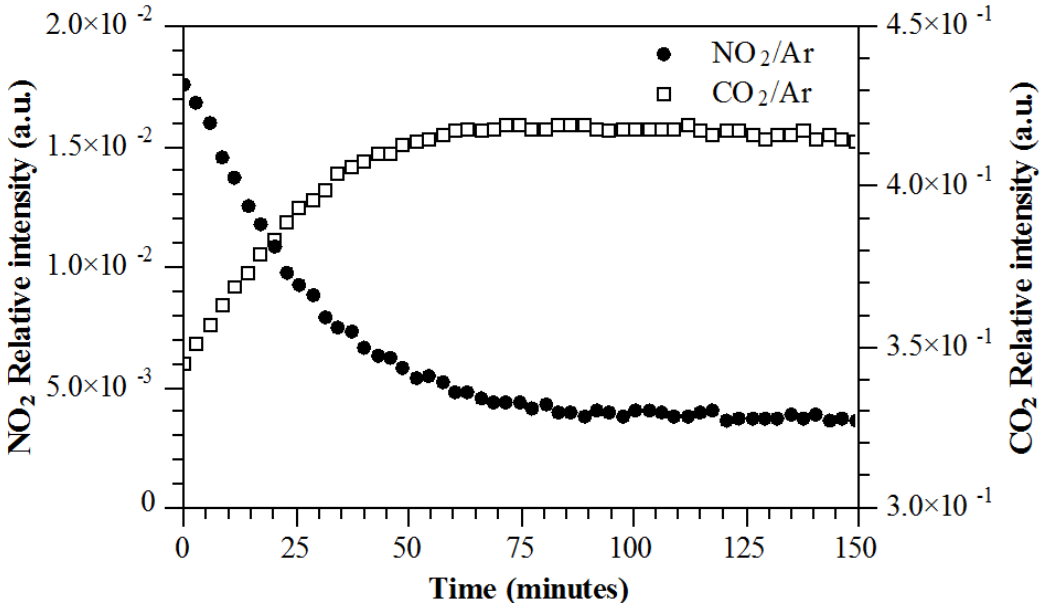

Figure 4.11 - Relative intensity of CO_2 and NO_2 normalised with the partial pressure of Ar over time with the empty chamber in the dark. Left 'y' axis shows the relative intensity for NO_2; right 'y' axis shows the relative intensity for CO_2

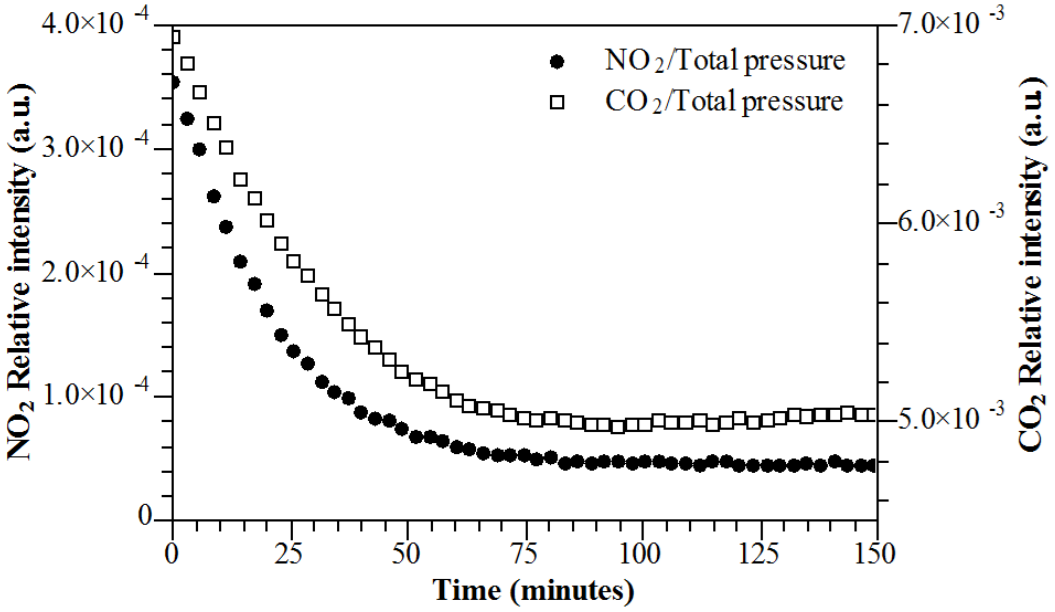

Figure 4.12 - Relative intensity of CO_2 and NO_2 normalised with total pressure between 0 and 150 min with the empty chamber in the dark. Left 'y' axis shows the relative intensity for NO_2; right 'y' axis shows the relative intensity for CO_2

From this research project, in 2014 [9] an alternative multiplicative approach was reported; considering the fractional changes of the gas of interest and compares it to that of an inert internal standard. Due to the limited reactivity of Ar, it is used to remove any absorption process' effect from the data collection, ensuring it will not affect the result. This effectively considers the shape of the curve for the partial pressure of an element irrespective of the absolute pressure. The fractional change of Ar during the experiment is defined as α, where the superscript '*max'* is the maximum value of its partial pressure for the data series; '*min'* is the minimum value of its partial pressure for the data series and 'i' is the partial pressure value for a given time during the experiment.

$$\alpha = \frac{Ar^{max} - Ar^{i}}{Ar^{max} - Ar^{min}} \qquad (4.9)$$

This treatment can be applied using similar methodology to the data relating to the m/z ratio of a molecule of interest, defined as *X*.

$$\varepsilon_X = \frac{X^{max} - X^{i}}{X^{max} - X^{min}} \qquad (4.10)$$

ε_X represents the relative change of the molecule '*X*'. This treatment normalises the data to a value between 0 and 1.

As a visual representation of the fractional change adjustment; Figure 4.13 shows the relative changes (resulting from applying Equation 4.10) of H_2O, N_2, CO_2, NO_2 and the total pressure. As it is shown, the relative changes fit in the Ar trend, being the total pressure and N_2 not adjusted to the Ar trend as H_2O, O_2, CO_2 and O_2 do.

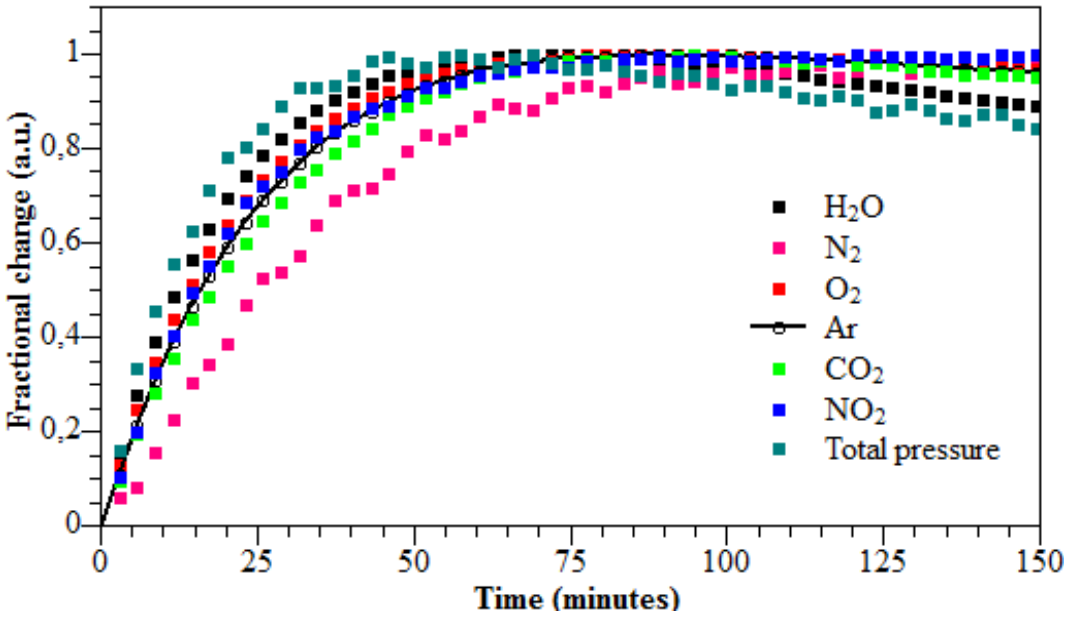

Figure 4.13 - Relative changes for Ar, H_2O, N_2, CO_2, NO_2 and the total pressure between 0 and 150 min

The fractional change of '*X*' considering the changes of Ar with time by mm^2 (area of the sample) in the Ar partial pressure scale is then defined as:

$$ {}^{i}_{N}X = \frac{\varepsilon_X - \alpha}{Area} \qquad (4.11) $$

The treatment allows to remove fluctuations related to the instrument limitations (i.e. absorption processes) by comparing with the Ar trend. It has been applied to all data expressed by Equations 4.9-4.11.

4.4 Case of study: reactivity of anatase

The reliability of the data treatment and the stability of the instrument despite of the cross-sensitivity effects were tested by carrying out an experiment with an empty chamber and replacing the quartz viewport for a stainless steel blanket to remove any potential photocatalytic effects. Although the lack of a sample inside the chamber would mean an area of 0 mm^2, Equation 4.11 would equal infinity, therefore an area was arbitrary set to that of experiments with a sample present (133 mm^2).

The average values after applying this data treatment for NO_2, O_2, H_2O and CO_2 during 150 min and their standard deviations are shown in table 4.3. The data indicates only small fluctuations in value and provides a baseline to which data corresponding to reactions can be compared.

Table 4.3 - Average and standard deviation values for NO_2, O_2, H_2O and CO_2 over 150 minutes of reading values of a gas mixture containing 190 ppm of NO_2, 6 % of air balance N_2 with the empty chamber in the dark

	Average	**Standard deviation**
H_2O	1.26×10^{-04}	4.18×10^{-04}
O_2	-1.12×10^{-04}	1.23×10^{-04}
CO_2	1.25×10^{-04}	1.09×10^{-04}
NO_2	-1.55×10^{-04}	1.26×10^{-04}

Figures 4.14-4.18 show the result of exposing aeroxide P25 to an atmosphere with a high NO_2 concentration (190 ppm) over 150 min. As it is shown, H_2O is consumed under both UV LEDs exposure, whereas O_2 only reacts under 381-392 nm. If their reductions are compared to CO_2 and NO_2 levels, there is a relationship between H_2O and NO_2 and O_2 and CO_2.

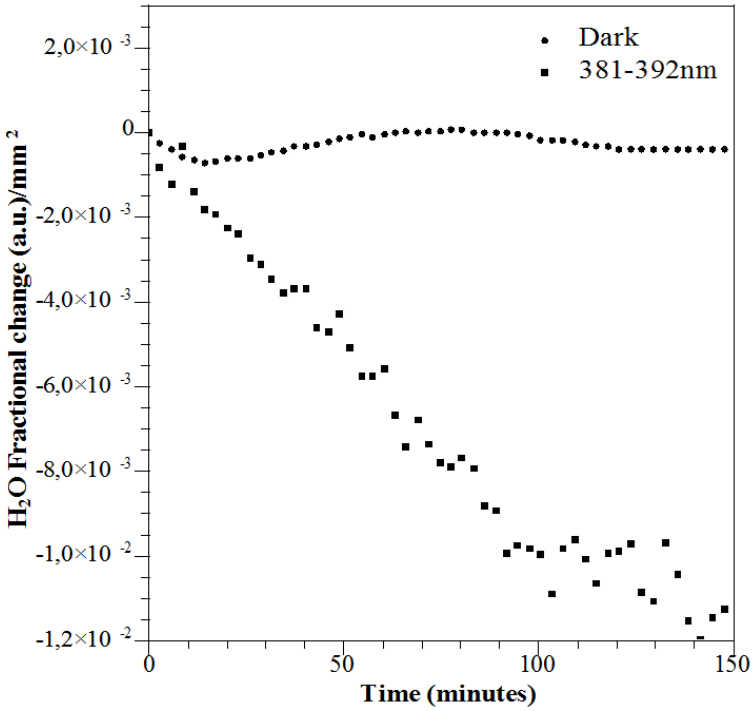

Figure 4.14- Fractional change of H_2O between 0 and 150 min for a sample in the dark and irradiated with a UV light of wavelength of 381-392 nm

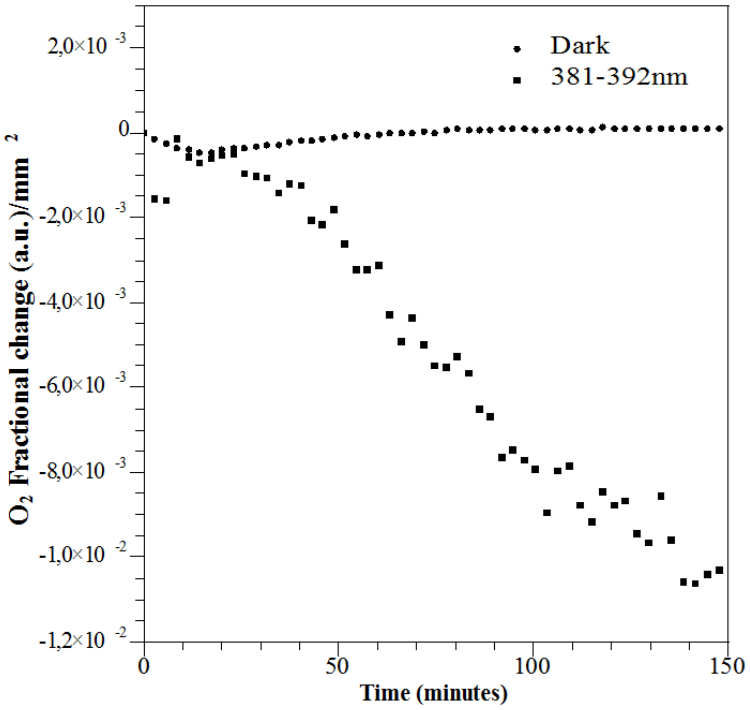

Figure 4.15 - Fractional change of O_2 between 0 and 150 min for a sample in the dark and irradiated with a UV light of wavelength of 381-392 nm

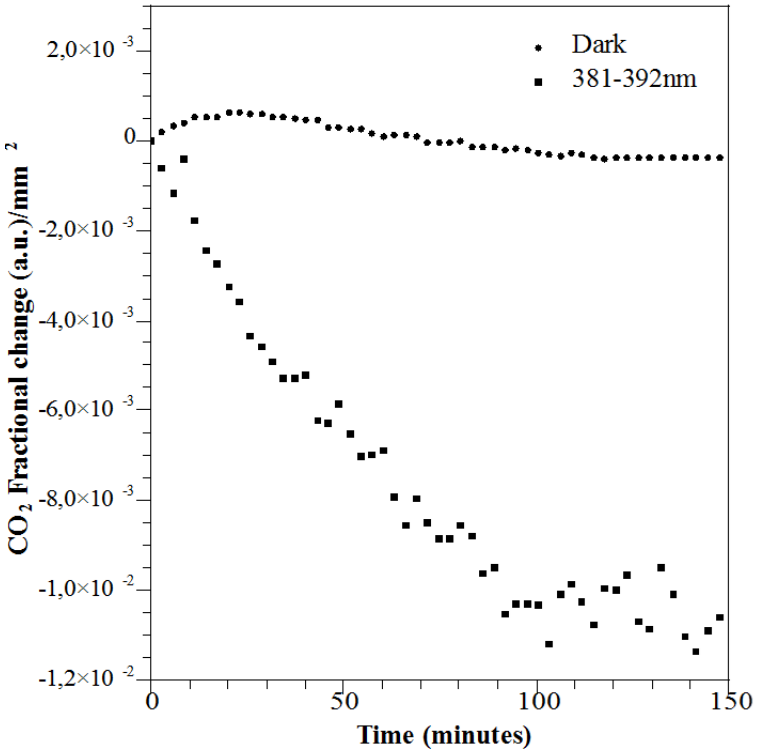

Figure 4.16 - Fractional change of CO_2 between 0 and 150 min for a sample in the dark and irradiated with a UV light of wavelength of 381-392 nm

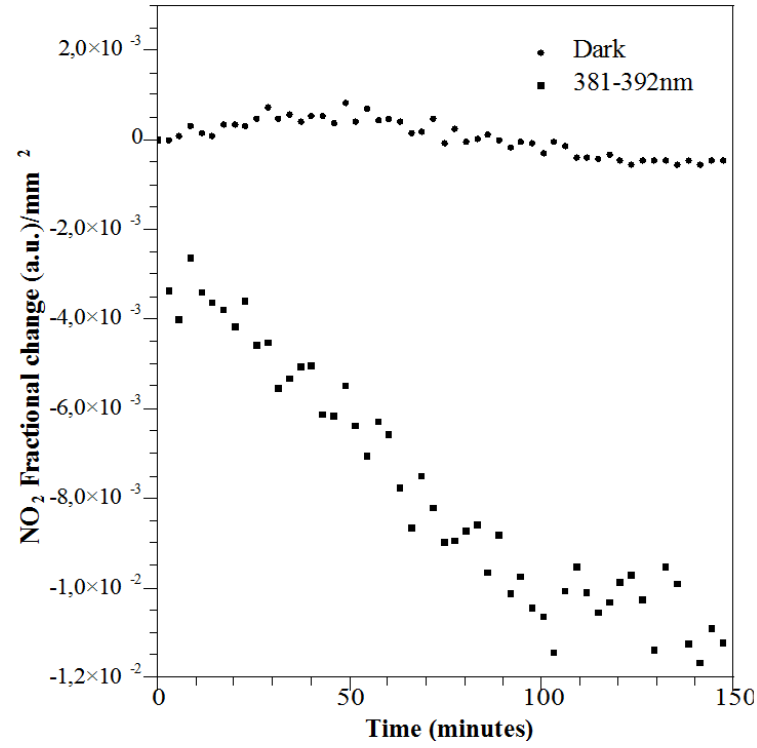

Figure 4.17 - Fractional change of NO_2 between 0 and 150 min for a sample in the dark and irradiated with a UV light of wavelength of 381-392 nm

The removal on gas phase of NO_2 was observed alongside with H_2O. As it has been previously shown, the formation of HNO_3 is the product of the reaction [10]–[13]. Not only NO_2 and H_2O are removed from the atmosphere; O_2 and CO_2 are also consumed.

This can be explained by anatase's band gap reported value 3.2 eV [13], [14], which is held in the range of the UV LED of wavelength range of 381-392 nm as Figure 4.18 shows.

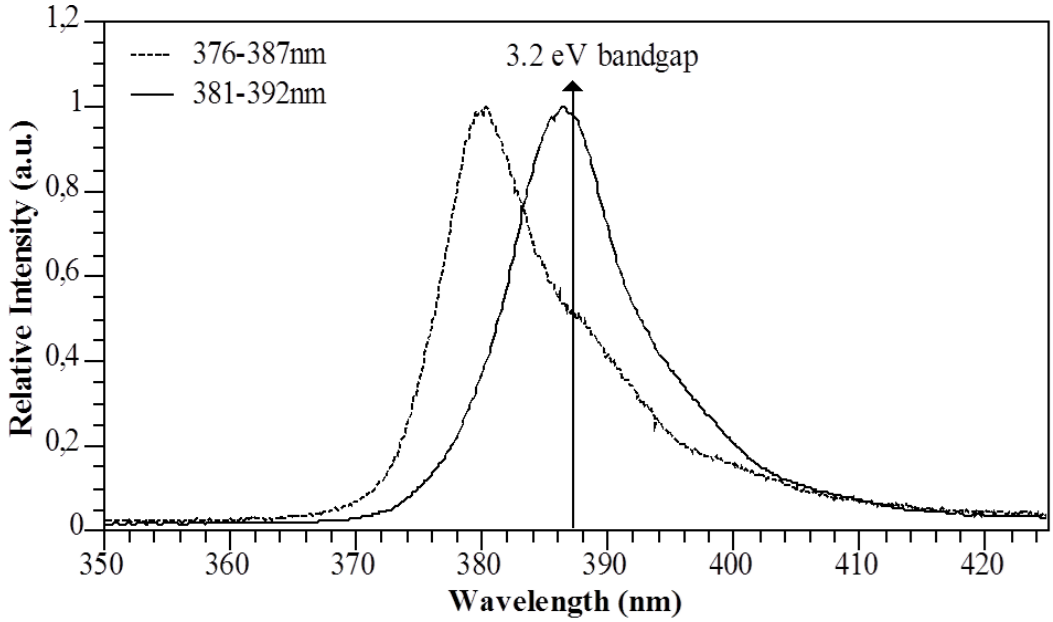

Figure 4.18 - Relative position of measured band gap and reported within the UV LED range

4.5 Summary

The experimental use of an electron impact-mass spectrometer has been implemented with success. Despite cross sensitivity effects and time-dependence signal that misled previous studies, a novel multipurpose reaction chamber has been designed, allowing modifications of parameters such as light source properties, gas composition and temperature for analysis of photocatalytic reactions. A new protocol has been established allowing the reduction of errors from instability in the mass spectrometer over time by comparing the fractional change in the specie of interest to that of an internal standard such as argon. Anatase P25 has been successfully tested with this system, showing the importance of the irradiated UV range in the photocatalytic performance against NO_2 and CO_2.

4.6 Bibliography

[1] D. A. Skoog, D. M. West, and F. J. Holler, *Fundamentals of analytical chemistry*. Saunders College Pub., 1988.

[2] M. Nuño, R. J. Ball, C. R. Bowen, R. Kurchania, and G. D. Sharma, "Photocatalytic activity of electrophoretically deposited (EPD) TiO_2 coatings," *J. Mater. Sci.*, vol. 50, no. 14, pp. 4822–4835, 2015.

[3] W. Hwang, Y.-K. Kim, and M. E. Rudd, "New model for electron-impact ionization cross sections of molecules," *J. Chem. Phys.*, vol. 104, no. 8, p. 2956, 1996.

[4] P. Turner, E. Clarke, C. Harwood, K. Cooke, H. Frampton, and S. Taylor, "Calibration effects during natural gas analysis using a quadrupole mass spectrometer," *Trends Anal. Chem.*, vol. 23, no. 4, pp. 281–287, 2004.

[5] L. Lieszkovszky and A. R. Filippelli, "Performance studies of partial pressure analysers," *Vacuum*, vol. 41, no. 7–9, pp. 2142–2143, 1990.

[6] R. A. Ketola, M. Ojala, V. Komppa, T. Kotiaho, J. Juujärvi, and J. Heikkonen, "A non-linear asymmetric error function-based least mean square approach for the analysis of multicomponent mass spectra measured by membrane inlet mass spectrometry," *Rapid Commun. Mass Spectrom.*, vol. 13, no. 8, pp. 654–662, 1999.

[7] W. P. Gardner, R. E. Shaffer, J. E. Girard, and J. H. Callahan, "Application of Quantitative Chemometric Analysis Techniques to Direct Sampling Mass Spectrometry," *Anal. Chem.*, vol. 73, no. 3, pp. 596–605, 2000.

[8] J. L. Pérez Pavón, M. del Nogal Sánchez, C. G. Pinto, M. E. Fernández Laespada, B. M. Cordero, and A. G. Peña, "Strategies for qualitative and quantitative analyses with mass spectrometry-based electronic noses," *TrAC Trends Anal. Chem.*, vol. 25, no. 3, pp. 257–266, 2006.

[9] M. Nuño, R. J. Ball, and C. R. Bowen, "Study of solid/gas phase photocatalytic reactions by electron ionization mass spectrometry," *J. Mass Spectrom.*, vol. 49, no. 8, pp. 716–726, 2014.

[10] S. Daito, T. Watanabe, and F. Tochikubo, "NO_x Removal Process in Pulsed Corona Discharge Combined with TiO_2 Photocatalyst," *Jpn. J. Appl. Phys.*, vol. 40, no. 4R, p. 2475, 2001.

[11] N. Negishi, K. Takeuchi, and T. Ibusuki, "Surface structure of the TiO_2 thin film photocatalyst," *J. Mater. Sci.*, vol. 33, no. 24, pp. 5789–5794, 1998.

[12] Y. Bedjanian and A. El Zein, "Interaction of NO_2 with TiO_2 Surface Under UV Irradiation: Products Study," *J. Phys. Chem. A*, vol. 116, no. 7, pp. 1758–1764, 2012.

[13] Y.-M. Lin, Y.-H. Tseng, J.-H. Huang, C. C. Chao, C.-C. Chen, and I. Wang, "Photocatalytic activity for degradation of nitrogen oxides over visible light responsive titania-based photocatalysts," *Environ. Sci. Technol.*, vol. 40, no. 5, pp. 1616–1621, 2006.

[14] K. Madhusudan Reddy, S. V Manorama, and A. Ramachandra Reddy, "Band gap studies on anatase titanium dioxide nanoparticles," *Mater. Chem. Phys.*, vol. 78, no. 1, pp. 239–245, 2003.

Chapter Five – Evaluation and characterisation of commercially available materials and coatings

The aim of this chapter is to assess the photocatalytic activity of commercially available materials. Pure TiO_2 and developed photocatalytic coatings were fully characterised and analysed by using XPS, XRD, UV-Visible diffusive spectroscopy, Raman spectroscopy, SEM, FESEM and TEM. Their photocatalytic performance was studied in aqueous as well as gas phase, previously explained in Chapter Three and Four. The XPS analysis was undertaken in Cardiff University, under the supervision of Prof Karen Wilson.

5.1 Characterisation of commercially available TiO_2 particles

Five commercially available TiO_2 powders were studied being in three different polymorphs. *Anatase* was supplied by three different companies:

i. *Anatase* in the form of Kronos vlp 7000 manufactured by Kronos Titan GmbH [referred as **7000**]
ii. *Anatase* in the form of CristalACTiV™ PC500 manufactured by Crystal Global (85 wt % TiO_2, 100 % anatase) [referred as **PC500**]
iii. *Anatase* in the form of Aeroxide® P25 manufactured by EVONIK Degussa Industries [referred as **P25**]
iv. *Rutile* in the form of TiPure® R-960 was supplied by DuPont (TiO_2 > 89 wt %; Al_2O_3 ~3.3 wt % and amorphous SiO_2 ~5.5 wt %) [referred as **rutile**]
v. *Brookite* was pursached as a single crystal of 40 × 20 × 5 mm [referred as **brookite**] and milled using an agate pestle and mortar prior testing its photoactivity.

5.1.1 Electron microscopy

In order to investigate the micro and nanostructure of TiO_2 powders, FESEM and TEM were used to characterise them at different magnifications. Calculated particle sizes are given in table 5.3 alongside with specific surface area, band gap and crystallite size.

5.1.1.1 7000

Anatase 7000 presented a distribution of micro and nanoparticles as Figures 5.1 and 5.2 show. TEM revealed an agglomeration of nanoparticles (>10 nm), being unable to determine an average particle size.

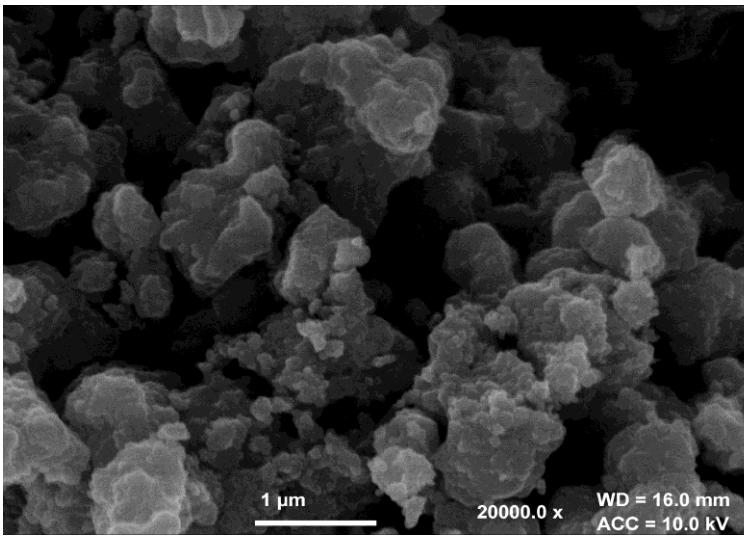

Figure 5.1 - FESEM image of anatase 7000

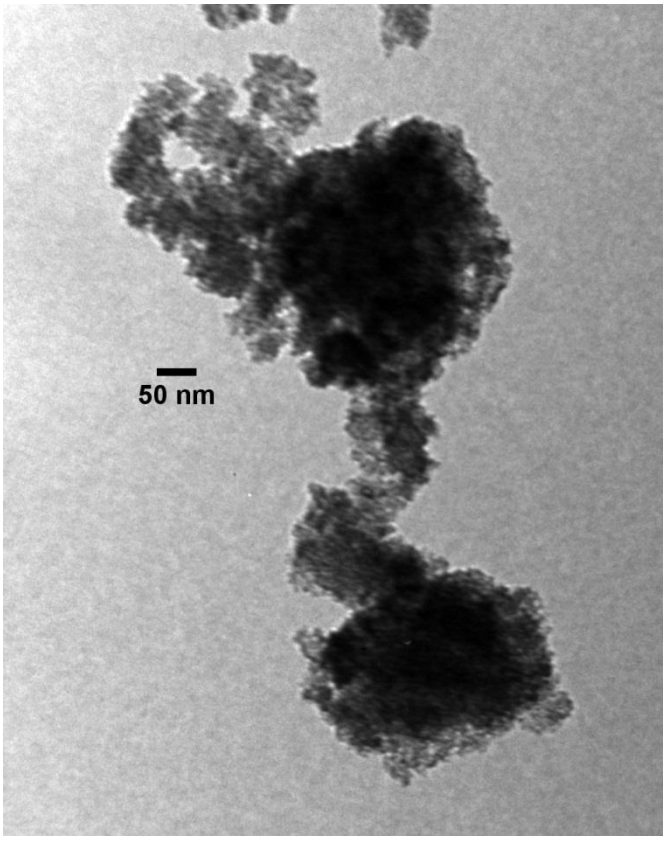

Figure 5.2 - TEM image of anatase 7000

5.1.1.2 PC500

FESEM revealed a large number of particles of ~ 600 nm as Figure 5.3 shows. Attending to the TEM image, the nanoparticle size distribution is uneven, being the average particle size in the range of 20 nm.

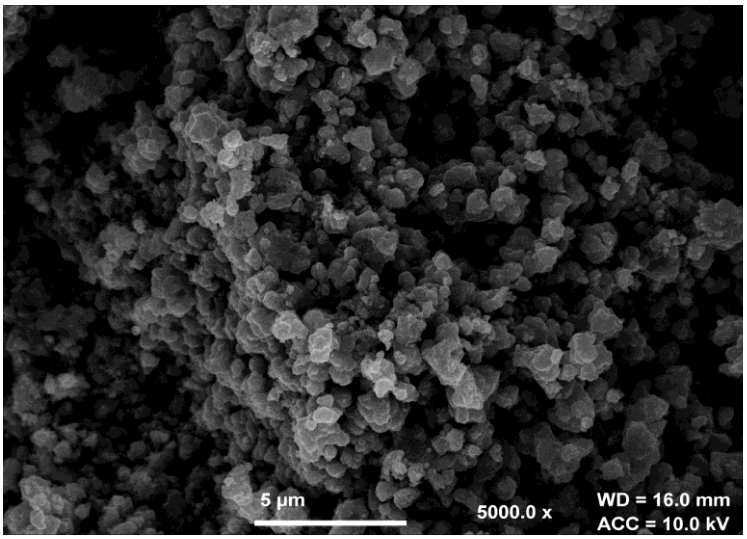

Figure 5.3 - FESEM image of anatase PC500

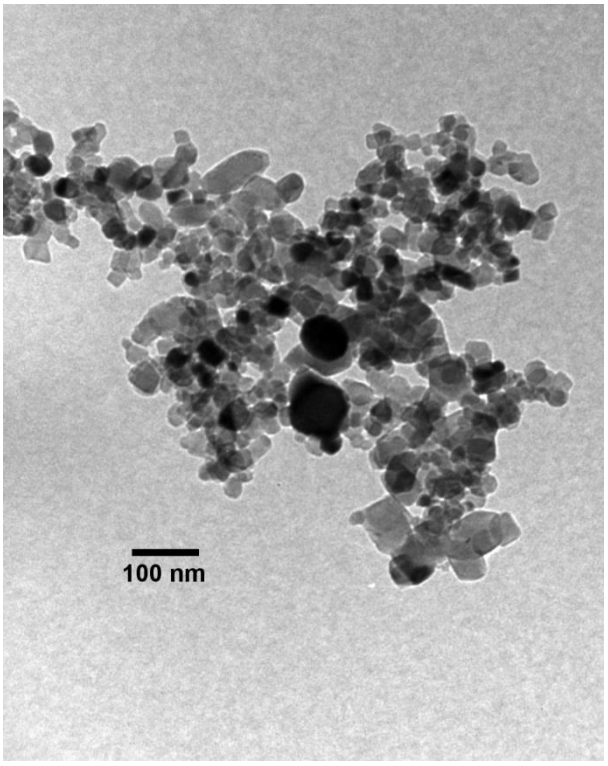

Figure 5.4 - TEM image of anatase PC500

5.1.1.3 P25

Anatase P25 showed the most homogeneous particle size distribution in FESEM (Figure 5.5) as well as in TEM (Figure 5.6), held in the range of 30 nm. This result is in the range as the technical datasheet provides (21 nm).

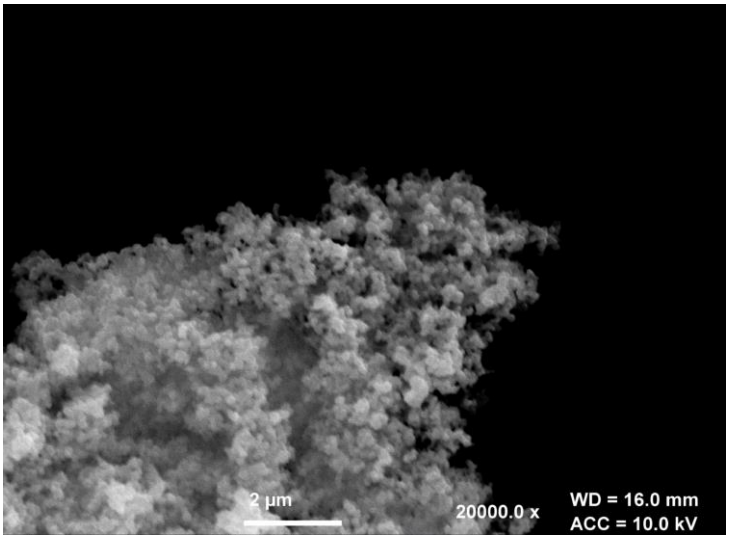

Figure 5.5 – FESEM image of anatase P25

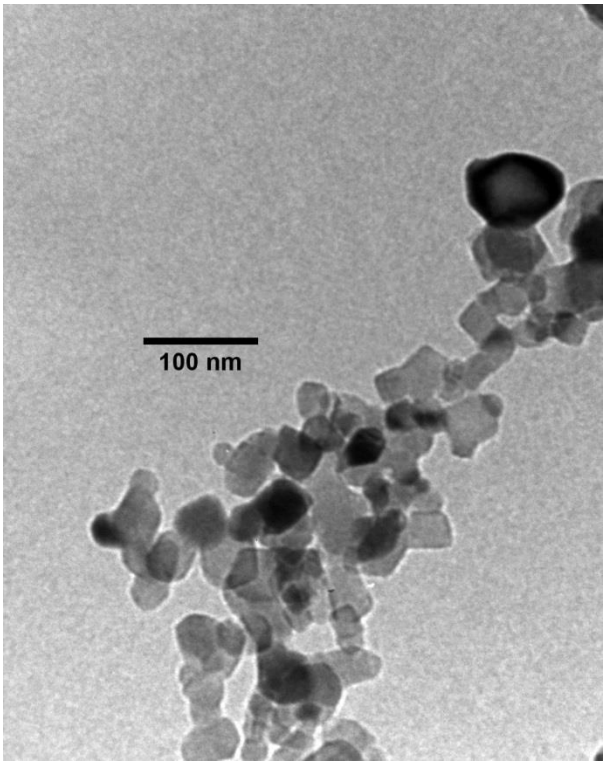

Figure 5.6 – TEM image of anatase P25

5.1.1.4 Rutile

Rutile TiPure shows a homogeneous particle size with 402 µm of average particle size which was calculated from FESEM images as Figure 5.7 shows. This was also corroborated with TEM calculations, as Figure 5.8 shows.

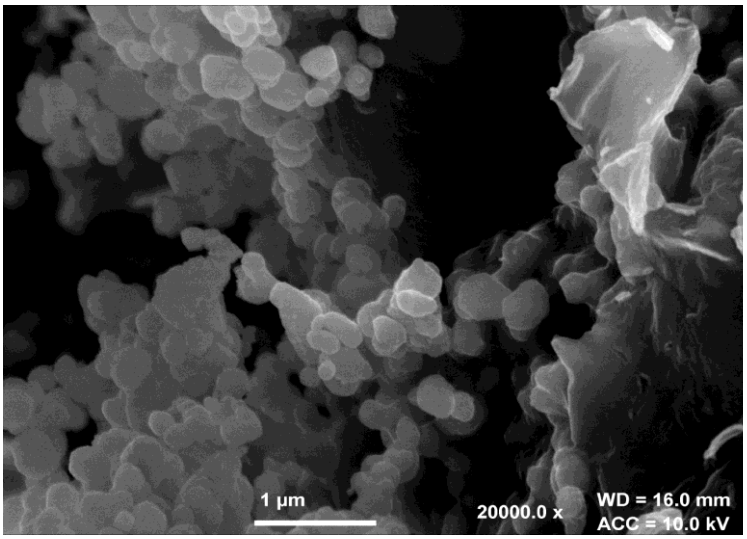

Figure 5.7 – FESEM image of rutile

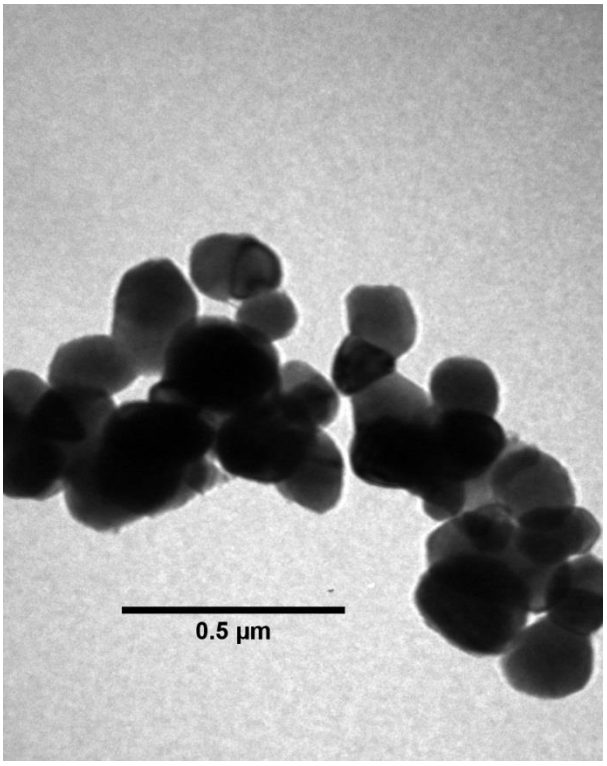

Figure 5.8 – TEM image of rutile

5.1.1.5 Brookite

Brookite powder was characterised by FESEM (Figure 5.9), showing particles in the range of 400 nm whereas TEM showed nanoparticles of smaller diameter (approximately ~300 nm) as Figure 5.10 shows.

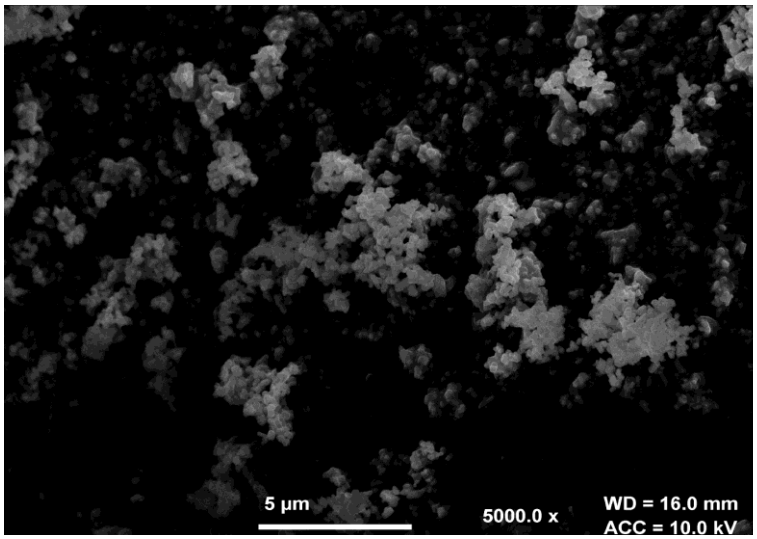

Figure 5.9 – FESEM image of brookite

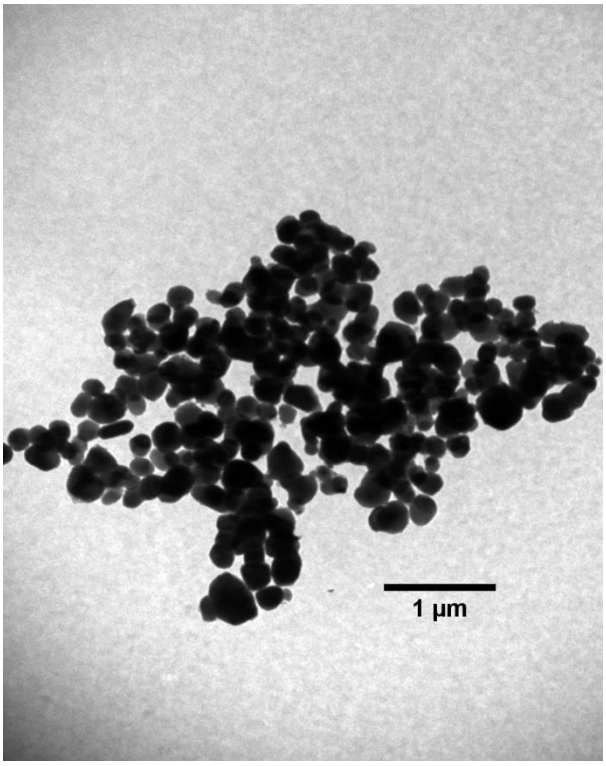

Figure 5.10 – TEM of brookite

5.1.2 Raman spectroscopy

Raman spectroscopy was conducted on the samples before exposure to reactive gases over the range 0 - 1000 cm^{-1} where the main vibrational modes can be observed. Figure 5.11 compiles Raman spectra for the five TiO_2 powders.

Anatase, as well as rutile, has a tetragonal crystal symmetry, but they belong to different space groups. Rutile has two TiO_2 formula units per cell (*$P4_2/mnm$*, symmetry D_{4h}) whereas anatase has four (*I4/amd*, symmetry D_{4h}). For the case of brookite, which has an orthorhombic crystal symmetry, with a space group Pbca and D_{2h} symmetry. From the possible vibrational modes, only those that cause a change in polarizability of the molecule will be active in Raman.

There are four lattice displacements for rutile which are active in Raman, B_{1g} (145 cm^{-1}) and E_g (445 cm^{-1}, most intense), where O^{2-} anions move respect the stationary Ti^{4+}; A_{1g} (610 cm^{-1}) which is an asymmetric bending move of O-Ti-O, and a multi-phonon process (240cm^{-1}) [1]–[4].

For anatase, there are six lattice displacements which are active in Raman, A_{1g} (513 cm^{-1}), B_{1g} (399 and 519 cm^{-1}) and E_g (144, 197 and 639 cm^{-1}) cause by Ti-O bond stretching and bending of the bond O-Ti-O [5], [6]. The peak at 197 cm^{-1} assigned to the E_g mode is very weak and it has not being listed in Figure 5.11 due to its low intensity (0.05 %). the peak B_{1g} at 519 cm^{-1} was reported at 73 K and it is not visible at room temperature.

In the case of brookite, due to a lower symmetry and a larger unit cell (in comparison with rutile and anatase), 36 Raman active modes are reported and 25 have been assigned [7]. Figure 5.11 highlights the most intense signals for [7]–[9].

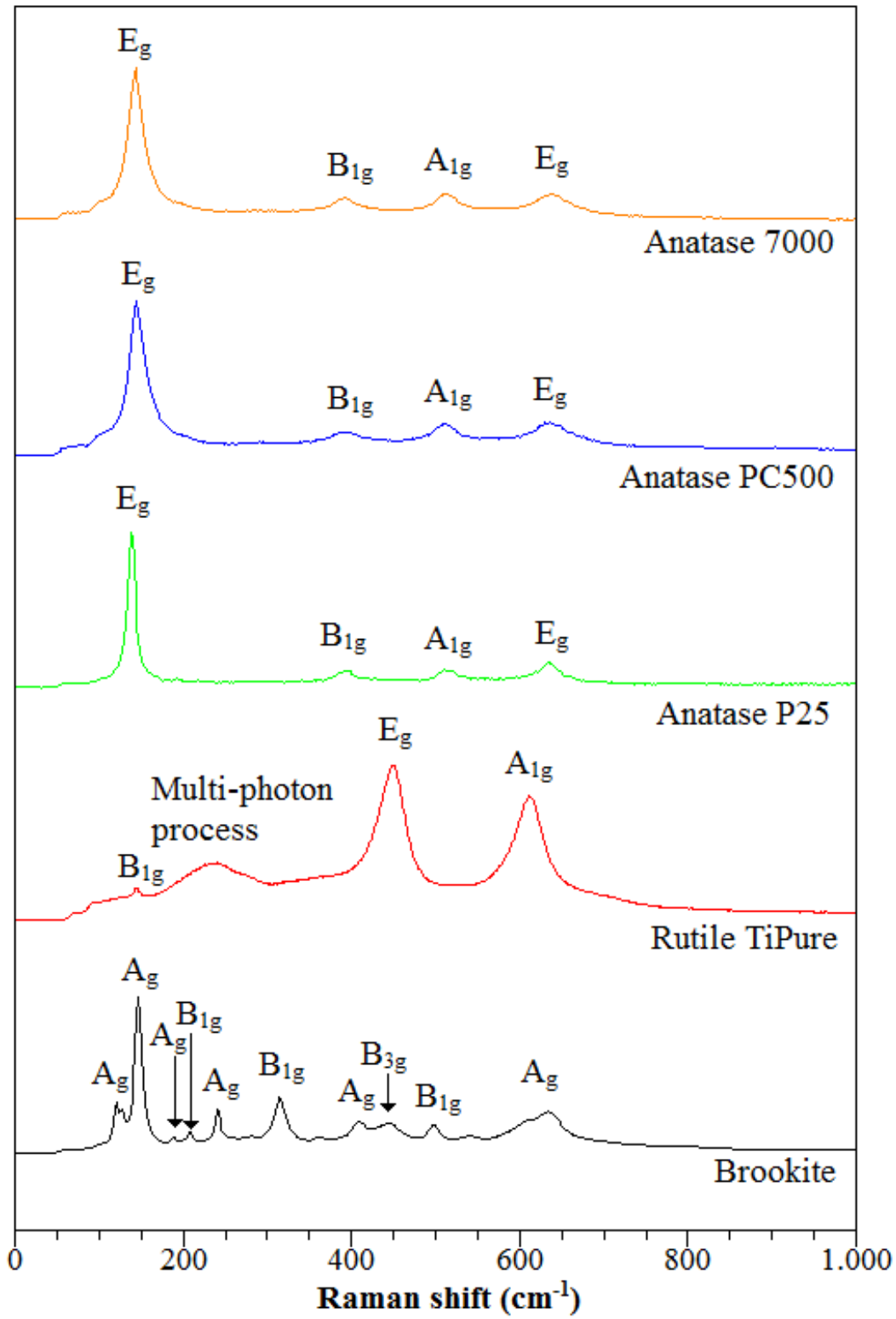

Figure 5.11 – Raman spectra from 0 to 1000 cm^{-1} of five different TiO_2 powders

5.1.3 X-ray photoelectron spectroscopy

Figure 5.12 shows a typical survey spectra of TiO_2 (P25) and table 5.1 shows the binding energies and elemental ratios for carbon, oxygen, calcium, silicon and titanium, calculated from higher resolution spectra in specific regions for the commercial powders.

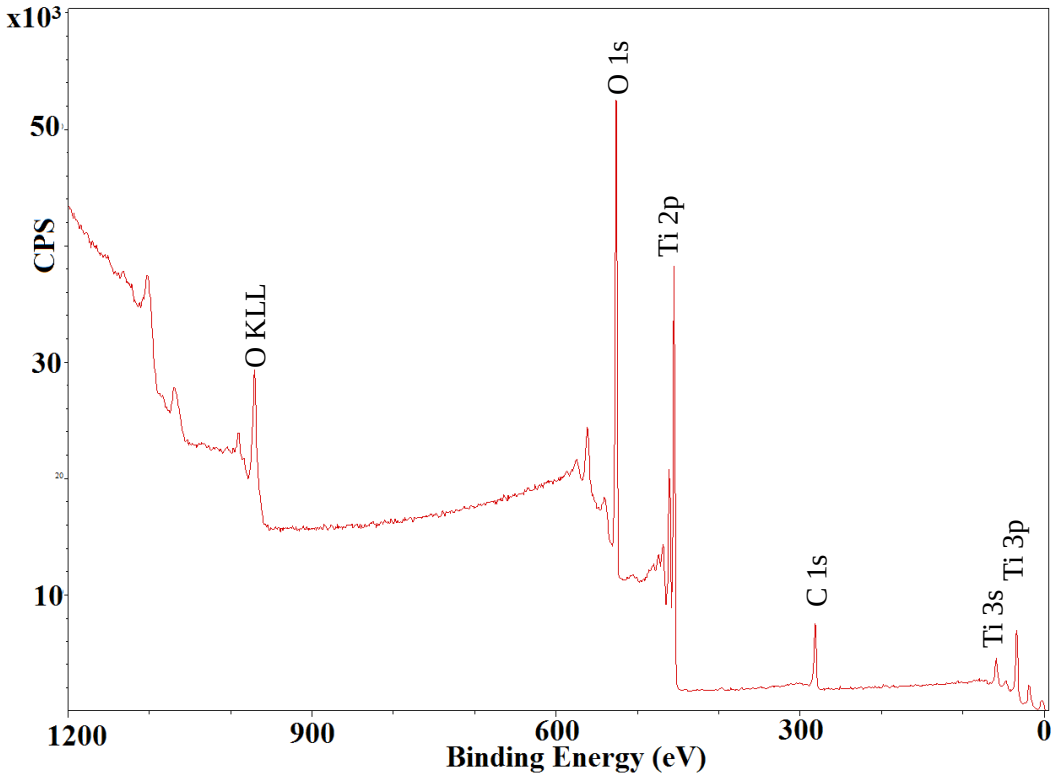

Figure 5.12 - XPS spectra of Aeroxide® P25

Table 5.1- Element ratios and chemical state derived from XPS analysis

	Binding energy (eV) / Relative concentration (at. %)									
	C 1s		**O 1s**			**Ca 2p ($CaCO_3$)**		**Si 2p (SiO_2)**	**Ti 2p (TiO_2)**	
	C-N	**CO_3^{2-}**	**TiO_2**	**CO_3^{2-}**	**SiO_2**	**Ca $2p_{3/2}$**	**Ca $2p_{1/2}$**	**Si 2p**	**Ti $2p_{3/2}$**	**Ti $2p_{1/2}$**
7000	**286.7**/3.7	**288.7**/1.8	**529.6**/57.1	**531.0**/11.5	-	-	-	-	**458.4**/17.4	**464.1**/8.5
PC500	**286.4**/5.4	**289.6**/4.5	**529.5**/37	**531.4**/18.9	**533.2**/1.7	**347.4**/2.6	**350.8**/1.3	**103.2**/2.2	**458.5**/17.6	**464.2**/8.8
P25	**287.1**/5.6	-	**529.1**/59.9	**531.3**/7.8	-	-	-	-	**458.4**/17.9	**464.1**/8.8
Rutile TiPure	-	**288.9**/5.2	**529.8**/71.3	-	**533.2**/9.1	-	-	**102.8**/12.3	**458.1**/1.3	**463.8**/0.7

As table 5.1 shows, KRONOS vlp 7000 and Aeroxide® P25 are the most pure TiO_2 powders, whereas PC500 and Rutile TiPure® contains $CaCO_3$ and SiO_2.

Binding energies for TiO_2 are related to titanium and oxygen. Ti 2p peaks varied between 458.1 and 458.5 eV in accordance with previous studies [10], [11], and for O 1s the observed peaks are within the range of 528.8-529.8 eV. These results agreed with studies carried by Dementjev [10] and Bedri [11], which showed Ti 2p binding energies from 458.0 to 459.4 eV and for O 1s from 529.4 to 530.6 eV.

The adventitious carbon contamination peak at 284.8 eV is not, however an additional peak C 1s corresponding to CO_3^{2-} was also identified as impurity in 7000, PC500 and rutile TiO_2 powders. The binding energy of this peak ranged between 288.7 and 289.6 eV which is in agreement with studies by Kang [12] and Demri [13] who report $CaCO_3$ binding energies of 288.6 and 289.2 eV. The binding energy for the Ca 2p peak identified at 347.4 eV which is in accordance with previous studies by Stipp [14] who reported $CaCO_3$ binding energy of 347.7 eV. For the case of SiO_2, the reported values for O 1s peak at 533.2 eV and ~103 eV agrees with previous results [15].

Although there was no XPS data for brookite, EDX was used to confirm titanium and oxygen were the main components as Figure 5.13 shows. The peaks that correspond to nickel and copper are from the TEM probe.

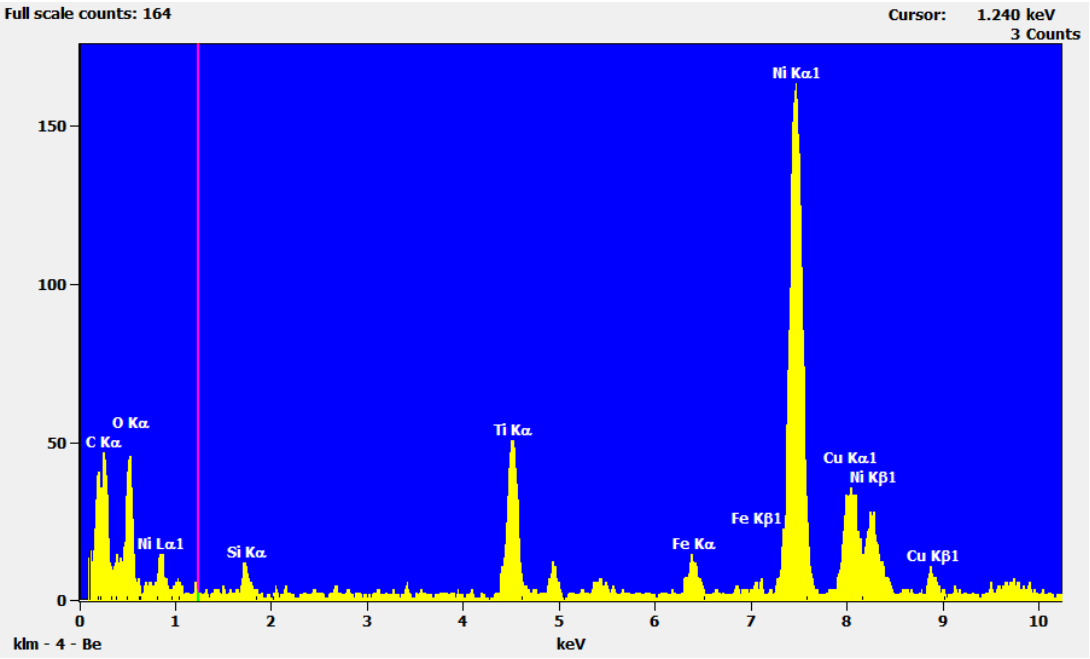

Figure 5.13 – EDX spectrum of brookite

5.1.4 X-ray diffraction

XRD was undertaken to characterise the crystal phase of the powders. Figure 5.14 compiles the normalised diffractograms for anatase (PC500, 7000 and P25), rutile and brookite crystal. Previous studies were used to identify and label peaks from different crystal phases [4], [5], [16]–[18] and table 5.2 compiles d spacing for those peaks.

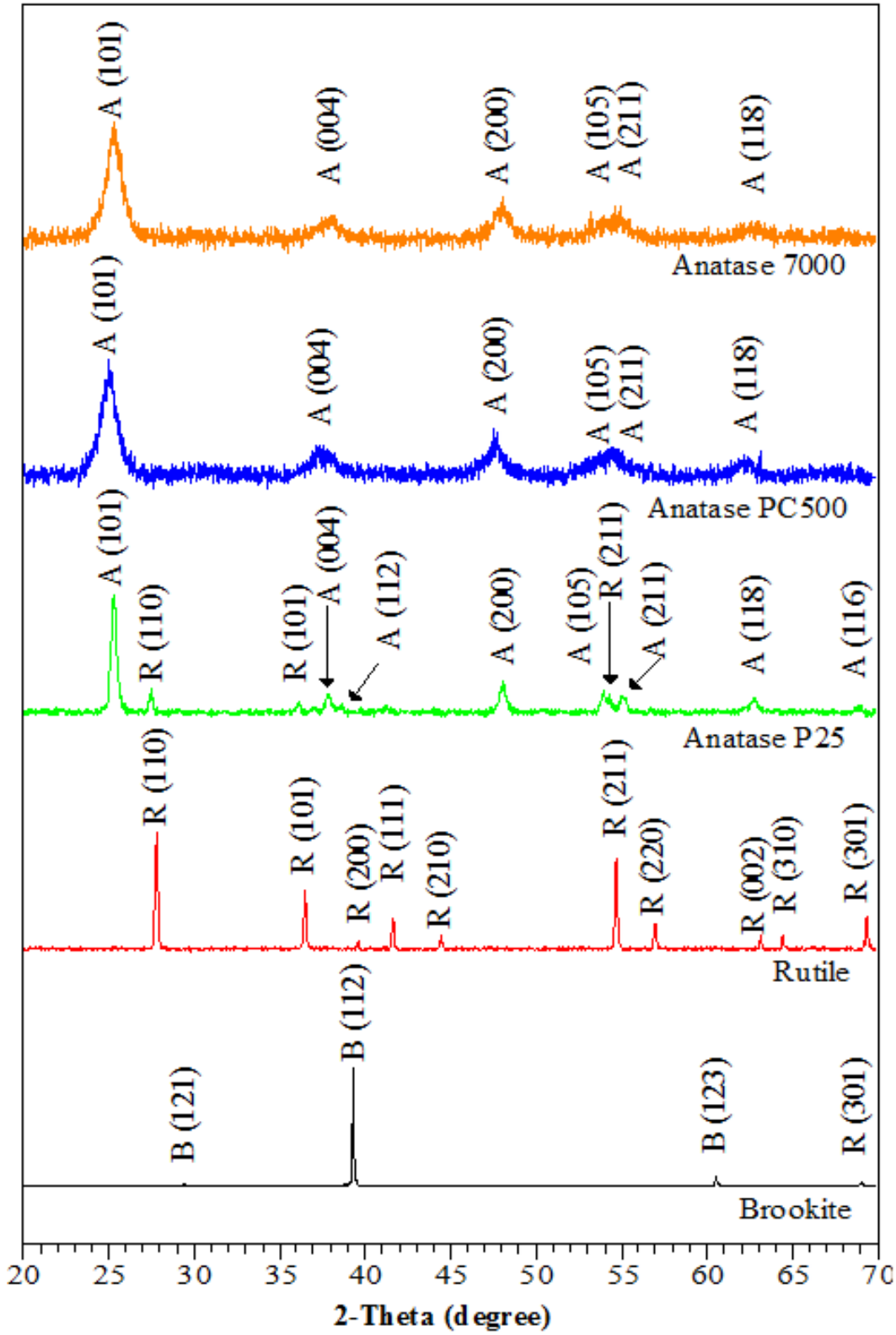

Figure 5.14 –X-ray diffractogram of brookite, rutile and anatase powders

Table 5.2 – d spacing extracted from the X-ray diffractogram of brookite, rutile and anatase powders

	Lattice plane	**7000** (Å)	**PC500** (Å)	**P25** (Å)	**Rutile** (Å)	**Brookite** (Å)
Anatase	(101)	3,502	3,496	3,518	-	-
	(004)	2,375	2,384	2,377	-	-
	(112)	-	-	2,486	-	-
	(200)	1,896	1,889	1,891	-	-
	(105)	1,684	1,675	1,699	-	-
	(211)	-	-	2,331	-	-
	(118)	1,485	1,483	1,480	-	-
	(116)	-	-	1,668	-	-
Rutile	(110)	-	-	3,245	3,200	-
	(101)	-	-	-	2,460	-
	(200)	-	-	-	2,276	-
	(111)	-	-	-	2,166	-
	(210)	-	-	-	2,037	-
	(211)	-	-	1,687	1,677	-
	(220)	-	-	-	1,614	-
	(002)	-	-	-	1,472	-
	(310)	-	-	-	1,445	-
	(301)	-	-	-	1,354	1,359
Brookite	(121)		-	-	-	3,028
	(112)	-	-	-	-	2,296
	(123)	-	-	-	-	1,529

In the case of anatase, P25 diffractogram is sharper than the PC500 and 7000, revealing more peaks that correspond to anatase. It also shows 12 % rutile (by comparing the maximum intensity of anatase crystallographic plane (101) with the maximum of rutile's (110)).

For PC500 and 7000, the number of peaks is fewer than P25; this is due to internal strains of the crystals and lattice defects broadening the peaks, and overlapped them.

Brookite does not show a typical diffractogram [19] as it was obtained from a single large crystal, showing only the reflection planes parallel to the sample´s surface, which verify Bragg's condition, displaying fewer peaks than expected.

From Scherrer´s Equation, the crystallite size was calculated from the most intense peaks for each powder. The values are listed in table 5.3 which compiles other results.

5.1.5 UV-Vis diffusive spectroscopy

UV-Visible reflectance of powders was measured from 250 to 800 nm for all the commercial powders. Figure 5.15 shows the reflectance of TiO_2 particles over a wavelength range on the abscissa. As it is shown, PC500 has a drop in the reflectance at 405 nm, 7000 at 377 nm, P25 at 381 and rutile shows it at 371 nm. For brookite, the reflectance has a decay at 378 nm.

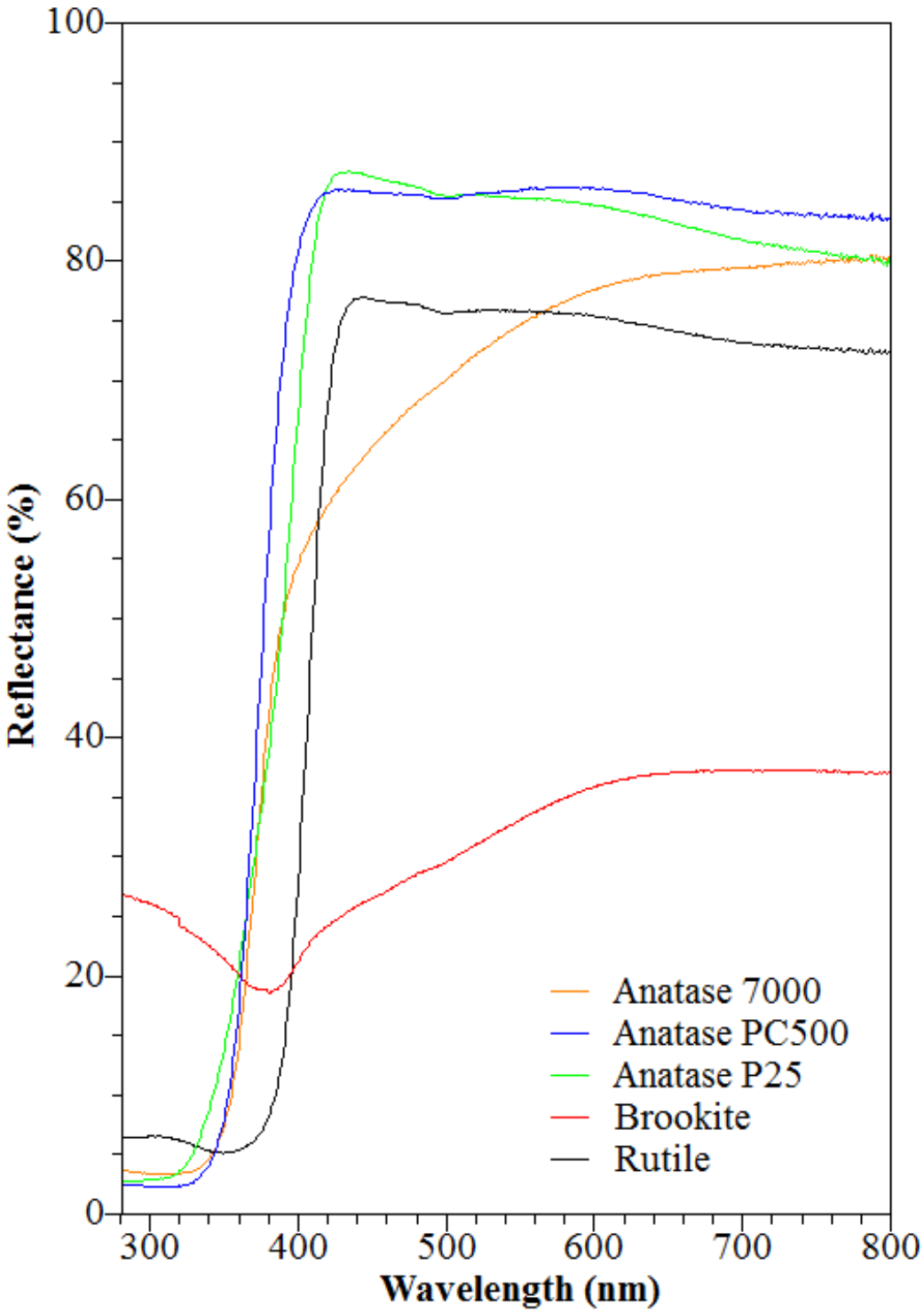

Figure 5.15 – Graphical representation of reflectance against wavelength for rutile, brookite and anatase powders

Table 5.3 compiles the calculated optical band gap, BET, average crystallite size (from XRD diffractogram using Scherrer's Equation) and average particle size calculated from TEM images. It also contains (when possible) particle size and BET from the material safety data sheets.

Table 5.3 – Particle size, BET and optical band gap for TiO_2 powders

	Particle size (nm)*	**Average particle size (nm)**	**Crystallite size(nm)**	**BET (m^2/g)***	**BET (m^2/g)**	**Band gap (eV)**
7000	15	<10	10.1	>250	225	3.37
PC500	5-10	20.8	9.5	350	312	3.35
P25	21	29.8	22.6	35-65	13	3.25
Rutile	500	402	50	-	3.3	3.00
Brookite	-	340	103	-	2	1.93

* From producer's datasheet

Particle size and BET results agreed with the information in the technical data sheets of anatase nanoparticles, and also with reported values in the literature [20]–[22]. 7000 showed an aggregation of nanoparticles, making it not possible to report an average particle size, as Figure 5.2 shows. It was determined the size of its nanoparticles was under 10 nm. Scherrer Equation's estimations are closed to the calculated values from TEM and FESEM. For the case of rutile, the estimated crystallite size was 50 nm. The explanation for the difference of an order of magnitude is a particle may be formed of different grains; the crystallite size is the size of those grains.

The estimated band gaps for anatase powders differ from each other; from 3.37 eV (for 7000) to 3.25 eV (for P25). Although those results show a small discrepancy in the band gap determination, previous researchers reported different values for P25 (3.10–3.15 eV) [21], [22]; as well as for 7000, carbon doped, with a band gap higher than 3.2 eV [23], [24]. PC500 also exhibits a wider band gap as it was expected for anatase, but as XPS revealed in table 5.1, as 7000, it also contains carbon, which would explain a higher gap. For PC500 and

7000 band gap, the optimum wavelength is 370 nm. Rutile's band gaps agree with the reported values [20], [25], [26]. For the case of brookite, 1.93 eV seems unrealistic in comparison with the reported values 3.1-3.4 eV [19], [25]. This is an approach from an optical technique to estimate an electronic property. In the case of brookite, this technique may not be sensitive enough due to reflectance attenuation caused for light absorption at low energies due to the surface quality. Therefore the linear fit to find the E_g will not be accurate due to lack of fitting.

5.1.6 Photocatalytic performance

The photocatalytic activity of the commercial powders was tested by following the dye degradation in aqueous phase and the degradation of NO_2 and CO_2 in gas phase under two different UV LEDs as described in Chapter Four.

5.1.6.1 Photocatalytic degradation of methylene blue

Three tests were undertaken for each TiO_2 powder; in the dark, to evaluate the amount of dye which was absorbed by the powders and two tests under UV light. Two different UV LEDs, described in Chapter Three were used separately to determine under which wavelength range TiO_2 was more effective.

Figure 5.16 shows the degradation of methylene blue for sixty minutes, and table 5.4 collates the dye removed per specimen at different light conditions.

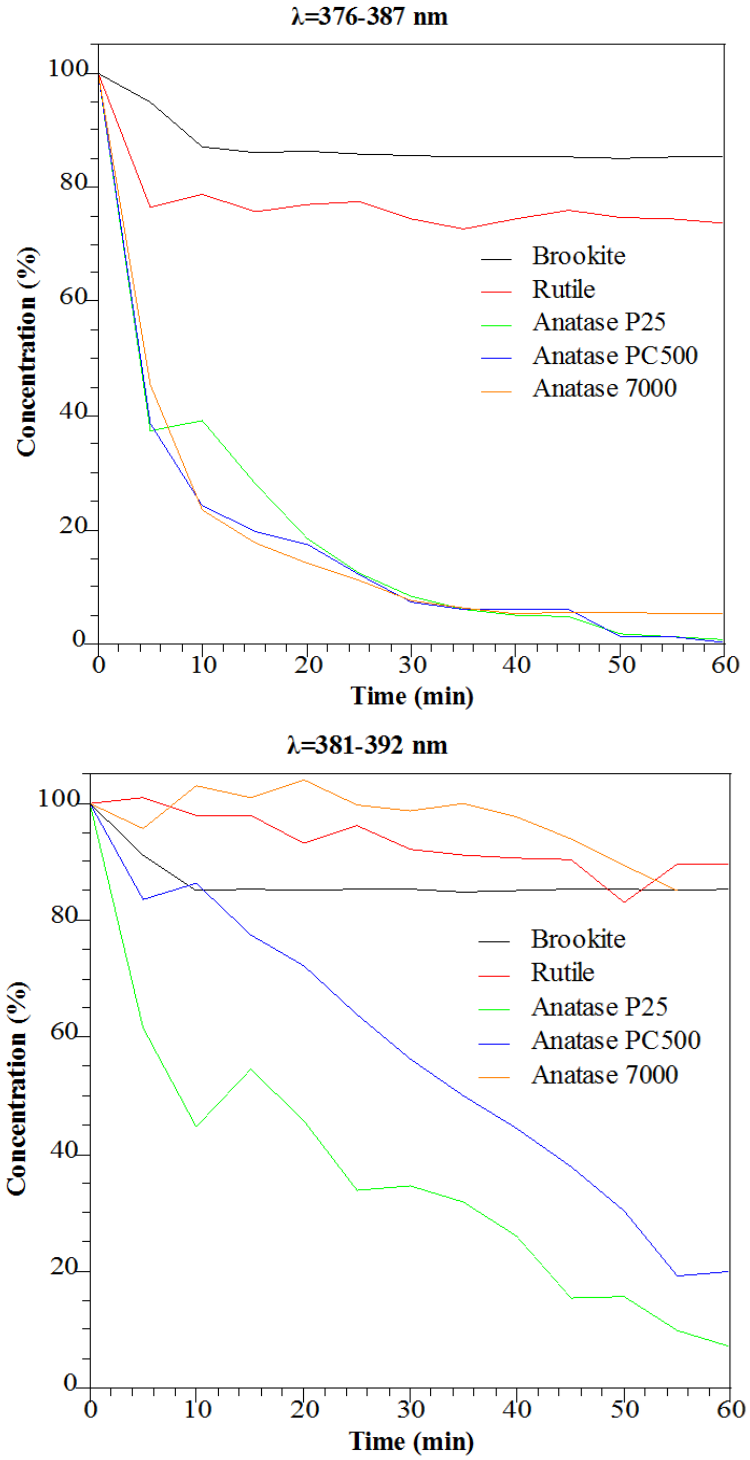

Figure 5.16 - Photo-reduction of aqueous solution of methylene blue irradiated under two different UV LED (I=4.7 W/m^2) for TiO_2 powders.

Table 5.4 – Percentage of absorbed and degraded dye after 60 min under two different UV LED and in the dark

	Absorbed dye (%) in the dark	**Degraded dye (%) under λ=376-387 nm**	**Degraded dye (%) under λ=381-392 nm**
7000	18.2	94.7	39.9
PC500	14.8	98.8	95.23
P25	18.2	99.8	92.8
Rutile	16.3	26.3	16.6
Brookite	15.2	14.7	14.8

Anatase P25 and PC500 successfully degraded more than 90 % of methylene blue under different UV light. In the case of 7000, the difference in its photoreactivity under different wavelengths is remarkable. Whereas the P25 band gap is in the 387 nm wavelength region, the PC500 and 7000 band gap are in the 370 nm region. This is the reason why under a wavelength range 381-392 nm 7000 was not able to degrade more than 40 % of dye; whereas under 376–387 nm degraded 95 % of methylene blue. Under the irradiation of the UV LED of 376–387 nm, 7000 received more photons with the required energy to initiate the photocatalytic process.

For rutile, if the percentage of absorbed dye is considered, it only worked under the UV LED with a wavelength of 381-392 nm, near to its band gap (413 nm) degrading less than 26 %. With a high particle size, low BET and a bandgap in the visible region, brookite did not show any photocatalytic property.

5.1.6.2 Photocatalytic degradation of gaseous pollutants

TiO_2 powders were compressed into pellets of 13 mm of diameter using a uniaxial press at 7 tons. Figures 5.17-5.20 show the fractional change of CO_2, NO_2 H_2O and O_2 related to Ar.

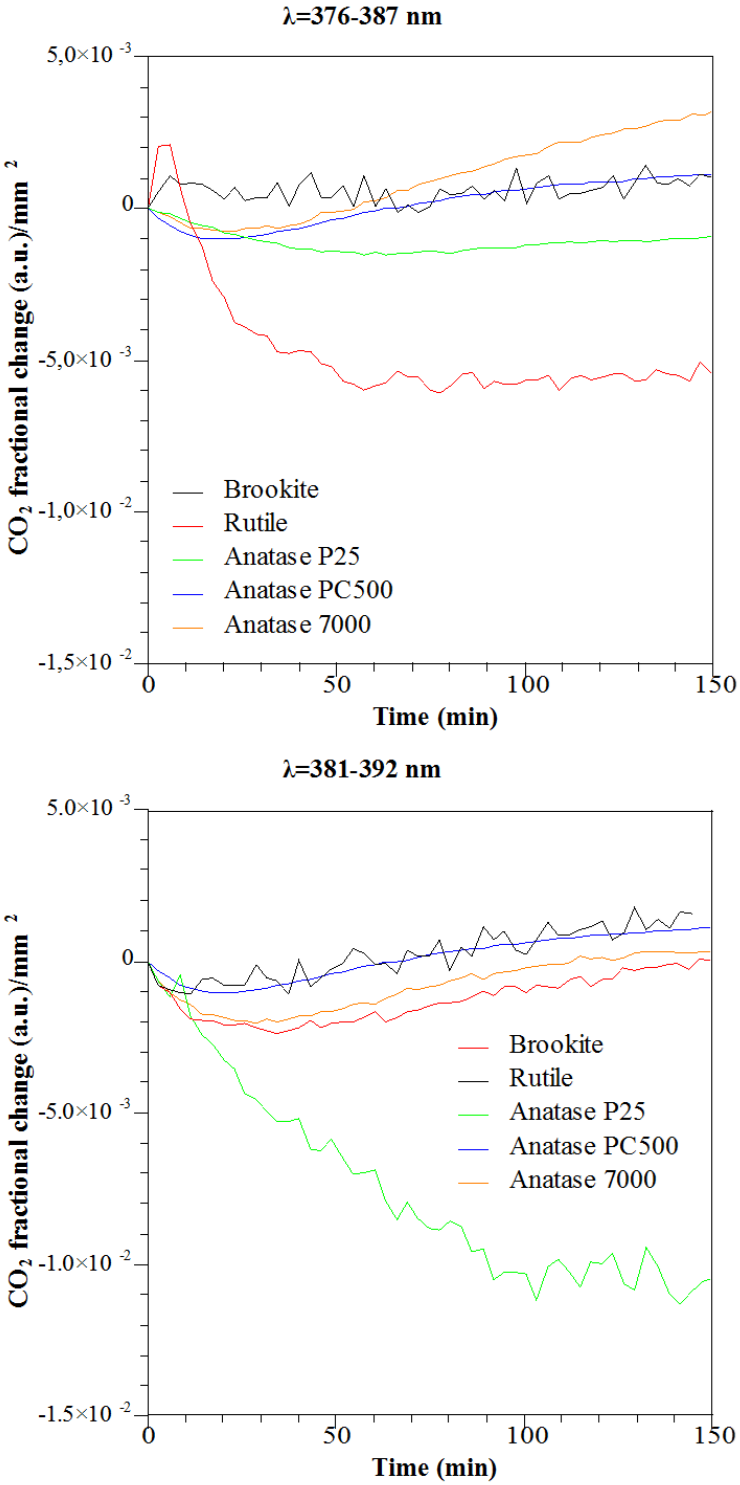

Figure 5.17 – Fractional reduction of CO_2 related to Ar over time irradiated under two different UV LED of wavelength of 376-387 nm and 381-392 nm (I=4.7 W/m^2)

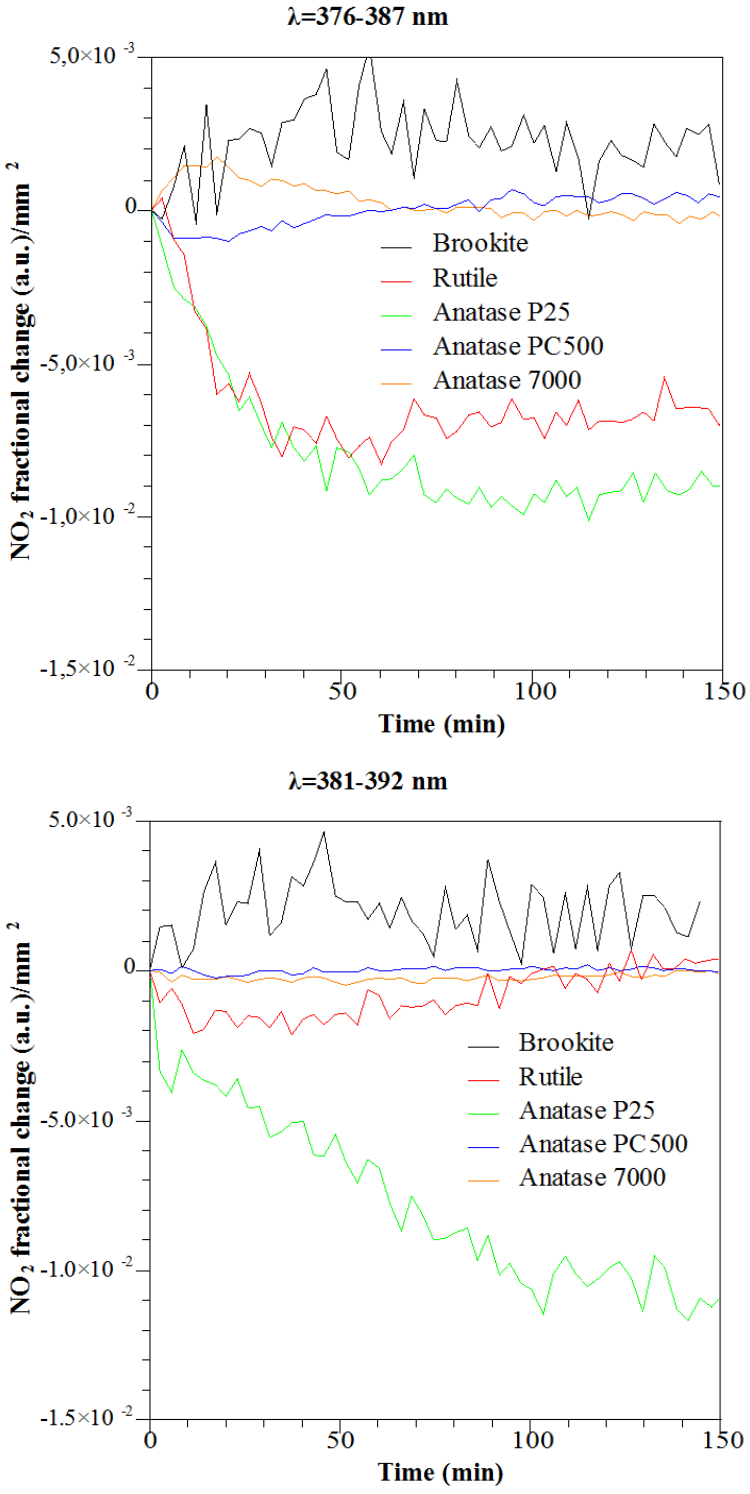

Figure 5.18 – Fractional reduction of NO_2 related to Ar over time irradiated under two different UV LED of wavelength of 376-387 nm and 381-392 nm (I=4.7 W/m^2)

The photocatalytic activity in the gas phase of the commercial powders was lower as the reactivity the powders exhibited in the aqueous phase. Whereas all the anatase powders were able to promote the reduction of methylene blue, not all the commercial anatase powders were able to degrade NO_2 and CO_2, only P25 removed those molecules successfully. Rutile, which was not effective in an aqueous solution, was able to remove CO_2 and NO_2 under UV irradiation. The fact that rutile exhibited a higher photocatalytic activity under the UV LED of wavelength of 376-387 nm corresponds to its band gap, which is held in the wavelength of 370 nm. Brookite, in the aqueous phase and gas phase, did not show any photocatalytic performance.

Based on the information provided in table 5.3, three different crystal phases of TiO_2 have been analysed, rutile and anatase being the only two with photocatalytic properties. From the photocatalytic TiO_2 powders, their sizes and physical properties differ from each other, from anatase 7000 with the smallest particle size and highest specific surface area, to rutile with the largest particle size and smaller specific surface area.

The media, in which those particles have been analysed, is critical. In the gas phase, the probability of direct contact of the TiO_2 surface with the molecules of interest (H_2O and O_2 to create radicals) and thereafter the collision of those radicals with NO_2 and CO_2 are much smaller than in aqueous phase.

For anatase PC500 and 7000, the high efficiency in the photodegradation of methylene blue is due to their low particle size and high specific surface area, which increase the contact of the exposed surface to H_2O and UV light. When those particles were analysed in gas phase, they showed a lower photon/e^--h^+ conversion yield, and were unable to promote a photocatalytic reaction under both LED exposure.

Figures 5.19 and 5.20 show the evolution with time of H_2O and O_2, which are required in the photocatalytic process to generate radicals. It can be observed how the decay of O_2 matches with the decomposition of CO_2 and H_2O does it with NO_2.

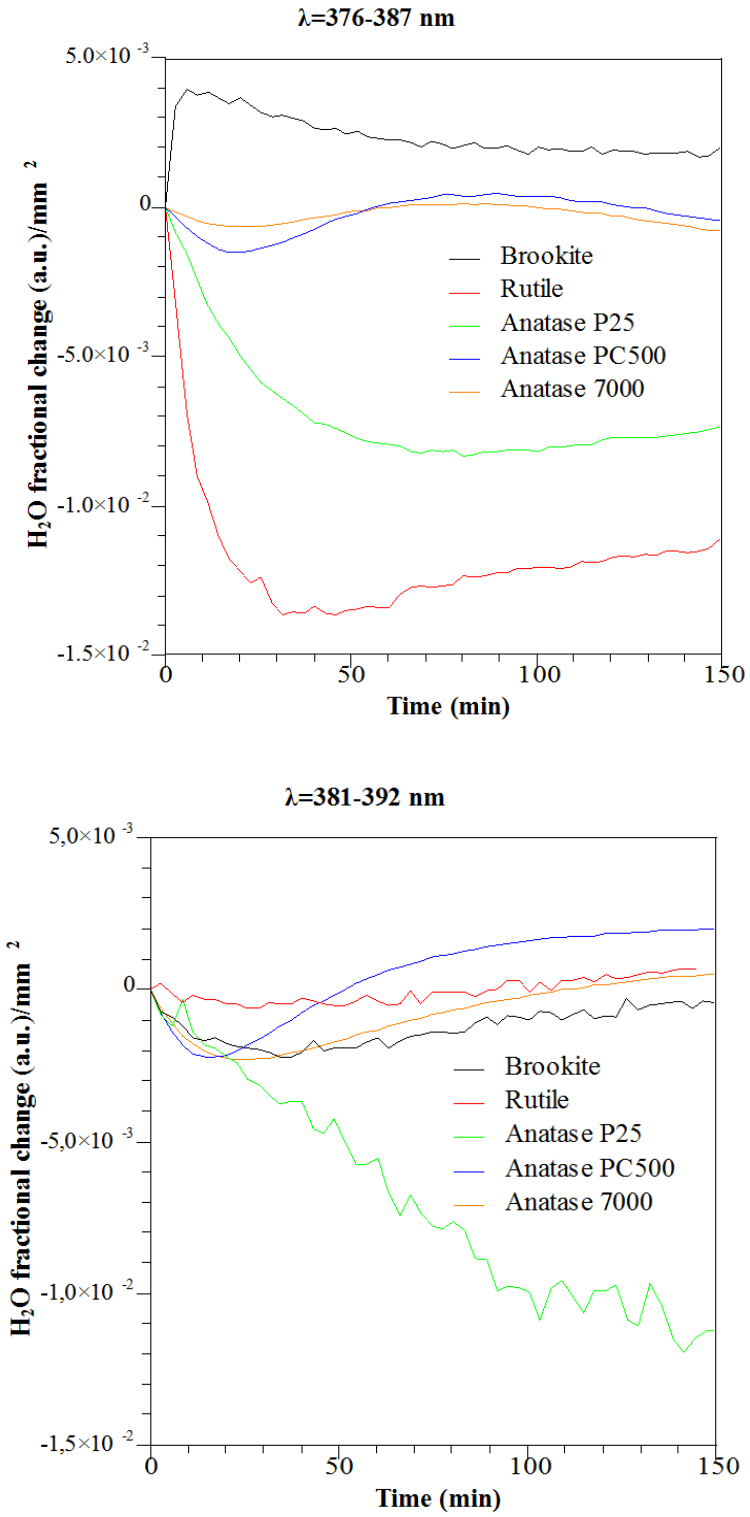

Figure 5.19 – Fractional reduction of H_2O related to Ar over time irradiated under two different UV LED of wavelength of 376-387 nm and 381-392 nm (I=4.7 W/m^2)

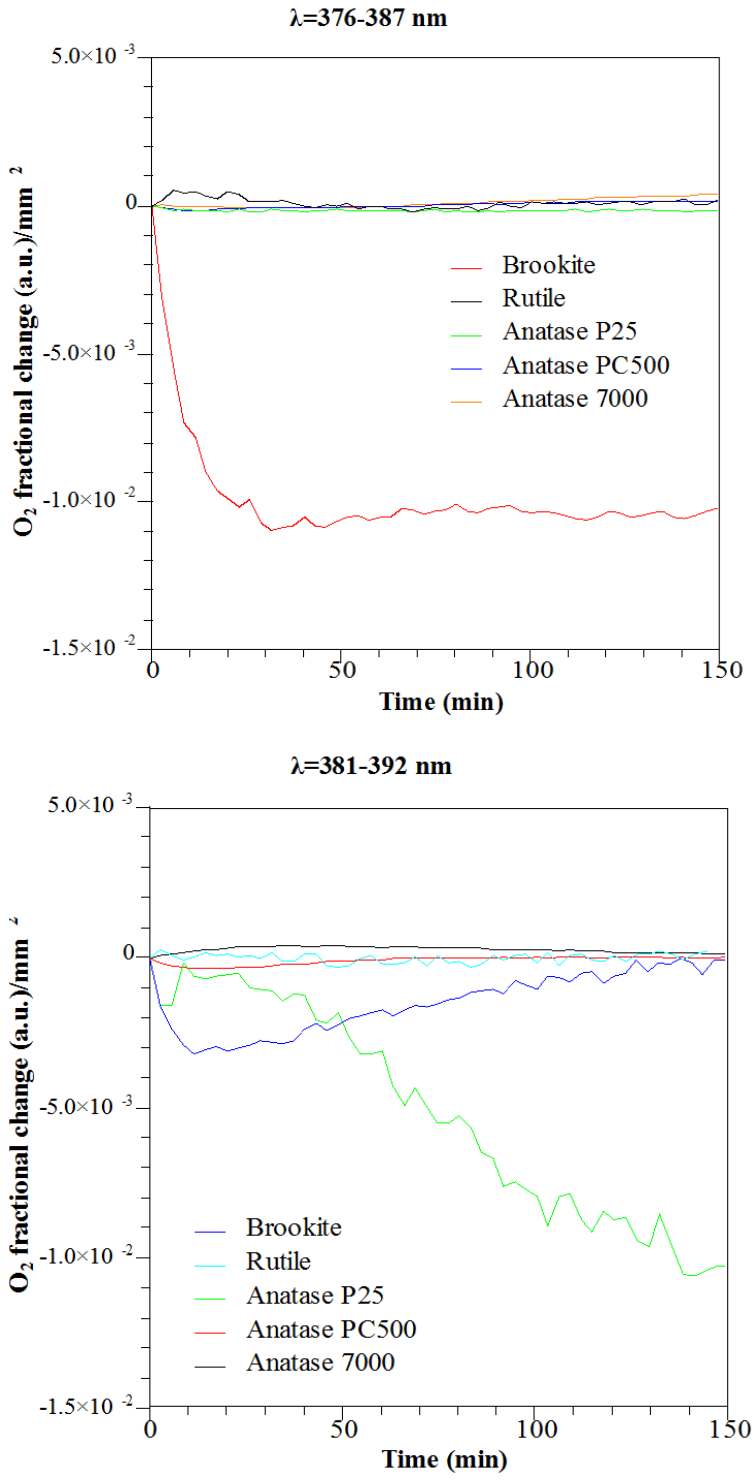

Figure 5.20 – Fractional reduction of O_2 related to Ar over time irradiated under two different UV LED of wavelength of 376-387 nm and 381-392 nm (I=4.7 W/m^2)

The reaction of NO_2 and H_2O promoted by TiO_2 under UV light has been previously reported, forming HNO_3 as a product of the reaction [27]–[30]. Under 376-387 nm, the removal of gas phase NO_2 was observed alongside with H_2O. Whereas by irradiating under 381-392 nm, in addition to NO_2 and H_2O being removed from the atmosphere, O_2 and CO_2 are also consumed in the same ratio.

This can be explained by anatase's band gap of 3.2 eV [26], [30], which is held in the range of the UV LED of wavelength range of 381-392 nm, as Figure 4.18 shows. This difference in energy would be sufficient to promote the radicalization of O_2 and, subsequently the reaction with CO_2.

The proposed mechanisms for CO_2 removal suggest that the molecule anchors on the photocatalyst´s surface, reducing CO_2 into CO and finally into C, desorbing CO and O [31], [32]. This mechanism would not explain the consumption of O_2. Nonetheless, if CO_2 anchors as Figure 5.21 shows, the oxidation of CO_2 in presence of $O_2^{\bullet-}$ on the TiO_2 surface would be feasible.

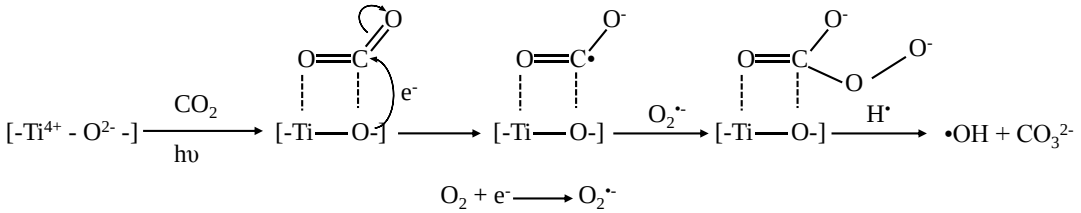

Figure 5.21 – Proposed mechanism of photo-oxidation of CO_2

5.2 Commercial coatings

Foret FMC kindly provided different commercial coatings, of which four were subjected to study. Due to their form, four different types of photocatalytic coatings were tested:

i. *Bionictile©* is a ceramic tile with a glass cover coated with TiO_2 [referred as **Bionictile**]
ii. *TiO_2 powder coating*. A thermal paint formulated with anatase and additional polymers and resins. An aluminium plate was used as substrate to deposit TiO_2 based paint [referred as **TiO_2 powder coating**]
iii. *Lafarge cement render with 3 % $OFFNO_x$* in its formulation. $OFFNO_x$ is a photocatalytic formulation based on anatase which was added as active compound [referred as **cement render**]
iv. *TiO_2 mesh* for air filter [referred as **TiO_2 mesh**]

Due to commercial confidentiality, further information of the products was not available. Therefore a full characterisation was required to understand and correlate their photocatalytic activity with their composition and morphology.

5.2.1 Electron microscopy

The microstructure of TiO_2 coatings was studied using SEM to characterise them at different magnifications.

5.2.1.1 Bionictile©

BionicTile is a ceramic tile with a glass cover coated with TiO_2. It is available in ceramic tiles for building construction, with a visible uneven texture as Figure 5.22 shows. The coating morphology was developed to reproduce the texture of leaves, with the intention to maximise the exposed area as Figure 5.23 shows. SEM images show an irregular surface leads to a high surface area due to a microporous structure. Raman spectra revealed the presence of TiO_2 but due to the presence of $CaCO_3$, the peaks were hidden under fluorescence signal.

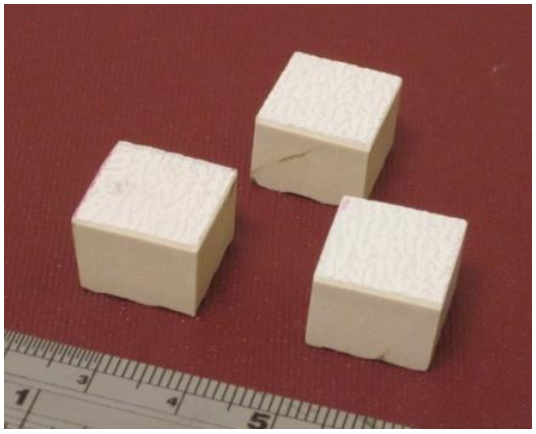

Figure 5.22 – Photography of Bionictile

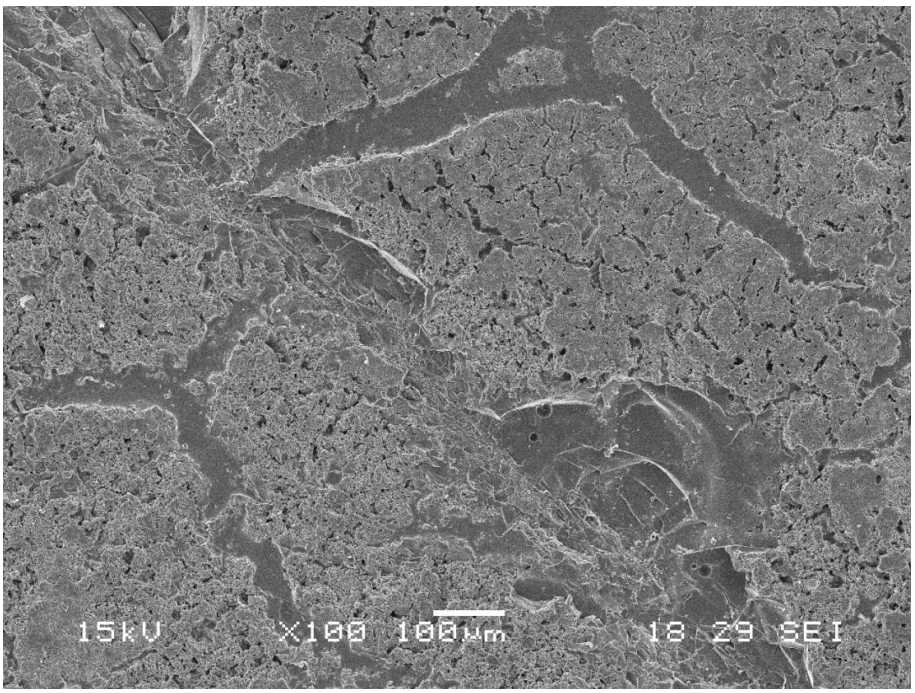

Figure 5.23 – SEM image of Bionictile

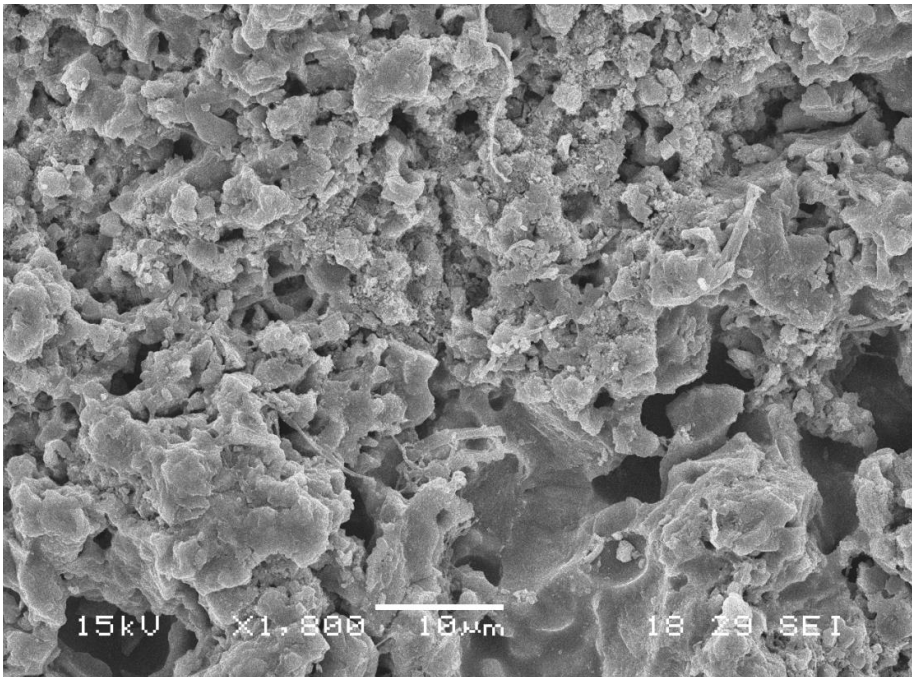

Figure 5.24 – SEM image of Bionictile

5.2.1.2 TiO_2 powder coating

Adapta is a thermal paint formulated with anatase as a photocatalyst with additional polymers and resins. This paint was developed to provide a self-cleaning surface after its application. Figures 5.25-5.27 show 3 images of this paint at different magnifications, with a uniform distribution of the coating over the aluminium substrate. Figure 5.26 shows a flake deposited on carbon tape, and Figure 5.27 shows a void in the coating, where it can be observed how the coating is composed.

Figure 5.25 – Photography of an aluminium plate with TiO_2 powder coating

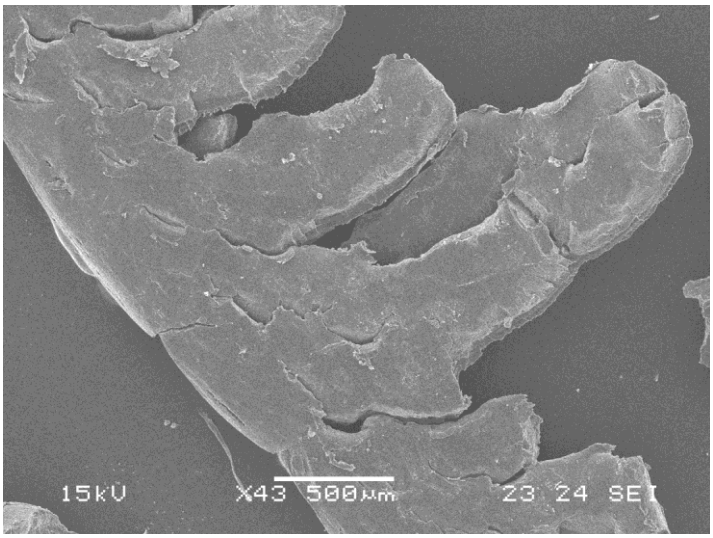

Figure 5.26 – SEM image of TiO_2 powder coating

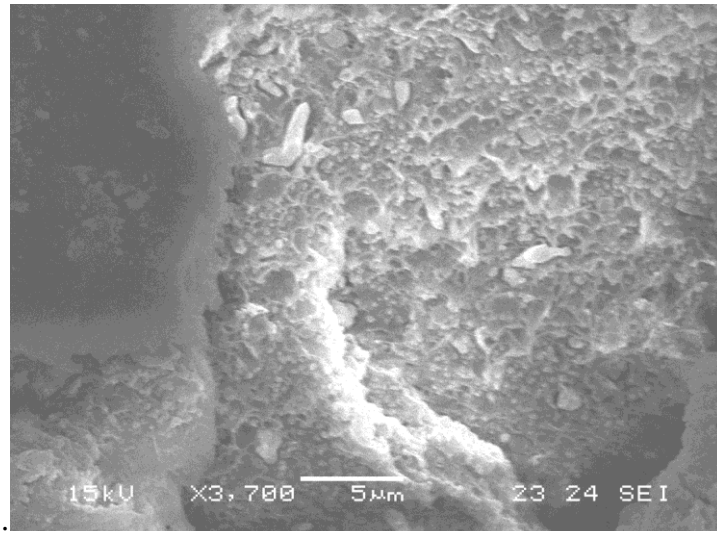

Figure 5.27 – SEM image of TiO_2 powder coating

5.2.1.3 Cement render

The cement render, in addition to fine sand, cement and lime, also contains 3 % photocatalytic additive called OFFNO$_x$. This additive is based on TiO_2. The porosity of the material gives it a high surface area compared to other coatings.

Figure 5.28 – Photography of cement render

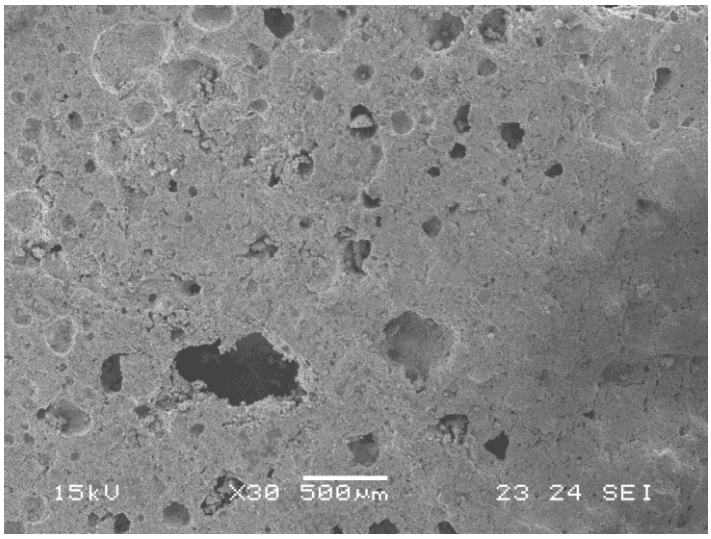

Figure 5.29 – SEM image of cement render

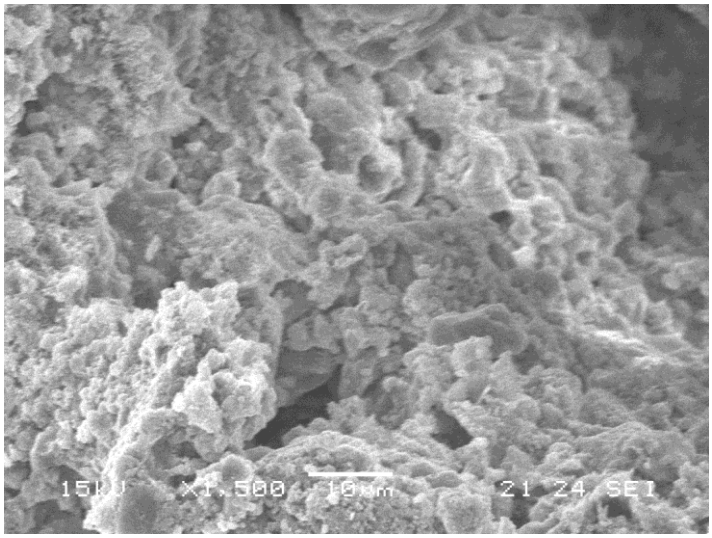

Figure 5.30 – SEM image of cement render

5.2.1.4 TiO_2 mesh

This TiO_2 mesh was designed for air filtration applications. It is made from a titanium grid electrolytic passivated to TiO_2. As Figures 5.32 and 5.33 show, its surface is uniformly coated with TiO_2.

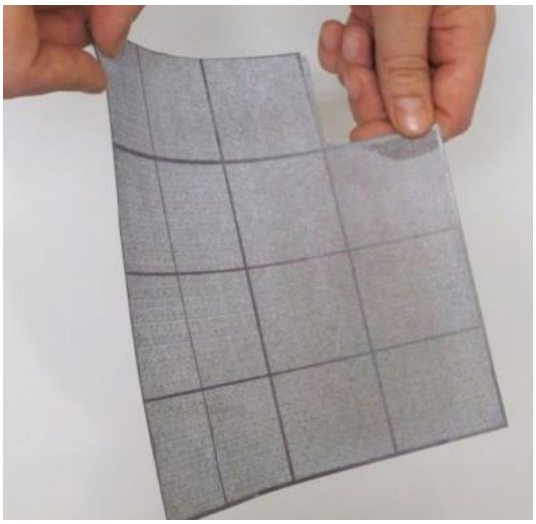

Figure 5.31 – Photography of TiO_2 mesh

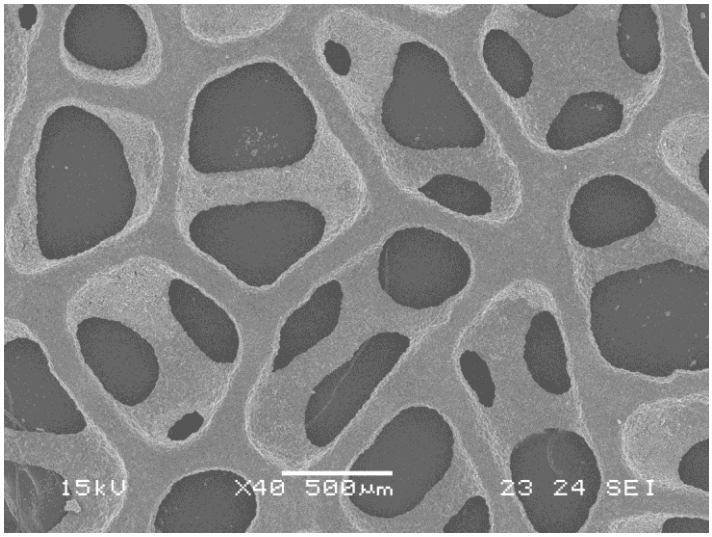

Figure 5.32 – SEM image of TiO_2 mesh at x500 magnification

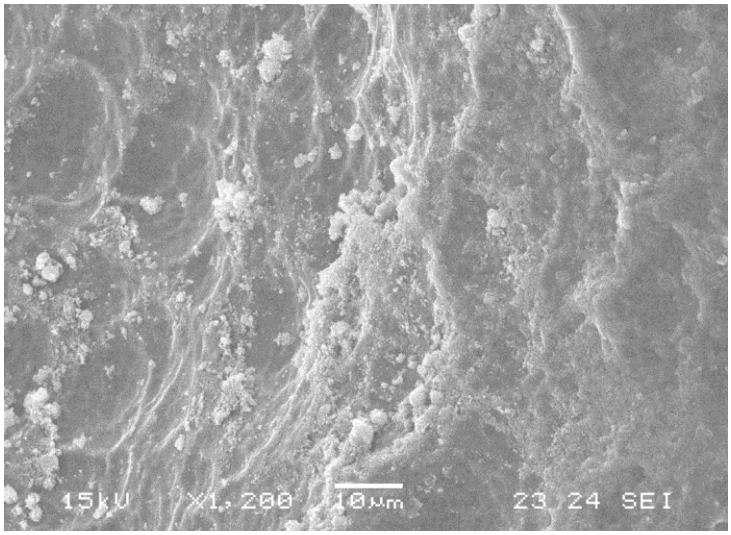

Figure 5.33 – SEM image of TiO_2 mesh at x1200 magnification

5.2.2 X-ray photoelectron spectroscopy

XPS data is presented in and table 5.5 and shows the binding energies and elemental ratios for carbon, oxygen, sodium, calcium, silicon and titanium, calculated to higher resolution spectra in specific regions for the commercial powders.

As table 5.5 shows, thermal powder coating and the TiO_2 mesh show the highest concentration of titanium on their surfaces, whereas Bionictile presented a concentration of TiO_2 under the detection limit of the instrument (0.01% atomic percentage). The presence of other additives, such as SiO_2, Al_2O_3 or $CaCO_3$ agrees with the technical description of the materials.

Table 5.5 - Element ratios and chemical state derived from XPS analysis

Specimen ID	**Binding energy (eV) /** Relative concentration (at. %)									
	C 1s	**Na 1s**	**O 1s**		**Ca 2p ($CaCO_3$)**		**Si 2p (SiO_2)**	**Al 2p (Al_2O_3)**	**Ti 2p (TiO_2)**	
	CO_3^{2-}		**Oxides**	**CO_3^{2-}**	**Ca $2p_{3/2}$**	**Ca $2p_{1/2}$**	**Si 2p**		**Ti $2p_{3/2}$**	**Ti $2p_{1/2}$**
Bionictile	**290.0**/18.8	**1067.5**/17.4	**531.4**/38.4	-	**347.2**/17.4	**351.0**/6.1	-	71.4/1.7	-	-
Powder coating	**288.3**/31.9	**1074.1**/1.9	**533.0**/47.4	**531.3**/5.1	**350.3**/0.4	**353.8**/0.2	**102.0**/2.8	-	**461.8**/7.0	**467.5**/3.4
TiO_2 Mesh	**289.3**/18.7	-	**529.4**/31.4	**531.2**/34.4	-	-	-	-	**458.2**/10.6	**464.0**/4.9
Mortar	**289.3**/13.1	**1071.6**/1.1	**531.5**/67.0	-	**347.0**/8.7	**350.6**/4.2	**102.7**/4.5	**74.28**/1.1	**458.5**/0.15	**463.6**/0.1

5.2.3 Photocatalytic performance

5.2.3.1 Photocatalytic degradation of methylene blue

Figure 5.34 shows the degradation rate of methylene blue for the different samples. Samples were held centred in the glass reactor using an alligator clip to keep them 3 cm from the magnetic stirrer. As Figure 5.34 shows, none of the coatings were able to degrade methylene blue. In comparison with the test performed with TiO_2 powders, where TiO_2 particles are suspended in solution; commercial coatings show small exposed areas. Another test in the dark was undertaken to distinguish between the percentage of dye that was absorbed by the sample to the percentage of dye that was degraded. For the case of the cement render, the absorption of methylene blue after 60 min was of 16%. Therefore, the reduction that was observed under UV irradiation is due to the absorbed dye.

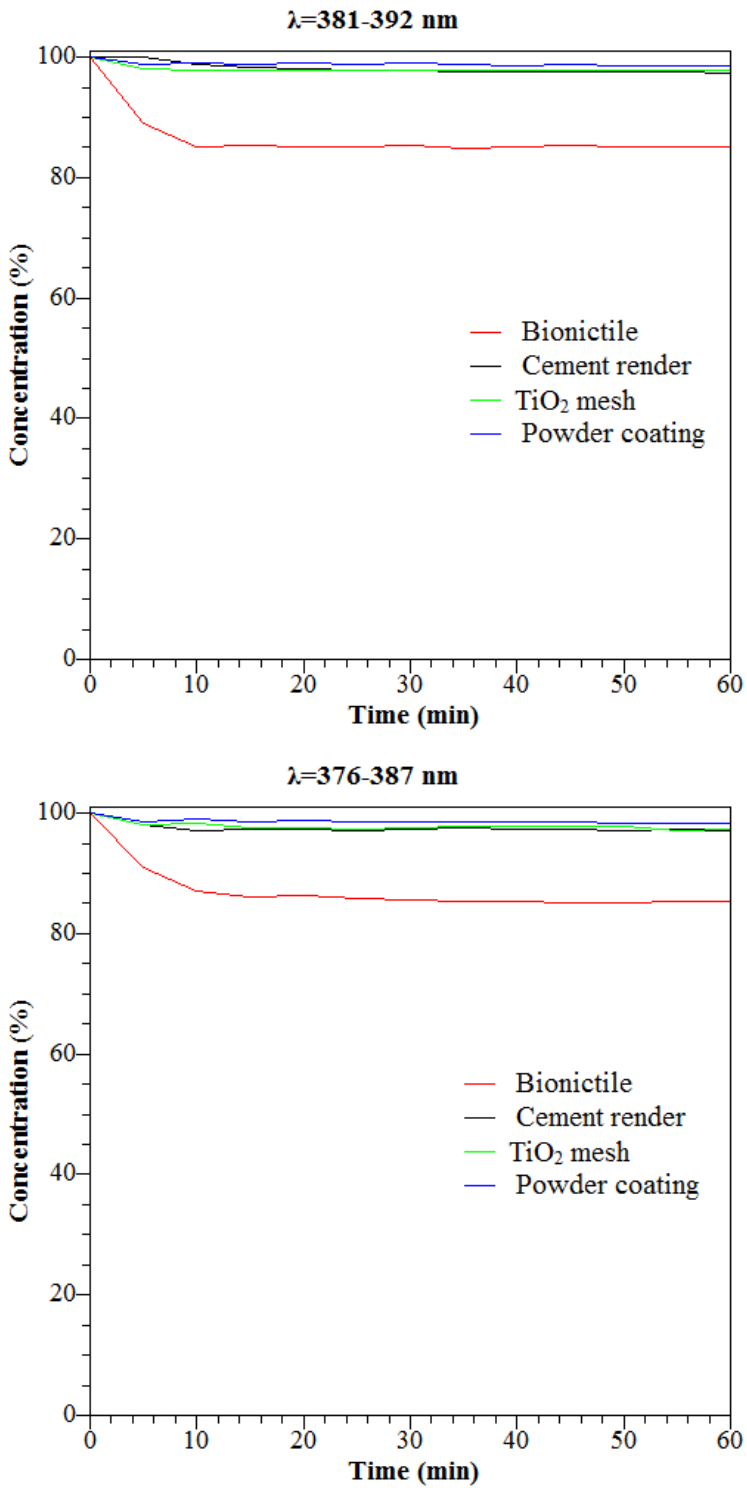

Figure 5.34- Photo-reduction of aqueous solution of methylene blue under different UV LED (I=4.7 W/m^2) for commercial TiO_2 coatings.

5.2.3.2 Photocatalytic degradation of gaseous pollutants

Sections of 1.5 × 1.5 cm were cut from the samples and analysed their photocatalytic activity in gas phase. As Figures 5.35 and 5.36 show, none of the commercial coatings were able to remove neither CO_2 nor NO_2.

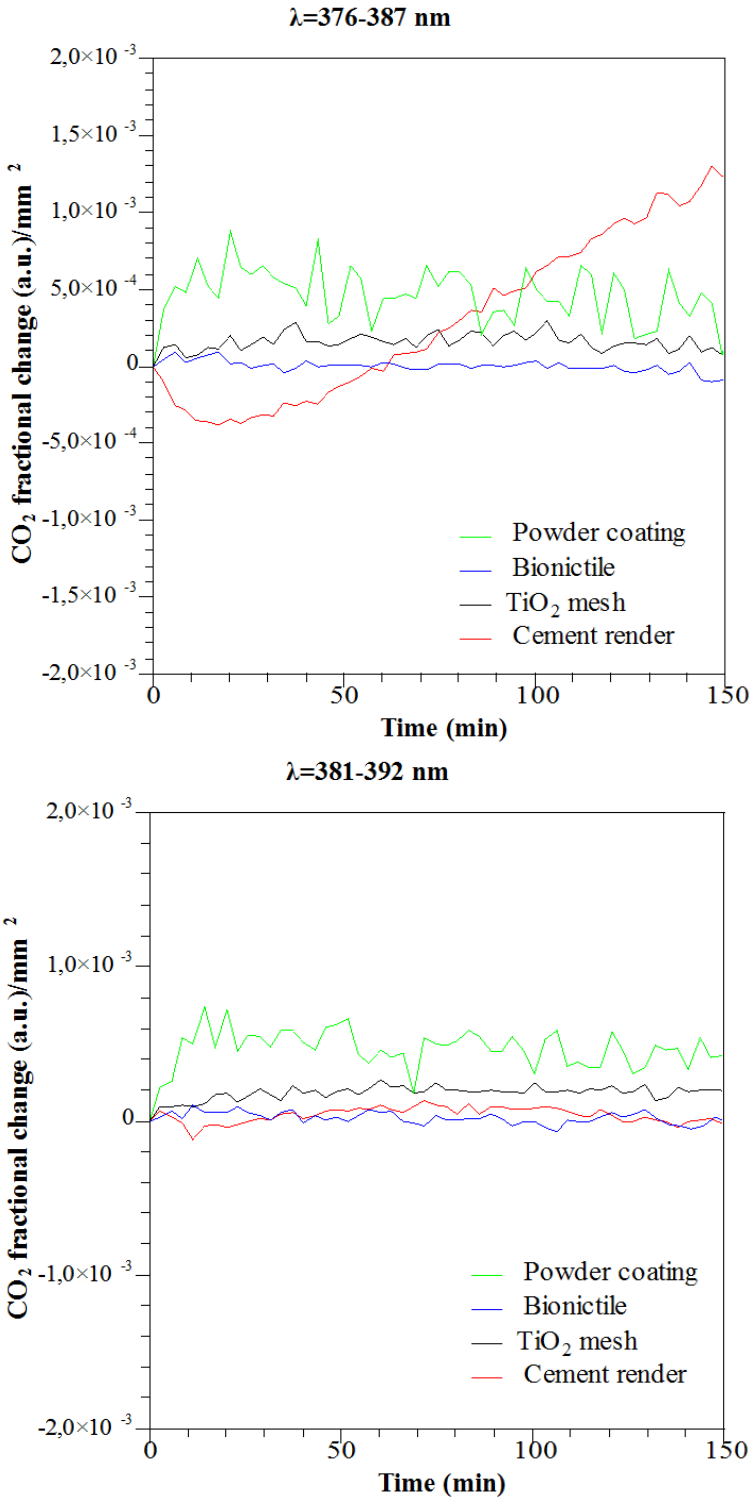

Figure 5.35 - Fractional reduction of CO_2 related to Ar over time under different conditions

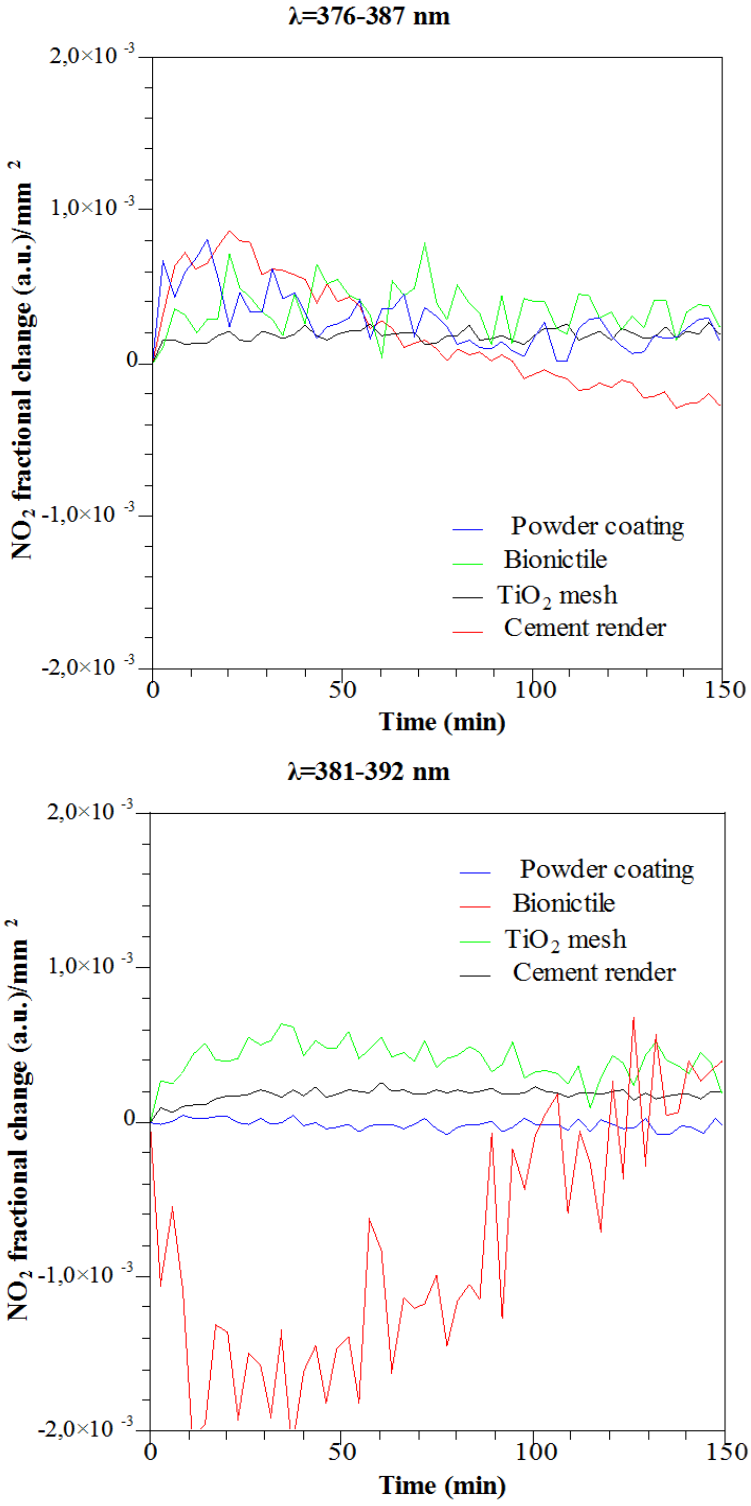

Figure 5.36 - Fractional reduction of NO_2 related to Ar over time under different conditions

5.2.3.3 Case of study, BionicTile

BionicTile's glass surface was ideal for a further surface analysis, which involved bacteria. *E. coli* was used (as Chapter Three describes) to determine microcyde properties of photocatalytic coatings. Also, Bionictile was able to resist the conditions of an autoclave (120 ◦C), which was a requirement for the experiment. Another ceramic tile with a glass coating was used as reference standard, since both tiles were manufactured by the same company under the same conditions. Figure 5.37 shows how tiles of 15 mm x 15 mm of area were distributed during UV irradiation.

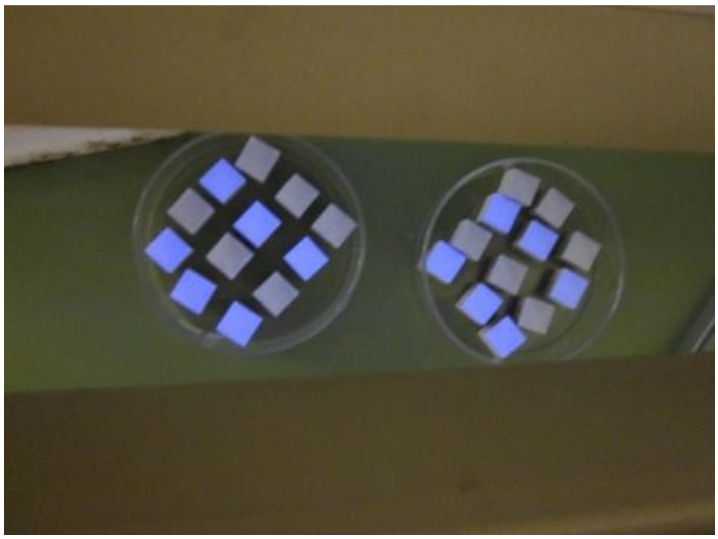

Figure 5.37 – Photography of glass tiles (blue) and Bionictiles (white) during UV exposure with a solution of *E. coli* on their surfaces

Figure 5.38 shows how Bionictile was able to kill 56 % of *E. coli* within 15 min, whereas the glass tile under UV irradiation did not affect the *E. coli* survival. Although the XPS analysis done on Bionictile did not reveal a detectable amount of TiO_2, this technique shows information from the outermost layer of a material, which can explain why TiO_2 was not detected. In comparison with the methylene blue test, this test was undertaken with a small amount of solution (75 µl) and very concentrated. Therefore the amount of *E. coli* is smaller than the dye.

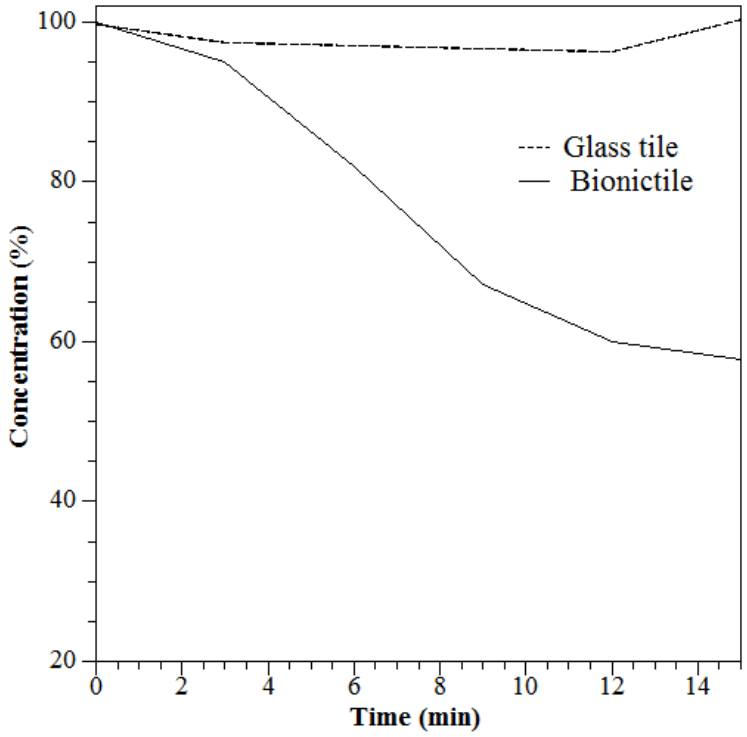

Figure 5.38 – *E. coli* deactivation under UV halogen lamp with a wavelength range of 364-383 nm with an intensity of 0.322 W/m^2

5.3 Summary

From three commercial available anatase powders, Aeroxide P25 proved to be the most efficient photocatalyst, in aqueous phase as well as gas phase. Rutile, the most stable polymorph also showed photocatalytic activity, whereas brookite was not able to promote a photocatalytic reaction.

The removal of NO_2 in presence of H_2O, with HNO_3 as product was observed. The capability of TiO_2 to decompose CO_2 in presence of O_2 was also noted.

From the preliminary tests done with commercial coatings, it was found that TiO_2 was not the main component on the surface. None of them worked in aqueous phase or in gas phase against NO_2 and CO_2. Bionictile was used to test the biocide properties of a photocatalytic coating against *E. coli*, being able to remove 56 % of the CFU within 15 min.

5.4 Bibliography

[1] Y. Zhang, C. X. Harris, P. Wallenmeyer, J. Murowchick, and X. Chen, "Asymmetric lattice vibrational characteristics of rutile TiO_2 as revealed by laser power dependent Raman spectroscopy," *J. Phys. Chem. C*, vol. 117, no. 45, pp. 24015–24022. 2013.

[2] T. Lan, X. Tang, and B. Fultz, "Phonon anharmonicity of rutile TiO_2 studied by Raman spectrometry and molecular dynamics simulations," *Phys. Rev. B*, vol. 85, no. 9, p. 094305. 2012.

[3] G. A. Samara and P. S. Peercy, "Pressure and Temperature Dependence of the Static Dielectric Constants and Raman Spectra of TiO_2 (Rutile)," *Phys. Rev. B*, vol. 7, no. 3, pp. 1131–1148. 1973.

[4] M. Rezaee, S. M. Mousavi Khoie, and K. H. Liu, "The role of brookite in mechanical activation of anatase-to-rutile transformation of nanocrystalline TiO_2: An XRD and Raman spectroscopy investigation," *Cryst. Eng. Comm.*, vol. 13, no. 16, p. 5055, 2011.

[5] W. F. Zhang, Y. L. He, M. S. Zhang, Z. Yin, and Q. Chen, "Raman scattering study on anatase TiO_2 nanocrystals," *J. Phys. D. Appl. Phys.*, vol. 33, no. 8, p. 912, 2000.

[6] T. Ohsaka, F. Izumi, and Y. Fujiki, "Raman spectrum of anatase, TiO_2," *J. Raman Spectrosc.*, vol. 7, no. 6, pp. 321–324. 1978.

[7] G. A. Tompsett, G. A. Bowmaker, R. P. Cooney, J. B. Metson, K. A. Rodgers, and J. M. Seakins, "The Raman spectrum of brookite, TiO_2 (Pbca, $Z = 8$)," *J. Raman Spectrosc.*, vol. 26, no. 1, pp. 57–62. 1995.

[8] M. N. Iliev, V. G. Hadjiev, and A. P. Litvinchuk, "Raman and infrared spectra of brookite (TiO_2): Experiment and theory," *Vib. Spectrosc.*, vol. 64, pp. 148–152. 2013.

[9] G. Meinhold, "Rutile and its applications in earth sciences," *Earth-Science Rev.*, vol. 102, no. 1–2, pp. 1–28, 2010.

[10] A. P. Dementjev, "Altered layer as sensitive initial chemical state indicator∗," *J. Vac. Sci. Technol. A Vacuum, Surfaces, Film.*, vol. 12, no. 2, p. 423. 1994.

[11] B. Erdem, R. A. Hunsicker, G. W. Simmons, E. D. Sudol, V. L. Dimonie, and M. S. El-Aasser, "XPS and FTIR Surface Characterisation of TiO_2 Particles Used in Polymer Encapsulation," *Langmuir*, vol. 17, no. 9, pp. 2664–2669. 2001.

[12] I.-C. Kang, Q. Zhang, S. Yin, T. Sato, and F. Saito, "Preparation of a visible sensitive carbon doped TiO_2 photo-catalyst by grinding TiO_2 with ethanol and heating treatment," *Appl. Catal. B Environ.*, vol. 80, no. 1–2, pp. 81–87. 2008.

[13] B. Demri and D. Muster, "XPS study of some calcium compounds," *J. Mater. Process. Technol.*, vol. 55, no. 3–4, pp. 311–314. 1995.

[14] S. L. Stipp and M. F. Hochella, "Structure and bonding environments at the calcite surface as observed with X-ray photoelectron spectroscopy (XPS) and low energy electron diffraction (LEED)," *Geochim. Cosmochim. Acta*, vol. 55, no. 6, pp. 1723–1736. 1991.

[15] T. Gross, M. Ramm, H. Sonntag, W. Unger, H. M. Weijers, and E. H. Adem, "An XPS analysis of different SiO_2 modifications employing a C 1s as well as an Au $4f_{7/2}$ static charge reference," *Surf. Interface Anal.*, vol. 18, no. 1, pp. 59–64. 1992.

[16] R. J. T. and P. K. S. and R. G. K. and R. V Jasra, "Photocatalytic degradation of dyes and organic contaminants in water using nanocrystalline anatase and rutile TiO_2," *Sci. Technol. Adv. Mater.*, vol. 8, no. 6, p. 455, 2007.

[17] Y. F. You, C. H. Xu, S. S. Xu, S. Cao, J. P. Wang, Y. B. Huang, and S. Q. Shi, "Structural characterisation and optical property of TiO_2 powders prepared by the sol–gel method," *Ceram. Int.*, vol. 40, no. 6, pp. 8659–8666. 2014.

[18] B. K. Mutuma, G. N. Shao, W. D. Kim, and H. T. Kim, "Sol-gel synthesis of mesoporous anatase-brookite and anatase-brookite-rutile TiO_2 nanoparticles and their photocatalytic properties.," *J. Colloid Interface Sci.*, vol. 442, pp. 1–7. 2015.

[19] A. Di Paola, G. Cufalo, M. Addamo, M. Bellardita, R. Campostrini, M. Ischia, R. Ceccato, and L. Palmisano, "Photocatalytic activity of nanocrystalline TiO_2 (brookite, rutile and brookite-based) powders prepared by thermohydrolysis of $TiCl_4$ in aqueous chloride solutions," *Colloids Surfaces A Physicochem. Eng. Asp.*, vol. 317, no. 1–3, pp. 366–376, 2008.

[20] M. Kete, E. Pavlica, F. Fresno, G. Bratina, and U. Štangar, "Highly active photocatalytic coatings prepared by a low-temperature method," *Environ. Sci. Pollut. Res.*, vol. 21, no. 19, pp. 11238–11249, 2014.

[21] K. Nagaveni, M. S. Hegde, N. Ravishankar, G. N. Subbanna, and G. Madras, "Synthesis and Structure of Nanocrystalline TiO_2 with Lower Band Gap Showing High Photocatalytic Activity," *Langmuir*, vol. 20, no. 7, pp. 2900–2907. 2004.

[22] R. López and R. Gómez, "Band-gap energy estimation from diffuse reflectance measurements on sol–gel and commercial TiO_2: a comparative study," *J. Sol-Gel Sci. Technol.*, vol. 61, no. 1, pp. 1–7, 2012.

[23] T. M. Triantis, T. Fotiou, T. Kaloudis, A. G. Kontos, P. Falaras, D. D. Dionysiou, M. Pelaez, and A. Hiskia, "Photocatalytic degradation and mineralization of microcystin-LR under UV-A, solar and visible light using nanostructured nitrogen doped TiO_2.," *J. Hazard. Mater.*, vol. 211–212, pp. 196–202. 2012.

[24] A. Manassero, M. L. Satuf, and O. M. Alfano, "Evaluation of UV and visible light activity of TiO_2 catalysts for water remediation," *Chem. Eng. J.*, vol. 225, pp. 378–386. 2013.

[25] D. Reyes-Coronado, G. Rodríguez-Gattorno, M. E. Espinosa-Pesqueira, C. Cab, R. de Coss, and G. Oskam, "Phase-pure TiO_2 nanoparticles: anatase, brookite and rutile," *Nanotechnology*, vol. 19, no. 14, p. 145605, 2008.

[26] K. Madhusudan Reddy, S. V Manorama, and A. Ramachandra Reddy, "Band gap studies on anatase titanium dioxide nanoparticles," *Mater. Chem. Phys.*, vol. 78, no. 1, pp. 239–245. 2003.

[27] S. Daito, T. Watanabe, and F. Tochikubo, "NO_x removal process in pulsed corona discharge combined with TiO_2 photocatalyst," *Jpn. J. Appl. Phys.*, vol. 40, no. 4R, p. 2475, 2001.

[28] N. Negishi, K. Takeuchi, and T. Ibusuki, "Surface structure of the TiO_2 thin film photocatalyst," *J. Mater. Sci.*, vol. 33, no. 24, pp. 5789–5794, 1998.

[29] Y. Bedjanian and A. El Zein, "Interaction of NO_2 with TiO_2 surface under UV irradiation: Products study," *J. Phys. Chem. A*, vol. 116, no. 7, pp. 1758–1764. 2012.

[30] Y.-M. Lin, Y.-H. Tseng, J.-H. Huang, C. C. Chao, C.-C. Chen, and I. Wang, "Photocatalytic activity for degradation of nitrogen oxides over visible light responsive titania-based photocatalysts," *Environ. Sci. Technol.*, vol. 40, no. 5, pp. 1616–1621. 2006.

[31] M. Anpo, H. Yamashita, Y. Ichihashi, and S. Ehara, "Photocatalytic reduction of CO_2 with H_2O on various titanium oxide catalysts," *J. Electroanal. Chem.*, vol. 396, no. 1–2, pp. 21–26. 1995.

[32] M. Anpo, H. Yamashita, K. Ikeue, Y. Fujii, S. G. Zhang, Y. Ichihashi, D. R. Park, Y. Suzuki, K. Koyano, and T. Tatsumi, "Photocatalytic reduction of CO_2 with H_2O on Ti-

MCM-41 and Ti-MCM-48 mesoporous zeolite catalysts," *Catal. Today*, vol. 44, no. 1–4, pp. 327–332. 1998.

Chapter Six – Titanium sub-oxide species

The previous chapter focused in the characterisation and the evaluation of the photocatalytic performance of commercial available TiO_2 particles and "photocatalytic" commercial coatings. After the evaluation of such coatings, the development of new TiO_2 particles and coatings are required to improve the photocatalytic activity. This chapter investigates how vacancies in the rutile lattice of reduced titania influence the phase structure, electrical conductivity and solid-gas photo-catalytic decomposition of nitrogen dioxide (NO_2) and carbon dioxide (CO_2) greenhouse gases.

6.1 Preparation of titanium sub-oxides species

Specimens were formed from commercial TiO_2 rutile powder (300 nm mean particle size, 99.5 % pure, Pi-kem, UK) which was processed by adding 2.5 % wt of an organic binder (polyethylene glycol-PEG 8000). By adding 1 % v/w of distilled water to the powder, a slurry was formed and ball milled for 24 h [1], [2]. Ball milling, further reduces the particle size and thoroughly mixing the organic binder with the ceramic powder prevents the formation of agglomerates. The slurry was then dried and the resulting powder sieved through a 45 μm mesh [3]. TiO_2 specimens were formed by dry cold pressing at a pressure of 250 MPa (20 kN over an area of 100 mm^2). The resulting green body was then pressureless sintered in a furnace, in air, at 1300 ^oC for 90 min with an initial dwell at 400 ^oC for 2 h to decompose the binder. This firing regime was previously optimised to achieve maximum density (98.65 ± 0.48 % of theoretical) and control grain growth (5-10 μm) [4].

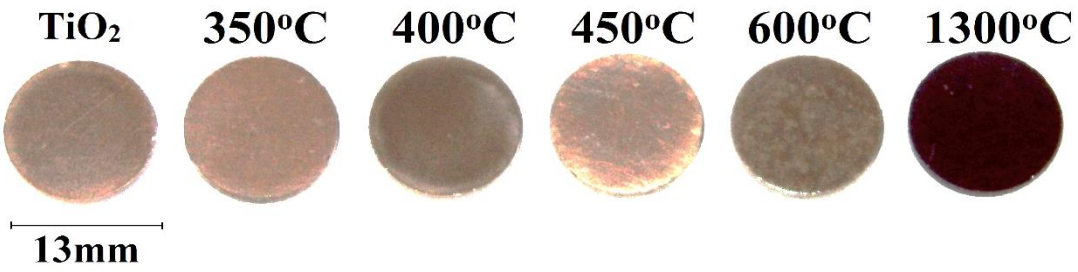

Figure 6.1 - Initial TiO_2 (left) and carbo-thermally reduced TiO_n samples. Temperatures indicate the reduction condition. Diameter of samples is 13mm

To introduce Ti^{3+} defects into the structure of TiO_2 carbo-thermal reduction was used (Equation 6.1) [5].

$$TiO_2 + C \rightarrow TiO_n + \frac{(2-n)}{2} CO_2 \qquad (6.1)$$

Carbo-thermal reduction of the sintered titania was performed in a tube furnace (LTF, Lenton, UK), under a constant flow of argon to prevent re-oxidation. A micro-environment was created by embedding the specimens in carbon black powder. The reduction treatment started with a heating ramp of 150 ^oC/h followed by a reduction stage of 24 h (reduction temperatures were 350, 400, 450, 600 and 1300 ^oC). A reduction temperature of 1300 ^oC is typical for the manufacturing of Magnéli [6], [7]. Once the reduction was complete, samples

were cooled to room temperature with a ramp of 150 ^{o}C/h. Differences in the visual appearance of the reduced TiO_2 specimens are highlighted in Figure 6.1.

The density of the samples was determined using the Archimedes method as described in the standard BS EN623:2.26 [8]. Theoretical Density (Dt) values for TiO_2 and TiO_n were assumed to be 4.26 g/cm^3 [9] and 4.30 g/cm^3 [1] respectively.

6.2 Characterisation of titanium sub-oxide species

X-ray diffraction Crystal phases were identified from the X-ray diffraction data. The XRD spectra, see Figure 6.2, indicated that rutile was the main crystallographic phase, even for the specimen reduced at 1300 ºC where Magnéli phases (Ti_4O_7, Ti_6O_{11}) were present.

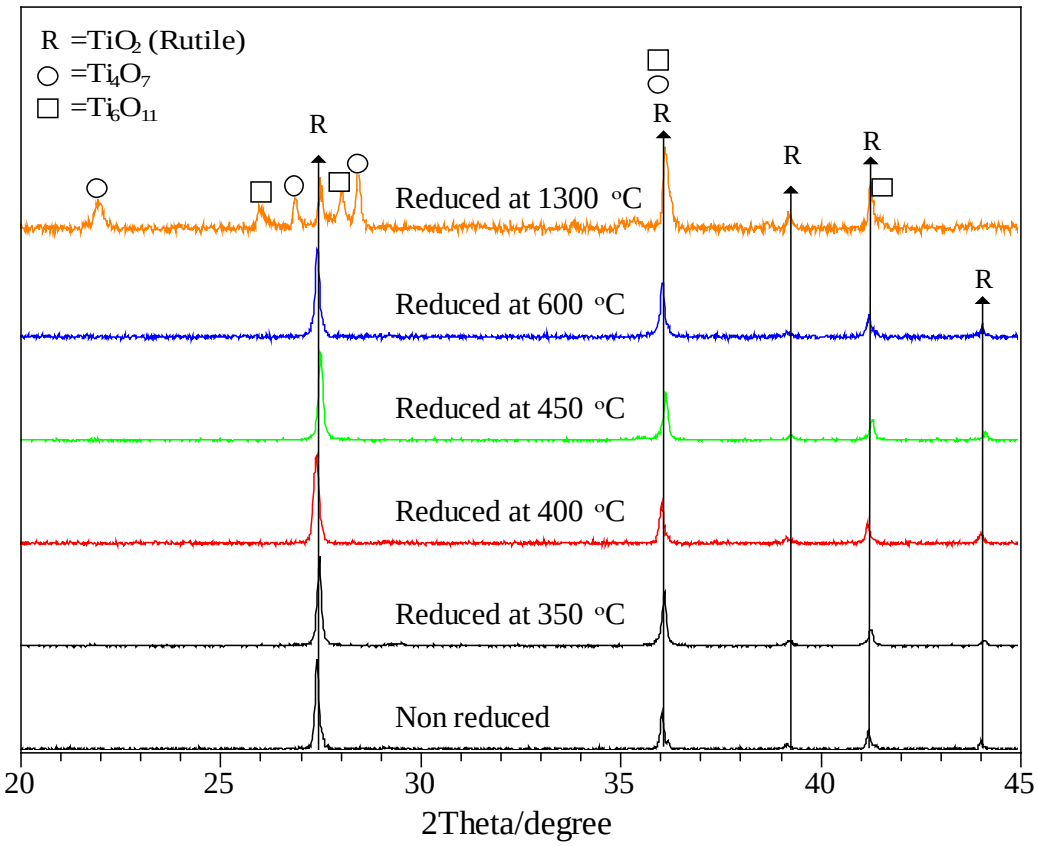

Figure 6.2 - XRD diffraction patterns of non-reduced rutile and TiO_n carbo-thermally reduced from 350 ºC to 1300 ºC

6.2.1 UV-visible diffuse reflectance spectroscopy

Changes in band gap with reduction conditions, were identified by the application of the Kubelka-Munk model as it was described in Section 2.5 (Chapter Two), however this was not applicable for the sample reduced at 1300 ºC containing significant conducting Magnéli phase as it was no longer a semiconductor. Figure 6.3 shows the reflectance of specimens over a range of wavelength. Only small changes in the band gap were observed with the maximum corresponding to the specimen reduced at 400 ºC.

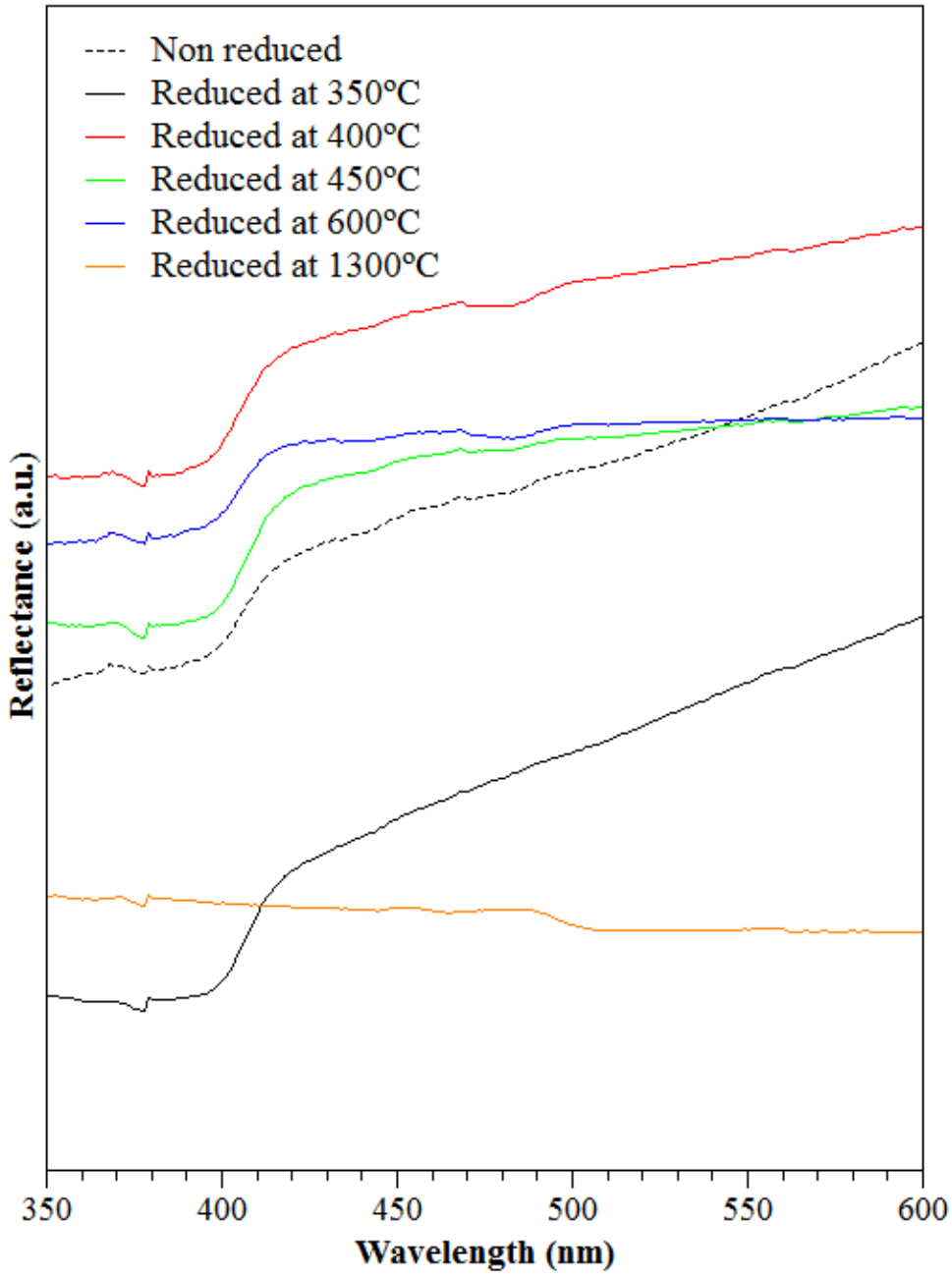

Figure 6.3 - Graphical representation of reflectance against wavelength for TiO_2 and TiO_n specimens

Table 6.1- Optical band gap of TiO_n specimens

Specimen -Reduction temp.	**Band gap (eV)**
Rutile TiO_2	3.03
TiO_n-350 ºC	3.04
TiO_n-400 ºC	3.06
TiO_n-450 ºC	3.04
TiO_n-600 ºC	3.05
TiO_n -1300 ºC	Overlapped bands

6.2.2 Electrical characterisation

It has been shown by Jonscher [10] that materials that contain conductive and insulating regions exhibit the 'universal dielectric response' (UDR) whereby at low frequency the bulk ac conductivity is frequency independent, σ_{dc}, while at higher frequencies the ac conductivity increases following a power law behaviour [11], [12]. Impedance spectroscopy was performed to identify correlations between the ac conductivity and the photo-activity of the specimens. Figure 6.4 shows that the ac conductivity of the non-reduced rutile TiO_2 rises linearly ($R^2 = 0.984$) with frequency and in this case the material is behaving predominately as a capacitor and the phase angle approaches 90º. At higher reduction temperatures the number of defects within the rutile lattice increases with a corresponding increase in conductivity (see Figure 6.4) with samples reduced at 350-400 ºC exhibiting the UDR. In specimens reduced at 450 ºC to 1300 ºC the defects are the dominant phase and the response is frequency independent, much like that of a resistor, with the phase angle approaching 0°. Changes in the conductivity are also shown in Figure 6.5, illustrating the frequency dependence of the complex impedance, again indicating the transition from capacitive and restive behaviour as the material is carbo-thermally reduced with a decrease in electrical conductivity.

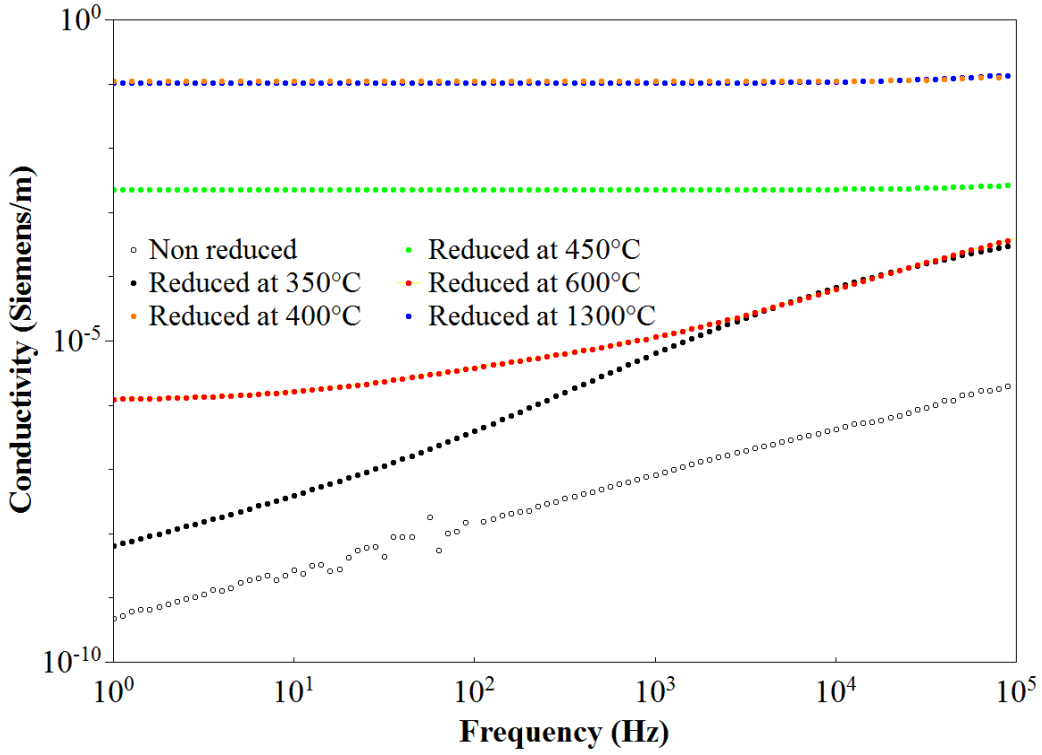

Figure 6.4 - AC conductivity of TiO_2 specimens over the frequency range 1 Hz and 0.1 MHz

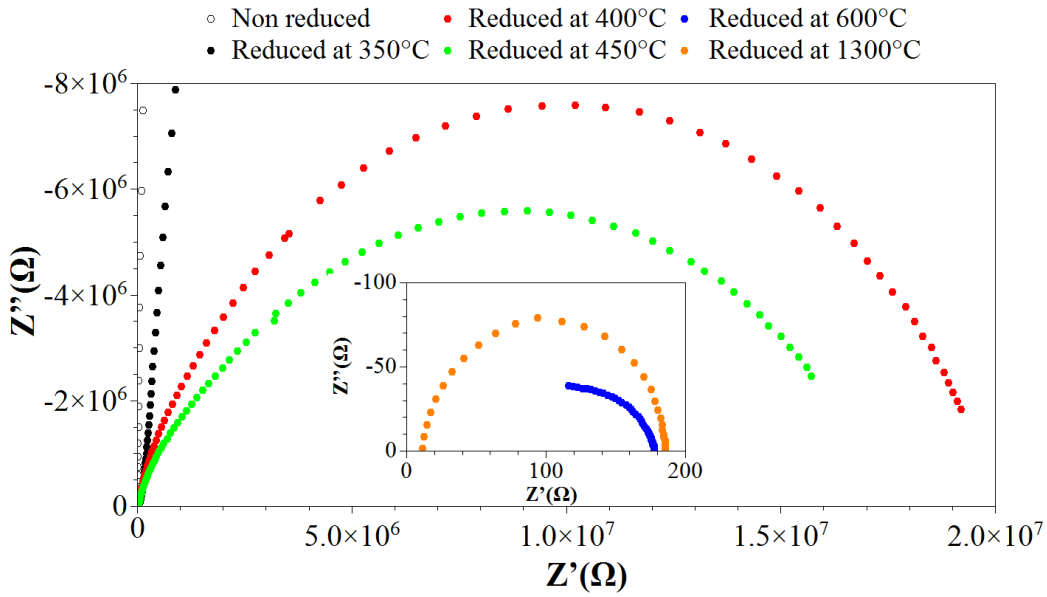

Figure 6.5 - Complex plane plot of real impedance (Z') vs imaginary impedance (Z'') for TiO_n specimens

6.2.3 Scanning electron microscopy (SEM)

Changes in specimen microstructure as a result of the reduction temperature was examined by SEM, revealing no significant changes in structure from the non-reduced TiO_2 and specimens reduced at temperatures up to 600 ºC. Figures 6a and 6b show the surface morphologies of the non-reduced TiO_2 and Magnéli phase based material reduced at 1300 ºC respectively. Due to the increased conductivity and diffusion processes during the reduction of TiO_2, there is significant grain growth when the material is reduced at this high temperature.

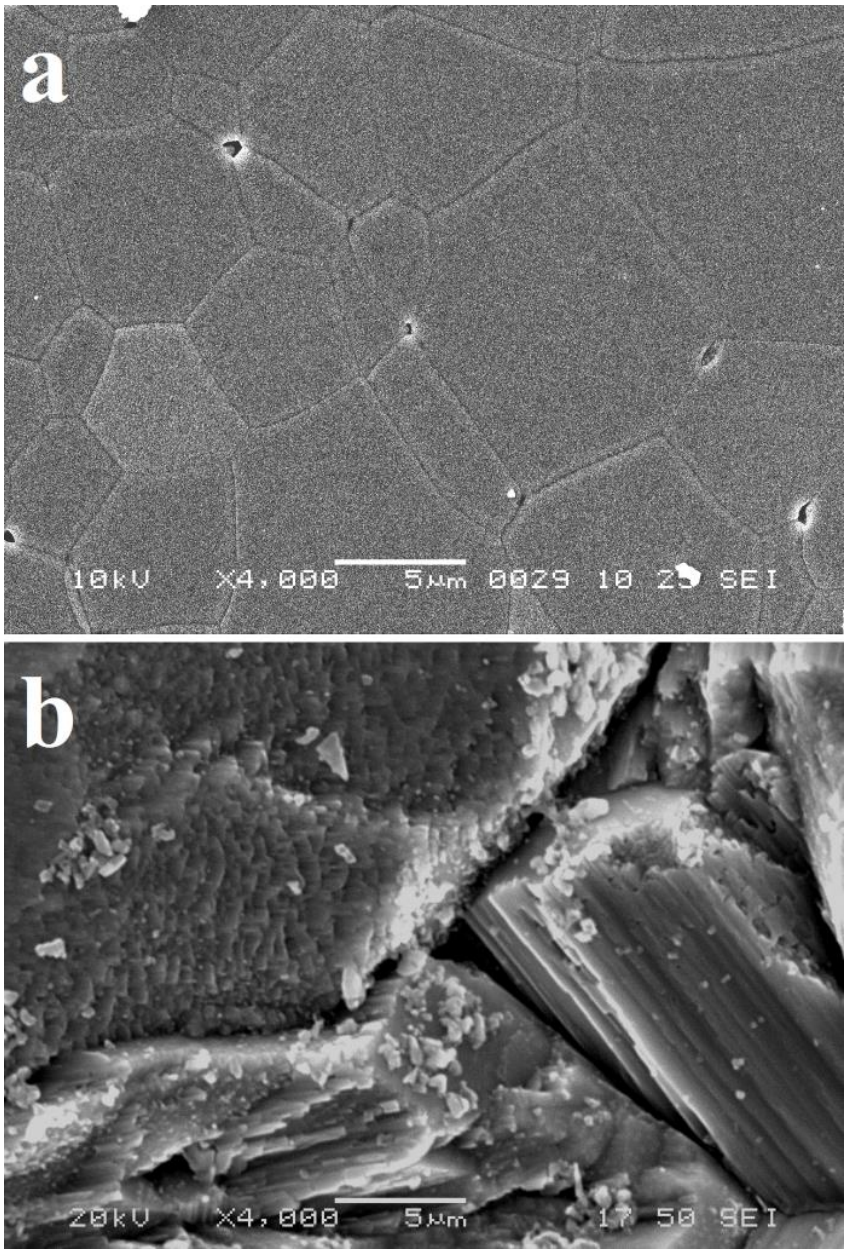

Figure 6.6 - SEM images of (a) non-reduced TiO_2, (b) TiO_2 carbo-thermally reduced at 1300 ºC

6.2.4 Photo-catalytic performance

The degradation of methylene blue in aqueous phase as well as the degradation of CO_2 and NO_2 in gas phases by rutile and titanium sub-oxide specimens reduced at temperatures ranging from 300 ºC to 1300 ºC were examined. Results from the photocatalytic reduction of methylene blue at wavelengths of 376-387 nm and 381-392 nm are shown in Figures 6.7. Figures 6.8 and 6.9 show the degradation in gas phase of CO_2 and NO_2 at different UV wavelengths.

For the test in aqueous phase, rutile and titanium sub-oxide specimens were milled using an agate pestle and mortar prior testing its photoactivity. The absorption of methylene blue in those powders varies between 2.0–3.0 % the initial concentration. As Figure 6.7 shows, at wavelengths of 376-387 nm, rutile and the specimen reduced at 350 ºC were able to reduce 20 % of methylene blue, whereas the specimens reduced at 400 and 450 ºC only achieved 7 and 4 % respectively. Magnéli and the titanium sub-oxide reduced at 600 ºC did not show any photocatalytic activity.

When the aqueous suspension was irradiated with the UV LED of wavelength range of 381-392 nm, the performance of rutile and the specimen reduced at 350 ºC decreased 10 %. Only the specimen reduced at 450 ºC improved by reducing 5 % more methylene blue than at 376-387 nm. In summary, the performance of sub-oxide specimens was reduced in comparison with rutile.

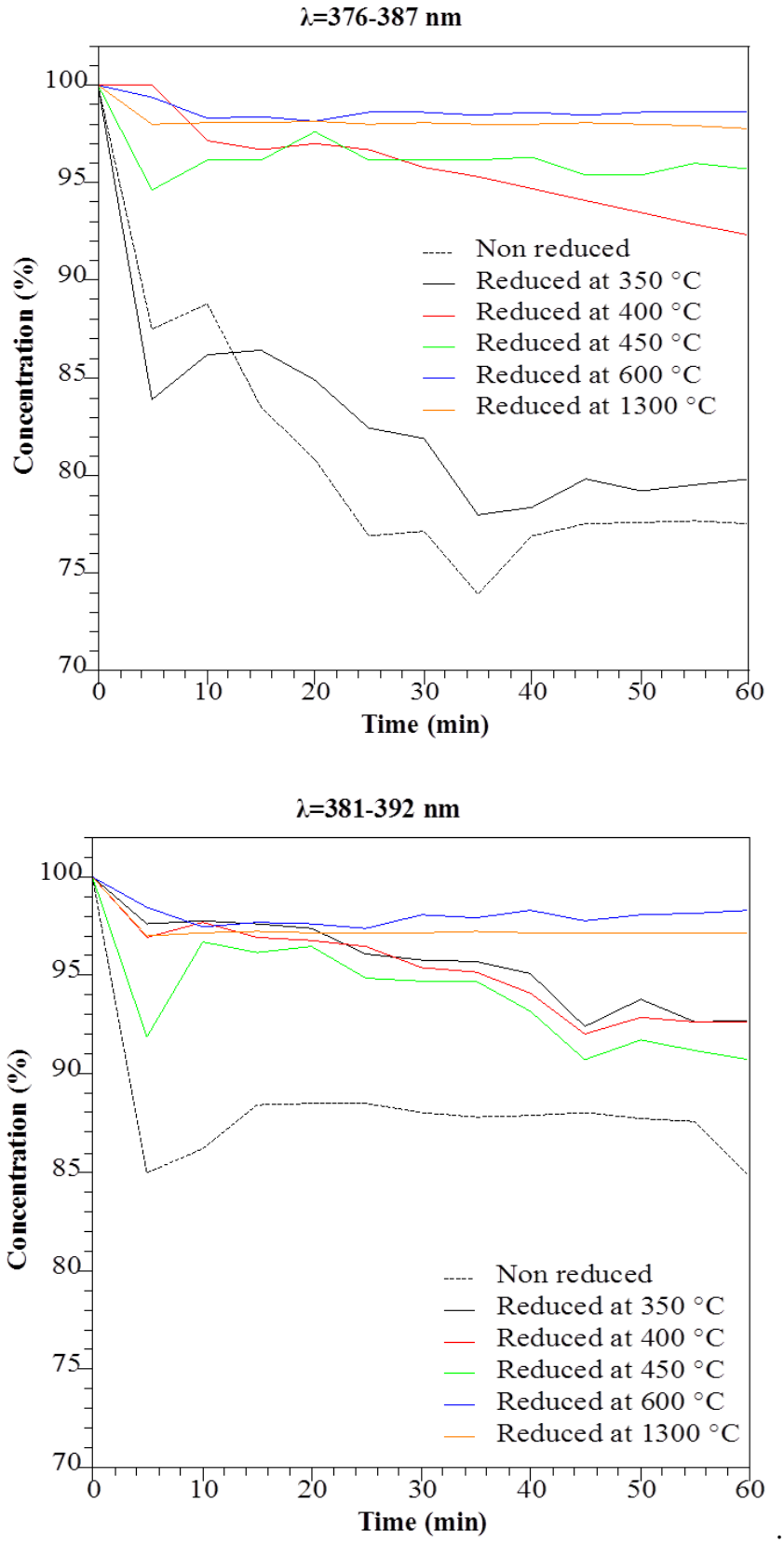

Figure 6.7 – Photo-reduction of methylene blue in aqueous solution under two different UV LED of wavelength of 376-387 nm and 381-392nm (I = 4.7 W/m^2) for TiO_2 and reduced samples.

Results from the gas phase analysis show an increase of photo-activity under wavelengths of 381-392 nm for the titanium sub-oxide sample reduced at 400°C for both NO_2 and CO_2, whereas the maximum degradation of NO_2 was observed for the titanium sub-oxide reduced at 350 °C when irradiated with a wavelength of 376-387 nm. Based on the results shown in Figure 6.8 and 6.9 it is thought that when the TiO_2 was reduced at temperatures under 350 °C, insufficient defects were created within the lattice. The low frequency ac conductivity increased by a factor of ten, compared to non-reduced rutile (see Figure 6.4), for the sample reduced at 350 °C and up to twenty times for the sample reduced at 400 °C, leading to enhanced photo-activity.

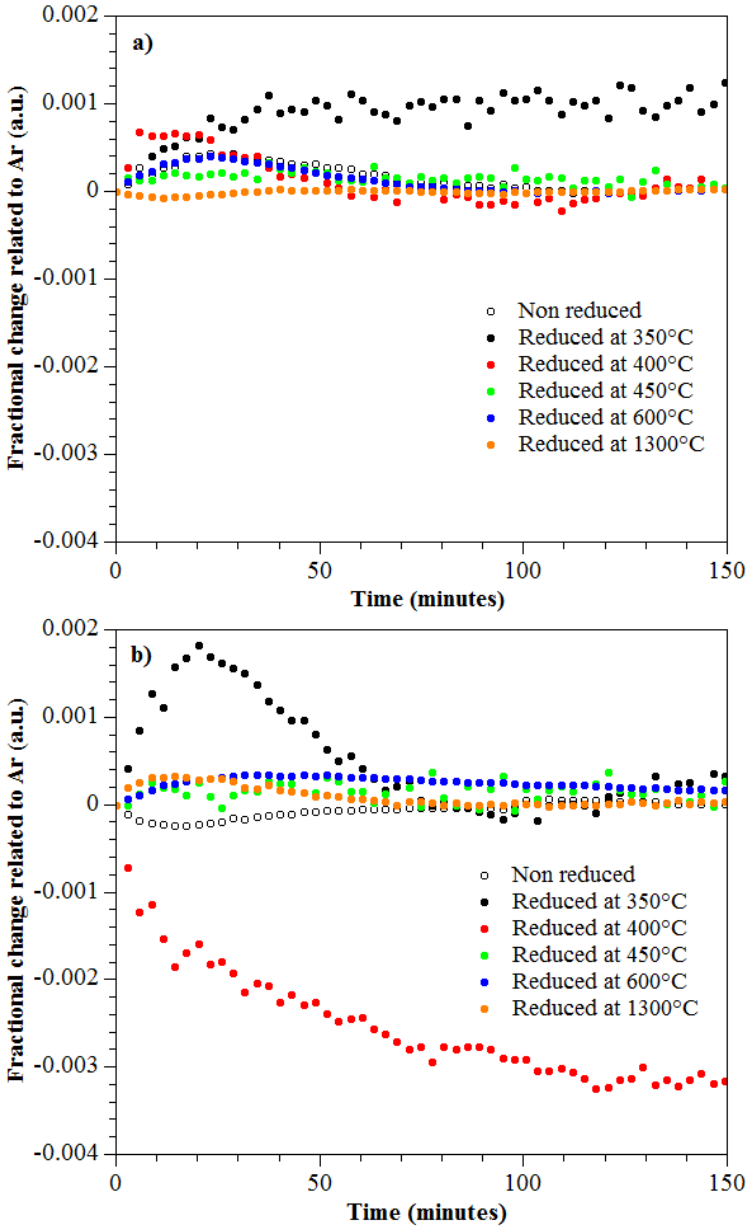

Figure 6.8 – Fractional reduction of CO_2 over 150 minutes under UV of wavelengths (a) 376-387 nm and (b) 381-392 nm

This increase in the conductivity, due to the presence of Ti^{3+} in the bulk, improved the efficiency of the electron-hole separation and stabilisation of the charge distribution. As a result, the photo-activity of the material increased. In comparison with the analysis in aqueous phase, the need of stabilising the charge distribution is not required due to the permanent contact with H_2O. When an electron or hole is generated, it will react immediately with H_2O with radicals as products.

When the material was subjected to a greater degree of reduction, i.e. at reduction temperatures above 450 °C, a higher concentration of defects are produced which leads to localisation of defects, thereby reducing photo-activity. Tailoring the degree of reduction therefore offers a route to balance these effects to produce improved photo-catalytic materials.

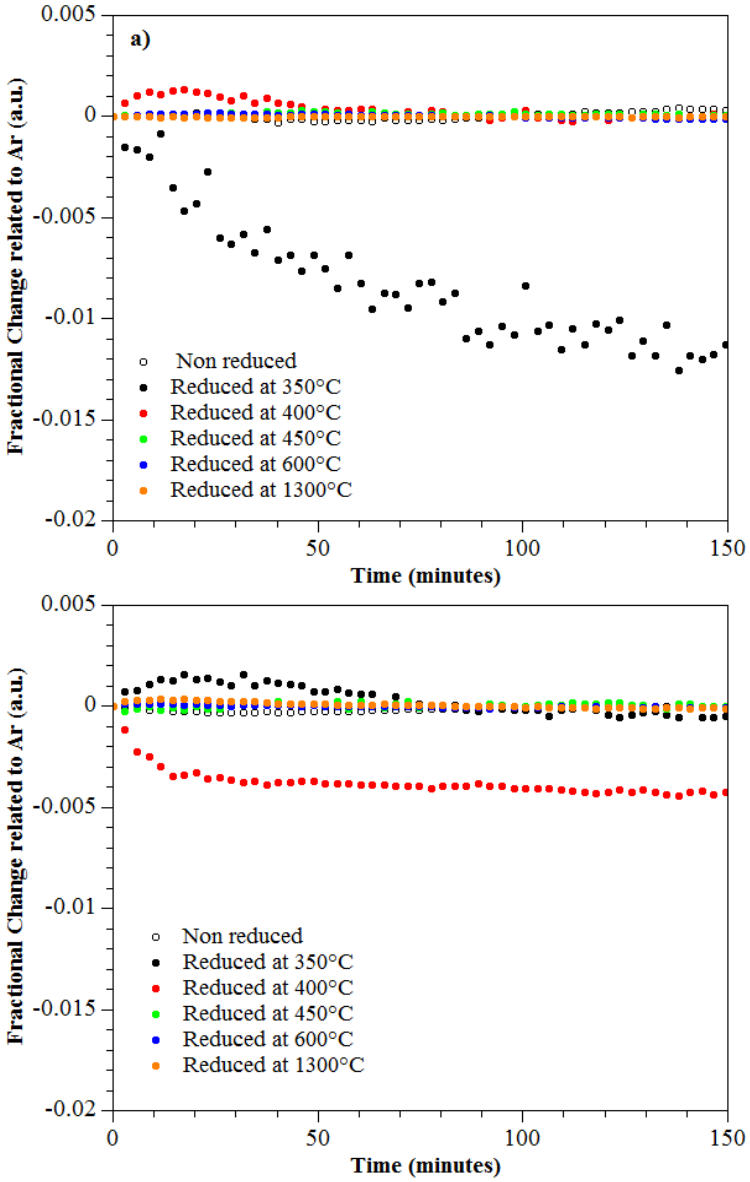

Figure 6.9 - Fractional reduction of NO_2 over 150 minutes under UV wavelengths of (a) 376-387 nm and (b) 381-392 nm

6.3 Summary

This chapter shows how rutile's photocatalytic properties in gas phase can be enhanced by reducing TiO_n phases under an inert atmosphere at temperatures from 350 °C to 400°C. The motivation for this research was to show a novel and different approach to tailoring TiO_2 photocatalytic properties, as most of the reported research focuses on adding atoms to distort the crystal lattice and thereby modifying its electronic properties. This enhancement is attributed to improvements in the charge distribution process. Subjecting rutile to reduction temperatures above 400 °C created localized titanium sub-oxide species containing Magnéli phases. While the presence of these phases increased the electrical conductivity it did not enhance the photo-catalytic activity of the material as the Magnéli phase is not photo-active.

The optimum temperature range to enhance photo-catalytic properties was 350 °C to 400 °C and demonstrates that the photo-catalytic performance of TiO_2 can be improved by the introduction of defects into the lattice by carbo-thermal reduction. The enhancement is attributed to improvements in the charge distribution process. This strategy constitutes an important alternative to doping TiO_2 with other elements to modify the band gap and thus photo-catalytic performance for applications such as air purification.

6.4 Bibliography

[1] S. R. Sangawar, J. P. Agarwal, and D. B. Sarwade, "A comprehensive study on some binders for piezo-electric ceramics," *Indian J. Eng. Mater. Sci.*, vol. 8, no. 1, pp. 26–35, 2001.

[2] F. N. Bradley, "The relation of ceramics processing to materials properties for electronic application," *IEEE Trans. Parts, Hybrids Packag.*, vol. 8, no. 4, pp. 17–23, 1972.

[3] Rahaman MN, *Ceramic Processing*. Boca Raton, FL: CRC Press/Taylor & Francis, 2006.

[4] S. J. Kalita, S. Qiu, and S. Verma, "A quantitative study of the calcination and sintering of nanocrystalline titanium dioxide and its flexural strength properties," *Mater. Chem. Phys.*, vol. 109, no. 2–3, pp. 392–398, 2008.

[5] F. C. Walsh and R. G. A. Wills, "The continuing development of Magnéli phase titanium sub-oxides and Ebonex® electrodes," *Electrochim. Acta*, vol. 55, no. 22, pp. 6342–6351, 2010.

[6] P. C. S. Hayfield, *Development of a New Material: Monolithic Ti_4O_7 Ebonex Ceramic*. Cambridge: Royal Society of CHemistry, 2002.

[7] V. Adamaki, F. Clemens, P. Ragulis, S. R. Pennock, J. Taylor, and C. R. Bowen, "Manufacturing and characterisation of Magnéli phase conductive fibres," *J. Mater. Chem. A*, vol. 2, no. 22, pp. 8328–8333, 2014.

[8] W.-E. Wang and Y. S. Kim, "A thermodynamic evaluation of the titanium–oxygen system from O/Ti=0 to 3/2," *J. Nucl. Mater.*, vol. 270, no. 1–2, pp. 242–247, 1999.

[9] K. P. Surendran, P. V Bijumon, P. Mohanan, and M. T. Sebastian, "$(1-x)MgAl_2O_{4-x}TiO_2$ dielectrics for microwave and millimeter wave applications," *Appl. Phys. A*, vol. 81, no. 4, pp. 823–826, 2005.

[10] A. K. Jonscher, "The `universal´ dielectric constant", *Nature*, vol. 267, no. 5613, pp. 673-679, 1977

[11] D. P. Almond and B. Vainas, "The dielectric properties of random R - C networks as an explanation of the `universal' power law dielectric response of solids," *J. Phys. Condens. Matter*, vol. 11, no. 46, pp. 9081–9093, 1999.

[12] D. P. Almond and C. R. Bowen, "Anomalous Power Law Dispersions in ac Conductivity and Permittivity Shown to be Characteristics of Microstructural Electrical Networks," *Phys. Rev. Lett.*, vol. 92, no. 15, p. 157601, 2004.

Chapter Seven – Electrophoretic deposited coatings of anatase TiO_2

The previous chapter described how defects on the TiO_2 lattice lead to a change on its electric and optical properties. This chapter describes the work undertaken in the coating application of TiO_2 for different building materials. The preparative technique focuses on the preparation and application of an anatase coating for prefabricated panels consisting of steel, glass or titanium, as there are used widely construction materials. Coatings were manufactured during a granted internship to the LNM Institute of Information Technology (Jaipur) funded by the British Council under their UKIERI programme

7.1 Materials and preparation of anatase TiO_2 coatings

7.1.1 Titanium dioxide

Anatase Aeroxide® P25 (previously described in Chapter Five) with a thermal expansion coefficient of 8.4×10^{-6}/K (CAS 13463-67-7) was used as photocatalyst.

7.1.2 Substrates

The three electrically conductive substrate materials that were evaluated were:

i. Stainless steel of grade AISI 304L (1.0 mm thickness) with an electrical resistivity of 7.2×10^{-5} Ωcm at 20 °C and a thermal expansion coefficient of 1.7×10^{-5}/K
ii. 99.6 % purity titanium sheet (1.0 mm thickness) supplied by Advent Research Materials Ltd. with an electrical resistivity of 4.2×10^{-5} Ωcm at 20 °C and a thermal expansion coefficient of 8.6×10^{-6}/K.
iii. Soda glass coated in a conductive fluorine doped tin oxide film (thickness 3.2 mm) of sheet resistance 8 Ω/sq and a thermal expansion coefficient of 9×10^{-6} /K was supplied by Visiontek Systems Ltd.

All the substrate materials were cut into sections of 25 mm × 25 mm, and to remove surface contaminants, the substrates were ultrasonicated in deionised water for 15 min, washed in acetone and finally air-dried using a hot air blower.

7.1.3 Medium

As it was discussed in Section 1.1.6.1 (Chapter One), electrophoretically deposited coating using isopropanol and acetylacetone showed a uniform distribution and high durability. For this reason two different solutions were studied:

i. Isopropanol based solution: 30 ml of isopropanol, 15 ml of acetone and 0.5 ml of acetylacetone, 0.1 % w/v of iodine and 1 % w/v of anatase [1].
ii. Acetylacetone based solution: 30 ml of acetylacetone, 0.1 % w/v of iodine and 1 % w/v of anatase.

Table 7.1 – Physical properties of different solvents

Solvent	Isopropanol	Acetone	Acetylacetone
Density (g/cm^3)	0.786 at 20 °C	0.791 at 25 ºC	0.975 at 25 °C
Relative dielectric constant	18.23 at 25 °C	21.01 at 20 ºC	23.1 at 20 ºC
Vapour pressure (mmHg)	40 at 23.8 °C	184 at 20 °C	6 at 20 ºC
Viscosity (Pa×s)	0.196 at 25 °C	0.306 at 25 ºC	

7.1.4 Reactor, power supply and furnace conditions

A glass cell reactor containing a platinum counter electrode (section of 1.00 mm × 2.50 mm × 0.50 mm) with an inter electrode distance of 2.7 cm. As power supply, a Keithley model 2400 was used, with a voltage range of this 5 μV to 210 V, programming resolution of 5 mV and maximum power of 22 W. The basic accuracy at 23 °C ± 5 °C was 0.012 % of the reading voltage ± 24 mV. The noise, peak to peak, between 0.1 and 10 Hz was 5 mV.

After deposition, the coated samples were dried at room temperature and calcined in a conventional furnace, with a ramp program of 1 °C per minute until reached 450 °C. Samples were held inside the furnace at 450 °C for 2 h before being naturally cooled down to room temperature.

7.2 Electrophoretic deposition parameters

The optimum coating conditions were investigated by systematically changing the exposure time, solvent, voltage and substrate material. By modifying these physicochemical parameters, the electrophoretic kinetics (electric field [2]–[6], physical properties of solvent and substrate [3], [4]) can be modified over a series of experiments, which are detailed in the following sections.

7.2.1 Effect of deposition time

High exposure time implies a greater coating thickness, however a critical thickness was identified at which point the coating became unstable and cracks formed on the surface after

calcination. Exposure sequences during EPD investigated were: 5 s, 10 s, 30 s, 50 s, 100 s, 300 s, 500 s, 900 s and 1200 s.

Figure 7.1a shows the effect of deposition time for stainless steel and FTO coated glass in acetylacetone based solution deposited at 80 V. All the coatings prepared at 80 V for 500 s failed during the calcination process because of the large number of cracks in the thicker coatings, which is attributed to the stress caused by thermal mismatch between the coating and the substrate.

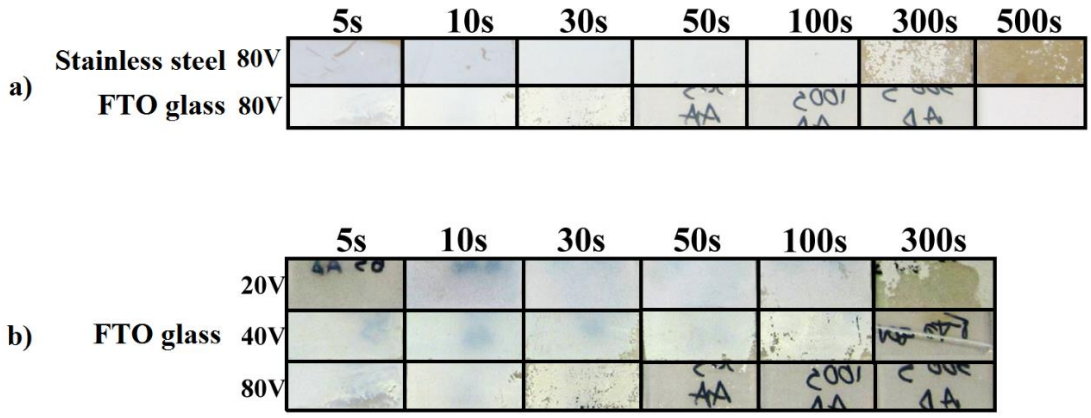

Figure 7.1 - a) Images of TiO_2 films that were electrophoretically prepared in acetylacetone based solution at 80 V after calcination; b) Images of TiO_2 coated FTO coated glass electrophoretically prepared in acetylacetone based solution at 20 V, 40 V and 80 V

As shown in Figure 7.1a, stainless steel was successfully coated with an exposure time under 50, whereas FTO coated glass was successfully coated under 30 s. Figure 7.1b shows the evolution of the deposited coatings on FTO coated glass that was electrophoretically prepared in acetylacetone based solution at 20 V, 40 V and 80 V at different time sequences. Higher voltages required less time to deposit an anatase coating whereas at a lower voltage of 20 V longer exposure times are required to obtain a uniform thickness. The transparent FTO glass samples were labelled on their reverse side using black permanent marker pen and this writing is clearly visible on the thinly coated samples and provides a useful visual indication of the coating thickness.

7.2.2 Effect of applied voltage

It is well known that the thickness of the resultant coating is proportional to the applied voltage and the deposition time [6]–[8]. To study the effect of the voltage and time, the substrate and solvent were fixed (FTO coated glass was used for the substrate in an acetylacetone based solution). As Figure 7.1b shows, at 20 V a uniform coating requires a 50 s deposition time whereas at 40 V, 30 s deposition time is required; and at 80 V a 10 s deposition time is sufficient to provide a uniform and stable coating. Coatings prepared for durations over 100 s produced poorly adhered coatings following the drying and calcination stage of the process.

7.2.3 Effect of substrate

FTO coated glass, titanium and stainless steel substrates were used to evaluate deposition voltages of 20 V, 40 V and 80 V for 900 s as shown in Figure 7.2a. The deposition time was chosen to ensure the coating formation achieved the maximum thickness; but only the metallic substrates were coated successfully at 20 V, showing a similar behaviour between stainless steel and titanium. Figure 7.2b shows another experiment performed under the same conditions of voltage and solvent, but with different time exposures for FTO coated glass and stainless steel (as a representative metallic sample). FTO coated glass requires less exposure time to be coated than stainless steel, whereas coatings formed on stainless steel remained stable after exposure times of 100 s and 300 s. Considering the stability of the coatings after calcination, FTO glass and stainless steel showed the highest adhesion to the substrate-TiO_2. This was attributed to the thermal expansion coefficient´s of FTO coated glass being closest to TiO_2 anatase, reducing thermal mismatch stresses generated during the calcination process.

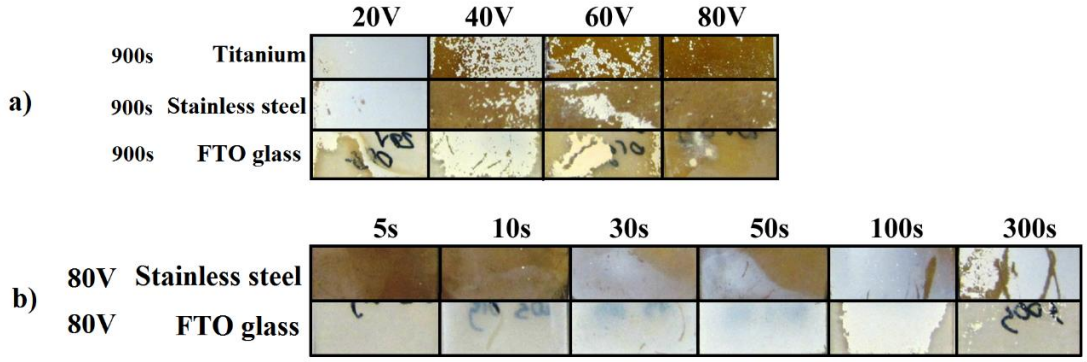

Figure 7.2 - a) Images of TiO_2 films coated at 20 V, 40 V, 60 V and 80 V under isopropyl based solution in three different substrates; b) Images of TiO_2 films coated at 80V under isopropyl based solution

7.2.4 Effect of solvent

As described in the experimental methods, both isopropanol based and acetylacetone based solutions were used. Figure 7.3 shows the difference between coatings obtained electrophoretically at 80 V in isopropanol and acetylacetone based solutions for a stainless steel substrate. The acetylactone based solution yields a coating with greater uniformity over a wider range of times compared to the isopropyl solution. This is due to acetylactone´s physical and electrical properties, low viscosity and high dielectric constant increasing the mobility of charged particles in the solution. A comparison with FTO coated glass can be made by referring to Figure 7.4 (bottom two rows). Similar to the steel, the acetylacetone solution gave a better coating on FTO compared to the isopropyl solution, however this was only observed at 5s and 10 s indicating that the steel yielded more consistent coatings at short deposition times.

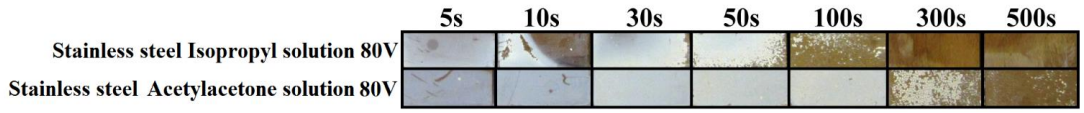

Figure 7.3 - Images of TiO_2 films coated stainless steel at 80 V under isopropyl based solution and acetylacetone based solution

Figure 7.4 shows the differences when the deposition voltage is reduced from 80 V to 20 V using these solutions on an FTO glass substrate. In all cases the acetylacetone based solution was the most effective solvent forming a uniform and stable TiO_2 coating under high voltages or longer deposition times.

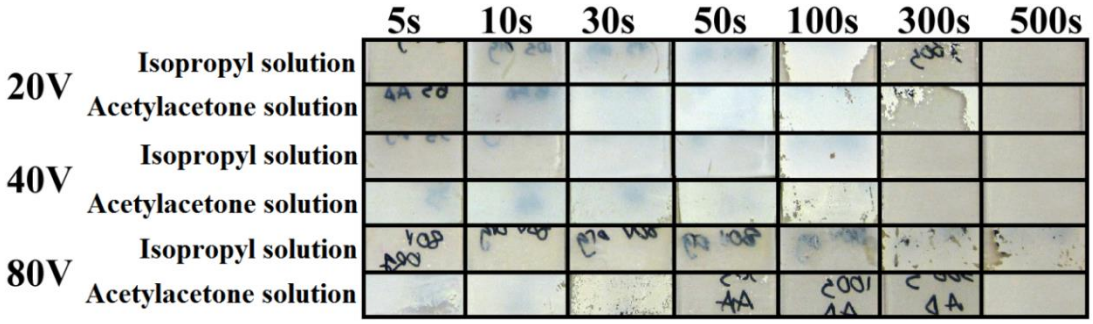

Figure 7.4 - Images of TiO_2 films coated FTO coated glass at 20, 40 and 80 V under isopropyl based solution and acetylacetone based solution

7.3 Coating characterisation

7.3.1 Crystal phase composition

The phase composition of the coatings was determined using X-ray diffraction and Raman spectroscopy as presented in Figures 7.5 and 7.6. Figure 7.5 shows the XRD pattern of the initial anatase P25 and the coating produced by electrophoretic deposition on FTO coated glass at 20 V for 50 s in an isopropanol based solution. Anatase was confirmed as the predominant phase in P25 as expected. However the presence of rutile was also indicated by a number of peaks in the XRD diffractogram and in the Raman spectra. Peaks for both of these phases corresponding to the standard JCPDS XRD data files for anatase (JCPDS No. 21-1272) and rutile (JCPDS No. 21-1276). The XRD pattern of the coating produced by electrophoretic deposition on FTO coated glass was typical of all the coatings characterised and showed the same peaks for the anatase crystal phase with traces of the rutile crystal phase. In addition, in the case of the FTO coated glass, peaks corresponding to SnO_2 from the conductive fluorine doped SnO_2 coating were also observed [9], [10] (JCPDS-041-1445). A comparison of the raw P25 spectra with that of the coatings confirmed that during the coating and annealing process, anatase did not transform into rutile as the ratio anatase/rutile was unaltered.

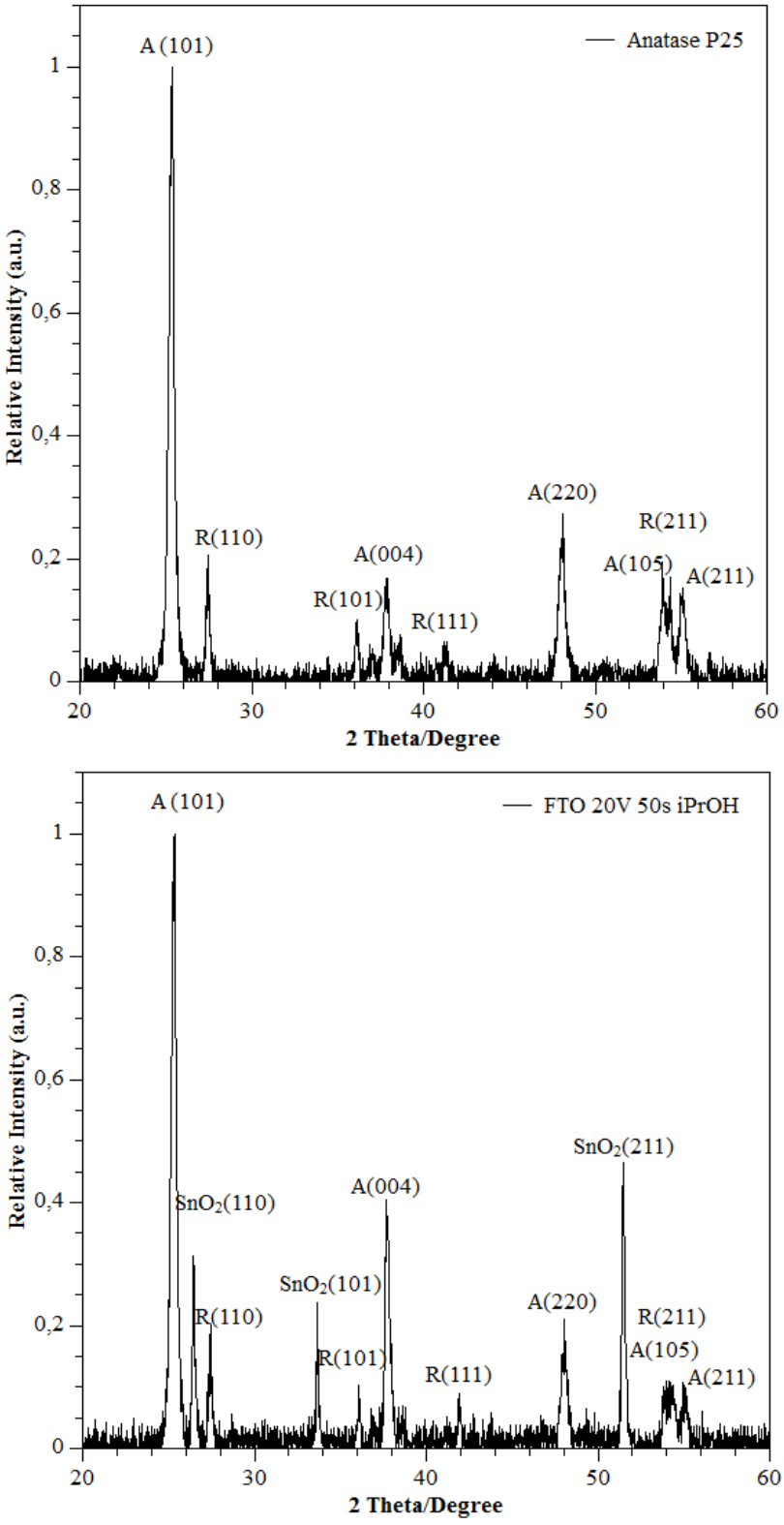

Figure 7.5 - XRD Spectra of TiO_2 anatase P25 and a typical XRD spectrum of the films (in this case, FTO-coated glass coated at 20 V for 50 s in isopropanol based solution). R=Rutile, A=Anatase

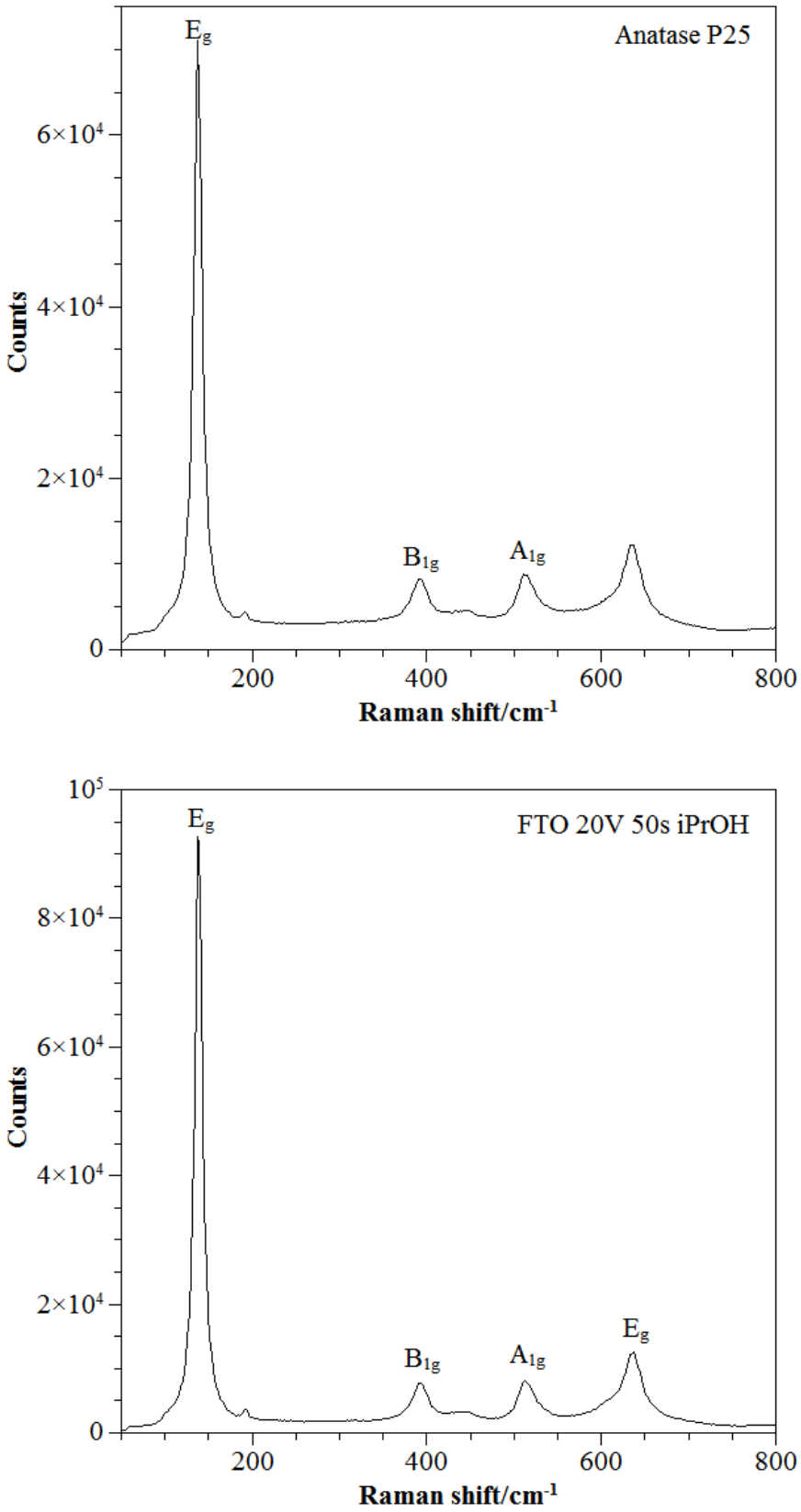

Figure 7.6 - Raman spectra of anatase P25 (top) and the characteristic Raman spectra TiO_2 coatings produced by electrophoretic deposition for all the films

Figure 7.6 shows the Raman spectra of anatase P25 and the typical Raman spectra of the coated substrates. Anatase shows four main peaks, 138 cm^{-1} (100 % relative intensity),392 cm^{-1} (11% relative intensity), 513 cm^{-1} (12% relative intensity) and 636 cm^{-1} (17% relative intensity). Two different coatings representative of the deposition methods were identified for study by surface mapping. TiO_2 deposited on titanium foil for 15 min in isopropanol based solution at 20 V, which represented a metallic coating at a long deposition time; and TiO_2 supported on FTO coated glass for 50 s which represented a coating grown on FTO coated glass formed for a short period of time. The results extracted from the data revealed anatase as main component of the surface coating.

7.3.2 Surface morphology

Following careful examination of all the samples manufactured the ten coatings (samples a-j) with the most uniform and coherent coatings were subjected to further testing and analysis.

The morphology of the coatings was evaluated at low magnifications using a VHX-5000 Digital optical microscope equipped with a CMOS image sensor (virtual pixels: 1600 (H)x x1200(V)) provided by Keyence. Higher magnification images were obtained using a JEOL JSM64802V scanning electron microscope (SEM) with an accelerator voltage of 10 kV and a spot size of 25 nm. Where necessary the samples were coated with a 10 nm film of chromium to prevent charging. Coating thickness was calculated from an average of three measurements taken from an SEM image of a cross-section. Table 7.2 shows the experimental conditions for each of these coatings and Figure 7.7 shows representative images taken using an optical microscope.

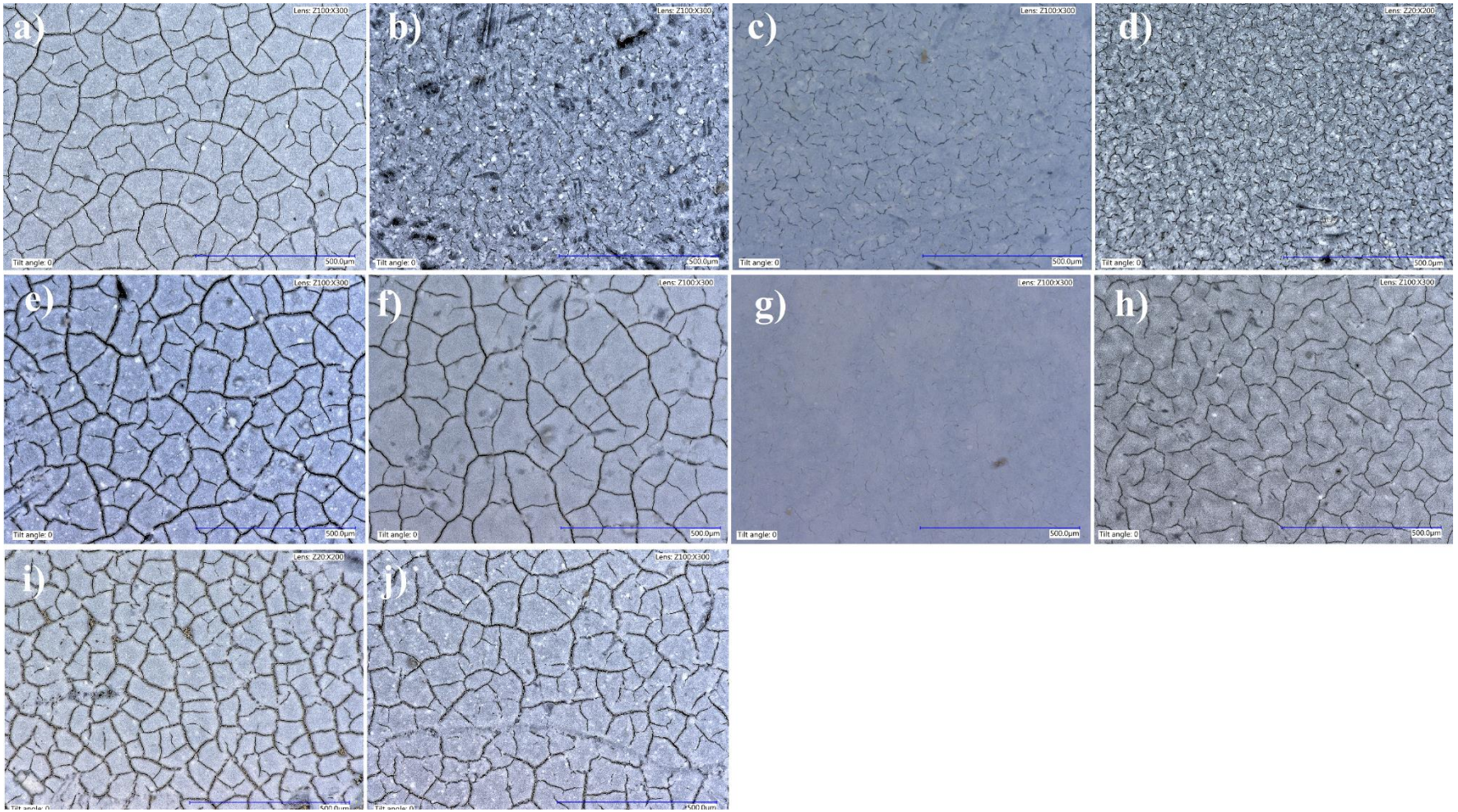

Figure 7.7 – Images of the TiO_2 coatings described in table 7.2

To study the three-dimensional morphology of the surface, samples were analysed using a Proscan 2000. Figures 7.8 shows an example for sample (j) where cracks can be discerned on the coating´s surface, increasing the roughness value. In Table 7.2 shows the surface texture; average roughness, mean peak to valley height, root mean square average roughness and the thickness for all the coatings. The data shows consistent average roughness values, with coatings deposited at 80 V with high roughness values between 1.21 and 1.84 µm, in comparison those produced at 20 V or 40 V which had lower roughness' between 0.56 and 0.88 µm. The coatings thicknesses were however not only influenced by the voltage, but also the deposition time, where longer times resulted in thicker coatings.

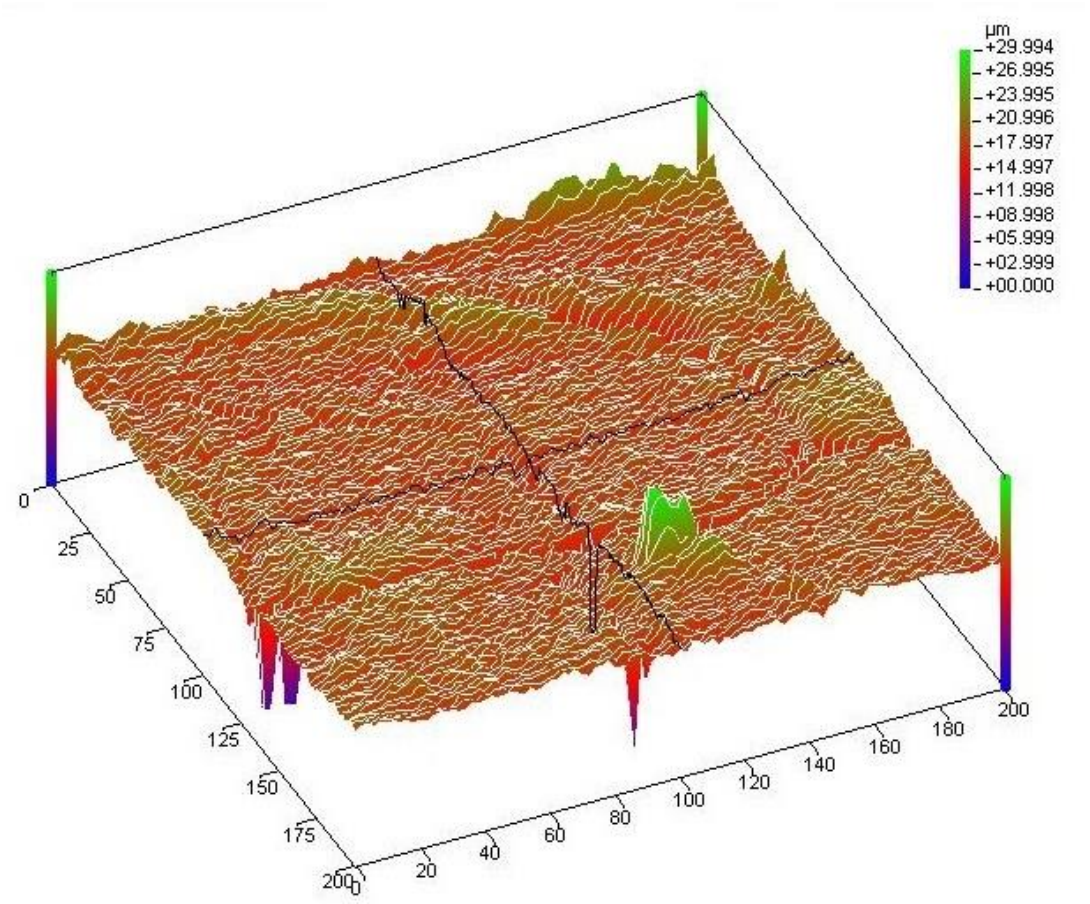

Figure 7.8 - Surface mapping of titanium plate coated with TiO_2 at 20 V suspended in isopropanol based solution during 15 min obtained from non-contact optical profilometry

Table 7.2 – Profile roughness parameters and thickness for the studied coatings

ID	Substrate	Based solution	Voltage	Time	Average roughness (µm)	Mean peak to valley height (µm)	Root mean square average roughness (µm)	Thickness (µm)
a	FTO	Acetylacetone	20 V	30 s	0.77	3.11	0.99	16.4
b	FTO	Isopropanol	20 V	50 s	0.56	5.14	0.77	12.2
c	FTO	Acetylacetone	40 V	10 s	0.75	3.40	0.96	7.3
d	FTO	Isopropanol	40 V	50 s	0.72	3.09	0.92	6.0
e	FTO	Acetylacetone	80 V	10 s	1.21	4.92	1.80	14.5
f	Steel	Isopropanol	20 V	900 s	0.88	3.40	1.13	11.9
g	Steel	Isopropanol	20 V	100 s	0.81	3.22	1.12	9.0
h	Steel	Acetylacetone	80 V	30 s	1.33	6.78	2.13	18.2
i	Steel	Acetylacetone	80 V	50 s	1.84	7.95	3.61	22.3
j	Titanium	Isopropanol	20 V	900 s	0.84	3.95	1.28	15.1
k	Pellet	-	-	-	0.15	0.76	0.19	-

Characterisation of the samples by SEM reveals the microstructure formed from the deposited anatase particles. Figure 7.9 shows SEM images obtained from FTO coated glass, coated for 30 s at 20 V in acetylacetone based solution. The microstructure observed in this instance looked similar to that obtained on the other samples which were coated under different deposition conditions. This suggests that the significant differences responsible for the coating behaviour were macro structural.

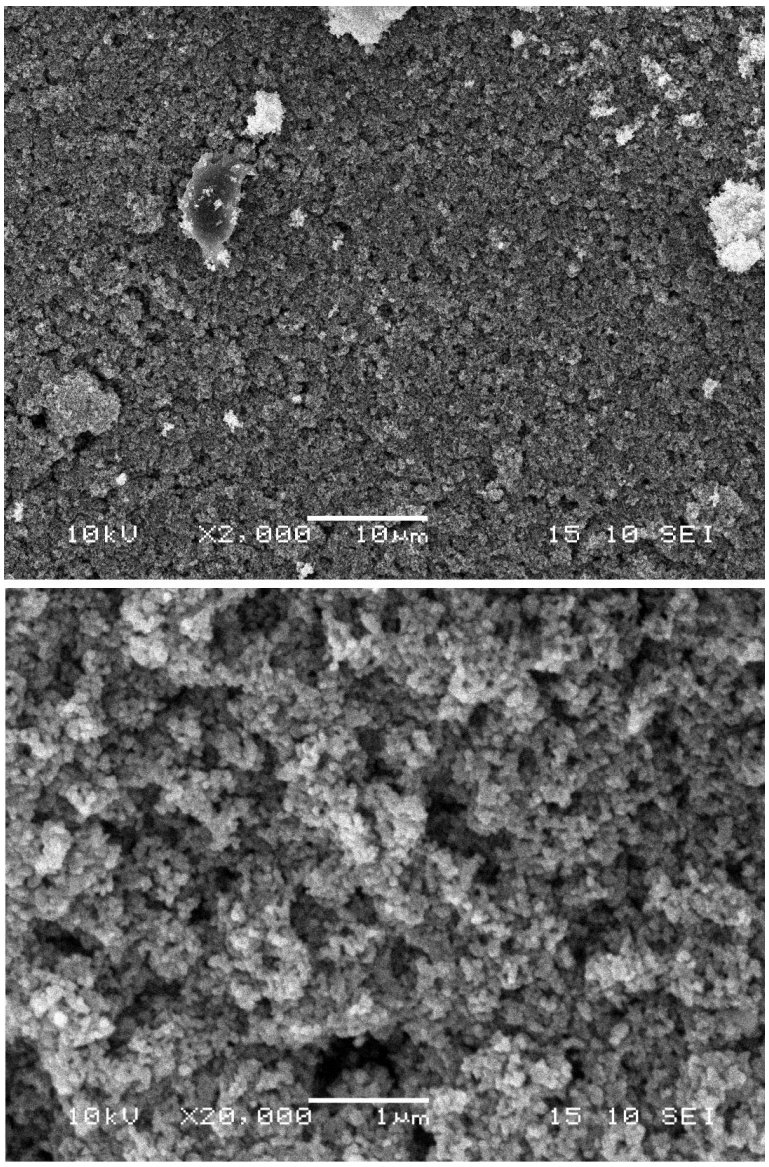

Figure 7.9 – Typical SEM images of TiO_2 electrophoretically deposited coatings on FTO coated glass at 20 V for 30 s in isopropyl based solution

7.3.3 Photocatalytic degradation of NO_2

The selected coatings were also tested in a reaction chamber coupled to a quadrupole mass spectrometer (as described in Chapter 4). To aid comparison values were normalised relative to the performance of an anatase P25 pressed pellet. Figure 7.10 shows an example of both experiments for the FTO coated glass coated for 30 s at 20 V in acetylacetone based solution. Figure 7.10 shows the degradation for the active coatings and anatase pellet per mm^2 under a UV irradiation of wavelength (λ) 376-387 nm. Figure 7.11 shows samples that were coated on FTO coated glass, in acetylacetone based solution at 20 V for 30 s and at 40 V for 10 s were extremely reactive. In comparison, stainless steel coated in acetylacetone based solution at 80 V for 50 s achieved the same performance as an anatase pellet.

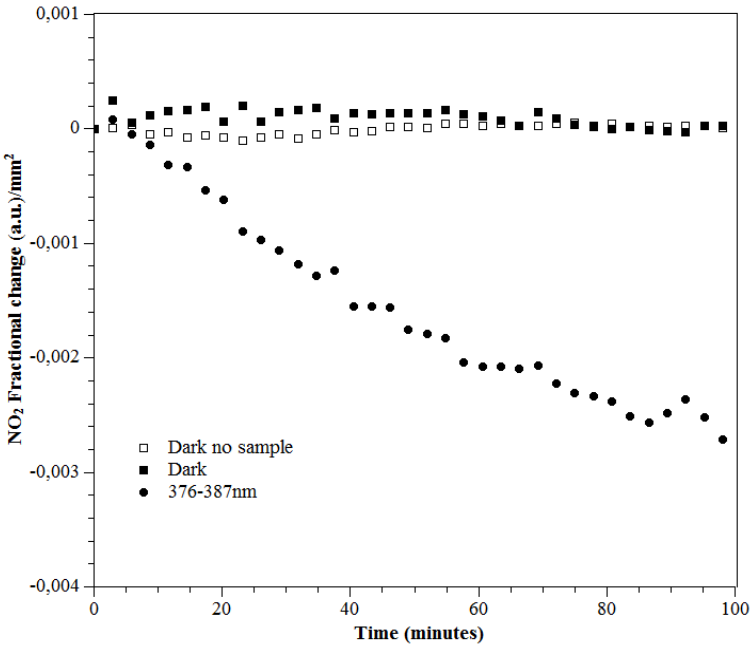

Figure 7.10 – NO_2 breakdown under 376-387 nm carried by FTO coated glass coated at 20 V during 30 s in acetylacetone based solution

The highest efficiency photodegradation ratios were achieved from the coatings prepared on FTO coated glass. The two most active were formed at 20 V for 30 s at 40 V for 10 s in an acetylacetone based solution. The formation of O_2 and N_2 were observed during the photocatalytic reaction, detecting an increment of the O_2 peak, which indicates a reduction of NO_2 into N_2. The stoichiometric is not fully adjusted for O_2, since the O_2 peak is the convolution of species that contains oxygen, such as NO_2, CO_2, H_2O and O_2.

The differences in photocatalytic activity highlighted by Figure 7.11 indicate that the process of electrophoretic deposition can have a dramatic influence on the gaseous photocatalytic activity. The optical microscopy images (Figure 7.7) clearly show differences in the coating microstructure and the presence of varying degrees of surface cracking. It is likely that the presence of surface cracks increase the effective surface area of TiO_2 accessible to the UV irradiation and gases consequently improving influence performance. Figure 7.12 shows two high magnification SEM images which compare the compressed pellet and electrophoretic coating. Agglomerates of nanoparticles are clearly visible on the surface of the compressed pellet, shown in brighter contrast due to surface charging. It is widely accepted that nanoparticles aggregate due to electrostatic forces and would remain in this state during pressing of the pellet. In comparison, when introduced into a liquid, such as the electrolyte used for the deposition process, the particles can de-flocculate. The electrophoretic deposition process provides the opportunity for the nano-particles to adopt a new structure with improved gas and light penetration resulting in a modified photo activity.

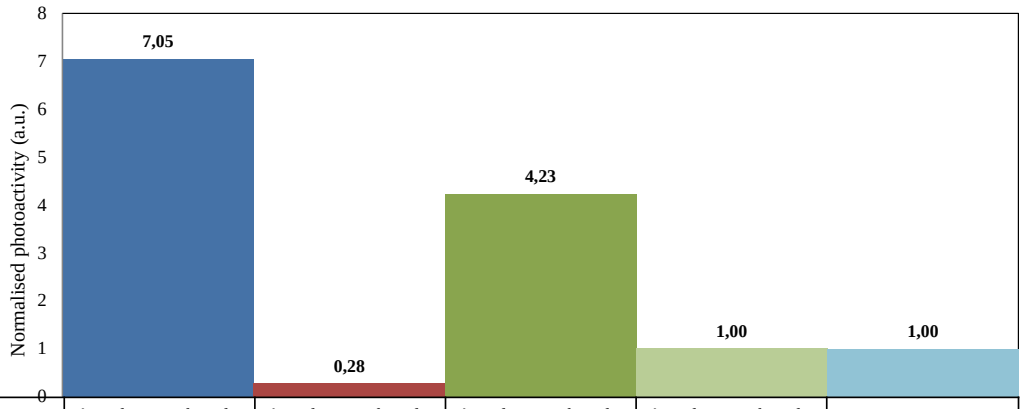

Solvent	Acetylacetone based solution	Acetylacetone based solution	Acetylacetone based solution	Acetylacetone based solution	
Voltage	20V	20V	40V	80V	
Time	30 seconds	50 seconds	10 seconds	50 seconds	
Substrate	FTO glass	FTO glass	FTO glass	Stainless steel	
Photoactivity	7.05	0.28	4.23	1.00	*1*
Picture (scale 500μm)	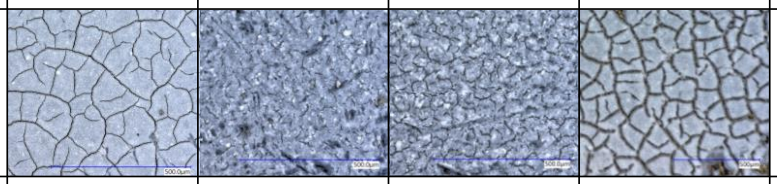				n/a
Thickness	16.4µ	12.2µ	7.3µ	22.3µ	n/a
Roughness	0.77µ	0.56µ	0.75µ	1.84µ	0.15µ
ID	a	b	c	i	n/a

Figure 7.11 – Bar chart of NO_2 decomposition of 5 samples under 376-387 nm for 100 min

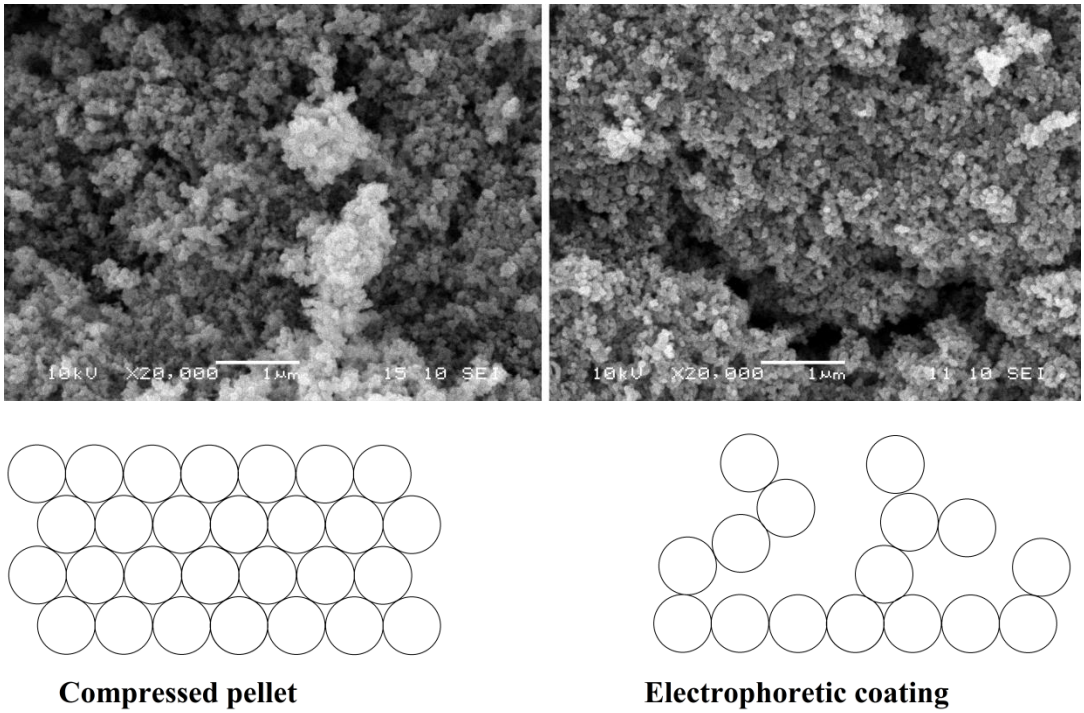

Figure 7.12 – Schematic explanation of how microfractures increase the surface area

Results indicate that the surface morphology at both nano and micro scales play an important role in influencing the photocatalytic performance. In particular these can be summarised as micro surface fractures, identified using digital microscopy in the 100μm range (Figure 7.7) and non-contact profilometry in the 2 μm range (Figure 7.8 and Table 7.2); and nano surface fractures in the order of 0-200 nm, identified by SEM (Figures 7.9 and 7.12).

7.4 Summary

Electrophoretic deposition has been successfully demonstrated to produce TiO_2 anatase coatings on fluorine doped tin oxide (FTO) coated glass, stainless steel and titanium substrates. In terms of mechanical stability, surface roughness and thickness, those parameters were successfully controlled by varying the applied voltage (between 20 and 80 V), deposition time between (10 and 900 s) and electrolyte composition, which was either isopropanol or acetylacetone based. The most uniform and mechanically stable coatings were formed on the FTO coated glass due to the minimization on the stress caused by the thermal mismatch when the sample was calcined at 450 ^{o}C.

The acetylacetone based electrolyte provided better stability to the TiO_2 nano-particle suspension and, performed particularly well for longer exposure times and higher voltages. The photocatalytic degradation of NO_2 exhibited by those coatings are significantly higher photocatalytic activities compared to a press pellet; whilst also displaying good adhesion to the substrate and surface uniformity.

Micro and nano structural analysis of the coatings revealed that the thickness was not a determining factor influencing photocatalytic activity. It is postulated that introduction of nanoparticle agglomerates into the electrolyte allowed the individual particles to disperse thereby promoting the formation of a new nanostructure upon deposition, with improved photocatalytic performance.

7.5 Bibliography

[1] N. N. Ghraïri and Ghrairi, "Structural, morphological and optical properties of TiO_2 thin films synthesized by the Electro-Phoretic deposition technique," *Nanoscale Res. Lett.*, vol. 7, no. 1, p. 357, 2012.

[2] I. G. and L. Binder, "Electrodeposition of nanostructured coatings and their characterisation—a review," *Sci. Technol. Adv. Mater.*, vol. 9, no. 4, p. 43001, 2008.

[3] A. R. Boccaccini, S. Keim, R. Ma, Y. Li, and I. Zhitomirsky, "Electrophoretic deposition of biomaterials," *J. R. Soc. Interface*, vol. 7, no. Suppl 5, pp. S581–S613, 2010.

[4] H. Farnoush, J. A. Mohandesi, and D. H. Fatmehsari, "Effect of Particle Size on the Electrophoretic Deposition of Hydroxyapatite Coatings: A Kinetic Study Based on a Statistical Analysis," *Int. J. Appl. Ceram. Technol.*, vol. 10, no. 1, pp. 87–96, 2013.

[5] G. Mohanty, L. Besra, S. Bhattacharjee, and B. P. Singh, "Optimization of electrophoretic deposition of alumina onto steel substrates from its suspension in iso-propanol using statistical design of experiments," *Mater. Res. Bull.*, vol. 43, no. 7, pp. 1814–1828, 2008.

[6] E. M. Wong and P. C. Searson, "ZnO quantum particle thin films fabricated by electrophoretic deposition," *Appl. Phys. Lett.*, vol. 74, no. 20, 1999.

[7] Y. Hara, J. R. S. Brownson, and M. A. Anderson, "Fabrication of thin-films composed of ZnO nanorods using electrophoretic deposition," *Int. J. Appl. Ceram. Technol.*, vol. 9, no. 1, pp. 115–123, 2012.

[8] X. Nie, A. Leyland, and A. Matthews, "Deposition of layered bioceramic hydroxyapatite/TiO_2 coatings on titanium alloys using a hybrid technique of micro-arc oxidation and electrophoresis," *Surf. Coatings Technol.*, vol. 125, no. 1–3, pp. 407–414, 2000.

[9] C. O. Ayieko, R. J. Musembi, S. M. Waita, B. O. Aduda, and P. K. Jain, "Structural and Optical Characterisation of Nitrogen-doped TiO_2 Thin Films Deposited by Spray Pyrolysis on Fluorine Doped Tin Oxide (FTO) Coated Glass Slides," *Int. J. Energy Eng.*, vol. 2, no. 3, pp. 67–72, 2012.

[10] S. Peng, F. Cheng, J. Liang, Z. Tao, and J. Chen, "Facile solution-controlled growth of $CuInS_2$ thin films on FTO and TiO_2/FTO glass substrates for photovoltaic application," *J. Alloys Compd.*, vol. 481, no. 1–2, pp. 786–791, 2009.

Chapter Eight – Nano structured lime/anatase photocatalytic coatings

Chapter Seven described the electrophoretic coating of materials used for building facades with titanium dioxide. This chapter focuses on the performance of photocatalytic coatings for heritage applications. Coatings were based on a nanolime binder and P25 anatase photocatalytic nano particle component. Nanolime is commonly used in limestone based building as a coating to consolidate weathered stone and enhance mechanical properties. Here, the photocatalytic effect of titanium dioxide on the carbonation of nanolime and its influence of the mixed phase coating on the degradation processes in polluted environments is reported. The SEM/EDX work undertaken in this section was done by Panayiotis Xenophontos as part of his dissertation.

8.1 Material and sample preparation

This section describes the materials that were used, as well as how they prepared.

8.1.1 Substrate

As Bath stone is a widely used as building material in the South West of England, it was used as substrate. A newly quarried Bath stone extracted from the Combe Down mines in Bath (UK) was used. The stone was cut into test specimens 5 × 10 × 10 mm where all surfaces were freshly cut (un-weathered). Each piece was individually cleaned with acetone and distilled water to remove impurities prior to being dried in an oven at 60 ^{o}C for 12 h.

8.1.2 $Ca(OH)_2$ suspension

Nanolime suspension was supplied by IBZ-Salzchemie GmbH & Co. KG (Germany) under the trade name CaLoSiL®. A product with a concentration of 25 g/l in ethanol was used in all cases.

8.1.3 $Ca(OH)_2$-TiO_2 suspension

Anatase in the form of Aeroxide® P25 was supplied by Sigma Aldrich (as described in Chapter Five). It was found that a maximum amount of anatase in CaLoSiL® as a stable colloidal suspension was 7.4 % wt/vol. Therefore, 7.4 %wt/vol of anatase was dispersed and sonicated for about 20 s before the coating application.

8.2 Coating preparation

The coating was applied by immersing the specimens in the suspensions for 10 s, five sides of each specimen (main face of 10 × 10 mm and four sides of 5 × 10 mm) to be evenly covered. After immersion, the specimens remained in air at room temperature for less than a minute to allow evaporation of the ethanol before being placed in the reactor for further tests. Two different coatings were prepared on Bath stone:

i. A specimen coated with nanolime
ii. A specimens coated with a mixture of nanolime and TiO_2.

8.3 Experimental performance

Photocatalytic activity was evaluated for the specimens exposed to different pollutants for 120 hours to atmospheres produced with:

i. Artificial air containing 7 ppm SO_2
ii. Artificial air containing 7 ppm NO_2
iii. Artificial air containing 3.5 ppm SO_2 and 3.5 ppm NO_2.

The concentration of pollutants was set to 7 ppm in all the experiments; previous research showed optimum results after exposing to 5-10 ppm pollutants [1], [2] as well RH remained constant at 7 ppm exposure and 30 % respectively. Table 8.1 shows details of the experimental conditions.

The assessment of the photocatalytic performance was taken in a glass reactor described in Section 3.4 (Chapter Three) under 7 ppm SO_2 exposure and both UV and daylight radiation. UV radiation was obtained from a UV-LED with a wavelength range of 376–387 nm, as described in Section 3.1 (Chapter Three) and total intensity of 8 W/m^2. All other specimens were only exposed daylight to simulate external environmental conditions. The power of the light in the UVA range was 3 mW/m^2.

Table 8.1 – Experimental conditions showing the gas flow and the RH of each experiment. Pollutant concentrations (in ppm) are calculated considering the initial concentration and the mixed volumes of gas. All the experiments were carried for five days

Exposed pollutant	**SO_2 flow (ml/min)**	**NO_2 flow (ml/min)**	**100 % humid air (ml/min)**	**Light irradiation**
7 ppm SO_2	22	-	10	Daylight cycles
7 ppm NO_2	-	22	10	Daylight cycles
3.5ppm SO_2 and 3.5 ppm NO_2	10	10	10	Daylight cycles
7 ppm SO_2 under UV	22	-	10	Constant 8W/m^2

8.4 PHREEQC modelling

Simulations applied in this work were based on previously reported PHREEQC protocols [3]. Initial conditions consisted of 1 kg of pure water at 25 °C with pH=7 (this was set to be as an adjustable parameter to achieve charge balance). The equilibrium phases included two species: gas and solid. CO_2, SO_2 and NO_2 were considered as gas with the respective concentrations calculated according to Table 8.1 and the log of p_{CO2} (in bar) was set to simulate the different partial pressures. The number of moles considered was set to 100 to model the equilibrium with infinite reservoirs. Solid phases considered were modelled using an infinite number of moles and a saturation index (SI) of 0 so that these had to be in equilibrium with the solution at the end of the simulation. Simulations were performed with the thermodynamic data from the Lawrence Livermore National Laboratory database of Berkeley (the LLNL database built in PHREEQC). The PHREEQC input file used is shown in Algorithm 8.1.

Algorithm 8.1 – PHREEQC code used to simulate the dissolution of CO_2, NO_2 and SO_2 and water with and without solid phases. The code shows the model used to simulate the dissolution of 7 ppm of SO_2 and 385 ppm of CO_2 in pure water and in absence of solid phases as initial conditions (‘*hashtags’* inform the software to ignore the code lines where these are located). For each condition described in table 8.1, the gas phases, the gas concentrations and the solid phases were modified by commenting or un-commenting the code with a *hashtag*.

```
SOLUTION 1
 temp 25
 pH 7 charge
 pe 4
 redox pe
 units mol/kgw
 density 1
 Alkalinity 0
 -water 1 # kg
EQUILIBRIUM_PHASES 1
# Calcite 0 1000
# Portlandite 0 1000
 CO2(g) -3.408822658 100
# NO2(g) -5.149185348 100
 SO2(g) -5.149185349 100
END
```

8.4.1 PHREEQC SIMULATION

Table 8.2 reports the activity of CO_3^{2-}, SO_4^{2-} and NO_2^- ions in pure water (i.e. no solid phase was introduced as the initial condition) as calculated by PHREEQC, as Section 1.2.1.2.1 (Chapter One) described, by using different gas mixes and the model shown in Algorithm 8.1 (the simulation number is equivalent to the experiment number in table 8.1). The data show that in pure water, the activity of SO_4^{2-} ion is several order magnitudes higher than the activity of NO_2^- and CO_3^{2-} ions in all conditions.

Table 8.2 - Activity of CO_3^{2-}, SO_4^{2-} and NO_2^- ions in pure water as calculated by the PHREEQC

Simulation number	**Gas phases**	**Ion activity as calculated by PHREEQC**		
		CO_3^{2-}	**SO_4^{2-}**	**NO_2^-**
1	385 ppm CO_2 7 ppm SO_2	1.047×10^{-24}	4.089×10^{-3}	-
2	385 ppm CO_2 7 ppm NO_2	2.700×10^{-24}	-	2.160×10^{-14}
3	385 ppm CO_2 3.5 ppm SO_2 3.5 ppm NO_2	8.872×10^{-26}	6.028×10^{-3}	8.203×10^{-15}

Table 8.3 shows the activity of CO_3^{2-}, SO_4^{2-} and NO_2^- ions when Calcite is introduced as the main solid phase in contact with the solution. Calcite used in this model since it simulates the presence of $CaCO_3$ formed during the carbonation of nanolime. Results show that, as in pure water, the activity of the SO_4^{2-} ion is several order magnitudes higher than the activity of NO_2^- and CO_3^{2-} ions and that in these conditions Anhydrite ($CaSO_4$), Bassanite ($CaSO_4 \cdot 0.5H_2O$) and Gypsum ($CaSO_4 \cdot 2H_2O$) can be formed as solid phases.

Table 8.3 - Activity of CO_3^{2-}, SO_4^{2-} and NO_2^- ions in pure water in equilibrium with calcite and solid phases formed at the end of the simulation

Simulation set up			**Ion activity**			**Solid phases formed**
N.	**Gas phase /ppm**	**Solid phases**	**CO_3^{2-}**	**SO_4^{2-}**	**NO_2^-**	
1	CO_2/385ppm SO_2/7ppm	Calcite	8.031×10^{-9}	1.721×10^{-1}	-	$CaSO_4$ $CaSO_4\cdot0.5H_2O$ $CaSO_4\cdot2H_2O$
2	CO_2/385ppm NO_2/7ppm	Calcite	1.808×10^{-8}	-	2.463×10^{-11}	-
3	CO_2/385ppm SO_2/3.5ppm NO_2/3.5ppm	Calcite	9.270×10^{-9}	1.822×10^{-1}	1.594×10^{-11}	$CaSO_4$ $CaSO_4\cdot0.5H_2O$ $CaSO_4\cdot2H_2O$

Table 8.4 shows the activity of CO_3^{2-}, SO_4^{2-} and NO_2^- ions when both, Calcite and Portlandite are included in the simulation. Portlandite used in this model simulates the presence of uncarbonated nanolime particles during the tests. The results show that, as well as in pure water, and in presence of calcite, the activity of SO_4^{2-} ion is several orders of magnitude higher than the activity of NO_2^- and CO_3^{2-} ions. Furthermore, the results suggest that Anhydrite ($CaSO_4$), Bassanite ($CaSO_4\cdot0.5H_2O$) and Gypsum ($CaSO_4\cdot2H_2O$) are the only solid phases that could be formed at the end of the test.

Table 8.4 - Activity of CO_3^{2-}, SO_4^{2-} and NO_2^- ions in pure water in equilibrium with Calcite and Portlandite, and solid phases that could be produced at the end of the tests

Simulation set up			Ion activity			Solid phases formed
N.	**Gas phases /ppm**	**Solid phases**	**CO_3^{2-}**	**SO_4^{2-}**	**NO_2^-**	
1	CO_2/385ppm SO_2/7ppm	Calcite Portlandite	6.775×10^{-9}	7.822×10^{-2}	-	$CaSO_4$ $CaSO_4\cdot0.5H_2O$ $CaSO_4\cdot2H_2O$
2	CO_2/385ppm NO_2/7ppm	Calcite Portlandite	1.968×10^{-8}	-	1.672×10^{-9}	-
3	CO_2/385ppm SO_2/3.5ppm NO_2/3.5ppm	Calcite Portlandite	1.063×10^{-8}	1.451×10^{-1}	1.032×10^{-9}	$CaSO_4$ $CaSO_4\cdot0.5H_2O$ $CaSO_4\cdot2H_2O$

8.5 Coating characterisation

Micro-morphologies of the Bath stone and coatings used in the tests were evaluated using a JEOL JSM64802V scanning electron microscope, as described in Section 2.3.1 Chapter Two) with a working distance of 10 mm, an accelerating voltage of 15 kV and a spot size of 30 nm. Specimens were coated with a 20 nm thick layer of gold using an Edward Sputter S150B coater to prevent surface charging. Energy Dispersive Spectroscopy (EDX) analysis was performed on uncoated specimens using a working distance of 10 mm, accelerating Voltage of 25 kV and a spot size of 51 nm in high vacuum (25 MPa). Due to its penetration depth (1-2 μm), this technique was used to evaluate the degradation processes carried within the bulk of the coating.

The surface layers (within 1-10 nm) were characterised using X-ray Photoelectron Spectroscopy (XPS) using a Thermo Scientific Theta Probe with an AlK_α (1486 eV) X-ray source, operated at 100 W (Thermo Fisher Scientific Inc., Waltham, MA.) using a flood gun in an operating vacuum of 10^{-8} mbar. The adventitious hydrocarbon C 1s peak at 284.8 eV was used to correct the spectra for specimen charging. The software CASAXPS 2.3.16 RP 1.6 (Casa Software Ltd., Teingmouth, Devon, UK) was used for the peak fitting. The atomic percentage of each element detected was calculated from the peak areas, assuming a Shirley

background and fitted using a Gaussian/Lorentzian ratio and asymmetry factors to give the best fit to the peaks. All the fitted peaks were normalised excluding the area of the adventitious carbon peak.

Wide scan survey spectra were obtained between 0 and 1400 eV binding energy (BE) with pass energy of 200 eV and dwell time of 50 ms. In addition, scans of higher resolution were taken at different BE ranges with pass energy of 40 eV and dwell time of 100 ms for C 1s, N 1s, O 1s, S 2p, Ca 2p and Ti 2p regions.

8.5.1 SEM imagining

Figure 8.1 shows the surfaces of the control specimen (a), of the specimen coated with nanolime (b) and of the specimen coated with the mixed nanolime-titania coating (c) after exposure to SO_2. Figure 8.1a shows how the structure of Bath stone is formed; a distributed set of clusters composed by oolites makes the stone's structure very porous. Bath stone was previously characterised by mercury intrusion porosimetry (MIP) using a Micrometrics AutoPore III [4]. The mayority of the pores were around 10 and 0.1 μm in diameter, and the macro pores were over 100 μm and micropores (between oolites) which are between 10 and 1 μm in diameter. There was no significat change of the control specimen prior to pollutants' exposure. Figure 8.1b shows how the nanolime is evenly distributed on the surface and within the surface pores of the stone, covering the Oolites and making them invisible. Figure 8.1c shows Bath stone covered with a photocatalytic mixed phase nanolime coating. The presence of TiO_2 in the photocatalytic nanolime coating is not visible in the SEM images. Figure 8.1b and 8.1c show a coating with a high surface area. By comparing the coated and uncoated stone images the macropores are not blocked allowing gas and liquid vapour to diffuse into the stone and out.

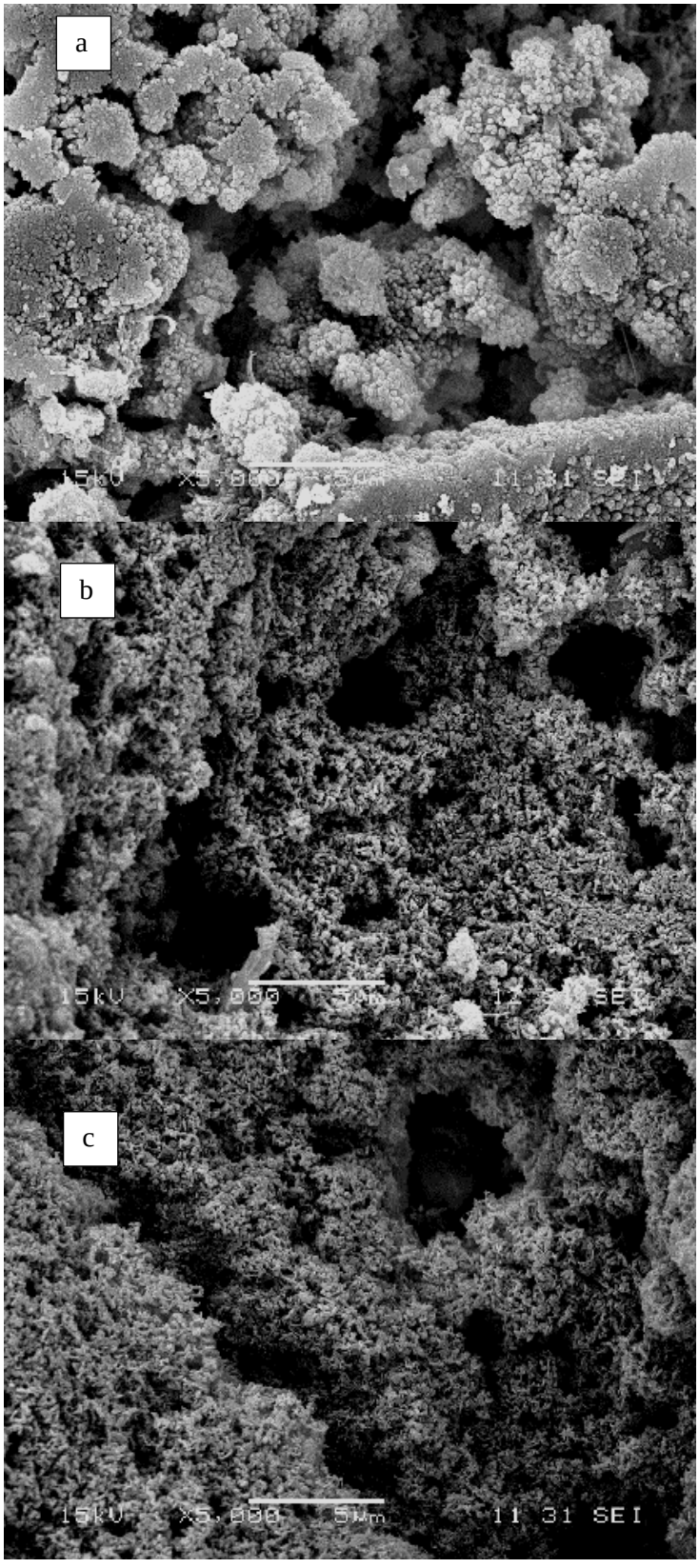

Figure 8.1 - SEM images of: a) uncoated Bath stone after SO_2 exposure; b) nanolime coated Bath stone specimen after SO_2 exposure; c) Bath stone treated with the photocatalytic nanolime coating after SO_2 exposure

8.5.2 EDX analysis

Following exposure to the conditions in Table 8.1, quantitative analysis of the specimens was carried out using energy dispersive X-ray analysis, the results of which are shown in table 8.5. The data in the table is an average calculated from the results of five individual analyses, each carried out at a randomly selected representative location of the specimen surface.

Table 8.5 – Specimen composition determined by EDX spectroscopy on specimens following experimental conditioning exposure

	Specimen	**S (at. %)**	**Ti (at. %)**
7 ppm NO_2 33 %RH Daylight cycles	Untreated	-	-
	Nanolime coating	-	-
	Photocatalytic Nanolime	-	4.4
7 ppm SO_2 33 %RH Daylight cycles	Untreated	0.37	-
	Nanolime coating	2.36	-
	Photocatalytic Nanolime	1.77	7.12
3.5 ppm NO_2+3.5 ppm SO_2 33 % RH Daylight cycles	Untreated	0.56	-
	Nanolime coating	0.34	-
	Photocatalytic Nanolime	1.68	4.4
7 ppm SO_2 33 % RH UV-light	Untreated	0.72	-
	Nanolime coating	2.38	-
	Photocatalytic Nanolime	4.45	6.6

EDX analysis did not detect the presence of nitrogen based molecules in the surface of specimens exposed to 7 ppm of NO_2. Between 4.4 and 7.12 atomic percentage titanium was identified on the specimens coated with TiO_2 whereas no appreciable amount was detected on the other specimens. However in comparison to the specimen exposed to 7 ppm SO_2, results indicated the presence of sulphur, with higher values in the specimens coated with nanolime and photocatalytic nanolime. Exposure to the 3.5 ppm NO_2 and 3.5 ppm SO_2 gas mixture showed a reduction in the amount of sulphur detected on the nanolime coated specimen (0.34 atomic %), compared with the 7 ppm SO_2 exposure, which was within the range of detected sulphur in the untreated specimens (0.37 and 0.56 atomic 0.72 %). The photocatalytic nanolime coating showed a 1.68 atomic % of sulphur which was comparable to the value of 1.77 atomic % obtained for the 7 ppm of SO_2.

8.5.3 X-ray photoelectron spectroscopy

The nature of the surface layer of the specimens after five days exposure was evaluated using XPS analysis, a survey spectra is shown in Figure 8.2. Binding energies and elemental ratios for carbon, nitrogen, oxygen, sulphur, calcium and titanium, calculated to higher resolution spectra in specific regions, are shown in Table 8.6.

The adventitious carbon contamination peak at 284.8 eV was identified on all the specimens examined and used to calibrate the spectra for surface charging, however an additional peak corresponding to $CaCO_3$ was also identified. The binding energy of this peak ranged between 288.6 and 289.2 eV which is in agreement with studies by Kang [5] and Demri [6] who report $CaCO_3$ binding energies of 288.6 and 289.2 eV. The binding energy for the Ca 2p peak ranged between 346.3 and 347.5 eV which is in accordance with previous studies by Ming [7] and Stipp [8] who reported $CaCO_3$ binding energies of 346.5 and 347.7 eV.

The specimens exposed to 7 ppm NO_2 diluted in air did not show the presence of sulphur, indicating that no significant amount of sulphur was present in the specimen stone before testing, and that any sulphur detected on the surface of the specimens exposed to SO_2 originated from a surface reaction. Peaks corresponding to N 1s were identified between binding energies of 399.1 to 400.6 eV, related to the presence of a carbon-nitrogen bond within an organic matrix [9]. In the spectral region corresponding to nitrate (N 1s 407.5 eV) [10] no signal was detected suggesting that $Ca(NO_3)_2$ was not formed.

Binding energies for Ti 2p peaks varied between 458.1 and 459.0 eV, and for O 1s the observed peaks are within the range of 528.8-529.5 eV. These results agreed with studies

carried by Dementjev [11] and Bedri [12], where showed Ti 2p binding energies from 458.0 to 459.4 eV and for O 1s from 529.4 to 530.6 eV. These were attributed to the TiO_2 in the coatings.

The XPS spectra of specimens exposed to 3.5 ppm NO_2 and 3.5 ppm SO_2 also showed S 2p 3/2 peaks at binding energies between 167.8 and 168.3 eV which corresponded to $CaSO_3$. Calculated atomic percentages of 0.5, 0.3 and 0.1 for the untreated, nanolime coating, and photocatalytic nanolime were less than that observed on the specimens exposed to 7 ppm SO_2. These smaller concentrations may be attributed to the lower concentration of SO_2.

The XPS spectra from specimens exposed to 7 ppm SO_2 diluted in air at a relative humidity of 33 % with daylight cycles all showed peaks corresponding to sulphur. The binding energies between 166.6 and 168.6 eV are in agreement with studies by Siriwardane and Hong [13], [14] and characteristic of calcium sulphite (SO_3^{2-}). Compositions of 1.3, 4.5 and 6.7 atomic % for the untreated (stone surface), nanolime coating, and photocatalytic nanolime indicated that the nanolime is more reactive when compared to the stone substrate. This may be attributed to the higher solubility of $Ca(OH)_2$ compared to $CaCO_3$ and the higher surface area of the nanolime compared to stone.

The XPS spectra from specimens exposed to 7 ppm SO_2 diluted in air at 33 % RH under UV light also showed peaks corresponding to sulphur. The binding energies between 168.4 and 168.6 eV observed for the nanolime and untreated stone are in agreement with studies by Siriwardane and Hong [13], [14] and characteristic of calcium sulphite (SO_3^{2-}). The atomic percentages of 3.0 and 5.6 are slightly higher, but still comparable with the equivalent specimens exposed to daylight cycles.

The specimen containing photocatalytic nanolime exposed to UVA had a Ca 2p binding energy of 348.2 eV which was higher than values between 346.3 and 347.5 eV which was detected for all the other specimens. This is comparable to a Ca 2p binding energy of 348 eV observed by Siriwarde [13] for calcium sulphate. A higher binding energy for S 2p 3/2 of 169.9 eV, compared to values ranging between 167.8 and 168.6 eV, is also in agreement with previous research by Moulder et al. [9] who observed a binding energy of 169.4 eV for sulphate. The difference in behaviour of the photocatalytic nanolime under UV irradiation is illustrated in Figure 8.3 which shows the spectra over the S 2p range for the nanolime coated specimen and photocatalytic nanolime. A shift of approximately 2 eV is observed between the S 2p peaks of nanolime coating and photocatalytic coating. On nanolime $CaSO_3$ was observed whereas for the photocatalytic coating $CaSO_4$ was generated.

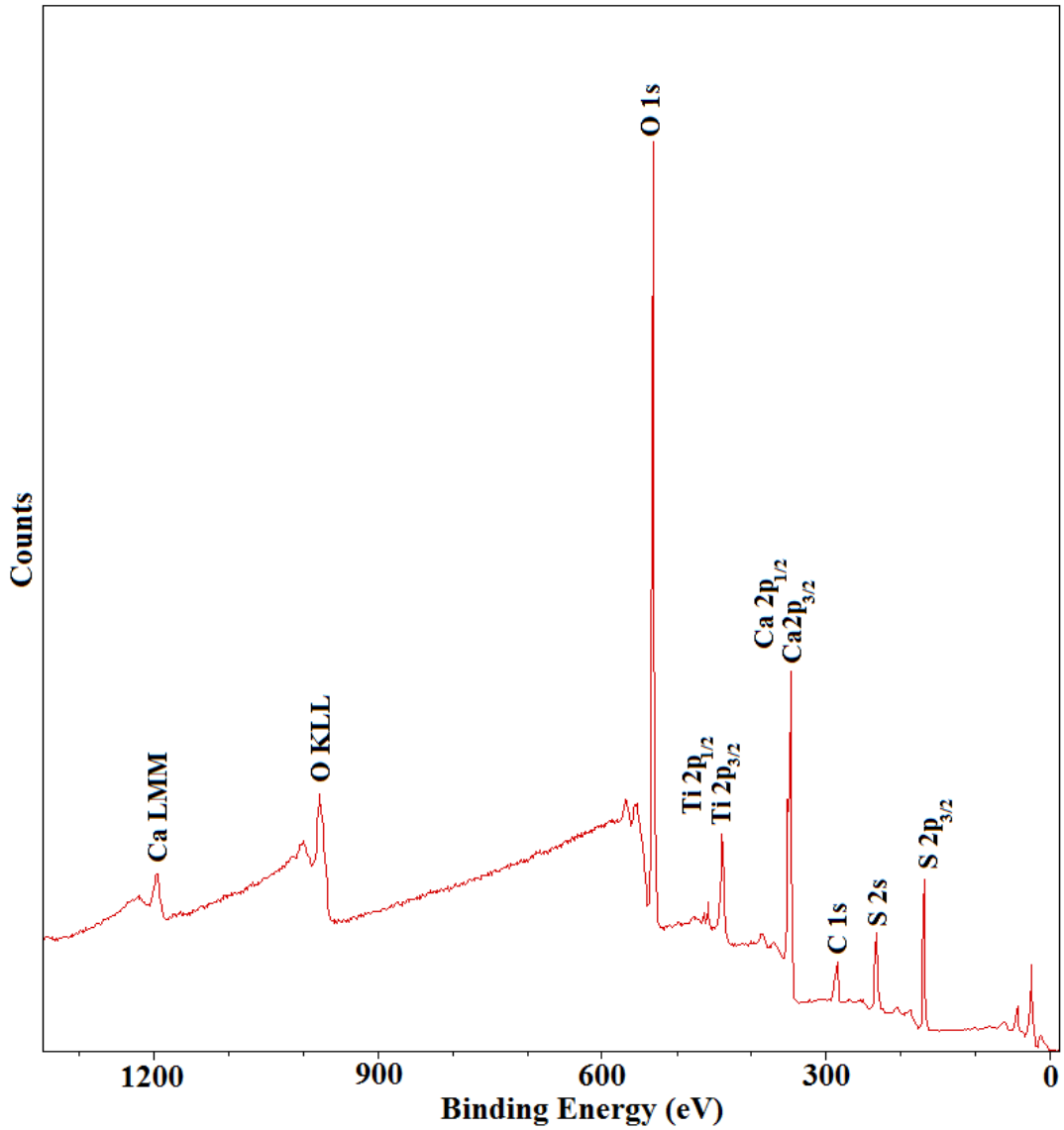

Figure 8.2 – XPS spectra of photocatalytic nanolime coated Bath stone after five days of 7 ppm SO_2 exposure under UV irradiation

Table 8.6 – Element ratios and chemical state derived from XPS analysis

Experimental conditions	Specimen ID	**Binding energy (eV)**/Relative concentration (at. %)							
		C 1s	**N 1s**	**O 1s**		**S $2p_{3/2}$**		**Ca $2p_{3/2}$**	**Ti $2p_{3/2}$**
		CO_3^{2-}	**Organic matrix**	**CO_3^{2-}**	**TiO_2**	**SO_3^{2-}**	**SO_4^{2-}**	**Ca^{2+}**	**TiO_2**
7 ppm NO_2 33 % RH Daylight cycles	Untreated	**288.6**/ 9.0	**399.5**/ 1.5	**531.5**/82.1	-	-	-	**346.4**/7.4	-
	Nanolime coating	**289.1**/ 13.2	**399.2**/ 0.4	**531.3**/69.2	-	-	-	**346.8**/17.2	-
	Photocatalytic Nanolime	**288.8**/ 11.2	**399.3**/ 0.7	**530.9**/66.4	**528.8**/2.1	-	-	**346.6**/14.5	**458.1**/ 5.1
7 ppm SO_2 33 % RH Daylight cycles	Untreated	**288.9**/14.2	**399.3**/ 0.9	**531.0**/70.6	-	**167.9**/ 1.3	-	**346.3**/13.0	-
	Nanolime coating	**288.7**/13.4	**399.1**/ 0.3	**530.9**/64.7	-	**166.6**/ 4.5	-	**346.4**/17.2	-
	Photocatalytic Nanolime	**288.8**/ 3.2	**399.1**/ 0.6	**532.0**/74.1	-	**168.6**/ 6.7	-	**347.3**/13.4	**459.0**/ 2.0
3.5 ppm NO_2 +3.5 ppm SO_2 33 % RH Daylight cycles	Untreated	**288.8**/ 8.5	**399.7**/ 1.7	**531.7**/81.6	-	**167.9**/ 0.7	-	**346.7**/7.7	-
	Nanolime coating	**289.0**/ **1**5.2	**399.8**/ 0.7	**530.8**/66.8	-	**167.8**/ 0.4	-	**346.3**/16.9	-
	Photocatalytic Nanolime	**289.1**/10.9	**399.2**/ 0.1	**531.0**/65.3	**528.9**/3.8	**168.3**/ 0.2	-	**346.7**/13.8	**458.9**/ 5.9
7 ppm SO_2 33 % RH UV exposure	Untreated	**288.8**/ 9.3	**399.7**/ 1.5	**531.7**/75.2	-	**168.6**/ 3.0	-	**346.9**/11.0	-
	Nanolime coating	**289.0**/ 6.4	**400.6**/ 0.2	**532.2**/74.8	-	**168.4**/ 5.6	-	**347.5**/13.1	-
	Photocatalytic Nanolime	**287.8**/ 2.2	**400.2**/ 0.3	**532.4**/61.1	**529.5**/8.3	-	**169.4**/ 12.1	**348.2**/12.1	**459.0**/ 4.0

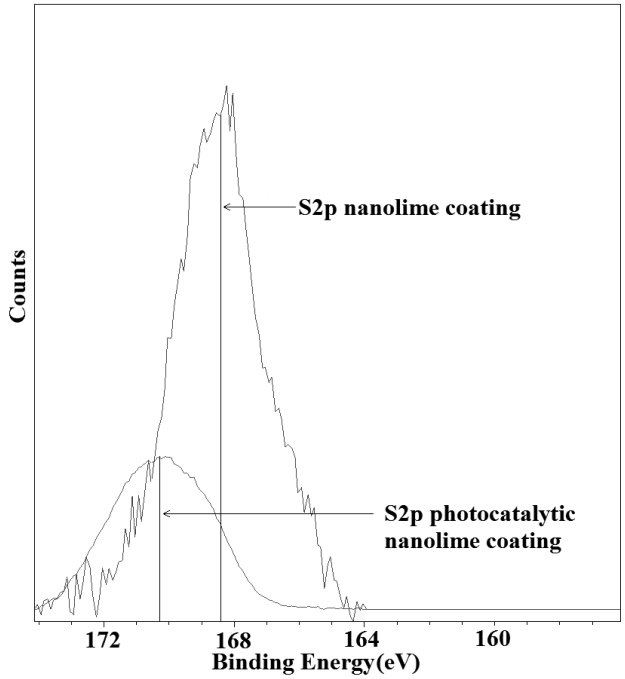

Figure 8.3 –XPS spectra of sulphur $2p_{3/2}$ region for nanolime and photocatalytic nanolime coated Bath stone after five days exposure to 7 ppm SO_2 under UV irradiation

8.6 Photocatalytic degradation of gaseous pollutants

The photocatalytic coating which was exposed to UV light was selected to study its photocatalytic activity in gas phase under two different UV LED light source. Figure 8.4 and 8.5 show the fractional change of CO_2 and NO_2 related to argon over a period of 100 min.

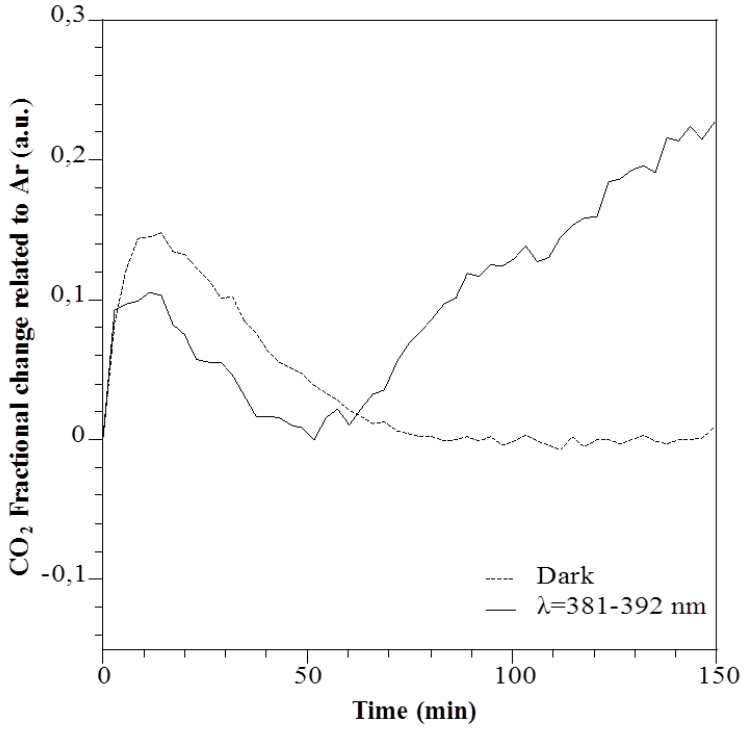

Figure 8.4 - Fractional reduction of CO_2 related to Ar over time under different conditions

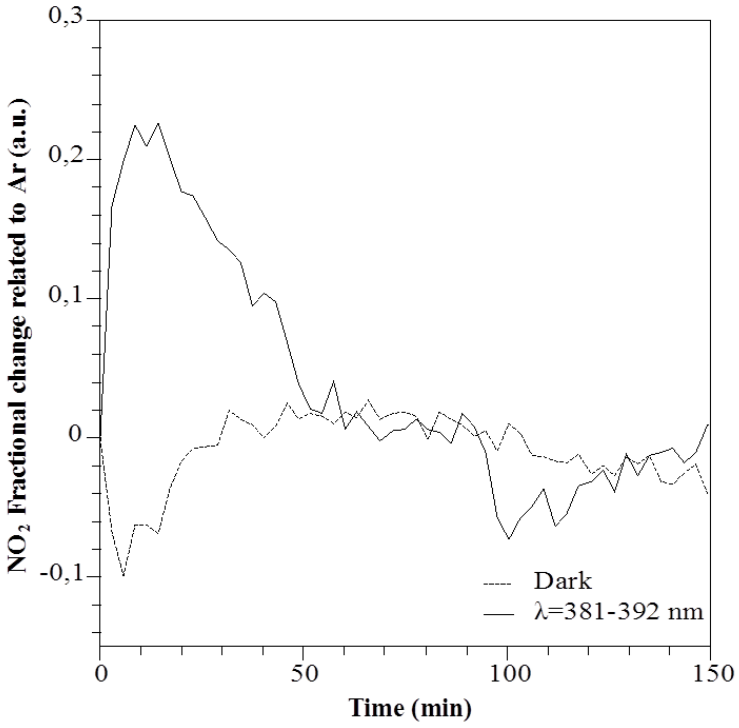

Figure 8.5 - Fractional reduction of NO_2 related to Ar over time under different conditions

As Figures 8.4 and 8.5 show, there was no stability of the baseline signal. Even when the experiment was carried in the dark, the signal of the detected gaseous molecules was erratic. This was due to the physical properties of the sample. Bath stone is very porous; prior starting the experiment, the reactor is purged (up to 10^{-6} bar) and filled with the desired gas composition, thereby changing the balanced gas composition inside the stone's pores.

8.7 Discussion

The combined results given by EDX and XPS reveal a difference in the elemental concentration between the bulk of the coating (1-2 μm) and the surface layer (maximum 10 nm). The concentration of CO_2 in the gas mixture was approximately 55 times higher than that of the NO_2 and SO_2, however the concentration of sulphur compounds detected on the surface was similar to the $CaCO_3$ detected. Simulations using PHREEQ suggest that, because of the very low activity of the NO_2^- ion in aqueous solution only the solid phases produced by the interaction of SO_2 with the system should be detected at the end of the experiments.

For the experiment that exposed specimens to 7 ppm of NO_2, the exposure did not affect the composition within the bulk; it is possible that the gas concentration or the activity of nitrogen ions was too low to produce phases detectable by EDX. In addition, XPS showed a small amount of organic matrix in the outermost layer.

The formation of $CaSO_4$ on the surface of carbonate containing materials historically used in construction, such as limestone, is widely accepted. However previous research, under atmospheric conditions, by Chin [15] describes the formation of $CaSO_4$ as a two stage process involving the initial formation of $CaSO_3$ (IV) which is followed by further oxidation to sulphate (VI) [15]. The rate of these two reactions is dependent on the local water and oxygen concentrations.

Analysis of the S $2p_{3/2}$ binding energies obtained for the XPS spectra from the specimens indicated the presence of SO_3^{2-} in the form of calcium sulphite. This phase was identified on the uncoated limestone surface in addition to nanolime and photocatalytic nanolime surfaces. The concentration of sulphur on surfaces coated with nanolime and photocatalytic nanolime was three times higher than that on the stone surface due to the presence of more reactive $Ca(OH)_2$ and the associated higher surface area. EDX indicated a six-fold increase, the higher value compared to XPS, was attributed to the greater penetration depth of the analysis into the specimen surface.

The addition of anatase to the nanolime, increased the surface area and the absorption of SO_2 and NO_x onto the outermost layer of material. When the photocatalytic nanolime coating was exposed to UV irradiation, XPS revealed the presence of SO_4^{2-} as calcium sulphate. Compared to all the other specimens examined the amount of $CaCO_3$ detected was considerably lower.

The presence of calcium sulphate suggests reaction with sulphuric acid opposed to sulphurous acid. Margitan [16] demonstrated that a hydroxyl radical can initiate the oxidation of SO_2 into SO_3 as described by Equations 8.1-8.2. This radical is known to readily form on the surface of photocatalysts such as anatase under illumination with UV light [17]–[19].

$$SO_2 + \bullet OH \rightarrow HOSO_2 \bullet \quad (8.1)$$

$$HOSO_2 \bullet + \bullet OH \rightarrow H_2O + SO_3 \quad (8.2)$$

Sulphuric acid can form by the reaction of SO_3 with water as shown in Equation 8.3, however reaction with the hydroxyl radical has also been shown to lead to the formation of sulphuric acid as in Equation 8.4.

$$SO_3 + H_2O \rightarrow H_2SO_4 \quad (8.3)$$

$$SO_2 + 2 \bullet OH \rightarrow H_2SO_4 \quad (8.4)$$

When the sulphuric acid is formed, it reacts with $Ca(OH)_2$ and $CaCO_3$ as shown in Equations 8.5 and 8.6 to form calcium sulphate.

$$H_2SO_4 + Ca(OH)_2 \rightarrow 2H_2O + CaSO_4 \quad (8.5)$$

$$H_2SO_4 + CaCO_3 \rightarrow CaSO_4 \quad (8.6)$$

8.8 Summary

This chapter focused into the effect of the addition of photocatalytic TiO_2 on the carbonation process of nanolime and its degradation process when exposed to SO_2. There was no evidence of nitration under exposure to 7 ppm NO_2 for all the materials evaluated in this study. The concentration of nitrogen deposited as organic matrix was increased when the gas composition consisted of 3.5 ppm of SO_2 and 3.5 ppm of NO_2.

In the case of the specimens coated with nanolime the results show a preferential reaction of $Ca(OH)_2$ with SO_2 relative to CO_2, which is further enhanced in presence of anatase and UV light.

Results show the presence of anatase increased the deposition of sulphur and nitrogen when the specimens were exposed to 7 ppm of SO_2 and UV light, and the $CaSO_4$ generated reduced carbonation. This was attributed to the oxidation of SO_2 to SO_3 by hydroxyl radicals generated on the surface of nano-anatase thus forming sulphuric acid opposed to sulphurous acid.

Results from the photocatalytic nanolime formulation suggest they could be used to reduce atmospheric pollutant levels through creation of a sacrificial layer which reacts preferentially with SO_2. Such coatings have the potential to prevent further damage to limestone façades and could be applied in cities where pollution is detrimental to historic buildings. In addition to the absorption of CO_2 and SO_2 during the healing process, this coating would carry further photocatalytic reactions once the carbonation process of $Ca(OH)_2$ is completed.

8.9 Bibliography

[1] G. C. Allen, A. El-Turki, K. R. Hallam, D. McLaughlin, and M. Stacey, "Role of NO_2 and SO_2 in degradation of limestone," *Br. Corros. J.*, vol. 35, no. 1, pp. 35–38, 2000.

[2] G. C. Allen, A. El-Turki, K. R. Hallam, D. McLaughlin, and M. Stacey, "Role of NO_2 and SO_2 on the degradation of limestone," in *Stone deterioration in polluted urban environments*, vol. 3, D. J. Mitchell and D. E. Searle, Eds. CRC publisher, 2004, pp. 119–130.

[3] C. A. J. Appelo and D. Postma, *Geochemistry, Groundwater and Pollution, Second Edition*. Boca Raton, FL: CRC Press/Taylor & Francis, 2005.

[4] G. L. Pesce, D. Morgan, D. Odgers, A. Henry, M. Allen, and R. J. Ball, "Consolidation of weathered limestone using nanolime," *Proc. ICE - Constr. Mater.*, vol. 166, pp. 213–228, 2013.

[5] I.-C. Kang, Q. Zhang, S. Yin, T. Sato, and F. Saito, "Preparation of a visible sensitive carbon doped TiO_2 photo-catalyst by grinding TiO_2 with ethanol and heating treatment," *Appl. Catal. B Environ.*, vol. 80, no. 1–2, pp. 81–87, 2008.

[6] B. Demri and D. Muster, "XPS study of some calcium compounds," *J. Mater. Process. Technol.*, vol. 55, no. 3–4, pp. 311–314, 1995.

[7] M. Ni and B. D. Ratner, "Differentiation of Calcium Carbonate Polymorphs by Surface Analysis Techniques – An XPS and TOF-SIMS study," *Surf. Interface Anal.*, vol. 40, no. 10, pp. 1356–1361, 2008.

[8] S. L. Stipp and M. F. Hochella, "Structure and bonding environments at the calcite surface as observed with X-ray photoelectron spectroscopy (XPS) and low energy electron diffraction (LEED)," *Geochim. Cosmochim. Acta*, vol. 55, no. 6, pp. 1723–1736, 1991.

[9] J. F. Moulder, W. F. Stickle, P. E. Sobol, and K. D. Bomben, *Handbook of X-ray photoelectron Spectroscopy*. Eden Prairie: Perkin-Elmer Corporation, 1992.

[10] A. B. Christie, J. Lee, I. Sutherland, and J. M. Walls, "An XPS study of ion-induced compositional changes with group II and group IV compounds," *Appl. Surf. Sci.*, vol. 15, no. 1–4, pp. 224–237, 1983.

[11] A. P. Dementjev, "Altered layer as sensitive initial chemical state indicator," *J. Vac. Sci. Technol. A Vacuum, Surfaces, Film.*, vol. 12, no. 2, p. 423, 1994.

[12] B. Erdem, R. A. Hunsicker, G. W. Simmons, E. D. Sudol, V. L. Dimonie, and M. S. El-Aasser, "XPS and FTIR surface characterisation of TiO_2 particles used in polymer encapsulation," *Langmuir*, vol. 17, no. 9, pp. 2664–2669, 2001.

[13] R. V Siriwardane and J. M. Cook, "Interactions of SO_2 with sodium deposited on CaO," *J. Colloid Interface Sci.*, vol. 114, no. 2, pp. 525–535, 1986.

[14] H. Lu and P. G. Smirniotis, "Calcium oxide doped sorbents for CO_2 uptake in the presence of SO_2 at high temperatures," *Ind. Eng. Chem. Res.*, vol. 48, no. 11, pp. 5454–5459, 2009.

[15] T. Chin, R. Yan, and D. T. Liang, "Study of the reaction of lime with HCl under simulated flue gas conditions using X-ray diffraction characterisation and thermodynamic prediction," *Ind. Eng. Chem. Res.*, vol. 44, no. 23, pp. 8730–8738, 2005.

[16] J. J. Margitan, "Mechanism of the atmospheric oxidation of sulfur dioxide. Catalysis by hydroxyl radicals," *J. Phys. Chem.*, vol. 88, no. 15, pp. 3314–3318, 1984.

[17] A. Z. Fujishima X., "Titanium dioxide photocatalysis: present situation and future approaches," *Comptes Rendus Chim.*, vol. 9, no. 5–6, pp. 750–760, 2006.

[18] A. Fujishima, T. N. Rao, and D. A. Tryk, "Titanium dioxide photocatalysis," *J. Photochem. Photobiol. C Photochem. Rev.*, vol. 1, no. 1, pp. 1–21, 2000.

[19] O. Carp, C. L. Huisman, and A. Reller, "Photoinduced reactivity of titanium dioxide," *Prog. Solid State Chem.*, vol. 32, no. 1–2, pp. 33–177, 2004.

Chapter Nine – General discussion

Over the previous chapters, results have been shown and analysed. Chapter Three and four focused on experimental techniques to assess photocatalytic activity of TiO_2. Chapter Five characterised and discussed the photocatalytic activity of commercially available TiO_2 powders and TiO_2 coatings. In Chapter Six, titanium sub-oxide species were developed to improve the efficiency in the photocatalytic process, and Chapters Seven and Eight described the preparation of novel coatings based on TiO_2 and their characterisation. This chapter brings the experimental results from the Chapters Five, Six and Seven together.

9.1 Assessment of TiO_2 photocatalysis

The experimental use of an electron impact-mass spectrometer has been proved as an important technique to study photocatalysis. The main advantage of this technique amongst others more common is its versatility to analyse different gaseous molecules and simultaneously to modify parameters such as light source properties, gas composition and temperature, if required. A new protocol has been established allowing the reduction of errors that are usually a result of instability in the mass spectrometer over time.

To compare the results obtained from gas phase, results from the degradation of methylene blue in aqueous phase were presented. Under UV irradiation, the photoactivity of TiO_2 was different between gas and aqueous phase.

Due to its simplicity, the degradation of methylene blue in aqueous phase is a widely used method. Anatase powders were able to degrade more than 90 % of the dye in aqueous phase, but only P25 performed in gas phase. 7000 and PC500 band gaps were found at ~370 nm, whereas P25 was ~380 nm. This difference in the band gaps was critical when the photoactivity of the powders was studied under gas phase. An insufficient number of photons with the required energy were irradiated on the photocatalyst's surface. In addition to this, reactions in gas phase have lower probabilities of collision between molecules due to a fewer amount of molecules than in aqueous phase.

Bionictile's photocatalytic property was also studied for bacterial degradation. Although in aqueous phase, bionictile did not degrade methylene blue, it was very effective against *E. coli*. This is due to the smaller volume used for this test (75 µl), whereas for methylene blue, a solution of 60 ml was used instead. Considering the exposed area was 2.3 cm^3, the ratio area/volume is three orders of magnitude higher for the bacteria analysis, being a fundamental factor. In the gas phase, bionictile, and all the rest of the commercially available coatings were unable to remove both CO_2 and NO_2.

For anatase P25 and rutile, it was found that H_2O was not the key reactant against pollutants. The reactivity of NO_2 on a photocatalytic surface with H_2O to form HNO_3 has been widely reported and in this research project, confirmed. In the case of CO_2 removal, it was found that the radicals that reacted against it were generated from O_2. A mechanism has been proposed, involving a first step in which CO_2 anchors on TiO_2 surface. Once it is anchored, an electron transfer would break a double bond C-O, allowing C to react with a superoxide radical to generate CO_3^{2-}, being the reason why there is a net loss of CO_2 in the gas phase.

From the three most common polymorphs of titania, rutile, anatase and brookite; anatase revealed the best performance over the others. This result is in accordance with the literature.

Therefore P25 was chosen as reference material and photocatalyst for the coatings.

9.2 Tailing photocatalytic properties

Chapter six showed how rutile's photocatalytic can be enhanced by reducing TiO_n phases. This is attributed to improvements in the charge distribution process. Localized titanium sub-oxide phases increased the electrical conductivity. Working at different reduction temperatures, the amount of those sub-oxide phases was controlled. The analysis in aqueous phase showed how titanium sub-oxide phases, present in rutile resulted in a decay on the photoactivity. This is due to the contact of the catalyst with H_2O that does not require an improvement in the charge distribution process, because each generated electron and hole will react with H_2O producing radicals.

In gas phase, the optimum temperature range to enhance photo-catalytic properties was 350°C to 400°C and demonstrates that the photo-catalytic performance of TiO_2 can be improved by the introduction of defects into the lattice by carbo-thermal reduction.

9.3 TiO_2 Coatings

Electrophoretic deposition was used as potential technique to coat pre-fabricated panels for construction. The only requirement is the conductivity of the substrate. Parameters, such as solvent, deposition time and voltage were studied in order to optimise them. The acetylacetone based electrolyte provided better stability to the TiO_2 nano-particle suspension and, performed particularly well for longer exposure times and higher voltages. The photoactivity of coatings was significantly higher than the reference material (compressed pellet of pure anatase P25), revealing how the micro and nano structure the coatings was a determining influence of their photocatalytic activity. In this thesis, it was proposed that agglomerates of nanoparticles during the electrophoretic deposition process allowed the individual particles to disperse thereby promoting the formation of a new nanostructure upon deposition, with improved photocatalytic performance.

A dip coating technique was used to mimic how a coating would be applied in historic buildings. Nanolime, which is a commercial limestone consolidant, was used as binder in a formulation which its active material was anatase P25. When $Ca(OH)_2$ is in presence of CO_2

and H_2O, it carbonates. Therefore, limestone will be reinforced with $CaCO_3$, which is the main component of limestones.

Results from the application of anatase alongside with nanolime, showed a highly reactivity with SO_2 than CO_2, forming $CaSO_3$. When this formulation was exposed to UV light, the main component was $CaSO_4$ instead of $CaSO_3$. This was attributed to the oxidation of SO_2 to SO_3 by hydroxyl radicals generated on the surface of nano-anatase. The resulting generated acid in contact with H_2O was sulphuric acid opposed to sulphurous acid.

Chapter Ten – Conclusions and further work

The research presented in this thesis has explored the use of photocatalysis for pollution remediation in urban areas. The methodology focuses on the characterisation of TiO_2 particles for a better understanding of the properties most influential in determining the photocatalytic activity. For this purpose, the use of an electron impact-mass spectrometer for the study of gas phase photocatalysis was described in **Chapter Four**. The design of a bespoke instrument able to simultaneously analyse a range of gaseous molecules to study photocatalytic reactions in gas phase was the first stage of the research detailed in this thesis.

i. The optimum working conditions to stabilise the mass spectrometer ion source were at 70 eV electron energy and 1.2 mA of emission current, increasing the detection for NO_2.
ii. To reduce errors from instability in the ion source over time, a novel protocol that compares the fractional change in the specie of interest to that of an internal standard (argon) was proposed. This allowed gaseous absorption on the samples to be distinguished from pure photocatalytic degradation.

In **Chapter Five**, three polymorphs of TiO_2 were studied. These included three different commercially available anatase powders, commercially available rutile and a natural mineral sample of brookite. Physical and chemical properties were characterised using techniques such as: Raman spectroscopy, XPS, XRD, band gap characterisation, BET and surface morphology analysis, while their photocatalytic properties were evaluated using dye removal in an aqueous phase and gaseous pollutant removal.

Aeroxide P25 proved to be the most efficient photocatalyst, in aqueous phase as well as gas phase. Rutile, the most stable polymorph, also showed photocatalytic activity, being more active in the gas phase, whereas brookite was unable to promote a photocatalytic reaction.

The removal of NO_2 in the presence of H_2O, with HNO_3 as product was observed. The capability of TiO_2 to decompose CO_2 in the presence of O_2 was also detected, and a mechanism to explain the decrease of CO_2 and O_2 via CO_2 anchoring on the TiO_2 surface has been proposed.

XPS examination of the commercial coatings revealed a small concentration of TiO_2 on the surface. This was due to the coating procedure which covered the photocatalyst with other compounds, such as Al_2O_3 or SiO_2. Therefore TiO_2 was unable to absorb UV light, inactivating its photocatalytic properties. From the photocatalytic assessment analysis, none of the coatings showed photoactivity in the aqueous or the gas phase against NO_2 and CO_2.

Bionictile was used to test the biocide properties of a photocatalytic coating against *E. coli*. It was able to kill 56 % of bacterial cells within 15 min.

In order to improve rutile's photocatalytic properties without adding a doping agent, the reduction of TiO_2 under an inert atmosphere was studied (**Chapter Six)**. Specimens reduced over a range of temperatures which started at 300 °C and finished at 1300 °C was studied. The optimum temperature range to enhance photo-catalytic properties was from 350 °C to 400 °C, which was attributed to improvements in the charge distribution process.

The final stage of the thesis aimed to assess the application of photocatalytic coatings suitable for the built environment. For this, two techniques were studied; electrophoretic deposition for application *off site* and dip coating for applications *in situ.*

In **Chapter Seven** electrophoretic deposition has been successfully demonstrated to produce TiO_2 anatase coatings on FTO-coated glass, stainless steel and titanium substrates. Electrophoretic parameters were optimised by varying the applied voltage between 20 and 80 V, deposition time between 10 and 900 s, substrate and electrolyte composition, which was either isopropanol or acetylacetone based. Deposition using an acetylacetone electrolyte at voltages from 20 to 40 V and a deposition time no longer than 30 s produced coatings with the highest photoactivity.

Coatings on FTO-coated glass showed the most uniform and mechanically stable coating. This is attributed to the minimisation on the stress caused by the thermal mismatch when the sample was calcined at 450 ºC.

In **Chapter Eight**, the effect of the addition of photocatalytic TiO_2 on the carbonation process of nanolime was studied under different gas compositions.

i. There was no evidence of nitration under exposure to 7 ppm NO_2 nor 3.5 ppm of SO_2 and 3.5 ppm of NO_2.
ii. Under exposure to 7 ppm SO_2, $Ca(OH)_2$ reacted preferentially with SO_2, producing only $CaSO_3$.
iii. Under exposure to 7 ppm SO_2, $Ca(OH)_2$ in presence of anatase and UV light $Ca(OH)_2$ reacted preferentially with SO_2, producing only $CaSO_4$ due to the photocatalytic oxidation of SO_2 to SO_3 by hydroxyl radicals.

In **Chapter Nine,** the results from Chapters Four, Five, Six, Seven and Eight were discussed as a whole. Commercially available TiO_2 powders have shown photocatalytic activity; although testing them in the aqueous phase cannot be relied on as a direct measurement to predict their performance for the removal of pollutants in a gaseous environment. Coatings prepared from anatase P25 showed a greater ability to photo catalytically remove CO_2 and NO_2 compared to a pressed pellet of differing surface morphology. These results give great promise for the application of photo-catalysts in the built environment and demonstrate the feasibility of using such coatings. Moreover, the combined use of anatase with nanolime for the consolidation and protection of limestone masonry represents an area worthy of further study. In particular the effect of free radicals generated from photocatalytic oxidation in combination with species normally present and responsible for the carbonation of $Ca(OH)_2$.

The implications of titanium suboxide species on the photocatalytic process revealed a new approach to improve photocatalysts beyond changing their bandgaps. By stabilising the charge separation process (hole/electron) via electric conductivity, the photocatalytic activity in the gas phase was shown to increase.

10.1 Further work

In the present work, the use of TiO_2 for pollution removal was evaluated by mass spectrometry. Unfortunately nowadays not only NO_2, SO_2 and CO_2 are a matter of concern, but VOC's, such as benzene, toluene, formaldehyde or methyl tert butyl ether are a major issue for indoor air quality. The versatility of mass spectrometry would allow its use as a detector for VOC's.

Regarding the decomposition of CO_2 in presence O_2, further investigations should be performed to resolve the mechanism that has been proposed in this thesis. Computational studies, such as Monte Carlo simulations would allow modelling and surface analysis immediately after the reactions can discern the structure of the product. In addition to this calculation, the use of a FT-IR coupled to the reaction chamber would allow study of the evolution of the C=O band, in the absorption region of 1500-1900 cm^{-1}.

Doped-TiO_2 has been extensively studied and optimised, but the area of self-doped anatase (Ti^{3+}-Ti^{4+}) is promising. An effective routine of reducing anatase under inert atmosphere to TiO_x should be studied in greater detail.

Growing concerns over the safety of nanoparticles are leading to the introduction of greater safety measures in their use. Thus, the potential application of TiO_2 nanoparticles as photocatalyst is at risk. Chemical routes to prepare (doped or undoped) TiO_2 are well known, allowing titanium precursors to hydrolyse and create nanoparticles with relative ease to control. The inherent risk of such small particles is an important motive for further research to allow more 'real world' applications.

To avoid such problem, functionalising bigger particles with TiO_2 or insertion into zeolites is proving to be effective, however in some cases this comes with a loss of photocatalytic activity. A potential advantage can be the use of nanosized $Ca(OH)_2$, hexagons with a nanometric thickness and a large area, which can react with titanium precursors to create "encored TiO_2" with a high surface area. The stability of TiO_2 on those large particles would be optimum, as it would be anchored to $Ca(OH)_2$ before complete carbonation, allowing the TiO_2 particles to adhere to the surface, as shown in Equations 10.1-10.3 (^{i}PrO stands for $(CH_3)CH_2O$):

$$Ca(OH)_2 + Ti(^iPrO)_4 \rightarrow Ca(OH)\{TiO(^iPrO)_3\} + {}^iPrOH \quad (10.1)$$

$$CO_2 + Ca(OH)\{TiO\,(^iPrO)_3\} \xrightarrow{H_2O} Ca(HCO_3)\{TiO_3\} + {}^iPrOH \quad (10.2)$$

$$Ca(HCO_3)\{TiO_3\} \xrightarrow{\Delta T} CaO - TiO_2 + CO_2 \uparrow \quad (10.3)$$

For novel methods to formulate TiO_2 coatings, the use of monomers as solvent/binder must be considered. Certain polymers, well known in industry due to their wide range of applications, such as polyvinyl acetate, are prepared via free radical polymerisation. Vinyl acetate, which is a colourless liquid, can be the medium where TiO_2 is dispersed. When TiO_2 is irradiated by a UV photon, the creation of an e^--h^+ pair will initiate the free radical polymerisation.

Publications

These papers have been removed due to copyright concerns.

The papers in question are:

Nuño, M., Ball, R. J. and Bowen, C. R. (2014), Study of solid/gas phase photocatalytic reactions by electron ionization mass spectrometry. J. Mass Spectrom., 49: 716–726.

http://dx.doi.org/10.1002/jms.3396

Nuño, M, Ball, RJ, Bowen, CR, Kurchania, R & Sharma, GD (2015), Photocatalytic activity of electrophoretically deposited (EPD) TiO_2 coatings *Journal of Materials Science*, vol 50, no. 14, pp. 4822-4835

http://dx.doi.org/10.1007/s10853-015-9022-0

Building and Environment 92 (2015) 734–742

Contents lists available at ScienceDirect

Building and Environment

journal homepage: www.elsevier.com/locate/buildenv

Environmental performance of nano-structured $Ca(OH)_2/TiO_2$ photocatalytic coatings for buildings

Manuel Nuño [a], Giovanni L. Pesce [a], Chris R. Bowen [b], Panayiotis Xenophontos [a], Richard J. Ball [a, *]

[a] BRE Centre for Innovative Construction Materials, Department of Architecture and Civil Engineering, University of Bath, Claverton Down, BA2 7AY, UK
[b] Department of Mechanical Engineering, University of Bath, Claverton Down, BA2 7AY, UK

ARTICLE INFO

Article history:
Received 17 March 2015
Received in revised form
5 May 2015
Accepted 18 May 2015
Available online 27 May 2015

Keywords:
Stone decay
Photocatalysis
Pollutant
Sulphur dioxide
Nitrogen dioxide
Calcium hydroxide
Limestone

ABSTRACT

This paper describes the environmental performance of a mixed phase coating (photocatalytic nanolime) manufactured from a colloidal nano-structured calcium hydroxide in alcohol (nanolime) combined with titanium dioxide. While nanolime is used as a consolidant in the field of cultural heritage and titanium dioxide is used as a photocatalytic material for self-cleaning coatings and environmental pollution control within the construction industry both materials are often used separately. We report in this paper an approach to combine both materials for the development of a photocatalytic nanolime coating. The photocatalytic effect of titanium dioxide on the carbonation of nanolime and its influence on the degradation processes in polluted environments is assessed. A suspension of 25 g/l of nanolime in ethanol and 7.4% wt/vol titanium dioxide was applied to specimens of Bath stone. For comparison, additional specimens were treated only with the nanolime. The specimens were exposed to oxides of nitrogen and sulphur under 30% relative humidity (RH) for 120 h. Exposure was carried out under both, UV and daylight. After exposure, the effect of titanium dioxide on the carbonation of nanolime and on the degradation processes was investigated using scanning electron microscopy (SEM), energy dispersive X-ray analysis (EDS) and X-ray photo electron spectroscopy (XPS). Results were evaluated considering the dissolution processes of the two oxides in water and modelled using PHREEQC. Nanolime and the photocatalytic nanolime coatings were shown to promote the reaction of SO_2. Results from the photocatalytic nanolime formulation suggest they could be used to reduce atmospheric pollutant levels through creation of a sacrificial layer. Such coatings have the potential to prevent further damage to limestone façades and could be applied in cities where pollution is detrimental to historic buildings.

1. Introduction

Since the industrial revolution, concentrations of the acid forming pollutants sulphur dioxide (SO_2) and nitrogen oxides (NO_x) have increased. This has resulted in the accelerated degradation of new and historic buildings in city centres and industrial areas. The introduction of more resistant materials and coatings to reduce these undesirable effects represent a challenge for the modern construction industry.

The processes of chemical decay of calcium carbonate ($CaCO_3$), which is one of the main constituents of limestone, has been the focus of numerous studies. The most aggressive chemical attack is mainly attributed to the oxides of sulphur and nitrogen. When SO_2 dissolves in water sulphurous acid (H_2SO_3) is formed whereas dissolution of SO_3 in water generates sulphuric acid (H_2SO_4). Both acids are strong enough to dissolve $CaCO_3$ contained in the stones or renders that are used as outer skins of buildings. Equations (1)–(7) show the proposed mechanism for sulfonation and the role of NO_2 in the oxidation of SO_2 [1,2]:

$$SO_2 + H_2O \rightarrow H_2SO_3 \quad (1)$$

$$H_2SO_3 + CaCO_3 \rightarrow CaSO_3 + H_2CO_3 \quad (2)$$

$$SO_2 + NO_2 \rightarrow SO_3 + NO \quad (3)$$

$$SO_3 + H_2O \rightarrow H_2SO_4 \quad (4)$$

* Corresponding author.
E-mail addresses: m.nuno@bath.ac.uk (M. Nuño), r.j.ball@bath.ac.uk (R.J. Ball).

http://dx.doi.org/10.1016/j.buildenv.2015.05.028

$$H_2SO_4 + CaCO_3 \rightarrow CaSO_4 + H_2CO_3 \quad (5)$$

$$NO + NO_2 + 2H_2SO_4 \rightarrow 2NOHSO_4 + H_2O \quad (6)$$

$$2NOHSO_4 + SO_2 + 2H_2O \rightarrow 3H_2SO_4 + 2NO \quad (7)$$

Sulfonation, however, is not the only process that can lead to chemical degradation of $CaCO_3$. This, in fact, can also be degraded by the products formed by the dissolution of NO_2 in water, as shown in Equations (8) and (9) [3,4]:

$$NO_2 + H_2O \rightarrow H_2NO_3 + HNO_2 \quad (8)$$

$$2HNO_3 + CaCO_3 \rightarrow Ca(NO_3)_2 + H_2CO_3 \quad (9)$$

1.1. Nanolime

In this work nanolime is examined as the calcium hydroxide based material. Nanolime is a colloidal suspension of nano-sized particles of calcium hydroxide ($Ca(OH)_2$) in an alcohol such as ethanol or isopropanol. It is commonly used as a consolidant in the field of cultural heritage [5]. The material acts as a binding agent of degraded surfaces because after application the $Ca(OH)_2$ reacts with the atmospheric carbon dioxide (CO_2) to produce $CaCO_3$. In contrast to building lime, which is formed by burning a source of calcium carbonate, nanolime is produced by precipitation. Nano-sized $Ca(OH)_2$ crystals are precipitated following mixing of super-saturated aqueous solutions of calcium chloride ($CaCl_2$) and sodium hydroxide (NaOH) under carefully controlled conditions. Following precipitation, water is substituted with alcohol to extend the long term stability of the nano-sized $Ca(OH)_2$ crystals [6]. Precipitated crystals are plate-like with hexagonal shape and an aspect ratio of approximately 10:1. The average particle size is 150 nm (IBZ-Freiberg n.d.) although crystals can range from tens to several hundred nanometres [7]. The product was developed at the beginning of the new millennium as a consolidant for frescos [8,9] and as de-acidification treatment for paper and canvas [10]. Later, however, its use extended to stone consolidation [6,11] and as a nano-coating. When mixed with other materials such as titanium dioxide (TiO_2) the nanolime acts as a binding agent.

1.2. Titanium dioxide and photocatalysis

Titanium dioxide is the natural oxide of Ti^{+IV} which is a semi-conductor with three main crystallographic structures. Anatase is one of the polymorphs and is widely studied for its photocatalytic properties when exposed to UV radiation. Previous researchers have investigated the use of titanium dioxide and its photocatalytic reactions in a wide range of applications such as water treatment [12–14], air purification [15–19] self-cleaning surfaces [20–26] or for the development of new super hydrophilic surfaces [21].

Photocatalysis is a chemical phenomenon observed in certain compounds that are able to absorb UV photons which in turn promote the migration of electrons from the valence to the conduction band, creating a charge separation. This separation produces a reactive hole (h^+_{vb}) and electron (e^-_{cb}) that can migrate to the surface of the material. At the surface the holes and electrons are able to participate in a photocatalytic process by adsorbing and reacting with molecules such as H_2O and O_2. This leads to the formation of free radicals as described by Equations (10)–(15) [27–30].

$$TiO_2 \xrightarrow{h\nu} h^+_{vb} + e^-_{cb} \quad (10)$$

$$h^+_{vb} + H_2O \rightarrow \bullet OH + H^+ \quad (11)$$

$$e^-_{cb} + H^+ \rightarrow \bullet H \quad (12)$$

$$e^-_{cb} + O_2 \rightarrow O_2^{\bullet -} \quad (13)$$

$$h^+_{vb} + O_2^{\bullet -} \rightarrow {}^1O_2 \quad (14)$$

$$H^+ + O_2^{\bullet -} \rightarrow HO_2\bullet \quad (15)$$

This paper investigates the effect of a TiO_2 on the carbonation and sulphation of nanolime in SO_2 and NO_2 rich environments to produce nano-structured $Ca(OH)_2/TiO_2$ photocatalytic coatings for buildings. Surfaces consisting of nano-particles of anatase mixed with nanolime were applied to specimens of Bath stone: a porous building limestone that has been used for centuries in the South West of the United Kingdom.

2. Experimental method

All specimens used in this test were cut from a single piece of newly quarried Bath stone extracted from the Combe Down mines in Bath and North East Somerset, UK. The stone was cut into test specimens 5 × 10 × 10 mm where all surfaces were freshly cut (unweathered). Each piece was individually cleaned with acetone and distilled water to remove impurities prior to being dried in an oven at 60 °C for 12 h.

Three different specimens were used in each test: 1) a control specimen made of uncoated sound stone; 2) a specimen coated with nanolime and 3) a specimen coated with a mixture of nanolime and TiO_2.

Nanolime suspension was supplied by IBZ-Salzchemie GmbH & Co. KG (Germany) under the trade name CaLoSiL®. A product with a concentration of 25 g/l in ethanol was used in all cases. Anatase in the form of Aeroxide® P25 was supplied by Sigma Aldrich (≥99.5% trace metals basis, average particle size 21 nm, surface area from 35 m^2/g to 65 m^2/g). In order to obtain a stable colloidal suspension, 7.4% wt/vol anatase was dispersed in CaLoSiL® just before the application and then sonicated for approximately 20 s.

The coating was applied by immersing the specimens in the suspensions for approximately 10 s. This allowed five sides of each specimen (main face of 10 × 10 mm and four sides of 5 × 10 mm) to be evenly covered. After immersion, the specimens remained in air at room temperature for several seconds to allow evaporation of the ethanol before being placed in the reactor at 25 °C.

Photocatalytic activity was evaluated for the specimens exposed to SO_2 under both UV and daylight radiation. UV radiation was obtained from a 4x4 array of 16 individual GaN UV-LEDs with a wavelength range of 376–387 nm and total intensity of 8 W/m^2. All other specimens were only exposed to daylight simulating external environmental conditions. The power of the light in the UVA range was 3 mW/m^2.

All specimens were exposed for 120 h to atmospheres produced with: 1) artificial air containing 7 ppm SO_2; 2) artificial air containing 7 ppm NO_2; 3) artificial air containing 3.5 ppm SO_2 and 3.5 ppm NO_2. The concentration of pollutants was set to 7 ppm in all the experiments since previous research showed optimum results after exposing to 5–10 ppm pollutants [2,31], and the RH remained constant at 7 ppm exposure and 30% respectively. Table 1 shows details of the experimental conditions.

The cylindrical 3 mm thick soda glass reactor with a diameter of 78 mm used in the tests is shown in Fig. 1. The reactor contained two gas inlets, a gas outlet and a lid to facilitate introduction and

Table 1
Experimental conditions showing the gas flow and the RH of each experiment. Pollutant concentrations (in ppm) are calculated considering the initial concentration and the mixed volumes of gas. All the experiments were carried for five days, under the constant conditions.

Experiment number	Exposed pollutant	SO_2 flow (ml/min)	NO_2 flow (ml/min)	100% Humid air (ml/min)	Light irradiation
1	7 ppm SO_2	22	–	10	Daylight cycles
2	7 ppm NO_2	–	22	10	Daylight cycles
3	3.5 ppm SO_2 and 3.5 ppm NO_2	10	10	10	Daylight cycles
4	7 ppm SO_2 under UV	22	–	10	Constant 8 W/m^2

removal of the specimens. The gas system that allowed production of specific atmospheres was designed in order to be able to introduce all three gases at the same time. The desired gas compositions for the experiments were produced by introducing the following gases into the cell: 1) zero air grade (composition: 0.5 ppm H_2, 2 ppm He, 1 ppm CH_4, <5 ppm H_2O, 5 ppm Ne, ~20.95% O_2, 9300 ppm Ar, 385 ppm CO_2, 0.8 ppm N_2O, N_2 balance); 2) zero air grade containing 10.7 ppm of NO_2; 3) zero air grade containing 10.4 ppm of SO_2 in the appropriate proportions. All gases were supplied by BOC Gases Ltd. Each gas cylinder was connected to a gas flow meter capable of measuring gas flows from 5 cm^3/min to 100 cm^3/min with an accuracy of ±0.5 ml/min (Platon Gap meter Type NGX supplied by Roxspur Measurement & Control Ltd). The gas from the zero air grade cylinders was humidified by passing it through a glass bubbler containing deaerated water before being passed into the cell. The other gas inlet of the cell was used to introduce the dry gas from the other two cylinders that were mixed using a three-way valve.

3. PHREEQC modelling

To evaluate the experimental results, dissolution of SO_2, NO_2 and CO_2 in water was modelled using PHREEQC [32]. The program is based on equilibrium chemistry of aqueous solutions interacting with several phases, including gases. PHREEQC is routinely used in disciplines such as geochemistry, hydrology, environmental pollution, water treatment and the construction industry. PHREEQC has been used to simulate the ion–ion and the ion–solid interactions in the multi-ionic transport in concrete [33,34], chemical degradation of concrete [35–37], dissolution processes of calcium-silicate-hydrate [38,39], and phase and morphology evolution of $CaCO_3$ precipitated by carbonation of hydrated lime [40,41].

Simulations applied in this work were based on previously reported PHREEQC protocols [32]. Initial conditions consisted of 1 kg of pure water at 25 °C with pH = 7 (this was set to be as an adjustable parameter to achieve charge balance). The equilibrium phases included two species: gas and solid. CO_2, SO_2 and NO_2 were considered as gas with the respective concentrations calculated according to Table 1 and the log of p_{CO2} (in bar) was set to simulate the different partial pressures. The number of moles considered was set to 100 to model the equilibrium with infinite reservoirs. Solid phases considered were modelled using an infinite number of moles and a saturation index (SI) of 0 so that these had to be in equilibrium with the solution at the end of the simulation. Simulations were performed with the thermodynamic data from the Lawrence Livermore National Laboratory database of Berkeley (the LLNL database built in PHREEQC). The PHREEQC input file used is shown in Algorithm 1.

Fig. 1. Image of the glass reactor. Reactor diameter 78 mm for scale.

4. Chemical and physical characterisation

Micro-morphologies of the Bath stone and coatings used in the tests were evaluated using a JEOL JSM64802V scanning electron microscope (SEM) with a working distance of 10 mm, an accelerating voltage of 15 kV and a spot size of 30 nm. Specimens were coated with a 20 nm thick layer of gold using an Edward Sputter S150B Coater to prevent surface charging. Energy Dispersive X-ray Spectroscopy (EDS) was performed on uncoated specimens using a working distance of 10 mm, accelerating Voltage of 25 kV and a spot size of 51 nm in high vacuum (25 MPa). Due to its penetration depth (1–2 μm), this technique was used to evaluate the degradation processes carried within the bulk of the coating.

The surface layers (within 1–10 nm) were characterized using X-ray Photoelectron Spectroscopy (XPS) using a Thermo Scientific Theta Probe with an AlK_α (1486 eV) X-ray source, operated at 100 W (Thermo Fisher Scientific Inc., Waltham, MA.) using a flood gun in an operating vacuum of 10^{-8} mbar. The adventitious hydrocarbon C1s peak at 284.8 eV was used to correct the spectra for specimen charging. The software CASAXPS 2.3.16 RP 1.6 (Casa Software Ltd., Teingmouth, Devon, UK) was used for the peak fitting. The atomic percentage of each element detected was calculated from the peak areas, assuming a Shirley background and fitted using a Gaussian/Lorentzian ratio and asymmetry factors to give the best fit to the peaks. All the fitted peaks were normalized excluding the area of the adventitious carbon peak.

Wide scan survey spectra were obtained between 0 and 1400 eV binding energy (BE) with pass energy of 200 eV and dwell time of 50 ms. In addition, scans of higher resolution were taken at different BE ranges with pass energy of 40 eV and dwell time of 100 ms for C1s, N1s, O1s, S2p, Ca2p and Ti2p regions.

5. Results

5.1. PHREEQC simulation

Table 2 reports the activity of CO_3^{2-}, SO_4^{2-} and NO_2^- ions in pure water (i.e. no solid phase was introduced as the initial condition) as calculated by PHREEQC using different gas mixes and the model shown in Algorithm 1 (the simulation number is equivalent to the experiment number in Table 1). The data show that in pure water, the activity of SO_4^{2-} ion is many orders of magnitude higher than the activity of NO_2^- and CO_3^{2-} ions in all conditions.

Table 3 shows the activity of CO_3^{2-}, SO_4^{2-} and NO_2^- ions when calcite is introduced as the main solid phase in contact with the solution. Calcite used in this model since it simulates the presence of $CaCO_3$ formed during the carbonation of nanolime. Results show that, as in pure water, the activity of the SO_4^{2-} ion is several order magnitudes higher than the activity of NO_2^- and CO_3^{2-} ions and that under these conditions Anhydrite ($CaSO_4$), Bassanite ($CaSO_4 \cdot 0.5H_2O$) and Gypsum ($CaSO_4 \cdot 2H_2O$) can be formed as solid phases.

Table 4 shows the activity of CO_3^{2-}, SO_4^{2-} and NO_2^- ions when both, calcite and Portlandite are included in the simulation. Portlandite used in this model simulates the presence of uncarbonated nanolime particles during the tests. The results show that, as well as in pure water, and in presence of calcite, the activity of SO_4^{2-} ion is several orders of magnitude higher than the activity of NO_2^- and CO_3^{2-} ions. Furthermore, the results suggest that Anhydrite ($CaSO_4$), Bassanite ($CaSO_4 \cdot 0.5H_2O$) and Gypsum ($CaSO_4 \cdot 2H_2O$) are the only solid phases that could be formed at the end of the test.

5.2. SEM imagining

Fig. 2 shows the surfaces of the control specimen (a), the specimen coated with nanolime (b) and the specimen coated with the nanolime-titania coating (c) after exposure to SO_2. Fig. 2a shows the structure of Bath stone with a distributed set of clusters composed by Oolites that makes the stone's structure very porous. Bath stone was previously characterized by mercury intrusion porosimetry (MIP) using a Micrometrics AutoPore III [42]. The majority of the pores were around 10 and 0.1 μm in diameter, and the macro pores were over 100 μm and micropores (between Oolites) which are between 10 and 1 μm in diameter. Fig. 2b illustrates the even distribution of nanolime on the surface and within the surface pores of the stone, thereby covering the Oolites. Fig. 2c shows Bath stone covered with a photocatalytic mixed phase nanolime coating. The presence of TiO_2 in the photocatalytic nanolime coating is not visible in the SEM images due to their fine particle size. Fig. 2b and c shows a coating with a high surface area. By comparing the coated (Fig. 2b and c) and uncoated (Fig. 2a) stone images the macropores are not blocked allowing gas and liquid vapour to diffuse into and out of the stone.

5.3. Energy dispersive X-ray spectroscopy (EDS)

Following exposure to the conditions in Table 1, quantitative analysis of the specimens was carried out using EDS, the results of which are shown in Table 5. The data in the table is an average calculated from the results of five individual analyses, each carried out at a randomly selected representative location of the specimen surface.

EDS analysis did not detect the presence of nitrogen based molecules in the surface of specimens exposed to 7 ppm of NO_2. Between 4.4 and 7.12 atomic % titanium was identified on the specimens coated with TiO_2 whereas no appreciable amount was detected on the other specimens. However in comparison to the specimen exposed to 7 ppm SO_2, results indicated the presence of sulphur, with higher values in the specimens coated with nanolime and photocatalytic nanolime. Exposure to the 3.5 ppm NO_2 and 3.5 ppm SO_2 gas mixture showed a reduction in the amount of sulphur detected on the nanolime coated specimen (0.34 atomic %), compared with the 7 ppm SO_2 exposure, which was within the range of sulphur detected in the untreated specimens (0.37 and 0.56 atomic %). The photocatalytic nanolime coating showed 1.68 atomic % of sulphur which was comparable to the value of 1.77 atomic % obtained for the 7 ppm of SO_2.

5.4. X-ray photoelectron spectroscopy (XPS) results

The nature of the surface layer of the specimens after five days exposure was evaluated using XPS analysis, a survey spectra is shown in Fig. 3. Binding energies and elemental ratios for carbon, nitrogen, oxygen, sulphur, calcium and titanium, calculated from higher resolution spectra in specific regions, are shown in Table 6.

The adventitious carbon contamination peak at 284.8 eV was identified on all the specimens examined and used to calibrate the spectra for surface charging, however an additional peak corresponding to $CaCO_3$ was also identified. The binding energy of this peak ranged between 288.6 and 289.2 eV which is in agreement with studies by Kang [43] and Demri [44] who report $CaCO_3$ binding energies of 288.6 and 289.2 eV. The binding energy for the Ca 2p peak ranged between 346.3 and 347.5 eV which is in accordance with previous studies by Ming [45] and Stipp [46] who reported $CaCO_3$ binding energies of 346.5 and 347.7 eV.

The specimens exposed to 7 ppm NO_2 diluted in air did not show the presence of sulphur, indicating that no significant amount of sulphur was present in the specimen stone before testing, and that any sulphur detected on the surface of the specimens exposed to SO_2 originated from a surface reaction. Peaks corresponding to N 1s were identified between binding energies of 399.1–400.6 eV, related to the presence of a carbon–nitrogen bond within an organic matrix [47]. In the spectral region corresponding to nitrate (N 1s 407.5 eV) [48] no signal was detected suggesting that $Ca(NO_3)_2$ was not formed.

Table 2
Activity of CO_3^{2-}, SO_4^{2-} and NO_2^- ions in pure water as calculated by the PHREEQC.

Simulation number	Gas phases	Ion activity as calculated by PHREEQC		
		CO_3^{2-}	SO_4^{2-}	NO_2^-
1	385 ppm CO_2 7 ppm SO_2	1.047×10^{-24}	4.089×10^{-3}	–
2	385 ppm CO_2 7 ppm NO_2	2.700×10^{-24}	–	2.160×10^{-14}
3	385 ppm CO_2 3.5 ppm SO_2 3.5 ppm NO_2	8.872×10^{-26}	6.028×10^{-3}	8.203×10^{-15}

Table 3
Activity of CO_3^{2-}, SO_4^{2-} and NO_2^- ions in pure water in equilibrium with calcite and solid phases formed at the end of the simulation.

Simulation set up			Ion activity			Solid phases formed
N.	Gas phases	Solid phases	CO_3^{2-}	SO_4^{2-}	NO_2^-	
1	CO_2 (385 ppm) SO_2 (7 ppm)	Calcite	8.031×10^{-9}	1.721×10^{-1}	–	$CaSO_4$ $CaSO_4 \cdot 0.5H_2O$ $CaSO_4 \cdot 2H_2O$
2	CO_2 (385 ppm) NO_2 (7 ppm)	Calcite	1.808×10^{-8}	–	2.463×10^{-11}	–
3	CO_2 (385 ppm) SO_2 (3.5 ppm) NO_2 (3.5 ppm)	Calcite	9.270×10^{-9}	1.822×10^{-1}	1.594×10^{-11}	$CaSO_4$ $CaSO_4 \cdot 0.5H_2O$ $CaSO_4 \cdot 2H_2O$

Table 4
Activity of CO_3^{2-}, SO_4^{2-} and NO_2^- ions in pure water in equilibrium with calcite and portlandite, and solid phases that could be produced at the end of the tests.

Simulation set up			Ion activity			Solid phases formed
N.	Gas phases	Solid phases	CO_3^{2-}	SO_4^{2-}	NO_2^-	
1	CO_2 (385 ppm) SO_2 (7 ppm)	Calcite Portlandite	6.775×10^{-9}	7.822×10^{-2}	–	$CaSO_4$ $CaSO_4 \cdot 0.5H_2O$ $CaSO_4 \cdot 2H_2O$
2	CO_2 (385 ppm) NO_2 (7 ppm)	Calcite Portlandite	1.968×10^{-8}	–	1.672×10^{-9}	–
3	CO_2 (385 ppm) SO_2 (7 ppm) NO_2 (7 ppm)	Calcite Portlandite	1.063×10^{-8}	1.451×10^{-1}	1.032×10^{-9}	$CaSO_4$ $CaSO_4 \cdot 0.5H_2O$ $CaSO_4 \cdot 2H_2O$

Binding energies for Ti $2p_{3/2}$ peaks varied between 458.1 and 459.0 eV, and for O 1s the observed peaks are within the range of 528.8–529.5 eV. These results agreed with studies carried by Dementjev [49] and Bedri [50], which identified Ti $2p_{3/2}$ binding energies from 458.0 to 459.4 eV and for O 1s from 529.4 to 530.6 eV. These were attributed to the TiO_2 in the coatings.

The XPS spectra of specimens exposed to 3.5 ppm NO_2 and 3.5 ppm SO_2 also showed S $2p_{3/2}$ peaks at binding energies between 167.8 and 168.3 eV which corresponded to $CaSO_3$. Calculated atomic percentages of 0.5, 0.3 and 0.1 for the untreated, nanolime coating, and photocatalytic nanolimes were less than that observed on the specimens exposed to 7 ppm SO_2. These smaller concentrations may be attributed to the lower concentration of SO_2.

The XPS spectra from specimens exposed to 7 ppm SO_2 diluted in air at a relative humidity of 33% with daylight cycles all showed peaks corresponding to sulphur. The binding energies between 166.6 and 168.6 eV are in agreement with studies by Siriwardane and Hong [51,52], and characteristic of calcium sulphite (SO_3^{2-}). Compositions of 1.0, 3.2 and 4.6 atomic % for the untreated (stone surface), nanolime coating, and photocatalytic nanolime indicated that the nanolime is more reactive when compared to the stone substrate. This may be attributed to the higher solubility of $Ca(OH)_2$ compared to $CaCO_3$ and the higher surface area of the nanolime compared to stone.

The XPS spectra from specimens exposed to 7 ppm SO_2 diluted in air at 33% RH under UV light also showed peaks corresponding to sulphur. The binding energies between 168.4 and 168.6 eV observed for the nanolime and untreated stone are in agreement with studies by Siriwardane and Hong [51,52], and characteristic of calcium sulphite (SO_3^{2-}). The atomic percentages of 2.2 and 4.0 are slightly higher, but still comparable with the equivalent specimens exposed to daylight cycles.

The specimen containing photocatalytic nanolime exposed to UVA had a Ca $2p_{3/2}$ binding energy of 348.2 eV which was higher than values between 346.3 and 347.5 eV which was detected for all the other specimens. This is comparable to a Ca $2p_{3/2}$ binding energy of 348 eV observed by Siriwarde [51] for calcium sulphate. A higher binding energy for S $2p_{3/2}$ of 169.9 eV, compared to values ranging between 167.8 and 168.6 eV, is also in agreement with previous research by Moulder et al. [47] who observed a binding energy of 169.4 eV for sulphate. The difference in behaviour of the photocatalytic nanolime under UV irradiation is illustrated in Fig. 4 which shows the spectra over the S 2p range for the nanolime coated specimen and photocatalytic nanolime. A shift of approximately 2 eV is observed between the S 2p peaks of nanolime coating and photocatalytic coating. On nanolime $CaSO_3$ was observed whereas for the photocatalytic coating $CaSO_4$ was generated.

6. Discussion

The combined results given by EDS and XPS reveal a difference in the elemental concentration between the bulk of the coating (1–2 μm) and the surface layer (maximum 10 nm). The concentration of CO_2 in the gas mixture was approximately 55 times higher than that of the NO_2 and SO_2, however the concentration of sulphur compounds detected on the surface was similar to that of the $CaCO_3$ detected. Simulations using PHREEQ suggest that, because of the very low activity of the NO_2^- ion in aqueous solution only the solid phases produced by the interaction of SO_2 with the system should be detected at the end of the experiments.

For the experiment that exposed specimens to 7 ppm of NO_2, the exposure did not affect the composition within the bulk; it is possible that the gas concentration or the activity of nitrogen ions was too low to produce phases detectable by EDS. In addition, XPS showed a small amount of organic matrix in the outermost layer.

The formation of $CaSO_4$ on the surface of carbonate containing materials historically used in construction, such as limestone, is widely accepted. However previous research, under atmospheric conditions, by Chin [53] describes the formation of $CaSO_4$ as a two stage process involving the initial formation of $CaSO_3$ (IV) which is followed by further oxidation to sulphate (VI) [53]. The rate of these two reactions is dependent on the local water and oxygen concentrations.

Analysis of the S $2p_{3/2}$ binding energies obtained for the XPS spectra from the specimens indicated the presence of SO_3^{2-} in the form of calcium sulphite. This phase was identified on the uncoated limestone surface in addition to nanolime and photocatalytic

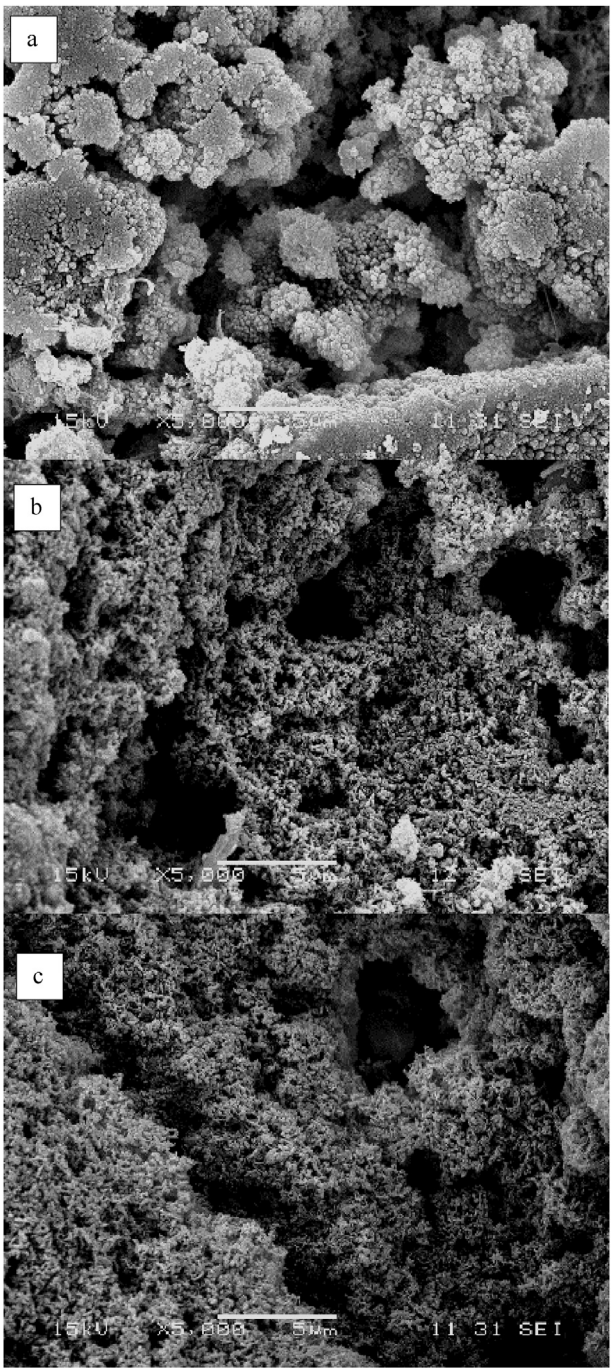

Fig. 2. SEM images of: a) Uncoated Bath stone after SO_2 exposure; b) Nanolime coated Bath stone specimen after SO_2 exposure; c) Bath stone treated with the photocatalytic nanolime coating after SO_2 exposure.

nanolime surfaces. The concentration of sulphur on surfaces coated with nanolime and photocatalytic nanolime was three times higher than that on the stone surface due to the presence of more reactive $Ca(OH)_2$ and the associated higher surface area. EDS indicated a six-fold increase, the higher value compared to XPS, was attributed to the greater penetration depth of the analysis into the specimen surface.

The addition of anatase to the nanolime, increased the surface area and the absorption of SO_2 and NO_x onto the outermost layer of material. When the photocatalytic nanolime coating was exposed to UV irradiation, XPS revealed the presence of SO_4^{2-} as calcium

Table 5
Specimen composition determined by EDS spectroscopy on specimens following experimental conditioning exposure.

	Specimen	S (at. %)	Ti (at. %)
7 ppm NO_2	Untreated	–	–
33%RH	Nanolime coating	–	–
Daylight cycles	Photocatalytic nanolime	–	4.4
7 ppm SO_2	Untreated	0.37	–
33%RH	Nanolime coating	2.36	–
Daylight cycles	Photocatalytic nanolime	1.77	7.12
3.5 ppm NO_2+3.5 ppm SO_2	Untreated	0.56	–
33% RH	Nanolime coating	0.34	–
Daylight cycles	Photocatalytic nanolime	1.68	4.4
7 ppm SO_2	Untreated	0.72	–
33% RH	Nanolime coating	2.38	–
UV-light	Photocatalytic Nanolime	4.45	6.6

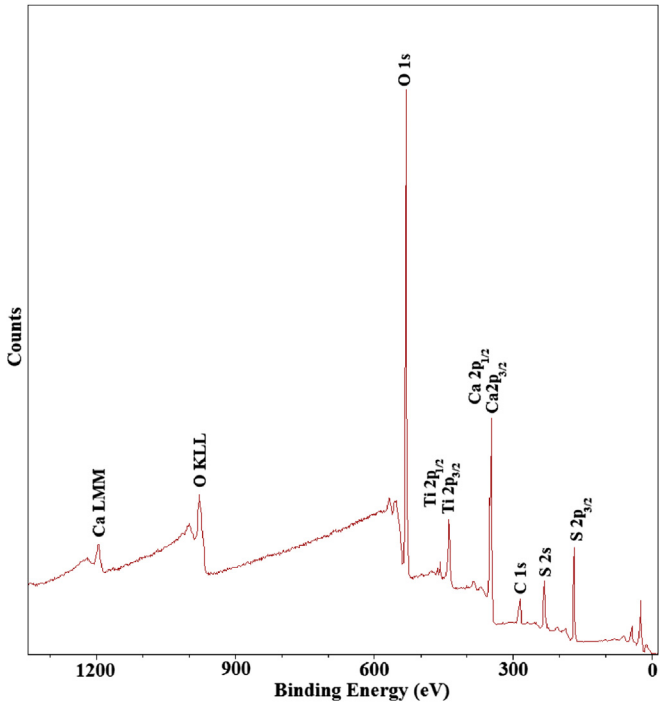

Fig. 3. Typical wide scan survey XPS spectrum for photocatalytic nanolime coated Bath stone after five days exposure to 7 ppm SO_2 under UV irradiation.

sulphate. Compared to all the other specimens examined the amount of $CaCO_3$ detected was considerably lower.

The presence of calcium sulphate suggests reaction with sulphuric acid opposed to sulphurous acid. Margitan [54] demonstrated that a hydroxyl radical can initiate the oxidation of SO_2 into SO_3 as described by Equations (14)–(16). This radical is known to readily form on the surface of photocatalysts such as anatase under illumination with UV light [28–30].

$$SO_2 + \bullet OH \rightarrow HOSO_2\bullet \quad (14)$$

$$HOSO_2\bullet + \bullet OH \rightarrow H_2O + SO_3 \quad (15)$$

Sulphuric acid can form by the reaction of SO_3 with water as shown in Equation (16), however reaction with the hydroxyl radical has also been shown to lead to the formation of sulphuric acid as in Equation (17).

Table 6
Binding energies and relative concentration in atomic percent of carbon, nitrogen, oxygen, sulphur, calcium and titanium obtained from XPS analysis.

Experimental conditions	Specimen ID	**Binding energy, eV**/Relative concentration in atomic %							
		C 1s	N 1s	O 1s		S $2p_{3/2}$		Ca $2p_{3/2}$	Ti $2p_{3/2}$
		CO_3^{2-}	Organic matrix	CO_3^{2-}	TiO_2	SO_3^{2-}	SO_4^{2-}		TiO_2
7 ppm NO_2	Untreated	**288.6**/3.3	**399.5**/0.9	**531.5**/78.8	–	–	–	**346.4**/17.0	–
33% RH	Nanolime coating	**289.1**/4.3	**399.2**/0.2	**531.3**/59.9	–	–	–	**346.8**/35.6	–
Daylight cycles	Photocatalytic nanolime	**288.8**/3.5	**399.3**/0.4	**530.9**/54.5	**528.8**/1.7	–	–	**346.6**/28.4	**458.1**/11.5
7 ppm SO_2	Untreated	**288.9**/5.0	**399.3**/0.6	**531.0**/65.0	–	**167.9**/1.0	–	**346.3**/28.4	–
33% RH	Nanolime coating	**288.7**/4.4	**399.1**/0.2	**530.9**/56.4	–	**166.6**/3.2	–	**346.4**/35.8	–
Daylight cycles	Photocatalytic nanolime	**288.8**/1.0	**399.1**/0.2	**532.0**/62.4	–	**168.6**/4.6	–	**347.3**/27.1	**459.0**/4.6
3.5 ppm NO_2 + 3.5 ppm SO_2	Untreated	**288.8**/3.1	**399.7**/1.0	**531.7**/77.9	–	**167.9**/0.5	–	**346.7**/17.5	–
33% RH	Nanolime coating	**289.0**/5.0	**399.8**/0.4	**530.8**/58.7	–	**167.8**/0.3	–	**346.3**/35.6	–
Daylight cycles	Photocatalytic nanolime	**289.1**/3.4	**399.2**/0.1	**531.0**/53.3	**528.9**/3.1	**168.3**/0.1	–	**346.7**/27.0	**458.9**/13.0
7 ppm SO_2	Untreated	**288.8**/3.3	**399.7**/0.9	**531.7**/69.4	–	**168.6**/2.2	–	**346.9**/24.2	–
33% RH	Nanolime coating	**289.0**/2.1	**400.6**/0.1	**532.2**/66.1	–	**168.4**/4.0	–	**347.5**/27.7	–
UV exposure	Photocatalytic nanolime	**287.8**/0.7	**400.2**/0.1	**532.4**/50.9	**529.5**/6.9	–	**169.4**/8.2	**348.2**/24.1	**459.0**/9.1

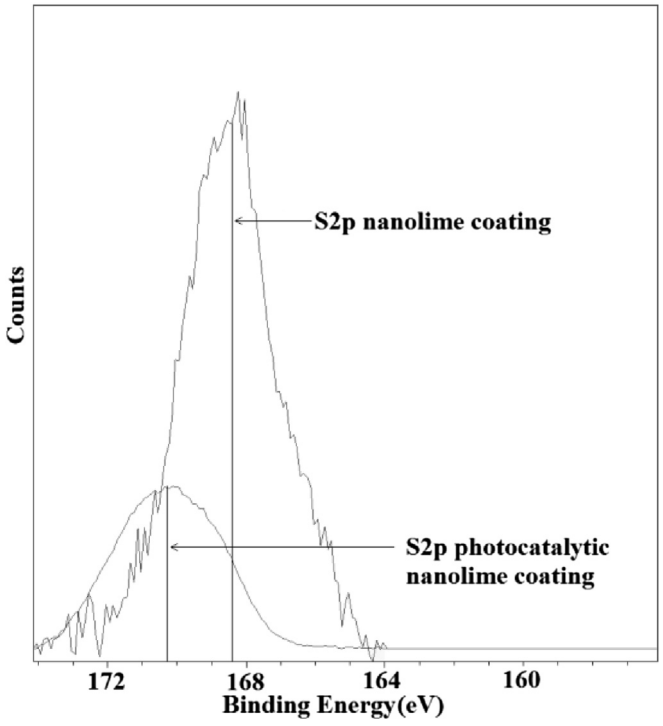

Fig. 4. XPS spectra of sulphur $2p_{3/2}$ region for nanolime and photocatalytic nanolime coated Bath stone after five days exposure to 7 ppm SO_2 under UV irradiation.

$$SO_3 + H_2O \rightarrow H_2SO_4 \quad (16)$$

$$SO_2 + 2 \bullet OH \rightarrow H_2SO_4 \quad (17)$$

When the sulphuric acid is formed, it reacts with $Ca(OH)_2$ and $CaCO_3$ as shown in Equations (18) and (19) to form calcium sulphate.

$$H_2SO_4 + Ca(OH)_2 \rightarrow 2H_2O + CaSO_4 \quad (18)$$

$$H_2SO_4 + CaCO_3 \rightarrow CaSO_4 \quad (19)$$

7. Conclusions

This study provides an insight into the effect of the addition of photocatalytic titanium dioxide on the carbonation process of nanolime and in its degradation process when exposed to SO_2.

There was no evidence of nitration under exposure to 7 ppm NO_2 for all the materials evaluated in this study. XPS data indicated the binding energies of the N 1s peak were characteristic of N–C bonds in an organic matrix. The concentration of nitrogen deposited was increased when the gas composition consisted of 3.5 ppm of SO_2 and 3.5 ppm of NO_2.

In the case of the specimens coated with nanolime the results show a preferential reaction of $Ca(OH)_2$ with SO_2 relative to CO_2, which is further enhanced in presence of anatase and UV light. Under these conditions the majority of the $Ca(OH)_2$ reacts with SO_2 to form calcium sulphate, and only a small amount reacted with CO_3^{2-} to form $CaCO_3$. Results show the presence of anatase increased the deposition of sulphur and nitrogen when the specimens were exposed to 7 ppm of SO_2 and UV light, and the $CaSO_4$ generated reduced carbonation. This was attributed to the oxidation of SO_2 to SO_3 by hydroxyl radicals generated on the surface of nano-anatase thus forming sulphuric acid opposed to sulphurous acid. Results from the photocatalytic nanolime formulation suggest they could be used to reduce atmospheric pollutant levels through creation of a sacrificial layer. Such coatings have the potential to prevent further damage to limestone façades and could be applied in cities where pollution is detrimental to historic buildings.

Acknowledgement

The authors acknowledge research funding from a University of Bath Research Studentship and the Engineering and Physical Sciences Research Council (EPSRC) through project EP/K025597/1. Thanks are also due to the National EPSRC XPS Users' Service, hosted by nanoLAB at the University of Newcastle, UK, in particular Dr Anders Barlow. The authors are grateful to Professor W. N. Wang for specifying the UV-LED source and to Dr John Mitchels and Ursula Potter for assistance with EDS spectroscopy and SEM imaging.

SEM and EDX data supporting this paper are provided in full in the results section. XPS data is openly available from the University of Bath Data Archive at http://dx.doi.org/10.15125/BATH-00097. PHREEQC results were obtained using PHREEQC Interactive version 3.1.7-9213 and using the algorithm described in algorithm 1 and the details specified within the Materials and Methods section.

Appendix

Algorithm 1. PHREEQC model used to simulate the dissolution of CO_2, NO_2 and SO_2 and water with and without solid phases. The code shows the model used to simulate the dissolution of 7 ppm of SO_2 and 385 ppm of CO_2 in pure water and in absence of solid

phases as initial conditions (hashtags inform the software to ignore the code lines where these are located). For each condition described in Table 1, the gas phases, the gas concentrations and the solid phases were modified by commenting or un-commenting the code with a hashtag.

```
SOLUTION 1
   temp      25
   pH        7 charge
   pe        4
   redox     pe
   units     mol/kgw
   density   1
   Alkalinity 0
   -water    1 # kg
EQUILIBRIUM_PHASES 1
#  Calcite 0 1000
#  Portlandite 0 1000
   CO2(g)    -3.408822658 100
#  NO2(g)    -5.149185348 100
   SO2(g)    -5.149185349 100
END
```

References

[1] A. Lancia, D. Musmarra, F. Pepe, Modeling of SO2 Absorption into limestone suspensions, Ind. Eng. Chem. Res. 36 (1) (Jan. 1997) 197–203.

[2] G.C. Allen, A. El-Turki, K.R. Hallam, D. McLaughlin, M. Stacey, Role of NO_2 and SO_2 in degradation of limestone, Br. Corros. J. 35 (1) (Jan. 2000) 35–38.

[3] Y.-N. Lee, S.E. Schwartz, Evaluation of the rate of uptake of nitrogen dioxide by atmospheric and surface liquid water, J. Geophys. Res. Ocean. 86 (C12) (Dec. 1981) 11971–11983.

[4] P. Kirkitsos, D. Sikiotis, Deterioration of Pentelic marble, Portland limestone and Baumberger sandstone in laboratory exposures to NO_2: a comparison with exposures to gaseous HNO_3, Atmos. Environ. 30 (6) (Mar. 1996) 941–950.

[5] L. Dei, B. Salvadori, Nanotechnology in cultural heritage conservation: nanometric slaked lime saves architectonic and artistic surfaces from decay, J. Cult. Herit. 7 (2) (Apr. 2006) 110–115.

[6] V. Daniele, G. Taglieri, Nanolime suspensions applied on natural lithotypes: the influence of concentration and residual water content on carbonatation process and on treatment effectiveness, J. Cult. Herit. 11 (1) (Jan. 2010) 102–106.

[7] V. Daniele, G. Taglieri, R. Quaresima, The nanolimes in cultural heritage conservation: characterisation and analysis of the carbonatation process, J. Cult. Herit. 9 (3) (Jul. 2008) 294–301.

[8] R. Giorgi, L. Dei, P. Baglioni, A new method for consolidating wall paintings based on dispersions of lime in alcohol, Stud. Conserv. 45 (3) (Sep. 2000) 154–161.

[9] P. Baglioni, R. Giorgi, Soft and hard nanomaterials for restoration and conservation of cultural heritage, Soft Matter 2 (4) (2006) 293–303.

[10] R. Giorgi, L. Dei, M. Ceccato, C. Schettino, P. Baglioni, Nanotechnologies for conservation of cultural heritage: paper and canvas deacidification, Langmuir 18 (21) (Sep. 2002) 8198–8203.

[11] P. López-Arce, L.S. Gomez-Villalba, L. Pinho, M.E. Fernández-Valle, M.Á. de Buergo, R. Fort, Influence of porosity and relative humidity on consolidation of dolostone with calcium hydroxide nanoparticles: effectiveness assessment with non-destructive techniques, Mater. Charact. 61 (2) (Feb. 2010) 168–184.

[12] A. Fujishima, X. Zhang, D.A. Tryk, TiO_2 photocatalysis and related surface phenomena, Surf. Sci. Rep. 63 (12) (2008) 515–582.

[13] S.-A. Lee, K.-H. Choo, C.-H. Lee, H.-I. Lee, T. Hyeon, W. Choi, H.-H. Kwon, Use of ultrafiltration membranes for the separation of TiO_2 photocatalysts in drinking water treatment, Ind. Eng. Chem. Res. 40 (7) (Mar. 2001) 1712–1719.

[14] J. Ryu, W. Choi, Substrate-specific photocatalytic activities of TiO_2 and multiactivity test for water treatment application, Environ. Sci. Technol. 42 (1) (Nov. 2007) 294–300.

[15] J. Kolarik, J. Toftum, The impact of a photocatalytic paint on indoor air pollutants: sensory assessments, Build. Environ. 57 (0) (2012) 396–402.

[16] G. Hüsken, M. Hunger, H.J.H. Brouwers, Experimental study of photocatalytic concrete products for air purification, Build. Environ. 44 (12) (Dec. 2009) 2463–2474.

[17] G. Ramakrishnan, A. Orlov, Development of novel inexpensive adsorbents from waste concrete to mitigate NOx emissions, Build. Environ. 72 (Feb. 2014) 28–33.

[18] A.M. Ramirez, K. Demeestere, N. De Belie, T. Mäntylä, E. Levänen, Titanium dioxide coated cementitious materials for air purifying purposes: preparation, characterization and toluene removal potential, Build. Environ. 45 (4) (2010) 832–838.

[19] M. Nuño, R.J. Ball, C.R. Bowen, Study of solid/gas phase photocatalytic reactions by electron ionization mass spectrometry, J. Mass Spectrom. 49 (8) (2014) 716–726.

[20] Y. Ohko, S. Saitoh, T. Tatsuma, A. Fujishima, Photoelectrochemical anticorrosion and self-cleaning effects of a TiO_2 coating for type 304 stainless steel, J. Electrochem. Soc. 148 (1) (Jan. 2001) B24–B28.

[21] Z. Wu, D. Lee, M.F. Rubner, R.E. Cohen, Structural color in porous, superhydrophilic, and self-cleaning SiO_2/TiO_2 bragg stacks, Small 3 (8) (Aug. 2007) 1445–1451.

[22] Y. Paz, Z. Luo, L. Rabenberg, A. Heller, Photooxidative self-cleaning transparent titanium dioxide films on glass, J. Mater. Res. 10 (11) (1995) 2842–2848.

[23] E.I. Cedillo-González, R. Riccò, M. Montorsi, M. Montorsi, P. Falcaro, C. Siligardi, Self-cleaning glass prepared from a commercial TiO_2 nanodispersion and its photocatalytic performance under common anthropogenic and atmospheric factors, Build. Environ. 71 (Jan. 2014) 7–14.

[24] A. Chabas, S. Alfaro, T. Lombardo, A. Verney-Carron, E. Da Silva, S. Triquet, H. Cachier, E. Leroy, Long term exposure of self-cleaning and reference glass in an urban environment: a comparative assessment, Build. Environ. 79 (Sep. 2014) 57–65.

[25] A. Chabas, T. Lombardo, H. Cachier, M.H. Pertuisot, K. Oikonomou, R. Falcone, M. Verità, F. Geotti-Bianchini, Behaviour of self-cleaning glass in urban atmosphere, Build. Environ. 43 (12) (Dec. 2008) 2124–2131.

[26] M. Nuño, R.J. Ball, C.R. Bowen, R. Kurchania, G.D. Sharma, Photocatalytic activity of electrophoretically deposited (EPD) TiO_2 coatings, J. Mater. Sci. 50 (14) (2015) 4822–4835.

[27] A. Fujishima, K. Honda, Electrochemical photolysis of water at a semiconductor electrode, Nature 238 (5358) (1972) 37–38.

[28] A.Z. Fujishima, Titanium dioxide photocatalysis: present situation and future approaches, Comptes Rendus Chim. 9 (5–6) (2006) 750–760.

[29] A. Fujishima, T.N. Rao, D.A. Tryk, Titanium dioxide photocatalysis, J. Photochem. Photobiol. C Photochem. Rev. 1 (1) (2000) 1–21.

[30] O. Carp, C.L. Huisman, A. Reller, Photoinduced reactivity of titanium dioxide, Prog. Solid State Chem. 32 (1–2) (2004) 33–177.

[31] G.C. Allen, A. El-Turki, K.R. Hallam, D. McLaughlin, M. Stacey, Role of NO_2 and SO_2 on the degradation of limestone, in: D.J. Mitchell, D.E. Searle (Eds.), Stone Deterioration in Polluted Urban Environments, vol. 3, CRC publisher, 2004, pp. 119–130.

[32] C.A.J. Appelo, D. Postma, Geochemistry, Groundwater and Pollution, Second Edition, CRC Press/Taylor & Francis, Boca Raton, FL, 2005, p. 683.

[33] Y. Elakneswaran, A. Iwasa, T. Nawa, T. Sato, K. Kurumisawa, Ion-cement hydrate interactions govern multi-ionic transport model for cementitious materials, Cem. Concr. Res. 40 (12) (Dec. 2010) 1756–1765.

[34] P. Brown, A. Doerr, Chemical changes in concrete due to the ingress of aggressive species, Cem. Concr. Res. 30 (3) (Mar. 2000) 411–418.

[35] D. Jacques, L. Wang, E. Martens, D. Mallants, Modelling chemical degradation of concrete during leaching with rain and soil water types, Cem. Concr. Res. 40 (8) (Aug. 2010) 1306–1313.

[36] D. Sugiyama, Chemical alteration of calcium silicate hydrate (C–S–H) in sodium chloride solution, Cem. Concr. Res. 38 (11) (Nov. 2008) 1270–1275.

[37] M. Moranville, S. Kamali, E. Guillon, Physicochemical equilibria of cement-based materials in aggressive environments—experiment and modeling, Cem. Concr. Res. 34 (9) (Sep. 2004) 1569–1578.

[38] C.S. Walker, D. Savage, M. Tyrer, K.V. Ragnarsdottir, Non-ideal solid solution aqueous solution modeling of synthetic calcium silicate hydrate, Cem. Concr. Res. 37 (4) (Apr. 2007) 502–511.

[39] F.X. Yao, M.C. Arbestain, S. Virgel, F. Blanco, J. Arostegui, J.A. Maciá-Agulló, F. Macías, Simulated geochemical weathering of a mineral ash-rich biochar in a modified soxhlet reactor, Chemosphere 80 (7) (Aug. 2010) 724–732.

[40] M. Serrapede, G.L. Pesce, R.J. Ball, G. Denuault, Nanostructured Pd hydride microelectrodes: in situ monitoring of pH variations in a porous medium, Anal. Chem. 86 (12) (Jun. 2014) 5758–5765.

[41] Ö. Cizer, C. Rodriguez-Navarro, E. Ruiz-Agudo, J. Elsen, D. Van Gemert, K. Van Balen, Phase and morphology evolution of calcium carbonate precipitated by carbonation of hydrated lime, J. Mater. Sci. 47 (16) (2012) 6151–6165.

[42] G.L. Pesce, D. Morgan, D. Odgers, A. Henry, M. Allen, R.J. Ball, Consolidation of weathered limestone using nanolime, Proc. ICE – Constr. Mater. 166 (2013) 213–228.

[43] I.-C. Kang, Q. Zhang, S. Yin, T. Sato, F. Saito, Preparation of a visible sensitive carbon doped TiO_2 photo-catalyst by grinding TiO_2 with ethanol and heating treatment, Appl. Catal. B Environ. 80 (1–2) (Apr. 2008) 81–87.

[44] B. Demri, D. Muster, XPS study of some calcium compounds, J. Mater. Process. Technol. 55 (3–4) (Dec. 1995) 311–314.

[45] M. Ni, B.D. Ratner, Differentiation of calcium carbonate polymorphs by surface analysis techniques – An XPS and TOF-SIMS study, Surf. Interface Anal. 40 (10) (Oct. 2008) 1356–1361.

[46] S.L. Stipp, M.F. Hochella, Structure and bonding environments at the calcite surface as observed with X-ray photoelectron spectroscopy (XPS) and low

energy electron diffraction (LEED), Geochim. Cosmochim. Acta 55 (6) (Jun. 1991) 1723–1736.
[47] J.F. Moulder, W.F. Stickle, P.E. Sobol, K.D. Bomben, Handbook of X-ray Photoelectron Spectroscopy, Perkin-Elmer Corporation, Eden Prairie, 1992.
[48] A.B. Christie, J. Lee, I. Sutherland, J.M. Walls, An XPS study of ion-induced compositional changes with group II and group IV compounds, Appl. Surf. Sci. 15 (1–4) (Apr. 1983) 224–237.
[49] A.P. Dementjev, Altered layer as sensitive initial chemical state indicator*, J. Vac. Sci. Technol. A Vac. Surfaces, Film. 12 (2) (Mar. 1994) 423.
[50] B. Erdem, R.A. Hunsicker, G.W. Simmons, E.D. Sudol, V.L. Dimonie, M.S. El-Aasser, XPS and FTIR surface characterization of TiO_2 particles used in polymer encapsulation, Langmuir 17 (9) (May 2001) 2664–2669.
[51] R.V. Siriwardane, J.M. Cook, Interactions of SO_2 with sodium deposited on CaO, J. Colloid Interface Sci. 114 (2) (Dec. 1986) 525–535.
[52] H. Lu, P.G. Smirniotis, Calcium oxide doped sorbents for CO_2 uptake in the presence of SO_2 at high temperatures, Ind. Eng. Chem. Res. 48 (11) (Jun. 2009) 5454–5459.
[53] T. Chin, R. Yan, D.T. Liang, Study of the reaction of lime with HCl under simulated flue gas conditions using X-ray diffraction characterization and thermodynamic prediction, Ind. Eng. Chem. Res. 44 (23) (Nov. 2005) 8730–8738.
[54] J.J. Margitan, Mechanism of the atmospheric oxidation of sulfur dioxide. Catalysis by hydroxyl radicals, J. Phys. Chem. 88 (15) (Jul. 1984) 3314–3318.